UNIVERSITAT POLITÈCNICA
DE CATALUNYA
BARCELONATECH

T-H-M coupling with large advection in fractured rock masses using zero-thickness interface elements

by

Adrià Pérez Carreras

ADVERTIMENT La consulta d'aquesta tesi queda condicionada a l'acceptació de les següents condicions d'ús: La difusió d'aquesta tesi per mitjà del repositori institucional UPCommons (http://upcommons.upc.edu/tesis) i el repositori cooperatiu TDX (http://www.tdx.cat/) ha estat autoritzada pels titulars dels drets de propietat intel·lectual **únicament per a usos privats** emmarcats en activitats d'investigació i docència. No s'autoritza la seva reproducció amb finalitats de lucre ni la seva difusió i posada a disposició des d'un lloc aliè al servei UPCommons o TDX. No s'autoritza la presentació del seu contingut en una finestra o marc aliè a UPCommons (*framing*). Aquesta reserva de drets afecta tant al resum de presentació de la tesi com als seus continguts. En la utilització o cita de parts de la tesi és obligat indicar el nom de la persona autora.

ADVERTENCIA La consulta de esta tesis queda condicionada a la aceptación de las siguientes condiciones de uso: La difusión de esta tesis por medio del repositorio institucional UPCommons (http://upcommons.upc.edu/tesis) y el repositorio cooperativo TDR (http://www.tdx.cat/?locale-attribute=es) ha sido autorizada por los titulares de los derechos de propiedad intelectual **únicamente para usos privados enmarcados** en actividades de investigación y docencia. No se autoriza su reproducción con finalidades de lucro ni su difusión y puesta a disposición desde un sitio ajeno al servicio UPCommons No se autoriza la presentación de su contenido en una ventana o marco ajeno a UPCommons (*framing)*. Esta reserva de derechos afecta tanto al resumen de presentación de la tesis como a sus contenidos. En la utilización o cita de partes de la tesis es obligado indicar el nombre de la persona autora.

WARNING On having consulted this thesis you're accepting the following use conditions: Spreading this thesis by the institutional repository UPCommons (http://upcommons.upc.edu/tesis) and the cooperative repository TDX (http://www.tdx.cat/?locale-attribute=en) has been authorized by the titular of the intellectual property rights **only for private uses** placed in investigation and teaching activities. Reproduction with lucrative aims is not authorized neither its spreading nor availability from a site foreign to the UPCommons service. Introducing its content in a window or frame foreign to the UPCommons service is not authorized (framing). These rights affect to the presentation summary of the thesis as well as to its contents. In the using or citation of parts of the thesis it's obliged to indicate the name of the author.

School of Civil Engineering of Barcelona
UPC BARCELONATECH

Department of Civil and Environmental Engineering

T-H-M coupling with large advection in fractured rock masses using zero-thickness interface elements

Doctoral Thesis submitted by:

ADRIÀ PÉREZ CARRERAS

Supervised by:

IGNACIO CAROL

PERE PRAT

Ph.D. program in Geotechnical Engineering

Division of Geotechnical Engineering and Geosciences

Barcelona, September 2018

Agradecimientos

Tras cinco años de trabajo en la realización de esta tesis y más de quince en la UPC, resulta complicado agradecer en unas pocas líneas a todas aquellas personas que han formado parte de mi vida a lo largo de este tiempo y me han ayudado, desde dentro o desde fuera, a poder llevar a cabo esta tesis y todos los cursos de grado y máster que ahora quedan atrás.

En primer lugar, agradecer a los directores de esta tesis, los profesores Ignacio Carol y Pere Prat de la Sección de Ingeniería del Terreno de la UPC por su dedicación, paciencia y consejo, que han hecho posible que esta tesis hoy sea una realidad.

Asimismo a todos los compañeros del grupo de investigación de Mecánica de Materiales (MECMAT) que me han ayudado en todo momento, especialmente los Drs. Daniel Garolera y Carlos María López.

Sería injusto no mencionar, de igual modo, a todos los profesores y docentes que me han inspirado a lo largo de todos estos años. Quisiera no olvidarme de nadie, por ello solo mencionar a la Escuela de Caminos de Barcelona (ETSECCPB) y al Departamento de Ingeniería Civil y Ambiental de la UPC.

A todo el personal de administración y servicios de la UPC, mi agradecimiento por ayudarme a lidiar con las muchas gestiones que han ido surgiendo a lo largo de estos años. Asimismo, mencionar al CIMNE por facilitarme herramientas que han sido muy importantes para la realización de esta tesis.

Requiere mención el soporte económico recibido por parte del *Departament d'Economia i Coneixement* de la *Generalitat de Catalunya* (ayuda FI-AGAUR), del Ministerio de Economía y Competitividad (ayuda FPU) y del convenio de colaboración entre la UPC y REPSOL S.A.

De forma especial agradecer a mi familia y amigos por haberme apoyado en todo momento, y por su compresión en mis muchas ausencias a lo largo de todos estos años, que no han sido pocas. En especial a mis padres, mi hermano y mi sobrino.

A los que me vieron empezar esta aventura y que lamentablemente no han podido verla finalizar. A mis abuelos.

El Vendrell, septiembre de 2018

Abstract

The study of hydro-mechanical (HM) coupled problems in different areas of civil, environmental or petroleum engineering is common in literature, but the effect of a thermal field by means of the heat transport by a fluid through the discontinuities is not considered in the current tools of analysis, in which the potential effect of the temperature gradient between the fluids flowing through the discontinuities and the in-situ thermal state are not taken into account. However, in most geomechanical problems the mechanical, hydraulic and thermal behaviour of the fractured porous medium may appear coupled with strong interactions between them.

In geomechanics modeling it is important to distinguish between the hydraulic behavior of the porous medium and that of the discontinuities, together generating a double-permeability system where the porous medium provides a small permeability to the whole system and discontinuities establish preferential flow paths providing a larger permeability. Because of high hydraulic velocities in the discontinuities, the advection (transport) may be the dominant heat transfer mode. Thus, the study of THM coupled processes with thermal advection in discontinuities is important in problems with a certain degree of coupling between the mechanical, hydraulic and thermal behavior, and in which the hydraulic flow transports heat with a significant speed through the discontinuities.

It is important to establish a numerical model to study the advection phenomena that differentiates the discontinuity network and the porous medium contributions. In this context, this thesis focuses on the study, formulation, numerical implementation and verification of a THM fully-coupled model with large advection, able to reproduce the advective behaviour that occurs in discontinuities or fractures, in which heat is transported by the fluid. This numerical approach is carried out in the geomechanical context of a fractured porous medium, using the finite element method (FEM) with zero-thickness interface elements to represent the discontinuities or fractures (discrete approach), and assuming saturated conditions, a single incompressible fluid (with constant density) and small strains. It is also assumed that all the non-linear behaviour occurs at the interface elements by means of an elasto-plastic constitutive law based on fracture mechanics, while poro-elasticity is assumed for the porous continuum medium.

Additionally, the numerical approach to the thermal advection presents a singularity in comparison with the pure diffusive problems. When the fluid velocities are low, the numerical formulation can be made by traditional Finite Element Methods (Galerkin). However, when the fluid velocities are high enough and the advection dominates the problem, the standard Galerkin weighting leads to oscillatory results, and consequently the advective term requires a special treatment to stabilize the numerical solution. In this context, a review of different methodologies to solve the large advective problem are presented, selecting the *Streamline Upwind Petrov-Galerkin* (SUPG) method to solve the steady-state, a well-known method that leads to stable solutions for large advective problems. For transient states, this thesis starts with the study of the existing explicit Characteristic Galerkin Method, which carries the

study of the advective phenomena in a Lagrangian manner, following the particle (or heat) with the fluid movement, by setting a moving coordinate system that depends on the fluid velocity and its position in time. Then the implicit form of this method is developed, and finally a new variation of this method is proposed adding a parameter (α) that allows to determine different temporal derivative positions of the advective volume, leading to the α-Implicit Characteristic Galerkin Method. With this new procedure, the large advective transient solution becomes stable if the Courant condition is fulfilled.

In order to verify the fully-coupled THM model with large advection for continuum medium and zero-thickness interface elements, several simple verification examples are presented. Finally, an application to hydraulic fracture (HF) with a single fracture in 2-D is introduced in order to understand the thermal mechanisms that occur in HF problems and how they affect the mechanical and hydraulic fields. In addition, these results are compared with those obtained using the HM model, where the thermal field is not considered.

Additionally, in order to improve the computational capacities of the FEM code, its parallelization has been carried out following a subdomain decomposition strategy, leading to a substantial improvement in the speed of the calculations and showing a good degree of scalability.

Resumen

El estudio de problemas hydro-mecánicos (HM) acoplados en diferentes áreas de ingeniería civil, ambiental o del petróleo es común en la literatura, pero los efectos térmicos del fluido transportando calor a través de fracturas o discontinuidades no se considera en las actuales herramientas de análisis, en las cuales el efecto de la diferencia de temperatura entre el fluido inyectado a través de las discontinuidades y la del medio in situ no se tiene en cuenta. No obstante, en algunos problemas geomecánicos los comportamientos mecánico, hidráulico y térmico del medio poroso fracturado pueden aparecer acoplados con fuertes interacciones entre ellos.

En modelación geomecánica es importante distinguir el comportamiento hidráulico del medio poroso del de las discontinuidades, ambas generando un sistema de doble permeabilidad en el cual el medio poroso proporciona una pequeña permeabilidad al sistema, mientras que las discontinuidades establecen caminos preferentes y proporcionan gran permeabilidad al mismo. Debido a las elevadas velocidades de fluido que se pueden desarrollar en las discontinuidades, la advección (transporte) puede ser el modo dominante de transferencia de calor. Por ello, el estudio de procesos THM acoplados con advección térmica en discontinuidades es importante en problemas con un cierto grado de acoplamiento entre los campos mecánico, hidráulico y térmico, y en los cuales el flujo hidráulico puede transportar calor a gran velocidad a través de las discontinuidades.

Por ello, es importante establecer un modelo numérico para estudiar el fenómeno advectivo que diferencie la contribución de la red de discontinuidades de la del medio continuo poroso. En este contexto, esta tesis está enfocada en el estudio, formulación, implementación numérica y verificación de un modelo THM acoplado monolítico con advección dominante que sea capaz de reproducir el comportamiento advectivo que ocurre en discontinuidades o fracturas, en las cuales el fluido transporta calor. Este estudio se lleva a cabo en el contexto geomecánico de un medio poroso fracturado, empleando el método de los elementos finitos (FEM) con elementos junta de espesor nulo para representar las discontinuidades o fracturas, suponiendo condiciones saturadas, un único fluido incompresible (con densidad constante) y pequeñas deformaciones. También se supone que todo el comportamiento no lineal se desarrolla en las juntas mediante el uso de una ley constitutiva elasto-plástica basada en mecánica de fractura, mientras que el medio continuo poroso se supone de comportamiento poro-elástico.

Adicionalmente, la solución numérica del problema térmico advectivo presenta singularidades con respecto a los problemas de difusión pura. Cuando las velocidades del fluido son bajas, la formulación numérica se puede llevar a cabo mediante Elementos Finitos tradicionales (Galerkin). No obstante, cuando las velocidades del fluido son suficientemente elevadas y la advección domina el problema el método estándar de Galerkin conduce a resultados oscilantes, por lo que el término advectivo requiere un tratamiento especial para estabilizar la solución numérica. En este contexto, se presenta una revisión de diferentes

metodologías para resolver el problema de advección dominante, seleccionando el método *Streamline Upwind Petrov-Galerkin* (SUPG) para resolver el problema en régimen permanente, un método bien conocido que conduce a soluciones estables con advección dominante. Para el régimen transitorio esta tesis empieza con el estudio del método de Características Galerkin explícito, un método existente en el que el fenómeno advectivo se estudia de modo Lagrangiano, siguiendo la partícula (o calor) con el movimiento del fluido, y estableciendo para ello un sistema de coordenadas móvil que depende de la velocidad del fluido y de su posición en el tiempo. Seguidamente se desarrolla la forma implícita de este método, y finalmente se propone una nueva variación del método, añadiendo un parámetro α que permite determinar diferentes posiciones de las derivadas temporales del volumen advectivo, concluyendo en el nuevo α-Implicit Characteristic Galerkin Method. Con esta nueva metodología se estabiliza el problema de gran advección en régimen transitorio si se cumple la condición de Courant.

Con el fin de verificar el modelo THM monolítico acoplado con advección dominante se presentan diversos ejemplos de verificación, tanto para medio continuo poroso como para elementos junta de espesor nulo. Finalmente, se presenta un caso de aplicación a fractura hidráulica (HF), llevando a cabo el análisis numérico de una sola fractura en 2-D con el objetivo de entender los mecanismos térmicos que ocurren en problemas de HF y como éstos afectan sobre los comportamientos mecánico e hidráulico. Además, los resultados de la modelación se comparan con los obtenidos empleando un modelo HM, en el cual no se consideran efectos térmicos.

Adicionalmente, con el objetivo de mejorar la eficiencia computacional del código de Elementos Finitos, se ha llevado a cabo la paralelización del mismo mediante una estrategia de partición de subdominios, resultando en una mejora sustancial de la velocidad de los cálculos y mostrando una buena escalabilidad de los mismos.

Contents

1. Introduction 1

1.1. Introduction and background 1

1.2. Motivation and objectives 2

1.3. Methodology 3

1.4. Structure of the thesis 6

2. Heat transfer with advection in continuous media 9

2.1. Heat transfer with small advection 10

2.2. Heat transfer with large advection 20

2.2.1. Numerical instabilities and Péclet number 20
2.2.2. Steady-state large advection problem 22
2.2.3. Transient large advection problem 30

3. Heat transfer with advection in zero-thickness interface elements 71

3.1. Numerical approach for discontinuities 72

3.2. Formulation of the thermal problem with small advection in interfaces 76

3.3. Formulation of the thermal problem with large advection in interfaces 84

3.3.1. Steady-state thermal problem with large advection in interfaces 84
3.3.2. Transient thermal problem with large advection in interfaces 88

4. Thermo-hydro-mechanical coupling with advection 99

4.1. THM couplings 100

4.1.1. Thermo-mechanical coupling 101
4.1.2. Hydro-thermal coupling 101
4.1.3. Hydro-mechanical coupling 103

4.2. Coupled THM scheme based on a staggered approach 103

4.3. Thermo-Hydro-Mechanical fully coupled formulation 106

4.3.1. THM formulation for continuum medium 106
4.3.2. THM formulation for zero-thickness interface elements 121

4.4. Mechanical constitutive law for interfaces 139

4.4.1. Constitutive model definition 139
4.4.2. Cracking surface 140
4.4.3. Plastic potential (dilatancy) 141
4.4.4. Evolution Law 143
4.4.5. Constitutive integration 146

5. THM model verification and practical applications………………………………………………………147
5.1. THM model verification examples ……………………………………………………………147
5.1.1. THM model verification examples for continuum medium …………………………147
5.1.2. THM model verification examples in interfaces …………………………………………173
5.2. Practical Application: Hydraulic Fracture ……………………………………………………180
5.2.1. Introduction to Hydraulic Fracture ………………………………………………………180
5.2.2. Single fracture modelling in 2-D …………………………………………………………182
6. Summary, conclusions and future research………………………………………………………201
6.1. Summary and conclusions: numerical solution of large advection problems using the FEM………202
6.2. Summary and conclusions: THM coupling with large advection …………………………203
6.3. Summary and conclusions: application to hydraulic fracture and parallel performance…..204
6.4. Future research ……………………………………………………………………………………205
References……………………………………………………………………………………………………207
Appendix A – Acronyms……………………………………………………………………………………215

Chapter 1

Introduction

1.1. Introduction and background

In most geomechanical problems the mechanical, hydraulic and thermal behaviour of the porous medium appear coupled with strong interactions between them. This is called thermo-hydro-mechanical (THM) coupling, and it is the main topic of this Thesis. Further, the creation and/or propagation of discontinuities or fractures through the porous medium may be strongly affected by the variation of fluid pressures and the heat that the fluid may transport trough these discontinuities, producing their opening or closing and leading to strong variations of deformability and permeability of the whole system.

While the study of hydro-mechanical (HM) coupled problems in different areas of civil, environmental or petroleum engineering is common in literature, the effect of a thermal field by means of the heat transport by a fluid through the discontinuities is not considered in the current tools of analysis, in which the potential effect of the temperature gradient between the fluids flowing through the discontinuities and the in-situ thermal state are not taken into account.

The study of coupled THM processes with transport (advection) in discontinuities is important in problems with a certain degree of coupling between the mechanical, hydraulic and thermal behavior, and in which the hydraulic flow transports heat with a significant speed through the discontinuities.

An important case of interest can be found in Petroleum Engineering, concretely in hydraulic fracture (HF) processes where the temperature of the injected fluid may lead to the generation of important temperature gradients that modify the fluid properties (such as viscosity or density) and the stress field by means of induced thermal deformations. These modifications may affect the fracture process, opening or closing of the fractures and, for instance, the production of the reservoir. In these cases, the hydraulic fracture area is situated at great depth, where the temperatures are high, while the injected fluid is located on the surface at ambient temperature. Thus, the injection of the fluid may produce important temperature gradients that could lead to significant variations on the mechanical behavior of these fractures and the oil and gas production of the reservoir.

1.2. Motivation and objectives

In rock and quasi-brittle materials modeling it is important to distinguish between the hydraulic behavior of the porous medium and that of the discontinuities, together generating a double-permeability system. While the porous media provides a small permeability to the whole system, the discontinuities establish preferential flow paths and provide the bigger permeability. Due to the high hydraulic velocities developed in the discontinuities, the main thermal transport may occur through them and the advection may be the dominant heat transfer mode. Thus, it is important to establish a numerical model to study the advection phenomena that differentiates the discontinuity network and the porous medium contributions.

In the geomechanical context of hydraulic fracture (HF), the current tools of analysis do not consider the potential effect of the difference in temperature between the fluids injected and the in-situ thermal state. However, this difference can be very significant, and existing literature suggests that its impact on hydraulic fracture may also be significant in some cases.

Additionally, the numerical approach to the thermal advection presents a singularity in comparison with the pure diffusive problems. When the fluid velocities are low, the formulation and implementation of the additional advective term in the equations can be made by traditional Finite Element Methods (Galerkin). However, when the fluid velocities are high enough, the standard Galerkin weighting leads to oscillatory results, and consequently the advective term requires a special treatment to stabilize the numerical solution. This occurs typically only in fractures or discontinuities, and not in the continuum medium. Determination of whether the fluid velocities are high or low is generally based on the so-called Péclet number (Pe), which is a non-dimensional quantity relating the velocity of advection of a flow and the rate of heat conduction/diffusion in that flow:$Pe \leq 1$ for conduction-dominated problems (small advection) and $Pe > 1$ for advection-dominated problems (large advection).

In this context, the main objective of this thesis is the study, formulation, numerical implementation and verification (with simple application examples) of a coupled numerical model able to reproduce the thermo-hydro-mechanical advective behaviour that occur in discontinuities or fractures in which heat is transported by the fluid. This numerical approach is carried out in the geomechanical context of a fractured porous medium, using the finite element method (FEM) with zero-thickness interface elements to represent the discontinuities or fractures (discrete approach), and assuming saturated conditions, a single incompressible fluid (with constant density) and small strains. It is also assumed that all the non-linear behaviour occurs at the interface elements by means of an elasto-plastic constitutive law based on fracture mechanics, while poro-elasticity is used for the porous continuum medium.

Due to the complexity of the problem (three fields: thermal, hydraulic and mechanical, with potential coupling between all including significant advective terms, even if single-phase flow based on field pressures is considered), a progressive plan for development/implementation/testing has been envisaged, dividing the main objective in different preliminary objectives as follows:

- Study of the numerical issues that arise in solving the large advection problem by the standard FEM procedures and present some numerical techniques which can be applied for its correct solution, both for steady-state and transient processes.
- Theoretical and numerical formulation of the thermal advective problem and its implementation in a new FEM code (T-DRAC) to solve the large advection problem with a known given velocity field (with no couplings) and verify the applicability of the numerical method used to stabilize the thermal advective solution, both for continuum medium and zero-thickness interface elements.
- Numerical implementation of the coupling loops between the available hydro-mechanical code DRAC4 and the new thermal-advective code T-DRAC in order to solve the THM coupled problem with large advection using a staggered strategy.
- Theoretical and numerical formulation of governing equations for THM advective coupling in fractured porous media using the FEM and zero-thickness interface elements (fully-coupled).
- Numerical implementation of the fully coupled formulation in the code DRAC4.
- Parallelization of the FEM code DRAC4 in order to improve the computational capacities of the code.
- Verification examples of the THM advective model and a 2-D application example of hydraulic fracture processes with temperature.

1.3. Methodology

The development of this thesis has been carried out using ingredients from different areas, such as geomechanics, numerical methods and fracture mechanics.

As mentioned in the previous section, the main objective of this thesis is the formulation and numerical implementation of a thermo-hydro-mechanical (THM) model with large advection in zero-thickness interface elements, with the aim of reproduce the initiation and propagation of fractures in a fractured porous media, in which the fluid induces the propagation of fractures and also transports heat. This model is finally applied to the numerical modelling of hydraulic fracture problems where the fluid transports heat at high speed through the fractures or discontinuities.

Due to the strong mechanical behaviour of hydraulic fracture problems, some concepts of geomechanics are necessary to study the initiation and propagation of fractures in a porous medium. This requires the use of concepts of fracture mechanics which are incorporated into the zero-thickness interface constitutive law, while the behaviour of the porous continuum is assumed poro-elastic. Additionally, the interaction of fluid pressures and heat with the mechanical problem forces the introduction of a coupled thermo-hydro-mechanical formulation with large advection.

The use of numerical methods is necessary to solve the differential equations, in this case by means of the FEM. It is important to notice that the solution of the thermal advective equation cannot be properly solved using the traditional Galerkin method when the advection dominates over the conduction (large advection). This situation occurs mainly in fractures or discontinuities, which are numerically represented by zero-thickness interface elements and where the flow can travel at high speed.

This thesis has been developed within the MECMAT (Geotechnics and Mechanics of Materials) research group at UPC (Technical University of Catalonia) taking as starting point several works developed in the past within the group, in particular the following:

a) the initial version of the mechanical FEM code DRAC (Prat, et al., 1993) that provides the possibility of evolutive geometry (construction/excavation) and the optimizations for iterative solvers and GiD post-processing done by Caballero (2005) and the HM coupling implementation in 3-D done by Garolera (2017).

b) the hydro-mechanical (HM) formulation for double-nodded zero-thickness interface elements proposed in 2-D by Segura (2007) and its extension to 3-D presented by Garolera (2017),

c) the elasto-plastic constitutive law for zero-thickness interface elements based on fracture mechanics originally proposed by Carol & Prat (1990) and Carol & Prat (1995) and subsequently modified by Carol, et al., (1997), Carol, et al., (2001) and López (1999) for 2D analysis and extended to 3D by Caballero, et al., (2008).

The specific lines of work of this thesis are described in the following paragraphs:

Literature review. The literature review of this thesis has been focused in the following aspects: 1) formulation of the hydro-mechanical coupling in zero-thickness interface elements; 2) numerical solution of the differential thermal equation with large advection using different methodologies, such as the SUPG method for steady-state or different Characteristic-based methods for transients; 3) numerical methods related to parallel computing; and 4) the state of art of hydraulic fracture and the existing modelling of the problem using a hydro-mechanical coupling with zero-thickness interface elements.

Numerical formulation. The numerical improvements of this thesis focus in the numerical formulation of the thermo-hydro-mechanical problem with large advection in zero-thickness interface elements. With the aim to reach stable solutions when the advection dominates the problem, different formulations have been considered, using finally the SUPG method to solve the steady-state and a new implicit approach based in a Characteristic procedure to solve the transients, which incorporates an α parameter that allows to determine different temporal derivative positions of the advective volume. After stabilizing the thermal advective problem, the fully coupled THM has been formulated for zero-thickness interface elements and for saturated continuum media, incompressible fluid and constant fluid density.

FEM code development. The FEM code development, made to provide the necessary tools for the numerical simulation, may be divided in the following four parts:

1) The thermal equation has been implemented into the available code DRAC4, with no couplings, leading to the code T-DRAC.
2) Then, a staggered strategy has been implemented to solve the coupled THM problem with advection, using the available code DRAC4 to solve the HM coupled problem and the new T-DRAC code to solve the thermal problem with large advection.
3) Finally, the fully coupled THM formulation with advection has been implemented in the code DRAC4, using a Newton-Raphson iteration strategy to solve the system of equations.
4) Additionally, in order to improve the efficiency of the calculations, the code DRAC4 has been parallelized, in a first phase the HM version of the code, in collaboration with other members of the group (Garolera, 2017), and in a second phase, its extension to the THM model with large advection. The changes have focused on the modification of the code structure, the optimal partitioning of the FEM mesh using the library *METIS* (METIS_WebPage, 2013), the implementation of the parallel library *PETSc* (PETSc_Software, 2018) –which provides several parallel solvers–, the implementation of the parallel reading and writing (*input/output*) operations using the library *HDF5* (The_HDF_Group, 2018), the adaptation of the *HDF5 outputs* to the format visualization of *Paraview* (Paraview_WebPage, 2018), the minimization of RAM use and the optimal distribution of tasks between processors.

Verification of the model and simulations. Different verification examples have been performed in order to check the numerical formulation and the code implementation of the THM problem with large advection, for both zero-thickness interface elements and continuum medium. A real application case of a 2-D hydraulic fracture problem with temperature is also presented. Additionally, a parallelization performance analysis of the THM fully-coupled FEM code is presented.

1.4. Structure of the thesis

This thesis consists of six chapters: this Introduction, three chapters dedicated to the development of the THM advective formulation, one chapter related to the verification of the formulations and numerical implementations and one chapter of conclusions and future work:

- **Chapter 2: Heat transfer with advection in continuum media.** The main objective of this chapter is to represent with a numerical model the advection phenomena that may occur due to the hydraulic flow in continuum media and the heat transport with the flow. This chapter is divided in two sections: section 2.1 presents the basis of the thermal advective problem and its solution using the standard FEM Galerkin weighting, that allows solving the problem when the conduction dominates the problem (small advection, $Pe \leq 1$); section 2.2 provides a discussion of the numerical problems that arise in solving the large advection problem ($Pe > 1$) with standard FEM procedures and presents some numerical techniques which can be applied for its correct solution, both for steady-state and transient processes. Finally, some examples of verification are presented.

- **Chapter 3: Heat transfer with advection in zero-thickness interface elements.** The main objective of this chapter is to represent with a numerical model the advection phenomena that occur due to the hydraulic flow present in the discontinuities and the heat transport with the flow. This chapter is divided in three sections: section 3.1 presents a brief review of different numerical approaches for the numerical FEM modeling of discontinuities, concluding in the use of double-nodded zero-thickness interface elements as the approach used in this thesis; section 3.2 presents a classical FEM formulation to solve the conduction-advection problem for zero-thickness interface elements, only valid for small advection ($Pe \leq 1$); section 3.3 presents the solution of the FEM problem with stabilization methodologies in order to solve large advection problems ($Pe > 1$). Finally, some examples of verification are presented.

- **Chapter 4: Thermo-hydro-mechanical coupling with advection.** The main objective of this chapter is to represent with a numerical model the THM advective problem for continuum medium and zero-thickness interface elements in the context of fractured and saturated porous media under the hypothesis of incompressible fluid. For this purpose, the stabilized thermal equations from chapters 2 and 3 and the existing hydro-mechanical model presented by Segura (2007) and Garolera (2017) are used as starting point. This chapter is divided in four sections: section 4.1 describes the main couplings between the three THM fields; section 4.2 describes the THM solution using a staggered coupled strategy; section 4.3 describes the fully coupled THM formulation with advection for continuum medium and interfaces and section 4.4 describes briefly the mechanical constitutive model for zero-thickness interface elements used in this thesis, based on fracture mechanics.

- **Chapter 5: Model verification and practical applications.** This chapter is divided in two sections: the first section presents the numerical verifications of the THM advective model developed in the previous chapters, with special interest in the analytical formulations used for the validation. The second section presents the application of the THM advective model to a hydraulic fracture problem with heat transport in 2-D. The numerical analysis has been performed using the parallel FEM code implemented for this purpose.

- **Chapter 6: Summary, conclusions and future work.** This chapter presents the main conclusions of this doctoral thesis and some considerations for future research.

Chapter 2

Heat transfer with advection in continuous media

Heat transfer is the exchange of thermal energy between and within physical systems. Heat transfer always occurs from a region of high temperature to another region of lower temperature and changes the internal energy of both systems involved according to the First and Second Laws of Thermodynamics.

The fundamental modes of heat transfer are four: thermal conduction, thermal advection, thermal convection and thermal radiation:

- **Thermal conduction** is a heat transfer process based on the direct contact between two bodies, without exchange of matter, in which the heat flows from one body with higher temperature to another one of lower temperature that is in contact with the first one.
- **Thermal advection** is a heat transfer process based on the transport of heat from one place to another by the movement of a fluid, usually a liquid. From the viewpoint of the numerical analysis, this is the advective heat flow.
- **Thermal convection** is a heat transfer process based on the transport of heat from one place to another by the movement of a fluid, usually a gas (e.g. air) and can be confused with the advection process. However, in this case, the fluid transports a quantity of heat that affects the boundary of a solid, and it is transferred to the same by conduction. This heat transfer process may be explained as a mix of the advection and the conduction. From the viewpoint of the numerical analysis, it is applied as a boundary condition of the thermal problem.
- **Thermal radiation** is a heat transfer process that occurs through a vacuum medium (without the presence of matter), transferring energy by means of photons in electromagnetic waves. All matter with a temperature above absolute zero radiates heat,

irrespective of the ambient temperature. This transfer mode is governed by the Stephen-Boltzmann Law.

This thesis is focused on the study of heat transfer by conduction and advection in geomechanical problems with discontinuities (fractures), and on the numerical simulation of those processes using the Finite Element Method.

This chapter is divided in two sections. Section 2.1 presents the basics of the thermal advective problem and its solution using the standard FEM Galerkin weighting, that allows the resolution of the problem when conduction dominates the problem (small advection). Section 2.2 provides a discussion of the numerical problems that arise in solving the large advection problem by the standard FEM procedures and presents some numerical techniques which can be applied for its correct resolution, both for steady-state and transients processes.

In geomechanics, it may be assumed that in the porous media (represented numerically by continuum elements) the fluid velocity is small enough to generally develop small advection. However, the discontinuities (Chapter 3) are generally preferential paths where the fluid flows at higher velocities and consequently the advection phenomena may be dominant. In both cases it is assumed saturated medium and incompressible fluid.

2.1. Heat transfer with small advection

This section describes the numerical solution of the thermal problem for small advection in continuous media. It must be noted that this procedure leads to numerical instabilities when fluid velocities becomes large and the advection dominates the problem.

Governing equations

According to Fourier's Law, the amount of heat Q^T per unit of time that flows through a wall of area A and thickness b (Figure 2.1) with prescribed temperatures at the wall borders ϕ_1 and ϕ_2 ($\phi_1 > \phi_2$) can be written as:

$$Q^T = \frac{k^T}{b} A(\phi_1 - \phi_2) \tag{2.1}$$

where k^T is the thermal conductivity, a property of the material that can be expressed in $[J/(s\ m\ {}^oC)]$. Additionally, the amount of heat that flows through a unit surface per unit of time is known as the *heat flow* and can be written as:

$$q^T = \frac{Q^T}{A} = \frac{k^T}{b}(\phi_1 - \phi_2) \tag{2.2}$$

The linear discretized form of Eq. (2.2) does not exist in transient processes due in general to the fact that the heat flow varies locally and with time. The differential equations equivalent to Eqs. (2.1) and (2.2) are:

$$dQ^T = -k^T \, dA \frac{\partial \phi}{\partial n} \tag{2.3}$$

$$q^T = \frac{dQ^T}{dA} = -k^T \, \frac{\partial \phi}{\partial n} \tag{2.4}$$

where n is the distance along the direction normal to the plane of a differential element of surface dA through which the heat flows. The minus sign of the equations means that the heat flows in the direction of decreasing temperatures.

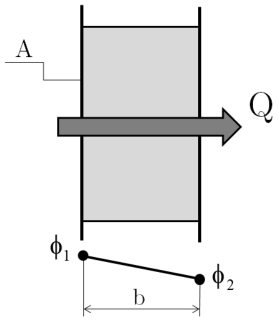

Figure 2.1: Heat conduction through a wall of thickness b and area A.

In the general case of a 3-D continuum, described by a Cartesian coordinate system (x, y, z), and assuming isotropic conductivity, the flux described by Eq. (2.4) mey be written as:

$$q_x^T = -k^T \, \frac{\partial \phi}{\partial x}, \qquad q_y^T = -k^T \, \frac{\partial \phi}{\partial y}, \qquad q_z^T = -k^T \, \frac{\partial \phi}{\partial z} \tag{2.5}$$

and the matrix form can be written as:

$$\mathbf{q}^T = -k^T \, \boldsymbol{\nabla} \phi \qquad \text{with} \qquad \mathbf{q}^T = \begin{bmatrix} q_x \\ q_y \\ q_z \end{bmatrix} \qquad \text{and} \qquad \boldsymbol{\nabla} = \begin{bmatrix} \partial/\partial x \\ \partial/\partial y \\ \partial/\partial z \end{bmatrix} \tag{2.6}$$

Equations (2.6) are only valid for thermally isotropic materials. For non-isotropic materials thermal conductivity varies with direction, and the equation (2.6) may be re-written as:

$$\mathbf{q}^T = -\mathbf{D}^T \, \boldsymbol{\nabla} \phi \tag{2.7}$$

where $\mathbf{D}^T$ is the symmetric second order conductivity tensor (constitutive matrix of the conduction problem), which is represented by the following 3x3 matrix in a three-dimensional problem:

$$\mathbf{D}^T = \begin{bmatrix} k_{xx}^T & k_{xy}^T & k_{xz}^T \\ k_{yx}^T & k_{yy}^T & k_{yz}^T \\ k_{zx}^T & k_{zy}^T & k_{zz}^T \end{bmatrix} \tag{2.8}$$

where $k_{xy}^T = k_{yx}^T$, $k_{xz}^T = k_{zx}^T$ and $k_{yz}^T = k_{zy}^T$.

Besides Fourier equation (2.7), the other fundamental equation of heat flow is the heat continuity (or heat conservation) equation. In 2-D (Figure 2.2) this equation may be written as:

$$q_x^T dy + q_y^T dx - \left(q_x^T + \frac{\partial q_x^T}{\partial x}dx\right)dy - \left(q_y^T + \frac{\partial q_y^T}{\partial y}dy\right)dx + Q^T dxdy = \rho c\frac{\partial \phi}{\partial t}dxdy \tag{2.9}$$

This equation may be interpreted physically as the heat entering less the heat leaving must be equal to the accumulated heat; ρ is the density $[kg/m^3]$ and c is the thermal capacity $[J/(kg\ °C)]$ of the material. Simplification of the equation and generalization to three dimensions leads to:

$$Q^{(T)} - \frac{\partial q_x^T}{\partial x} - \frac{\partial q_y^T}{\partial y} - \frac{\partial q_z^T}{\partial z} = \rho c\frac{\partial \phi}{\partial t} \tag{2.10}$$

where $Q^{(T)}$ is a source term that does not appear in most applications.

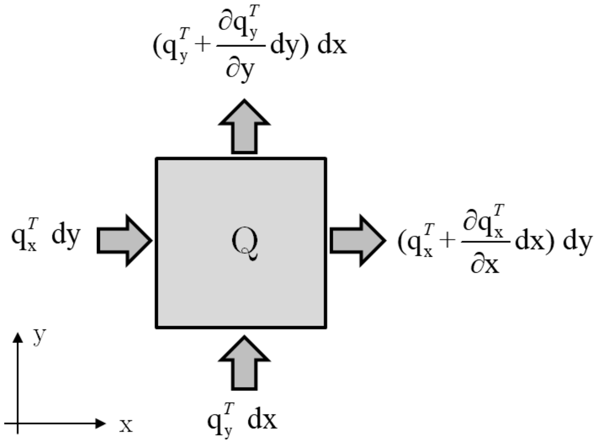

Figure 2.2: Balance of heat flow in a two-dimensional domain

If the solid body is porous and the fluid circulates within the pores, another type of heat transfer may take place consisting of the pore fluid transporting heat from one point to another within the body due to its movement. This phenomenon is known as advection.

If the pore fluid velocity vector (Darcy's velocity) is $\mathbf{v} = [v_x \quad v_y \quad v_z]^\top$, the heat flow vector defined by the equation of conduction in the transient problem (2.7) can be rewritten as:

$$\mathbf{q}^T = -\mathbf{D}^T \boldsymbol{\nabla}\phi \ + \ \rho c\phi\mathbf{v} \tag{2.11}$$

The field velocity $\mathbf{v}$ is usually obtained as the result of the solution of a pore fluid flow problem. Considering that $\mathbf{D}^T$ is expressed in principal directions (off-diagonal terms equal to zero), the Cartesian components of Eq. (2.11) becomes:

$$q_x^T = -k_x^T\frac{\partial \phi}{\partial x} + \rho c\phi v_x \quad ; \quad q_y^T = -k_y^T\frac{\partial \phi}{\partial y} + \rho c\phi v_y \quad ; \quad q_z^T = -k_z^T\frac{\partial \phi}{\partial z} + \rho c\phi v_z \tag{2.12}$$

Substituting Eqs. (2.12) in (2.10) results in the following:

$$Q^T + \frac{\partial}{\partial x}\left(k_x^T \frac{\partial \phi}{\partial x}\right) + \frac{\partial}{\partial y}\left(k_z^T \frac{\partial \phi}{\partial z}\right) + \frac{\partial}{\partial z}\left(k_z^T \frac{\partial \phi}{\partial z}\right) = \rho c \left(\frac{\partial \phi}{\partial t} + v_x \frac{\partial \phi}{\partial x} + v_y \frac{\partial \phi}{\partial y} + v_z \frac{\partial \phi}{\partial z}\right) \tag{2.13}$$

Generalizing the above equation to three dimensions and writing it in matrix form the *transient heat conduction-advection differential equation* is obtained:

$$\boxed{\rho c \left(\frac{\partial \phi}{\partial t} + [\mathbf{v}]^\top \ \boldsymbol{\nabla} \phi\right) - [\boldsymbol{\nabla}]^\top \ \mathbf{D}^T \ \boldsymbol{\nabla} \phi - Q^T = 0} \qquad \text{in} \qquad \Omega \tag{2.14}$$

where $\mathbf{D}^T$ is a diagonal matrix if the solid is thermally isotropic and $[\ \ ]^\top$ denotes the transposed of a vector or a matrix (not to be confused with super index T which stands for "thermal").

Note that the *transient heat conduction differential equation* is a particular case of Eq. (2.14), for $\mathbf{v} = 0$:

$$\rho c \frac{\partial \phi}{\partial t} - [\boldsymbol{\nabla}]^\top \ \mathbf{D}^T \ \boldsymbol{\nabla} \phi - Q^T = 0 \qquad \text{in} \qquad \Omega \tag{2.15}$$

In the same way, from Eq. (2.15) and leaving out the transient terms, it is possible to obtain the *steady-state heat conduction differential equation:*

$$[\boldsymbol{\nabla}]^\top \ \mathbf{D}^T \ \boldsymbol{\nabla} \phi + Q^T = 0 \qquad \text{in} \qquad \Omega \tag{2.16}$$

And the *steady-state heat conduction-advection differential equation* is also obtained from Eq. (2.14) by leaving out the transient terms:

$$\rho c \ [\mathbf{v}]^\top \ \boldsymbol{\nabla} \phi - [\boldsymbol{\nabla}]^\top \ \mathbf{D}^T \ \boldsymbol{\nabla} \phi - Q^T = 0 \qquad \text{in} \qquad \Omega \tag{2.17}$$

Boundary conditions

There are two basic kinds of boundary conditions applicable to the transient conduction-advection differential equation. The first one is the Dirichlet boundary condition, in which the temperature values are imposed on the part of a boundary Γ_ϕ:

$$\phi = \bar{\phi}(x, y, x, t) \qquad \text{on} \qquad \Gamma_\phi \tag{2.18}$$

The second one is the Neumann boundary condition, in which the normal heat flow is prescribed on the remaining part of the boundary Γ_q:

$$q_n^T = \bar{q}_n^T(x, y, z, t) \qquad \text{on} \qquad \Gamma_\mathrm{q} \tag{2.19}$$

where q_n^T is the flow normal to the boundary and $\bar{q}_n$ is the prescribed value of the flow. The flow q_n^T is calculated as the normal projection of the flow vector $\mathbf{q}^T$ on the boundary Γ_q. Using Eq. (2.11) this condition becomes:

$$q_n^T = [\mathbf{n}]^\top \mathbf{q}^T = -[\mathbf{n}]^\top \mathbf{D}^T \ \boldsymbol{\nabla}\phi \ + \ \rho c \phi v_n \tag{2.20}$$

where $v_n = [\mathbf{n}]^\top \mathbf{v}$ is the normal velocity at the boundary $\mathit{\Gamma}_q$. Using Eqs. (2.19) and (2.20) the same equation may be finally written as:

$$-\ \rho c \phi v_n + [\mathbf{n}]^\top \mathbf{D}^T \ \boldsymbol{\nabla}\phi + \bar{q}_n^T = 0 \qquad \text{on} \qquad \Gamma_\mathrm{q} \tag{2.21}$$

The term $\bar{q}_n$ may be a known normal heat flow applied to the boundary:

$$\bar{q}_n^T = \bar{q}^{\,T} \tag{2.22}$$

Additionally to the two basic types of boundary conditions, sometimes it may be necessary to consider a third type, which may be regarded as a generalization of the Neumann condition, and it is known as the convective boundary condition. This is applicable when a convective flow exists in the contact between the boundary of a solid and a fluid that surrounds it. The heat being transferred by convection in the boundary between both is defined with the Newton’s Law of Cooling:

$$\frac{dQ^T}{dt} = \alpha_{conv}^{BC} \ A_s(\phi - \phi_{ext}) \tag{2.23}$$

where α_{conv}^{BC} is the convection coefficient for the boundary condition ($J/(s\ m^2 {}^oC)$, A_s is the area of the solid in contact with the fluid, ϕ is the temperature of the solid surface and ϕ_{ext} is the temperature of the fluid that is in contact with the solid (usually air). From the viewpoint of the numerical analysis, the effect of the convection is treated as a mixed-type boundary condition and may be written as:

$$q_n^T = \alpha_{conv}^{BC} \ (\phi - \phi_{ext}) \tag{2.24}$$

Substituting Eqs. (2.22) and (2.24) in Eq. (2.20) results in the generalized Neumann boundary condition of the conduction-advection heat transfer problem:

$$-\ \rho c \phi v_n + [\mathbf{n}]^\top \mathbf{D}^T \ \boldsymbol{\nabla}\phi + \bar{q}^{\,T} + \alpha_{conv}^{BC} \ (\phi - \phi_{ext}) \ = 0 \qquad on \qquad \Gamma_\mathrm{q} \tag{2.25}$$

where $\rho c \phi v_n$ does not appear in pure conduction problems ($v_n = 0$).

Finally, the initial temperature condition for the transient problem can be written as:

$$\phi(x,y,z,t_0) = \phi_0(x,y,z) \qquad \text{in} \qquad \Omega \tag{2.26}$$

Spatial Discretization

Spatial discretization of Eq. (2.14) over the domain Ω by using Finite Elements is accomplished assuming that the temperature inside each finite element is written as:

$$\phi \cong \hat{\phi} = \sum_{a=1}^{n} N^{(a)} \ \phi^{(a)} = [\mathbf{N}]^\top \boldsymbol{\phi}_\mathrm{e} \tag{2.27}$$

where $\hat{\phi}$ is the approximate value of the temperature at a given point inside the element, $\phi^{(a)}$ is the value of $\hat{\phi}$ at node (a), $N^{(a)}$ is the shape function of node (a) and n is the number of nodes of the element. This notation with node indices within parenthesis and located as a super index, is borrowed from Zienkiewicz & Taylor (2000b) in order to avoid confusion with other indices necessary in the formulation.

Eq. (2.14) represents the strong form of the governing differential equations of the problem and Eqs. (2.18) and (2.25) the boundary conditions. Replacing the approximation $\hat{\phi}$ in Eqs. (2.14) and (2.25), leads to:

$$-\rho c \frac{\partial \hat{\phi}}{\partial t} - \rho c\ [\mathbf{v}]^{\top} \boldsymbol{\nabla} \hat{\phi} + [\boldsymbol{\nabla}]^{\top}\ \mathbf{D}^{T}\ \boldsymbol{\nabla} \hat{\phi} + Q = r_{\Omega} \qquad \text{on} \qquad \Omega \tag{2.28}$$

$$-\ \rho c \hat{\phi} v_n + [\mathbf{n}]^{\top} \mathbf{D}^{T}\ \boldsymbol{\nabla} \hat{\phi} +\ \bar{q}^{\,T} + \alpha_{conv}^{BC}\ \left(\hat{\phi} - \phi_{ext}\right) = r_{\Gamma} \qquad \text{on} \qquad \Gamma_{\mathrm{q}} \tag{2.29}$$

where r_{Ω} and r_{Γ} are the residuals from the finite element approximation. For the Dirichlet boundary conditions (2.18), it is assumed that the condition is satisfied exactly at prescribed nodes ($\hat{\phi} = \phi$).

Using the weighted residuals method to minimize r_{Ω} and r_{Γ}, the following integral expression is obtained:

$$\int_{\Omega} w\, r_{\Omega}\ \mathrm{d}\Omega + \int_{\Gamma_{\mathrm{q}}} \bar{w}\, r_{\Gamma}\ \mathrm{d}\Gamma = 0 \tag{2.30}$$

where w and $\bar{w}$ are weight functions. Substituting Eqs. (2.28) and (2.29) in (2.30), the weak form of the differential equation is obtained:

$$\begin{gathered}\int_{\Omega} w \left(-\rho c \frac{\partial \hat{\phi}}{\partial t} - \rho c\ [\mathbf{v}]^{\top}\ \boldsymbol{\nabla} \hat{\phi} + [\boldsymbol{\nabla}]^{\top}\ \mathbf{D}^{T}\ \boldsymbol{\nabla} \hat{\phi} + Q^{T}\right) \mathrm{d}\Omega \\ + \int_{\Gamma_{\mathrm{q}}} \bar{w} \left(-\ \rho c \hat{\phi} v_n + [\mathbf{n}]^{\top} \mathbf{D}^{T}\ \boldsymbol{\nabla} \hat{\phi} + \bar{q}^{T} + \alpha_{conv}^{BC}\ \left(\hat{\phi} - \phi_{ext}\right)\right) \mathrm{d}\Gamma = 0\end{gathered} \tag{2.31}$$

Assuming $\bar{w} = -w$ on the boundary and using the standard Galerkin weighing, in which the weight functions are made equal consecutively to each of the nodal interpolation functions ($w = N^{(1)}, N^{(2)}, \ldots$), the previous integral form is transformed into:

$$\begin{gathered}\int_{\Omega} N^{(a)} \left(-\rho c \frac{\partial \hat{\phi}}{\partial t} - \rho c\ [\mathbf{v}]^{\top}\ \boldsymbol{\nabla} \hat{\phi} + [\boldsymbol{\nabla}]^{\top}\ \mathbf{D}^{T}\ \boldsymbol{\nabla} \hat{\phi} + Q^{T}\right) \mathrm{d}\Omega \\ - \int_{\Gamma_{\mathrm{q}}} N^{(a)} \left(-\ \rho c \hat{\phi} v_n + [\mathbf{n}]^{\top} \mathbf{D}^{T}\ \boldsymbol{\nabla} \hat{\phi} + \bar{q}^{T} + \alpha_{conv}^{BC}\ \left(\hat{\phi} - \phi_{ext}\right)\right) \mathrm{d}\Gamma = \\ = 0\end{gathered} \tag{2.32}$$

In order to integrate by parts the first term of the above equation, the Divergence Theorem needs to be written in the form:

$$\int_{\Omega} \omega(\boldsymbol{\nabla}\cdot\boldsymbol{\psi})\,\mathrm{d}\Omega = \int_{\Omega} \boldsymbol{\psi}\cdot\boldsymbol{\nabla}\omega\,\mathrm{d}\Omega + \int_{\Gamma} \omega\;\boldsymbol{\psi}\cdot\mathbf{n}\,\mathrm{d}\Gamma \tag{2.33}$$

The application of this theorem to the first term of Eq. (2.32) leads to:

$$\begin{aligned} &\int_{\Omega} N^{(a)}\,\left([\boldsymbol{\nabla}]^{\top}\,\mathbf{D}^{T}\,\boldsymbol{\nabla}\hat{\phi}\right)\mathrm{d}\Omega \\ &\qquad = -\int_{\Omega}\left([\boldsymbol{\nabla}N^{(a)}]^{\top}\,\mathbf{D}^{T}\,\boldsymbol{\nabla}\hat{\phi}\right)\mathrm{d}\Omega + \int_{\Gamma} N^{(a)}\,\left([\mathbf{n}]^{\top}\mathbf{D}^{T}\,\boldsymbol{\nabla}\hat{\phi}\right)\mathrm{d}\Gamma \end{aligned} \tag{2.34}$$

Substituting Eq. (2.34) in (2.32) and noticing that $\Gamma = \Gamma_{\mathrm{q}} + \Gamma_{\boldsymbol{\phi}}$, results in:

$$\begin{aligned} \rho c\int_{\Omega} N^{(a)}\,\frac{\partial\hat{\phi}}{\partial t}\,\mathrm{d}\Omega + \int_{\Omega}[\boldsymbol{\nabla}N_i]^{\top}\,\mathbf{D}^{T}\,\boldsymbol{\nabla}\hat{\phi}\,\mathrm{d}\Omega + \rho c\int_{\Omega} N^{(a)}\,[\mathbf{v}]^{\top}\boldsymbol{\nabla}\hat{\phi}\,\mathrm{d}\Omega& \\ + \int_{\Gamma_{\mathrm{q}}} N^{(a)}\alpha_{conv}^{BC}\,\hat{\phi}\,\mathrm{d}\Gamma - \rho c\int_{\Gamma_{\mathrm{q}}} N^{(a)}v_n\hat{\phi}\,\mathrm{d}\Gamma& \\ = \int_{\Omega} N^{(a)}Q^{T}\,\mathrm{d}\Omega - \int_{\Gamma_{\mathrm{q}}} N^{(a)}(\bar{q}^{\,T} + \alpha_{conv}^{BC}\,\phi_{ext})\,\mathrm{d}\Gamma& \\ - \int_{\Gamma_{\boldsymbol{\phi}}} N^{(a)}[\mathbf{n}]^{\top}\,\mathbf{D}^{T}\,\boldsymbol{\nabla}\hat{\phi}\,\mathrm{d}\Gamma& \end{aligned} \tag{2.35}$$

where $\int_{\Gamma_{\boldsymbol{\phi}}} N^{(a)}\,[\mathbf{n}]^{\top}\mathbf{D}^{T}\,\boldsymbol{\nabla}\hat{\phi}\,\mathrm{d}\Gamma$ is the normal flow on the boundary $\Gamma_{\boldsymbol{\phi}}$ where the temperature is prescribed.

Substituting the nodal approximation of Eq. (2.27) in (2.35) the following algebraic system of equations is obtained:

$$\mathbf{C}\;\dot{\boldsymbol{\phi}} + \mathbf{K}\;\boldsymbol{\phi} = \mathbf{f} \tag{2.36}$$

where

$$\boldsymbol{\phi} = [\phi^{(1)}, \phi^{(2)}, \ldots \phi^{(n)}]^{\top} \qquad \text{and} \qquad \dot{\boldsymbol{\phi}} = \left[\frac{\partial\phi^{(1)}}{\partial t}, \frac{\partial\phi^{(2)}}{\partial t}, \ldots, \frac{\partial\phi^{(n)}}{\partial t}\right]^{\top} \tag{2.37}$$

are the nodal vector of temperatures and the nodal vector of temperatures rates at time t, $\mathbf{K}$ is the global stiffness matrix, $\mathbf{C}$ is the capacity matrix and $\mathbf{f}$ the vector of equivalent flow, which are obtained by the assembly of the contribution of each element of the mesh. Therefore the stiffness matrix $\mathbf{K}_{\mathrm{e}}$ and the force vector $\mathbf{f}_{\mathrm{e}}$ of each element must be calculated first. These are defined by:

$$\mathbf{C}_{\mathrm{e}} = \begin{bmatrix} C^{(11)} & \cdots & C^{(1n)} \\ & & \vdots \\ sym & & C^{(nn)} \end{bmatrix} \tag{2.38}$$

$$\mathbf{K}_{\mathrm{e}} = \begin{bmatrix} K^{(11)} & \cdots & K^{(1n)} \\ & & \vdots \\ sym & & K^{(nn)} \end{bmatrix} \tag{2.39}$$

$$\mathbf{f}_{\mathrm{e}} = [f^{(1)}, f^{(2)}, \dots, f^{(n)}]^{\top} \tag{2.40}$$

where

$$C^{(a,b)} = \rho c \int_{\Omega_{\mathrm{e}}} N^{(a)}\ N^{(b)}\, \mathrm{d}\Omega \tag{2.41}$$

$$\begin{aligned} K^{(a,b)} = &\int_{\Omega_{\mathrm{e}}} \left(\rho c\ N^{(a)}\ [\mathbf{v}]^{\top}\ \boldsymbol{\nabla} N^{(b)} + [\boldsymbol{\nabla}]^{\top} N^{(a)}\ \mathbf{D}^{T}\ \boldsymbol{\nabla} N^{(b)}\right) \mathrm{d}\Omega_{\mathrm{e}} - \rho c \int_{\Gamma_{\mathrm{q}}} N^{(a)} v_n\, N^{(b)} \mathrm{d}\Gamma \\ &+ \alpha_{conv}^{BC} \int_{\Gamma_{\mathrm{q}}} N^{(a)} N^{(b)}\, \mathrm{d}\Gamma \end{aligned} \tag{2.42}$$

$$f^{(a)} = \int_{\Omega_{\mathrm{e}}} N^{(a)} Q^{T}\ \mathrm{d}\Omega\ - \int_{\Gamma_{\mathrm{q}}} N^{(a)}\ \bar{q}^{\,T}\, \mathrm{d}\Gamma - \int_{\Gamma_{\mathrm{q}}} N^{(a)} (\alpha_{conv}^{BC}\ \phi_{ext})\, \mathrm{d}\Gamma - q_{n_i} \tag{2.43}$$

The term $\bar{q}^{\,T}$ appears only if the elements have some edge with an imposed flow on the boundary Γ_{q} and the terms with α_{conv}^{BC} coefficients appear only if the elements have some edge with an imposed convective boundary condition.

The term $q_{n_i} = \int_{\Gamma_{\phi}} N^{(a)}\ [\mathbf{n}]^{\top}\ \mathbf{D}^{T}\ \boldsymbol{\nabla} N^{(b)}\ \mathrm{d}\Gamma$ in Eq. (2.43) represents the node (a) component of the heat flow that leaves the element across boundary Γ_{ϕ}. This flow is calculated after obtaining the temperature values $\hat{\phi}$ in the entire domain, and has the meaning of the "reaction" flow vector on the nodes of the element where the variable is prescribed.

Also, the temperature gradient vector of the element can be written as:

$$\boldsymbol{\nabla}\phi = \boldsymbol{\nabla}([\mathbf{N}]^{\top} \boldsymbol{\phi}_{\mathrm{e}}) = [\boldsymbol{\nabla}\mathbf{N}]^{\top}\ \boldsymbol{\phi}_{\mathrm{e}} = [\mathbf{B}]^{\top} \boldsymbol{\phi}_{\mathrm{e}} \tag{2.44}$$

where $\mathbf{B}$ is the gradient matrix of the element:

$$\mathbf{B} = \boldsymbol{\nabla}\mathbf{N} = \left[\nabla N^{(1)}, \nabla N^{(2)}, \dots, \nabla N^{(n)}\right] = \left[\mathbf{B}^{(1)}, \mathbf{B}^{(2)}, \dots, \mathbf{B}^{(n)}\right] \tag{2.45}$$

Time Discretization

The second step in the transient problem formulation is to perform the time integration of the system of equations (2.36) using the finite difference method (FDM) assuming a linear evolution of the nodal temperatures between times n and $n+1$ (Figure 2.3).

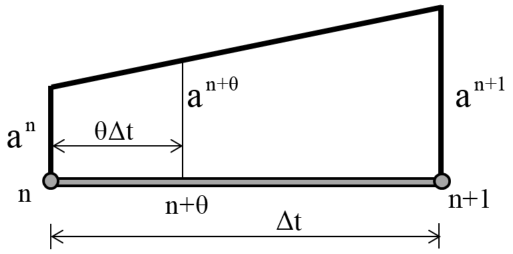

Figure 2.3: FDM Scheme: selection of an intermediate point in the interval $[t_n, t_{n+1}]$

From Figure 2.3 the following is obtained:

$$\phi = \phi_{n+\theta} = \phi_n + \theta \Delta\phi \tag{2.46}$$

$$\dot{\phi} = \frac{\Delta\phi}{\Delta t} = \frac{\phi_{n+\theta} - \phi_n}{\Delta t} \tag{2.47}$$

Assuming that the spatial discretization equations (2.35) are satisfied at $t_{n+\theta}$, replacing the corresponding expressions of $\boldsymbol{\phi}$ and $\dot{\boldsymbol{\phi}}$ into (2.36), and grouping terms appropriately, leads to the linear matrix equation for a generic time increment:

$$\left[\frac{1}{\Delta t}\mathbf{C} + \theta\ \mathbf{K}\right] \Delta\boldsymbol{\phi}_{\mathrm{e},n+1} = -\mathbf{K}\ \boldsymbol{\phi}_{\mathrm{e},n} + \mathbf{f} = 0 \tag{2.48}$$

In the previous equations, parameter θ defines the intermediate point $t_{n+\theta} = t_n + \theta\Delta t$ within the interval $[t_n, t_{n+1}]$, where the differential equation is satisfied in time.

It is known (Zienkiewicz & Taylor, 2000c) that the scheme is unconditionally stable when $\theta \geq 1/2$. If $0 \leq \theta < 1/2$ the scheme is conditionally stable and requires that:

$$\Delta t < \frac{2}{(1-2\theta)\omega_i} \qquad \text{with} \qquad \omega_i = \frac{K_i}{C_i} \tag{2.49}$$

Depending on the chosen value of θ, a different name for the time discretization method is adopted (Table 2.1). It is also known (Zienkiewicz & Taylor, 2000c) that the best scheme to approximate the solution is reached with $\theta = 2/3$.

Eqs. (2.50)-(2.60) presents a summary of the final FEM transient thermal problem for small advection in continuous media. Some particular cases of interest, as the steady-state problem or the pure conduction thermal problem are also presented.

Table 2.1: Values of θ for the time discretization of the problem

Value of $\boldsymbol{\theta}$	Name
$\boldsymbol{\theta = 0}$	Explicit Euler (“Forward”) scheme
$\boldsymbol{\theta = 1/2}$	Central finite difference (Crank-Nicholson)
$\boldsymbol{\theta = 1}$	Implicit Euler (“Backward”) scheme
$\boldsymbol{\theta = 2/3}$	Galerkin

It must be noted that the use of the standard Galerkin weighting method in the spatial discretization only leads to stable solutions for small advection problems. For this reason, when the advection dominates the problem, it is necessary to use a more appropriate numerical methods that does not result in oscillatory solutions. This methodology is developed in Section 2.2.

Summary 1 - Thermal equation with small advection in continuum media.

$$\left[\frac{1}{\Delta t}\mathbf{C}+\theta\left(\mathbf{K}+\mathbf{K_c}+\mathbf{K^{BC}_{adv}}+\mathbf{K^{BC}_{conv}}\right)\right]\Delta\boldsymbol{\phi}_{n+1} = -(\mathbf{K}+\mathbf{K_c}+\mathbf{K^{BC}_{adv}}+\mathbf{K^{BC}_{conv}})\boldsymbol{\phi}_n+\mathbf{f}_\mathrm{e}+\mathbf{f^{BC}_{conv}} \tag{2.50}$$

where $\boldsymbol{\phi}$ is the element nodal temperature vector (unknown), $\mathbf{C}$ is the thermal capacity matrix, $\mathbf{K}$ is the thermal conduction matrix, $\mathbf{K_c}$ is the thermal advective matrix, $\mathbf{K^{BC}_{adv}}$ is the boundary advective matrix, $\mathbf{f}_\mathrm{e}$ is the element force vector and $\mathbf{K^{BC}_{conv}}$ and $\mathbf{f^{BC}_{conv}}$ are the matrix and the vector resulting of the convective boundary condition, which only appears when this kind of boundary conditions are applied.

$$\mathbf{C}=\int_\Omega \rho c\,[\mathbf{N}]^\top\ \mathbf{N}\ \mathrm{d}\Omega \tag{2.51}$$

$$\mathbf{K}=\int_\Omega [\mathbf{B}]^\top\ \mathbf{D}^T\ \mathbf{B}\ \mathrm{d}\Omega \tag{2.52}$$

$$\mathbf{K_c}=\int_\Omega \rho c\,[\mathbf{N}]^\top\ \mathbf{v}\ \mathbf{B}\ \mathrm{d}\Omega \tag{2.53}$$

$$\mathbf{K^{BC}_{adv}}=-\int_{\Gamma_\mathrm{q}} \rho c\,[\mathbf{N}]^\top\ v_n\ \mathbf{N}\ \mathrm{d}\Gamma \tag{2.54}$$

$$\mathbf{f}_\mathrm{e}=\int_\Omega [\mathbf{N}]^\top\ Q^T\ d\Omega-\int_{\Gamma_\mathrm{q}}[\mathbf{N}]^\top\ \bar{\mathbf{q}}^T\ \mathrm{d}\Gamma \tag{2.55}$$

$$\mathbf{K^{BC}_{conv}}=\alpha^{BC}_{conv}\int_{\Gamma_\mathrm{q}}[\mathbf{N}]^\top\ \mathbf{N}\ \mathrm{d}\Gamma \tag{2.56}$$

$$\mathbf{f^{BC}_{conv}}=-\alpha^{BC}_{conv}\int_{\Gamma_\mathrm{q}}[\mathbf{N}]^\top\phi_{ext}\ \mathrm{d}\Gamma \tag{2.57}$$

From Eq. (2.50) and leaving out the transient terms, the *steady-state thermal equation with advection* can be written as:

$$\left(\mathbf{K}+\mathbf{K_u}+\mathbf{K^{BC}_{adv}}\right)\ \boldsymbol{\phi}=\mathbf{f}_\mathrm{e} \tag{2.58}$$

From Eq. (2.50) and leaving out the advective terms ($\mathbf{v}=0$), the *transient thermal conduction equation* is obtained as follows:

$$\left[\frac{1}{\Delta t}\mathbf{C}+\theta\left(\mathbf{K}+\mathbf{K^{BC}_{conv}}\right)\right]\boldsymbol{\phi}_{n+1}=\mathbf{f}_\mathrm{e}+\mathbf{f^{BC}_{conv}} \tag{2.59}$$

Finally, the *steady-state thermal conduction equation* is obtained leaving out the transient terms from the above equation:

$$\mathbf{K}\ \boldsymbol{\phi}=\mathbf{f}_\mathrm{e} \tag{2.60}$$

2.2. Heat transfer with large advection

It is well known that the standard Galerkin weighting in FEM is very well suited for diffusion-dominated problems, but it performs badly when transport effects prevail. For this reason, the main objective of this section is to represent with a numerical model the advection phenomena that occur due to the hydraulic flow present in the medium and that transports heat with the flow, that is, when the advection phenomenon dominates over the conduction (large advection).

This section is divided in three subsections. The first subsection provides a discussion of the numerical problems that arise in solving the large advective problem by the standard FEM (Galerkin, Section 2.1) and introduces the concept of Péclet number, that allows to determine when a problem (or an element of the FEM mesh) is advection-dominated or not. The second and third subsections present different numerical techniques that can be applied for its correct resolution, both for steady-state and transient problems.

2.2.1. Numerical instabilities and Péclet number

When the fluid velocities are low, the formulation and implementation of the additional term in the equations can be made by traditional FEM methods (Galerkin weighting, Section 2.2). However, when the fluid velocities are high enough, the advective term requires a special treatment. Determination of whether the fluid velocities are high or low is generally based on the so-called Péclet number. The Péclet number (Pe) is a non-dimensional number that relates the velocity of advection of a flow and the rate of heat conduction/diffusion in that flow:

$$Pe = \frac{\text{advective transport rate}}{\text{diffusive transport rate}} \tag{2.61}$$

In order to show the challenges of the numerical modelling of the advection-diffusion equation, considering first the one-dimensional steady-state problem. The governing equation can be written from Eq. (2.48) as:

$$v\frac{d\phi}{dx} - \frac{d}{dx}\left(k^T \frac{d\phi}{dx}\right) - Q^T = 0 \tag{2.62}$$

where ϕ is the unknown nodal variable (e.g. the temperature), v is a known velocity field (e.g. as a result of the hydraulic flow problem), k^T is the diffusion coefficient and Q^T represents the source or reaction term (v, k^T and Q^T are assumed to be constants and ϕ a scalar variable).

After discretizing a domain of length L into n elements of equal size h, and applying the standard Galerkin weighting method (weight functions equal consecutively to each of the interpolation shape functions $w = N^{(1)}, N^{(2)}, \dots$), the following equation is obtained for central nodes (not at the boundaries):

$$(-Pe-1)\hat{\phi}^{(a-1)}+2\hat{\phi}^{(a)}+(Pe-1)\hat{\phi}^{(a+1)}-\frac{Q^T h^2}{k^T}=0 \qquad a=2,n-1 \tag{2.63}$$

where n is the number of nodes and Pe is the Péclet number, which is defined as:

$$Pe=\rho c\,\frac{v\,h}{2k^T} \tag{2.64}$$

Eq. (2.63) is identical to the usual *central finite difference approximation* and can be solved leading to the solution of the problem $\hat{\phi}^{(a)}$. However, as the Péclet number increases the accuracy deteriorates and for $Pe \to \infty$, when only advective terms are of importance, the solution is purely oscillatory and bears no relation to the underlying problem, as shown in the next simple example (where $Q^T = 0$).

Simple academic example: oscillatory results in 1D

A simple academic example in 1-D is presented in order to demonstrate that the standard Galerkin weighting leads to oscillatory results when $Pe > 1$. The geometry (Figure 2.4) consists in a horizontal rod element divided in 8 segments of equal length. The boundary conditions are: prescribed temperature to 0℃ at the left-hand side node of the rod, prescribed temperature to 80℃ at the right-hand side node of the rod and a constant velocity from left to right. With the only variation of the velocity magnitude four results are obtained with different Péclet numbers (Figure 2.5), where it is observed that the solutions begins to oscillate when $Pe > 1$.

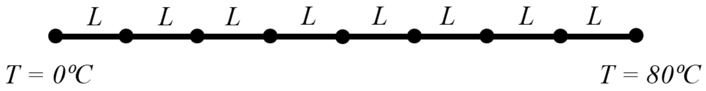

Figure 2.4: Geometry of the domain and boundary conditions.

Summarizing, the solution presented in section 2.2 for the conduction-advection heat transfer problem is only stable when $Pe \leq 1$. When the advection component of the thermal flow dominates over the diffusion thermal flow ($Pe > 1$), the resolution of the problem requires a special numerical treatment. This condition must be fulfilled for all the elements of the FEM mesh, since the Péclet number involves the size of each FE and the velocity of the flow that travels through it.

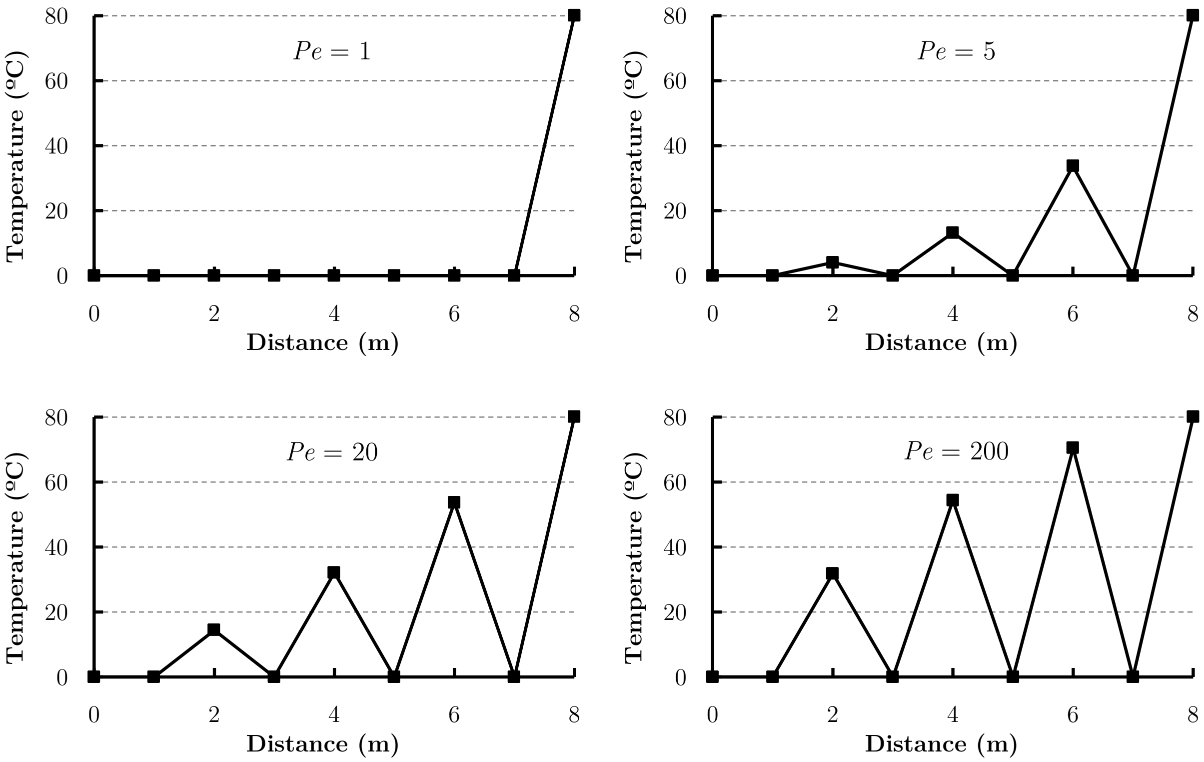

Figure 2.5: Solutions of the simple academic example for different velocities using the traditional Galerkin weighting method in FEM. Oscillations appears when $Pe > 1$.

2.2.2. Steady-state large advection problem

Since the Péclet number (2.64) governs the advection-diffusion equation, it is possible to solve this problem with the standard Galerkin weighting by refining the mesh until reaching a length h of the element small enough so that the Péclet number is equal or smaller than the unity. However, this procedure increase the number of elements of the mesh, and therefore the number of degrees of freedom and the size of the system of equation that must to be solved, making this procedure computationally impracticable for most applications.

For this reason, different methods were proposed to accurately solve the advection-diffusion problem without requiring such highly refined meshes as the Galerkin method does. This section presents the most common techniques to deal with the numerical problems presented in the previous section for the steady-state problems.

The most common method used in order to stabilize the diffusion-advection problem is the *Streamline Upwind Petrov-Galerkin* (SUPG) method, which is based on the modification of the stiffness matrix by using modified weighting functions ($w \neq N^{(1)}, N^{(2)}, \dots$) in order to give more weight to the information of the nodes located upwind. The first *upwind* approach was proposed by Zienkiewicz, et al. (1976) and was used by Christie, et al. (1976) and Zienkiewicz, et al. (1977), expanding the method for quadratic elements in Heinrich & Zienkiewicz (1977). Then Hughes & Brooks (1979) proposed a new weighting function, leading to the *Streamline Upwind* (SU) method. Due to the poor accuracy of this method, Brooks &

Hughes (1982) further developed the *Streamline Upwind Petrov-Galerkin* (SUPG) technique, with an optimal weight function, which was further justified in Johnson, et al. (1984). In parallel, a *Variational Principle* was introduced by Guymon, et al. (1970) and improved by Hughes & Atkinson (1980). Later, in addition, the *Galerkin Least-Squares* (GLS) method was presented by Hughes, et al. (1989), the *Bubble Functions Method* by Biaocchi, et al. (1993), the *Discontinuous Galerkin* methods by Cockburn, et al. (2000) and the *Finite Increment Calculus* (FIC) Method by Oñate (1998). Additionally, many other works have been published in order to improve the SUPG method, such as Hughes, et al. (1987), Hughes & Tezduyar (1984), Hughes & Mallet (1986), Codina, et al. (1992) or Codina (1992), among others.

Full Upwind Solution in 1-D

Following the developments of Section 2.2.1 and in order to obtain the *full upwind* solution, Eqs. (2.63) are transformed changing the central finite difference form to a lateral finite difference form, obtaining the *full upwind* solution as follows:

$$(-2Pe-1)\tilde{\phi}^{(a-1)}+(2+2Pe)\tilde{\phi}^{(a)}+\tilde{\phi}^{(a+1)}-\frac{Q^T h^2}{k^T}=0 \qquad (2.65)$$

With this upwind difference approximation, realistic (though not always accurate) solutions can be obtained through the whole range of Péclet numbers. However, exact nodal solutions are only obtained for pure advection ($Pe=\infty$), in a similar way as the Galerkin finite element form gives exact nodal solutions for pure diffusion (Zienkiewicz & Taylor, 2000c).

Streamline Upwind Petrov-Galerkin (SUPG) in 1-D

This method is introduced in order to improve the above approximations and stabilize the oscillatory solutions, the Petrov-Galerkin method (SUPG) is presented. The method is based on the modification of the stiffness matrix by using modified weighting functions such that instead of directly equal to $N^{(1)}, N^{(2)}, \ldots$ now w is defined consecutively as

$$w=N^{(a)}+\alpha w^{*} \qquad (2.66)$$

where w^{*} represent a set of functions, for which a convenient form is the following discontinuous function in 1-D:

$$w^{*}=\frac{h}{2}\frac{dN^{(a)}}{dx}(\text{sign } v) \qquad (2.67)$$

where h is the length of the element in the direction of flow.

With the above weighting functions the approximation equivalent to that of Eq. (2.63) becomes

$$[-Pe(\alpha+1)-1]\tilde{\phi}^{(a-1)}+[2+2\alpha Pe]\tilde{\phi}^{(a)}+[-Pe(\alpha-1)-1]\tilde{\phi}^{(a+1)}-\frac{Q^T h^2}{k^T}=0 \qquad (2.68)$$

where for $\alpha = 0$ the standard Galerkin approximation (2.63) is obtained, and for $\alpha = 1$ the *full upwind* solution is obtained, each giving exact nodal results for pure diffusion and for pure advection respectively.

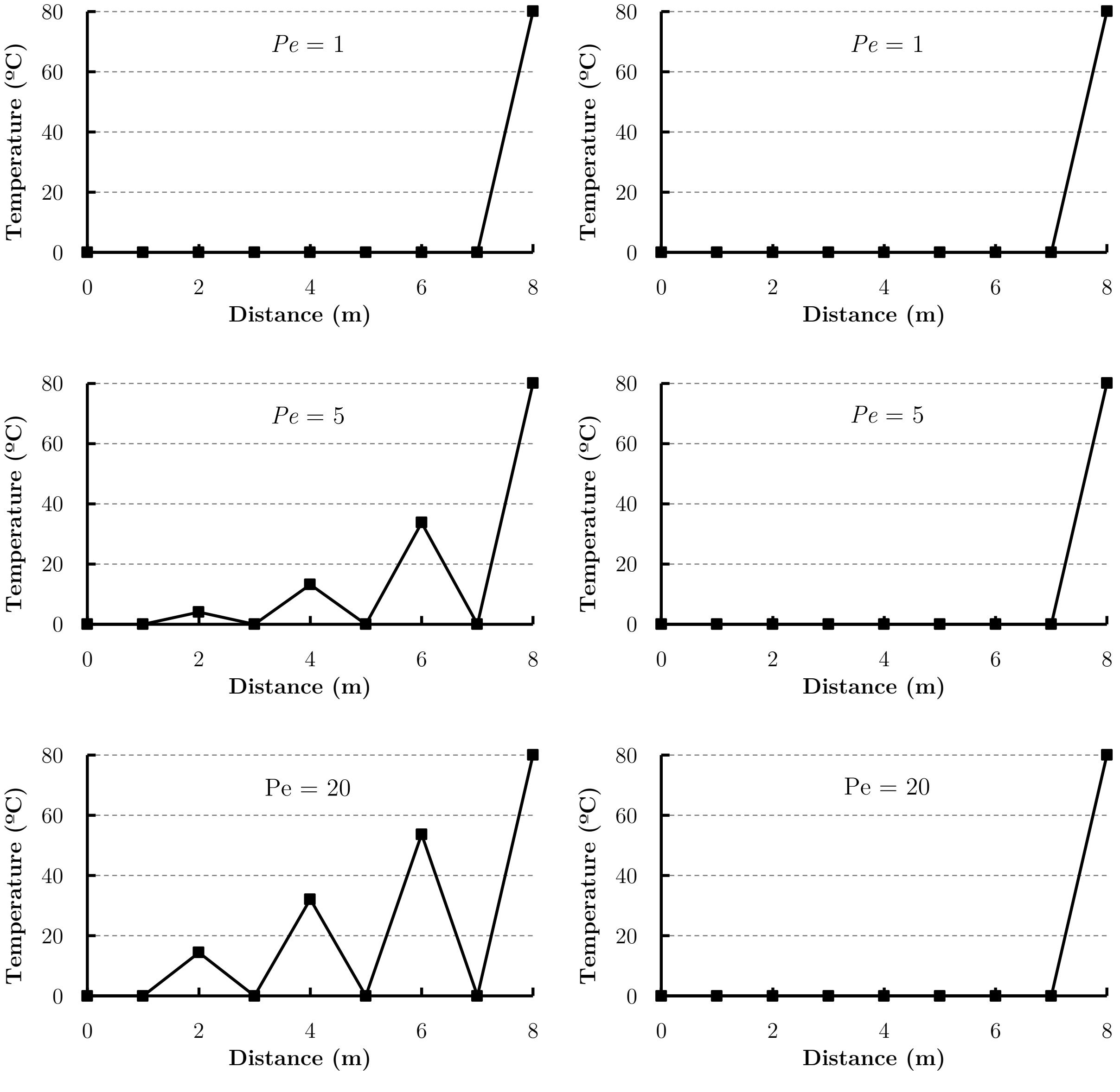

Figure 2.6: Results obtained in a one-dimensional case for a different Péclet numbers (k^T, v, h constants). Comparison between the results obtained using a standard Galerkin discretization (left) and the results obtained with the SUPG method (right), which stabilizes the solution.

In order to obtain exact nodal values for any Pe value, an optimal value of α (α_{opt}) must be used (Zienkiewicz & Taylor, 2000c):

$$|\alpha| = \alpha_{opt} = \coth|Pe| - \frac{1}{|Pe|} \tag{2.69}$$

Finally, in order to test the SUPG formulation in 1-D, the simple academic example of Section 2.2.1 (Figure 2.5) is repeated. Figure 2.6 shows the results using an standard Galerkin discretization in comparison with the results using the SUPG in 1-D. The SUPG method stabilizes the solution and leads to exact node results in 1-D.

Balancing Equation Method in 1-D

An alternative method to reach the same solution is the *Balancing Equation Method*, in which an additional or fictitious diffusion coefficient, k_b^T, is used:

$$k_b^T = \frac{1}{2}\alpha v h \tag{2.70}$$

This *artificial diffusion* is added to the ordinary diffusion of Eq. (2.62), and is solved using the standard Galerkin method. This method is simpler than the Petrov-Galerkin method, especially in 2-D and 3-D problems. However, this procedure is only valid for constant values of Q^T. Otherwise it leads to inaccurate results similar to those obtained for $\alpha = 0$.

Streamline Upwind Petrov-Galerkin Method (SUPG) in 3-D

The last stabilization method presented is the 3-D extension of the Streamline Upwind Petrov-Galerkin method (SUPG). This method has been widely tested and it is the method finally used in the developments and calculations of this thesis.

Expanding de SUPG method to 3-D one may write the 1-D weighting function (2.67) in indicial notation as:

$$w = N^{(a)} + \frac{\alpha_{opt}\, h_{car}}{2} \frac{v_i}{|\mathbf{v}|} \frac{\partial N^{(a)}}{\partial x_i} \tag{2.71}$$

where $N^{(a)}$ are the usual shape functions, v_i are the velocities, h_{car} is the characteristic length of the element (length of the element in the direction of the flow) and α_{opt} is defined by (2.69) in order the obtain exact nodal values for any Péclet value. In this expression, the Péclet number is defined as follows for thermal problems:

$$Pe = \rho c \frac{v\, h_{car}}{2k^T} \tag{2.72}$$

where k^T is the thermal conductivity, ρ is the density, c is the specific heat and the value of h_{car} can be approximated by the following expressions:

$$2-\mathrm{D}\colon h_{car} = \sqrt[2]{A} \qquad ; \qquad 3-\mathrm{D}\colon h_{car} = \sqrt[3]{V} \tag{2.73}$$

where A and V are the area (2-D) and the volume (3-D). This approximation can lead to incorrect solutions of the steady-state problem when one dimension of the element is much larger than the others, as shown in Figure 2.7.a. In this case it is very important to calculate the maximum size of the element in the direction of the velocity vector, as shown in Figure 2.7.b. As the Péclet number depends strongly on h_{car}, the solution will also do. An example confirming this fact is presented at the end of this section.

As presented in Section 2, the weak form for the conduction-advection steady-state problem is defined as follows:

$$\int_{\Omega} w\left(-\rho c\,[\mathbf{v}]^{\top}\boldsymbol{\nabla}\hat{\phi}+[\boldsymbol{\nabla}]^{\top}\,\mathbf{D}^{T}\,\boldsymbol{\nabla}\hat{\phi}+Q^{T}\right)\mathrm{d}\Omega+\int_{\Gamma_{\mathrm{q}}}\overline{w}\left([\mathbf{n}]^{\top}\mathbf{D}^{T}\,\boldsymbol{\nabla}\hat{\phi}+\bar{q}^{\,T}\right)\mathrm{d}\Gamma=0 \tag{2.74}$$

Assuming $\overline{w}\ =-w$, applying the Theorem of the Divergence to the first term of the equation, applying the spatial discretization defined by Eq. (2.27) and using the Petrov-Galerkin weighing of Eq. (2.73), the following system of equations is obtained:

Summary 2 - Steady-state thermal equation for large advection in continuum media.

$$(\mathbf{K}+\mathbf{K_{SUPG}})\ \boldsymbol{\phi}\ =(\mathbf{f}_{\mathrm{e}}+\mathbf{f_{SUPG}}) \tag{2.75}$$

where $\boldsymbol{\phi}$ is the element nodal temperature vector (unknown), $\mathbf{K}$ is the element thermal conduction-advection matrix, $\mathbf{f}_{\mathrm{e}}$ is the element force vector and $\mathbf{K_{SUPG}}$ and $\mathbf{f_{SUPG}}$ are the element thermal stabilization matrix and the element force stabilization vector from the SUPG method, respectively:

$$\mathbf{K}=\int_{\Omega}\left(\rho c\ \mathbf{N}\ [\mathbf{v}]^{\top}\ \mathbf{B}+[\mathbf{B}]^{\top}\ \mathbf{D}^{T}\ \mathbf{B}\right)\mathrm{d}\Omega \tag{2.76}$$

$$\begin{aligned}\mathbf{K_{SUPG}}=\int_{\Omega}\Bigg[&\rho c\left(\frac{\alpha_{opt}\ h_{car}}{2|\mathbf{v}|}\ [\mathbf{v}]^{\top}\ \mathbf{B}\right)[\mathbf{v}]^{\top}\ \mathbf{B}\\&+\left(\frac{\alpha_{opt}\ h_{car}}{2|\mathbf{v}|}\ [\mathbf{v}]^{\top}\ \boldsymbol{\nabla}\mathbf{B}\right)\mathbf{D}^{T}\ \mathbf{B}\Bigg]\mathrm{d}\Omega\end{aligned} \tag{2.77}$$

$$\mathbf{f}_{\mathrm{e}}=\int_{\Omega}[\mathbf{N}]^{\top}\ Q^{T}\ \mathrm{d}\Omega\ -\int_{\Gamma_{\mathrm{q}}}\mathbf{N}\ \bar{\mathbf{q}}^{T}\ \mathrm{d}\boldsymbol{\Gamma}\ -\mathbf{q}_{\mathbf{n}}^{T} \tag{2.78}$$

$$\mathbf{f_{SUPG}}=\int_{\Omega}\left[\left(\frac{\alpha_{opt}\ h_{car}}{2|\mathbf{v}|}\ [\mathbf{v}]^{\top}\ \mathbf{B}\right)\ Q^{T}\right]\mathrm{d}\Omega \tag{2.79}$$

The second term of Eq. (2.77) is cancelled for linear elements. Finally, the global matrices and vectors of the system of equations (2.75) are obtained by assembling of the contribution of each element of the mesh.

It must to be noted that the SUPG method is only applicable for steady-state problems, not for transient ones.

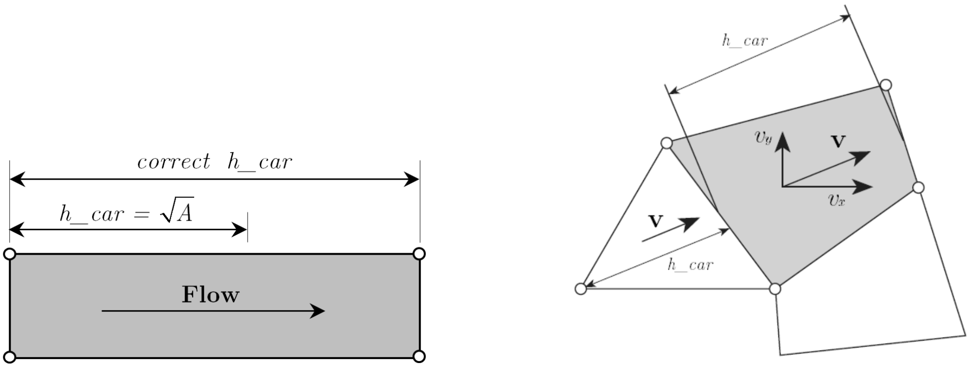

(a) (b)

Figure 2.7: (a) Finite continuum element with the flow direction and the correct h_{car}. Taking $h_{car} = \sqrt[2]{A}$ leads to a very different (and wrong) h_{car} value. (b) Determination of h_{car} as the maximum size of the element in the direction of the velocity vector for a 2-D problem.

Simple academic example 1: continuum medium in 2-D using the SUPG method

The objective of this example is to compare the solutions between the standard Galerkin FEM method and the SUPG and verify that the last one provides stable solutions when $Pe > 1$ in a 2-D simple example.

The geometry of this example consists of three horizontal layers composed of two different materials in a continuous medium (Figure 2.8.a). In order to observe the heat transport, a known and constant velocity field from left to right (Figure 2.8.a) is imposed in the intermediate layer, as a preferential conduction layer throughout the continuous medium.

The initial state of the thermal problem is shown in Figure 2.8.b, which is the result of a steady-state problem where two values of temperature have been imposed on the left and right hand side of the domain, obtaining a linear distribution of temperatures for $t = 0$ (Figure 2.8.b). The velocity field is imposed on the described initial state.

In the first calculations (Figure 2.9) the standard Galerkin weighting is used for a small advection problem (Péclet numbers of 0.3 and 0.9, respectively). In both cases the SUPG method leads to sable solutions.

Finally, the velocities are increased until reaching $Pe > 1$. Figure 2.10.a shows that the solution becomes oscillatory using the standard Galerkin weighting. However, using the new numerical solution (Petrov-Galerkin weighting, SUPG method), the solution is stabilized, as shown in Figure 2.10.b. In both cases the characteristic length of the element h_{car} is taken as the length of the element in the direction of the velocities.

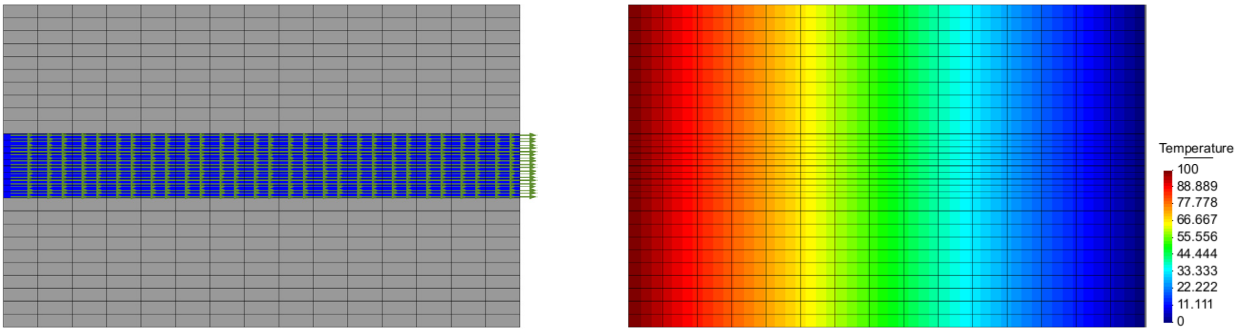

(a) *(b)*

Figure 2.8: (a) Imposed velocities in the intermediate layer and (b) steady-state temperature distribution at t=0 (after velocity application).

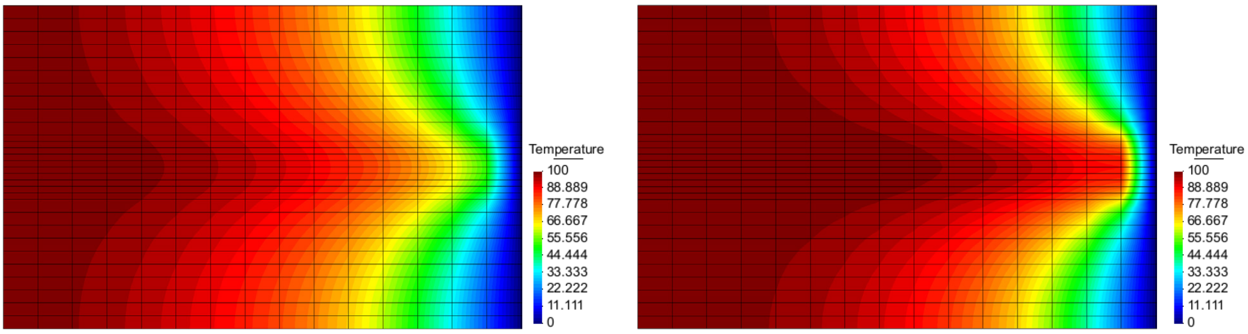

(a) *(b)*

Figure 2.9: (a) Temperature distribution due to the applied velocities and $Pe = 0.3$. (b) Temperature distribution due to the applied velocities when the Péclet number increases but $Pe < 1$ ($Pe = 0.9$).

As explained, the Petrov-Galerkin method involves the use of a characteristic length of the element (h_{car}), which is important for accuracy. In this example, taking $h_{car} = \sqrt{A}$ for each element, even using the SUPG weighting, the solution becomes also unstable, as shown in Figure 2.11.

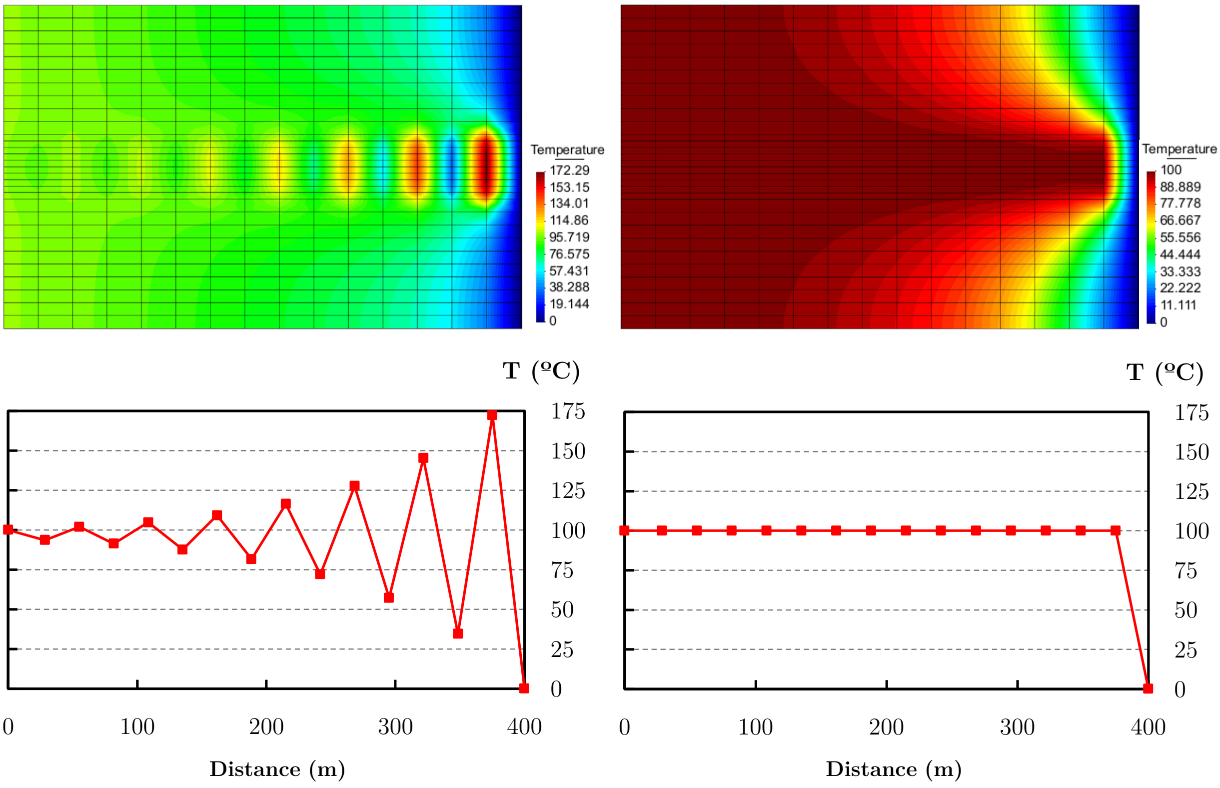

(a) *(b)*

Figure 2.10: (a) Oscillatory distribution of temperatures using the standard Galerkin weighting when Pe = 7.2 in the intermediate layer (the rest of the domain Pe = 0). (b) Correct distribution of temperatures using the SUPG method for the same problem. Graphs referred to the horizontal symmetry axis of the figures.

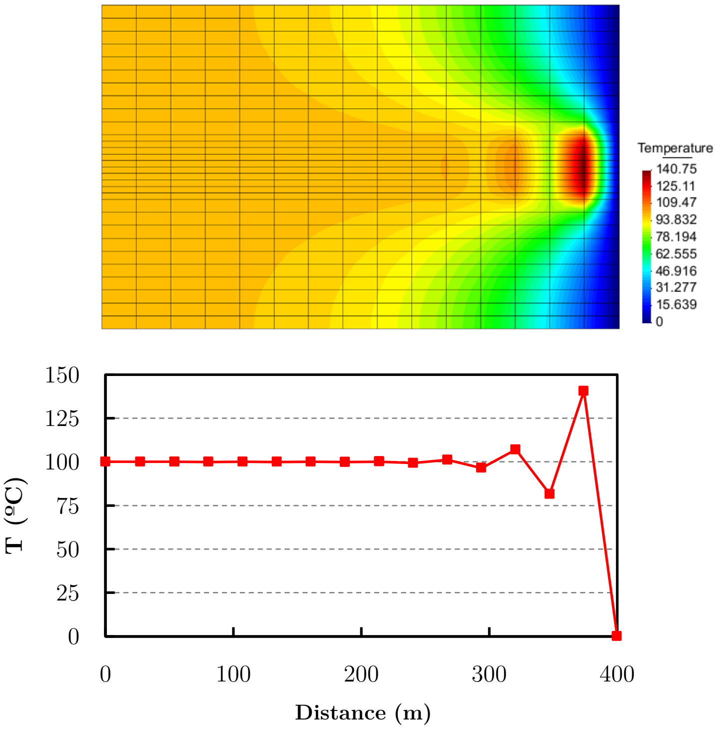

Figure 2.11: Distribution of temperatures using Petrov-Galerkin weighting when $Pe > 1$*, but using a bad value for* h_{car}*. The solution becomes unstable even using the SUPG method.*

2.2.3. Transient large advection problem

As in the steady-state conduction-advection problem (Section 2.2.2), the numerical solution of the conduction-advection transient problem using the FEM and the standard Galerkin weighting is not stable when $Pe > 1$. For this reason, when the advection dominates the problem, it is necessary to solve the problem using a more appropriate numerical method that does not result in oscillatory solutions.

In order to solve the transient problem, the first obvious approach would be to use the same techniques described in Section 2.2.2 for the steady-state problem. In this context, many authors have used the SUPG method, such as Yu & Heinrich (1986), Yu & Heinrich (1987), Johnson (1986), de Sampaio, et al. (1993), Cardle (1995), Idelsohn, et al. (1996), Codina (1998) or Maji & Biswas (1999), among others, but the non-symmetric mass matrices were difficult to use for any explicit method (Zienkiewicz & Taylor, 2000c). Also the Galerkin least squares (GLS) procedure has been used by Nguen & Reynen (1984), Carey & Jiang (1988) or Jiang & Carey (1988), among others, but the extension of this method to the transient problem involves the use of *space-time finite elements* (Zienkiewicz & Taylor, 2000c), which are computationally expensive and are not applicable to explicit schemes.

Since the application of the SUPG and GLS methods is not appropriate to solve the advective transient problem, other methodologies have been developed. The first and most significant ones are known as *Characteristic Methods*. The first characteristic method was proposed by Adey & Brebbia (1974) and it is known as the *"Mesh Updating method"*. Then Morton (1985) proposed the generalization of the same, leading to the so-called *Characteristic-Galerkin methods*. Many variants of this method have been developed successfully and described by Ewing & Russell (1981), Douglas & Russell (1982), Pironneau (1982), Bercovier, et al. (1982), Bercovier, et al. (1983), Lin & Morton (1997) or Pironneau et al. (1992), among others. However, due to its computational complexity, a *simple explicit Characteristic-Galerkin Method* was first published by Zienkiewicz, et al. (1984) and then discussed by others, such as Zienkiewicz, et al. (1984b), Löhner, et al. (1985), Zienkiewicz, et al. (1985) and Zienkiewicz, et al. (1986). Later, the Taylor-Galerkin method was introduced by Donea (1984), which is equivalent to the *Finite Difference Lax-Wendroff Method* (Hirsch, 1989) and gives, for scalar variables, an identical solution to the *Characteristic-Galerkin Method*. These methods also introduce a kind of artificial diffusion, as does the SUPG method (Zienkiewicz & Taylor, 2000c).

In order to solve the large heat advection transient problem, this thesis focuses in the use of the Characteristic-Galerkin procedures, which are more intuitive methods and fully justifies the numerical procedures used. Thus, starting from the simple explicit characteristic method, an extension to a new Implicit Characteristic Galerkin method is proposed (α-ICGM).

It is important to mention some other methods to solve the transient advective problem that appear in the literature, such as the *Galerkin Least-Squares* method (GLS) presented by Hughes, et al. (1989); the *Bubble Functions* method described by Brezzi, et al. (1992) and Franca & Farhat (1994); the *Finite Volume* method (Idelsohn & Oñate, 1994); the *Subgride*

Scale Models (SGS) described by Hughes (1995) and Codina (1998); the *Finite Increment Calculus* method (FIC) introduced by Oñate (1998); the *Mesh Free Finite Point Methods* described by Oñate & Idelsohn (1988), Oñate, et al. (1996) and Oñate, et al. (1996b); the *High Resolution SUPG* method described by Nadukandi, et al. (2010) and Nadukandi, et al. (2012) or the more recent techniques which applies the *Back and Forth Error Compensation and Correction* algorithm (BFECC) as described in Costarelli, et al. (2013).

2.2.3.1. Introduction to the Characteristic Methods

From Eq. (2.14) it is possible to write the differential equation for the conduction-advection transient problem in indicial notation as follows

$$\rho c\left(\frac{\partial \phi}{\partial t}+v_i\frac{\partial \phi}{\partial x_i}\right)-\frac{\partial}{\partial x_i}\left(k_{ij}^T\frac{\partial \phi}{\partial x_j}\right)-Q^T(x_i)=0 \tag{2.80}$$

In order to simplify the numerical resolution and determine the main behaviour patterns of this equation, a change of the independent variable x to x' is proposed. Considering a moving coordinate system x' defined by

$$dx'_i=dx_i-v_i dt \tag{2.81}$$

and noting that $\phi=\phi(x'_i,t)$, the material derivative of the temporal derivative of Eq. (2.80) can be written as

$$\begin{aligned}\left.\frac{\partial \phi}{\partial t}\right|_{x\equiv const} &= \left.\frac{\partial \phi}{\partial x'_i}\right|_{t\equiv const}\cdot\frac{\partial x'_i}{\partial t}+\left.\frac{\partial \phi}{\partial t}\right|_{x'\equiv const}\cdot\frac{\partial t}{\partial t}=\frac{\partial \phi}{\partial x'_i}\cdot\frac{\partial x'_i}{\partial t}+\left.\frac{\partial \phi}{\partial t}\right|_{x'\equiv const}\\ &= -v_i\cdot\frac{\partial \phi}{\partial x'_i}+\left.\frac{\partial \phi}{\partial t}\right|_{x'\equiv const}\end{aligned} \tag{2.82}$$

Performing a change of the independent variable x_i to x'_i on (2.80), the differential equation becomes simply:

$$\rho c\frac{\partial \phi}{\partial t}-\frac{\partial}{\partial x_i{}'}\left(k_{ij}^T\frac{\partial \phi}{\partial x_i{}'}\right)-Q^T(x_i{}')=0 \tag{2.83}$$

In the previous development has been assumed that the partial derivatives of x_i becomes partials of x'_i because are partial derivatives for $t\equiv const$

$$dx'_i=dx_i-v_i dt \xrightarrow{t\equiv const} dx'_i=dx_i \tag{2.84}$$

Equation. (2.83) has the same form as the traditional diffusion equation but formulated on the moving coordinate system x', where the advection term has disappeared. This type of equations can be solved using the standard discretization procedures with the standard Galerkin spatial approximation, as usual for the pure diffusion problems.

The coordinate system of Eq. (2.81) describes the so-called *characteristic directions* of the problem, and it is a moving coordinate system that depends on the velocity of the fluid (or particle) in a time increment, which means the distance travelled by the particle in a Δt. This concept leads to the so-called *Characteristic-based* methods (Zienkiewicz & Taylor, 2000c).

Considering a pure advection problem and leaving out the source terms of equation (2.83), the following expression results:

$$\frac{\partial \phi}{\partial t} = 0 \tag{2.85}$$

from which it is possible to deduce that $\phi(x') = \phi(x - v\Delta t)$ is constant along a characteristic. Indeed, this is the equation of a wave propagating with a velocity v in the x-direction (Figure 2.12) and shows the wave nature of the equations. In the case $k^T \neq 0$, the result is similar to a wave that attenuates with the distance travelled.

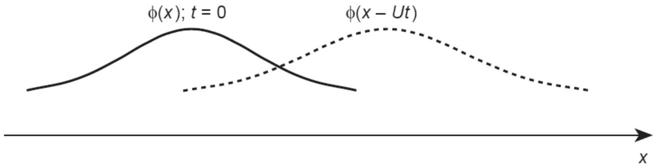

Figure 2.12: Solution for no diffusion and constant velocity v, similar to the propagation of a single undamped wave (Zienkiewicz & Taylor, 2000c).

These methods assume the study of the pure advective problem in a Lagrangian manner, studying the fluid from its updated position (with a movement defined by the velocities v_i and the chosen Δt), while the diffusion problem is studied in an eulerian manner (along x'). Thus, the *characteristic* based methods are known as quasi-Lagrangian methods.

The following sections present some methodologies derived from this concepts, as the *Mesh Updating Method* or the *Galerkin-Characteristics Methods*.

2.2.3.2. Mesh Updating and Interpolation Method

The mesh updating method was the first Characteristic-based method, introduced by Adey & Brebbia (1974).

As mentioned in the previous section, if the spatial coordinate is advective in the manner described by Eq. (2.81), then the advective term of Eq. (2.80) disappears and the resulting problem is a standard diffusion problem (2.83), which may be solved with the standard discretization procedures presented in Section 2.1.

The most obvious use of this concept in the FEM context is to update the position of the mesh points in a Lagrangian manner. For any i-node of the mesh and considering v as a constant in the considered time-step, the updated position of the node may be written as:

$$x_i^{n+1} = x_i^n + v_i\ \Delta t \tag{2.86}$$

Figure 2.13.a shows a mesh update for the one-dimensional problem of Eq. (2.83) during an interval Δt. On the "updated" mesh only the pure diffusion problem needs to be solved.

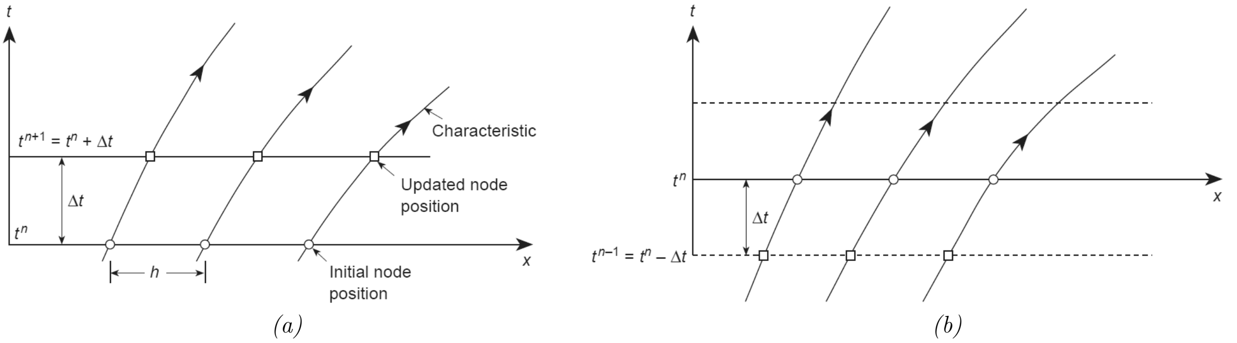

(a) (b)

Figure 2.13: Mesh updating and interpolation; (a) forward, (b) backward (Zienkiewicz & Taylor, 2000c).

The process of continuously updating the mesh and solving the diffusion problem on the new mesh is computationally not viable. When applied to 2D or 3D meshes, very distorted elements may result and difficulties will occur on the boundaries of the domain. Consequently, it seems obvious that after completion of a single time step, a return to the original mesh should be made by interpolating from the *updated values* to the original mesh positions (Figure 2.13.a).

In this context, the problem is split in two parts, with the diffusion and advection changes occurring separately. This idea can be generalized and gives the basis of the so-called Characteristic-Galerkin methods, as it is developed in the next section.

2.2.3.3. Characteristic-Galerkin Method

This method was first proposed by Morton (1985) as a generalization of the Mesh Updating Method, in which the study of the advection and the diffusion is carried out separately. Splitting the advection-diffusion equation in two parts such that:

$$\phi = \phi^{*} + \phi^{**} \tag{2.87}$$

and

$$\frac{\partial \phi^{*}}{\partial t} + v\ \frac{\partial \phi}{\partial x} = 0 \tag{2.88}$$

is a purely advective system, while:

$$\frac{\partial \phi^{**}}{\partial t} - \frac{\partial}{\partial x}\left(k^T \frac{\partial \phi}{\partial x}\right) - Q^T = 0 \tag{2.89}$$

represents the diffusion. Both ϕ^* and ϕ^{**} are approximated by:

$$\phi^* \approx \hat{\phi}^* = [\mathbf{N}]^\top \boldsymbol{\phi}^* \qquad\qquad \phi^{**} \approx \hat{\phi}^{**} = [\mathbf{N}]^\top \boldsymbol{\phi}^{**} \tag{2.90}$$

and in a single step t^n to $t^{n+1} = t^n + \Delta t$ it is assumed that the initial conditions are:

$$\phi^*(t^n) = 0 \qquad\qquad \phi^{**}(t^n) = \phi^n \tag{2.91}$$

Standard Galerkin discretization of the diffusion Eq. (2.89) allows to determine $\boldsymbol{\phi}^{**n+1}$ on the fixed mesh by solving the equation

$$\left(\frac{1}{\Delta t}\mathbf{M} + \theta\,\mathbf{K}\right)\Delta\boldsymbol{\phi}^{**n+1} = -\mathbf{K}\boldsymbol{\phi}^n + f \tag{2.92}$$

In solving the advective problem of Eq. (2.88) it is assumed that ϕ^* remains unchanged along the characteristic direction. However, the initial value of ϕ^{*n} interpolated by standard shape functions (2.90) at time n becomes shifted and distorted, as shown in Figure 2.14. The new value is given by:

$$\phi^{*n+1} = [\mathbf{N}(y)]^\top \boldsymbol{\phi}^{*n} \qquad\qquad y = x + v\Delta t \tag{2.93}$$

Because it is necessary to approximate ϕ^{*n+1} by standard shape functions, a projection for smoothing of these values may be written as

$$\int_\Omega [\mathbf{N}]^\top ([\mathbf{N}]^\top \boldsymbol{\phi}^{*n+1} - [\mathbf{N}]^\top(y)\boldsymbol{\phi}^{*n})\,dx = 0 \tag{2.94}$$

obtaining

$$\mathbf{M}\widehat{\boldsymbol{\phi}}^{*n+1} = \int_\Omega ([\mathbf{N}]^\top \mathbf{N}(y)dx)\,\boldsymbol{\phi}^{*n} \tag{2.95}$$

where $\mathbf{N} = \mathbf{N}(x)$ and $\mathbf{M} = \int_\Omega [\mathbf{N}]^\top \mathbf{N}\,dx$.

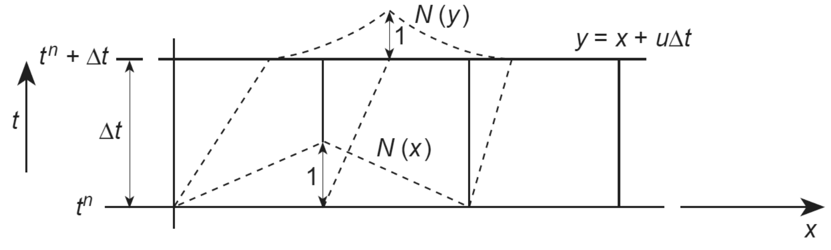

Figure 2.14: Distortion of advected shape functions (Zienkiewicz & Taylor, 2000c).

2.2.3.4. A simple explicit Characteristic Method

The methods proposed in the previous sections are computationally complex and time-consuming. Thus, a simple alternative method was proposed by Zienkiewicz, et al. (1984). This simple explicit method avoids the difficulties of the previous methods but is conditionally stable.

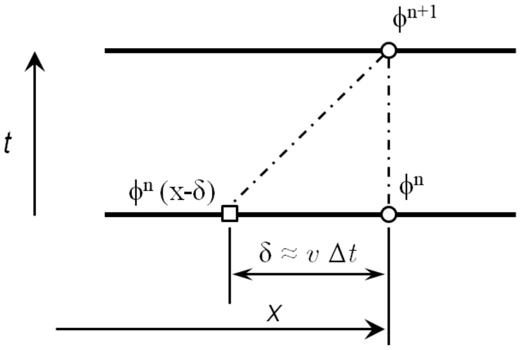

Figure 2.15: Basis of the characteristic-Galerkin method with an explicit scheme, that shows the distance travelled by the particle (δ) from time n to time n+1 (Zienkiewicz & Taylor, 2000c).

The first step of this procedure consists on the time discretization of Eq. (2.83) along the characteristic, using the FDM:

$$\rho c \frac{1}{\Delta t}\left(\phi^{n+1}|_x - \phi^n|_{(x-\delta)}\right) \approx \theta \left[\frac{\partial}{\partial x}\left(k^T\ \frac{\partial \phi}{\partial x}\right) - Q^T\right]^{n+1}\Bigg|_x + (1-\theta)\left[\frac{\partial}{\partial x}\left(k^T\ \frac{\partial \phi}{\partial x}\right) - Q^T\right]^{n}\Bigg|_{(x-\delta)} \tag{2.96}$$

where θ is equal to zero for explicit schemes and between zero and one for implicit schemes. The advective term disappears from the equation because it is evaluated along the characteristics. The boundary terms are the same as defined by equation (2.25).

In order to obtain the solution value at time $n+1$ it is necessary to evaluate the equations at time n but at the position $x-\delta$ (position at where the particle that is currently at x for time $n+1$, was at time n). δ is the distance travelled by the particle in the x direction (Figure 2.15) and can be expressed as

$$\delta = \bar{v}\Delta t \tag{2.97}$$

where $\bar{v}$ is the average value of v along the characteristic, which can be approximated as described in Zienkiewicz & Codina (1996) by the expression

$$\bar{v} = \frac{v^{n+1} + v^n|_{(x-\delta)}}{2} \tag{2.98}$$

The functions can be approximated at $x-\delta$ using Taylor expansions as follows:

$$\phi^n|_{(x-\delta)} \approx \phi^n - \delta \frac{\partial \phi^n}{\partial x} + \frac{\delta^2}{2} \frac{\partial^2 \phi^n}{\partial x^2} + O(\Delta t^3) \tag{2.99}$$

$$\left.\frac{\partial}{\partial x}\left(k^T \ \frac{\partial \phi}{\partial x}\right)^n\right|_{(x-\delta)} \approx \frac{\partial}{\partial x}\left(k^T \ \frac{\partial \phi}{\partial x}\right)^n - \delta \frac{\partial}{\partial x}\left[\frac{\partial}{\partial x}\left(k^T \ \frac{\partial \phi}{\partial x}\right)^n\right] + O(\Delta t^2) \tag{2.100}$$

$$Q^n|_{(x-\delta)} \approx Q^n - \delta \frac{\partial Q^n}{\partial x} + O(\Delta t^2) \tag{2.101}$$

$$v^n|_{(x-\delta)} \approx v^n - \Delta t \ v^n \frac{\partial v^n}{\partial x} + O(\Delta t^2) \tag{2.102}$$

Substituting Eqs. (2.97)-(2.102) into (2.96) and imposing $\theta = 0.5$ the following is obtained

$$\begin{aligned}
&\rho c \frac{1}{\Delta t}(\phi^{n+1} - \phi^n) \\
&\qquad = -\rho c \ V^{n+\frac{1}{2}} \frac{\partial \phi^n}{\partial x} + \rho c \ \frac{\Delta t}{2} v^n \frac{\partial V^n}{\partial x} \frac{\partial \phi^n}{\partial x} + \rho c \ \frac{\Delta t}{2} v^{n+1/2} \ v^{n+1/2} \frac{\partial^2 \phi^n}{\partial x^2} \\
&\qquad + \frac{\partial}{\partial x}\left(k^T \ \frac{\partial \phi}{\partial x}\right)^{n+1/2} - \frac{\Delta t}{2} v^{n+1/2} \frac{\partial}{\partial x}\left[\frac{\partial}{\partial x}\left(k^T \ \frac{\partial \phi}{\partial x}\right)^n\right] - Q^{n+1/2} \\
&\qquad + \frac{\Delta t}{2} v^{n+1/2} \frac{\partial Q^n}{\partial x}
\end{aligned} \tag{2.103}$$

where

$$\begin{aligned}
&\frac{\partial}{\partial x}\left(k^T \ \frac{\partial \phi}{\partial x}\right)^{n+1/2} = \frac{1}{2}\frac{\partial}{\partial x}\left(k^T \ \frac{\partial \phi}{\partial x}\right)^{n+1/2} + \ \frac{1}{2}\frac{\partial}{\partial x}\left(k^T \ \frac{\partial \phi}{\partial x}\right)^n \\
&Q^{n+1/2} = \frac{Q^{n+1} + Q^n}{2} \qquad\qquad v^{n+1/2} = \frac{v^{n+1} + v^n}{2}
\end{aligned} \tag{2.104}$$

In order to get the fully explicit scheme the terms at *n+1/2* can be approximated using their value at *n:*

$$\begin{aligned}
&\frac{\partial}{\partial x}\left(k^T \ \frac{\partial \phi}{\partial x}\right)^{n+1/2} = \frac{\partial}{\partial x}\left(k^T \ \frac{\partial \phi}{\partial x}\right)^n \\
&Q^{n+1/2} = Q^n \qquad\qquad v^{n+1/2} = v^n
\end{aligned} \tag{2.105}$$

And substituting Eq. (2.105) into (2.103) and generalizing to three dimensions, the final form of the explicit characteristic-Galerkin method may be written as:

$$
\begin{aligned}
\rho c\ \Delta\phi &= \rho c\ \left(\phi^{n+1}-\phi^{n}\right) \\
&= -\Delta t\left[\rho c\ v_j\frac{\partial\phi}{\partial x_j}-\frac{\partial}{\partial x_i}\left(k_{ij}^{T}\frac{\partial\phi}{\partial x_i}\right)+Q\right]^n \\
&+\frac{\Delta t^2}{2}v_k^n\frac{\partial}{\partial x_k}\left[\rho c\ v_j\frac{\partial\phi}{\partial x_j}-\frac{\partial}{\partial x_i}\left(k_{ij}^{T}\frac{\partial\phi}{\partial x_i}\right)+Q\right]^n
\end{aligned}
\tag{2.106}
$$

Finally, the spatial discretization can be performed using the FEM using the standard Galerkin weighting ($w = N^{(1)}, N^{(2)}, \ldots$) and applying the Theorem of the Divergence, resulting

$$\left(\frac{1}{\Delta t}\mathbf{C}\right)\Delta\boldsymbol{\phi}^{n+1} = -\left(\mathbf{K}+\mathbf{K}_{\mathbf{v}}+\frac{1}{2}\mathbf{K}_{\mathbf{s}}\right)\boldsymbol{\phi}^{n} + \left(\mathbf{f}_{\mathrm{e}}+\mathbf{f}_{\mathbf{s},\mathrm{e}}\right) \tag{2.107}$$

where

$$\mathbf{C} = \int_\Omega \rho c\ [\mathbf{N}]^\top \mathbf{N}\,\mathrm{d}\Omega \tag{2.108}$$

$$\mathbf{K}_{\mathbf{v}} = \rho c\int_\Omega [\mathbf{N}]^\top v_i\frac{\partial\mathbf{N}}{\partial x_i}\mathrm{d}\Omega \tag{2.109}$$

$$\mathbf{K} = \int_\Omega \frac{\partial\mathbf{N}^\top}{\partial x_i}k_{ij}^{T}\frac{\partial\mathbf{N}}{\partial x_j}\mathrm{d}\Omega \tag{2.110}$$

$$\mathbf{K}_{\mathbf{s}} = \Delta t\int_\Omega \rho c\ \frac{\partial[\mathbf{N}]^\top}{\partial x_i}v_i v_j\frac{\partial\mathbf{N}}{\partial x_j}\mathrm{d}\Omega \tag{2.111}$$

$$\mathbf{f}_{\mathrm{e}} = \int_\Omega [\mathbf{N}]^\top Q^T\,\mathrm{d}\Omega\ + b.\,t. \tag{2.112}$$

$$\mathbf{f}_{\mathbf{s},\mathrm{e}} = \frac{\Delta t}{2}\int_\Omega v_i\frac{\partial[\mathbf{N}]^\top}{\partial x_i}Q^T\ \mathrm{d}\Omega + b.\,t. \tag{2.113}$$

where $\mathbf{C}$ is the standard element mass matrix, $\mathbf{K}_{\mathbf{v}}$ is the element advective non-symetric matrix, $\mathbf{K}_{\mathbf{s}}$ is an *artificial diffusion* term similar to that shown using the SUPG method in the steady-state problem, $\mathbf{K}$ is the standard diffusion matrix and $\mathbf{f}_{\mathbf{s},\mathrm{e}}$ is the modified element force vector. Another term that may come from the boundary condition defined by Eq. (2.54) must be also considered in Eq. (2.107).

The explicit form presented above is only conditionally stable. As described by Zienkiewicz & Taylor (2000c), the stability condition for the explicit scheme is given by

$$\Delta t \le \Delta t_{crit} = \frac{\Delta t_\sigma \Delta t_\upsilon}{\Delta t_\sigma + \Delta t_\upsilon} \tag{2.114}$$

where

$$\Delta t_\sigma = \frac{h_{car}}{|\mathbf{v}|} \tag{2.115}$$

$$\Delta t_\upsilon = \frac{h_{car}}{2k^T} \tag{2.116}$$

where h_{car} is the characteristic length of the element described in Section 2.2.2. For pure advection, this stability condition turns to Δt_σ and may be rewritten as:

$$\mathrm{C} = \frac{|v|\Delta \mathrm{t}}{h_{car}} \leq 1 \tag{2.117}$$

where C is the Courant number of the element. This condition turns more restrictive when the diffusion term appears, as described by Eq. (2.114). However, if the explicit scheme is transformed to a *semi-implicit* scheme applying $\theta \geq 0.5$ to the diffusion term only, the stability condition turns to Δt_σ, that can be defined by Eq. (2.117), which can present an appreciable benefit (Zienkiewicz & Taylor, 2000c).

Finally, the time-increment condition due to the diffusion problem must also be satisfied:

$$\mathit{\Delta} t_{d,max} = \rho c \frac{h_{car}^2}{2k^T} \tag{2.118}$$

Comparison between the simple explicit Characteristic-Galerkin method and the SUPG method

It is of interest to examine the behaviour of the solution when the steady-state is reached with the simple explicit Characteristic-Galerkin procedure in comparison with the SUPG solution obtained in Section 2.2.2.

Leaving out the source and force terms, the SUPG steady-state solution defined by Eq. (2.75) can be written as:

$$(\mathbf{K} + \mathbf{K}_{\mathrm{SUPG}})\ \boldsymbol{\phi} = 0 \tag{2.119}$$

where $\mathbf{K}$, $\mathbf{K}_{\mathrm{SUPG}}$ and $\boldsymbol{\phi}$ are the element conductivity matrix, the element advective matrix and the element temperature vector, respectively. Developing Eq. (2.119) leads to

$$\left[\int_\Omega \rho c\ [\mathbf{N}]^\top \mathbf{v}\ \mathbf{B}\ \mathrm{d}\Omega + \int_\Omega [\mathbf{B}]^\top \mathbf{D}^T \mathbf{B}\ \mathrm{d}\Omega + \frac{1}{2}\frac{\alpha_{opt}\ h_{car}}{|\mathbf{v}|}\int_\Omega \rho c\ [\mathbf{B}]^\top \mathbf{v}\ [\mathbf{v}]^\top \mathbf{B}\ \mathrm{d}\Omega\ \right] \boldsymbol{\phi}^n = 0 \tag{2.120}$$

where $\alpha_{opt} = \coth|Pe| - \frac{1}{|Pe|}$.

In the same manner, the solution with the simple explicit characteristics method for the steady-state problem may be written from Eq. (2.107) by imposing $\Delta\boldsymbol{\phi} = 0$ as follows

$$(\mathbf{K} + \mathbf{K}_\mathbf{v} + \mathbf{K}_\mathbf{s})\boldsymbol{\phi}^n = 0 \tag{2.121}$$

Substituting the above equations into Eqs. (2.109)-(2.111) leads to:

$$\left[\int_\Omega \rho c\;[\mathbf{N}]^\top \mathbf{v}\;\mathbf{B}\,\mathrm{d}\Omega+\int_\Omega[\mathbf{B}]^\top\mathbf{D}^T\;\mathbf{B}\,\mathrm{d}\Omega+\frac{1}{2}\Delta\mathrm{t}\int_\Omega \rho c\;[\mathbf{B}]^\top\mathbf{v}\;[\mathbf{v}]^\top\;\mathbf{B}\,\mathrm{d}\Omega\right]\boldsymbol{\phi}^n=0 \qquad (2.122)$$

Note that the scheme based on the explicit method of characteristics for an infinite time (steady-state) is coincident with the SUPG method if

$$\Delta t=\frac{\alpha_{opt}\;h_{car}}{|\mathbf{v}|} \qquad (2.123)$$

where α_{opt} is coincident with the Courant number of the element:

$$\alpha_{opt}=\frac{|\mathbf{v}|\Delta t}{h_{car}}=\mathrm{C} \qquad (2.124)$$

Thus, the equivalence condition between both schemes always satisfies the Courant stability condition. It follows that for both schemes to be equivalent when the solution tends to steady-state, the time step to be applied has to be

$$\Delta t_{eq}=\frac{\alpha_{opt}\;h_{car}}{|\mathbf{v}|} \qquad (2.125)$$

However, each element of the domain may have a different characteristic dimension and a different fluid velocity, so it is very unlikely that all elements of the mesh reach simultaneously that condition: in irregular meshes and where fluid velocities vary between elements of the mesh, the value of Δt_{eq} would be different for each element, while the value of Δt is set equal for all the elements of the mesh.

As explained in Zienkiewicz & Taylor (2000c), with smaller time increments, the more accurate will be the transient solution. However, in this case, the optimal solution for transients and steady-state can't be reached simultaneosly and the optimum explicit characteristic formulation for the transient state will not be the optimal for the steady-state SUPG method.

Finally, examination of Eqs. (2.107) to (2.113) shows that the Characteristic-Galerkin method could have been obtained by applying a SUPG weighting such as

$$[\mathbf{N}]^\top+\frac{\Delta t}{2}v_i\frac{\partial[\mathbf{N}]^\top}{\partial x_i} \qquad (2.126)$$

to the various terms of the governing Eq. (2.83) excluding the term $\partial v/\partial t$, to which the standard Galerkin weighting of $[\mathbf{N}]^\top$ is attached.

2.2.3.5. An Implicit Characteristic-Galerkin Method

The preceding section presents a conditionally stable explicit characteristic procedure to solve large advection transient problems ($Pe > 1$), which was originally proposed by Zienkiewicz, et al. (1984). As an extension of that work, this thesis proposes the formulation of an implicit scheme that is unconditionally stable.

The first step of this procedure, as in the explicit scheme, consists on the time discretization of Eq. (2.83) along the characteristic, using the Finite Difference Method:

$$\begin{aligned}\rho c \frac{1}{\Delta t}\left(\phi^{n+1}\big|_x - \phi^n\big|_{(x-\delta)}\right) \\ \approx \theta \left[\frac{\partial}{\partial x}\left(k^T \frac{\partial \phi}{\partial x}\right) - Q^T\right]^{n+1}\Bigg|_x + (1-\theta)\left[\frac{\partial}{\partial x}\left(k^T \frac{\partial \phi}{\partial x}\right) - Q^T\right]^n\Bigg|_{(x-\delta)}\end{aligned} \tag{2.127}$$

where $0 \leq \theta \leq 1$; n indicates the n-th time-increment; and δ is the distance travelled by the particle (Figure 2.15). As in the explicit scheme, the advective term disappears from the equation because it is evaluated along the characteristics. The boundary terms are the same as defined in Eq. (2.25).

The functions can be approximate at $x - \delta$ using Taylor expansions as follows:

$$\phi^n\big|_{(x-\delta)} \approx \phi^n - \delta \frac{\partial \phi^n}{\partial x} + \frac{\delta^2}{2}\frac{\partial^2 \phi^n}{\partial x^2} + O(\Delta t^3) \tag{2.128}$$

$$\frac{\partial}{\partial x}\left(k^T \frac{\partial \phi}{\partial x}\right)^n\Bigg|_{(x-\delta)} \approx \frac{\partial}{\partial x}\left(k^T \frac{\partial \phi}{\partial x}\right)^n - \delta \frac{\partial}{\partial x}\left[\frac{\partial}{\partial x}\left(k^T \frac{\partial \phi}{\partial x}\right)^n\right] + O(\Delta t^2) \tag{2.129}$$

$$Q^{T^n}\big|_{(x-\delta)} \approx Q^{T^n} - \delta \frac{\partial Q^{T^n}}{\partial x} + O(\Delta t^2) \tag{2.130}$$

$$v^n\big|_{(x-\delta)} \approx v^n - \Delta t \; v^n \frac{\partial V^n}{\partial x} + O(\Delta t^2) \tag{2.131}$$

The distance δ travelled by the particle (Figure 2.15) can be expressed as

$$\delta = \bar{v}\Delta t \tag{2.132}$$

where $\bar{v}$ is the average value of v along the characteristic, which can be approximated by leaving out the second term of Eq. (2.131) as

$$\bar{v} = \frac{v^{n+1} + v^n\big|_{(x-\delta)}}{2} \approx \frac{v^{n+1} + v^n}{2} \tag{2.133}$$

And substituting Eq. (2.133) into (2.132):

$$\delta = \bar{v}\Delta t = \Delta t \frac{v^{n+1} + v^n}{2} = \Delta t \; v^{n+1/2} \tag{2.134}$$

Substituting Eqs. (2.128)-(2.134) in Eq. (2.127) the following is obtained:

$$
\begin{aligned}
&\rho c \frac{1}{\Delta t}\left(\phi^{n+1}-\phi^{n}\right)\\
&\qquad\qquad = -\rho c\ v^{n+1/2}\,\frac{\partial \phi^{n}}{\partial x} + \frac{\rho c}{2}\Delta t\ v^{n+1/2}\ v^{n+1/2}\,\frac{\partial^2 \phi^{n}}{\partial x^2}\\
&\qquad\qquad + \theta\left[\frac{\partial}{\partial x}\left(k^T\ \frac{\partial \phi}{\partial x}\right) - Q^T\right]^{n+1} + (1-\theta)\left[\frac{\partial}{\partial x}\left(k^T\ \frac{\partial \phi}{\partial x}\right) - Q^T\right]^{n}\\
&\qquad\qquad -\ (1-\theta)\left[\Delta t\ v^{n+1/2}\left(\frac{\partial}{\partial x}\left\{\frac{\partial}{\partial x}\left(k^T\ \frac{\partial \phi}{\partial x}\right)\right\} - \frac{\partial {Q^T}^{n}}{\partial x}\right)\right]
\end{aligned}
\tag{2.135}
$$

Leaving out the third order terms and performing the spatial discretization, applying the Theorem of the Divergence to the diffusion terms and using the FEM with the standard Galerkin weighting ($w = N^{(1)}, N^{(2)}, ...$) results in:

$$
\left(\frac{1}{\Delta t}\mathbf{C} + \theta\mathbf{K}\right)\Delta\boldsymbol{\phi} = -\left(\mathbf{K} + \mathbf{K_v} + \frac{1}{2}\mathbf{K_s}\right)\boldsymbol{\phi}^{n} + \left(\mathbf{f}_{\mathrm{e}} + \mathbf{f}_{\mathbf{s},\mathrm{e}}\right)
\tag{2.136}
$$

where

$$
\mathbf{C} = \int_\Omega \rho c\ [\mathbf{N}]^\top \mathbf{N}\,\mathrm{d}\Omega
\tag{2.137}
$$

$$
\mathbf{K} = \int_\Omega \frac{\partial [\mathbf{N}]^\top}{\partial x_i} k_{ij}^T \frac{\partial \mathbf{N}}{\partial x_j}\mathrm{d}\Omega
\tag{2.138}
$$

$$
\mathbf{K_v} = \int_\Omega \rho c\ [\mathbf{N}]^\top v_i^{n+1/2}\frac{\partial \mathbf{N}}{\partial x_i}\mathrm{d}\Omega
\tag{2.139}
$$

$$
\mathbf{K_s} = \Delta t\int_\Omega \rho c\ \frac{\partial [\mathbf{N}]^\top}{\partial x_i} v_i^{n+1/2} v_j^{n+1/2}\frac{\partial \mathbf{N}}{\partial x_j}\mathrm{d}\Omega
\tag{2.140}
$$

$$
\mathbf{f}_{\mathrm{e}} = (1-\theta)\int_\Omega [\mathbf{N}]^\top {Q^T}^{n}\,\mathrm{d}\Omega\ + \theta\int_\Omega [\mathbf{N}]^\top {Q^T}^{n+1/2}\,\mathrm{d}\Omega + b.\,t.
\tag{2.141}
$$

$$
\mathbf{f}_{\mathbf{s},\mathrm{e}} = (1-\theta)\Delta t\int_\Omega [\mathbf{N}]^\top v_i^{n+1/2}\frac{\partial \mathbf{N}}{\partial x_i}{Q^T}^{n}\ \mathrm{d}\Omega + b.\,t.
\tag{2.142}
$$

The time-integration scheme is always stable when $0.5 \leq \theta \leq 1$. Additionally, as in the implicit scheme, the Courant condition (Eq. (2.117)) must be satisfied for each element of the FEM mesh. For this reason, the maximum time-increment that can be applied due to the advection effect is:

$$
\mathit{\Delta} t_{c,max} = \frac{h_{car}}{v}
\tag{2.143}
$$

Eq. (2.143) shows that to satisfy the Courant condition it is necessary that the applied time-increment decreases as the size of the element decreases (for a fixed velocity). Also, as velocity increases, the time-increment has to decrease (for a fixed size of the element). It is important to note that while the applied time-increment is constant for the entire FE mesh, the velocities and the size of the elements are not. Thus, the element of the mesh with the smaller h_{car}/v ratio sets the maximum admissible time increment.

Finally, as in the explicit scheme, the time-increment condition due to the diffusion problem must also be satisfied as in Eq. (2.118).

2.2.3.6. A new Implicit Characteristic-Galerkin Method (α-ICGM)

This section introduces a new implicit Characteristics-Galerkin procedure to solve the transient advection-diffusion problem, which incorporates an implicit scheme generalized with an α parameter. This procedure will be called "α-ICG Method".

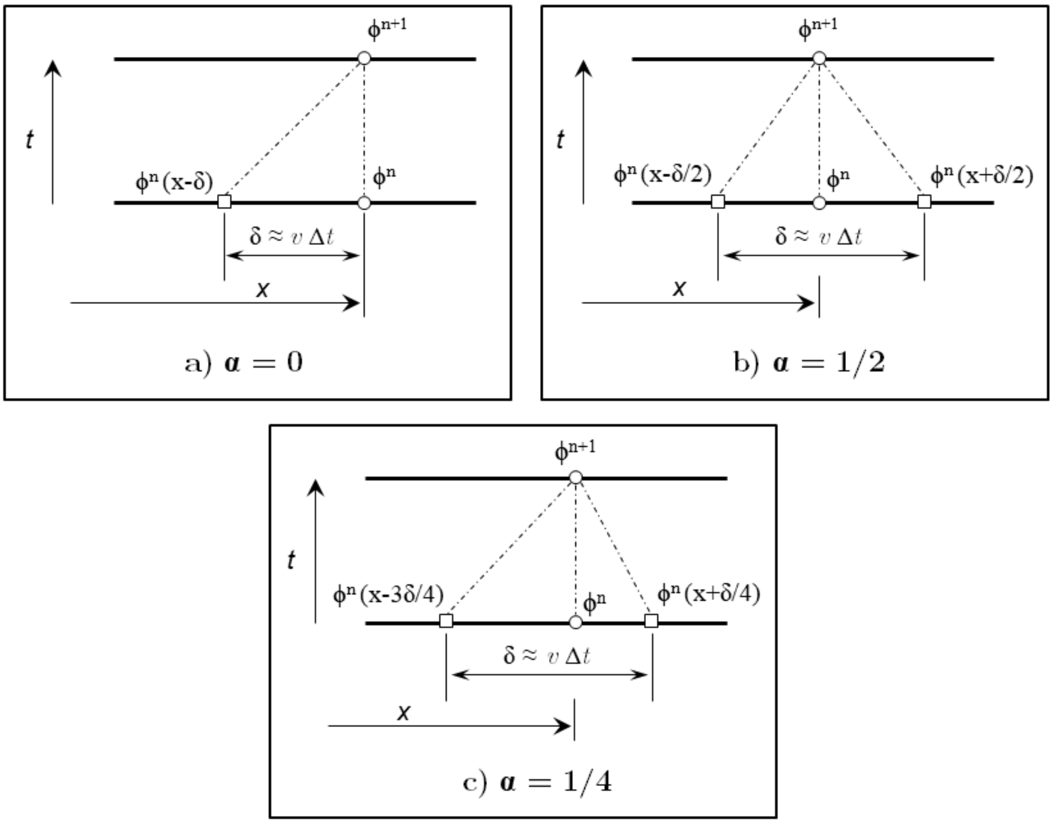

a) $\alpha = 0$

b) $\alpha = 1/2$

c) $\alpha = 1/4$

Figure 2.16: Basis of the α-ITCG Method method with an implicit scheme, that shows the distance travelled by the particle (δ) from time n to time $n+1$. Different α values determine different temporal derivative positions of the advective volume.

In the implicit method described in the previous section, the conduction terms are finally evaluated at x, while the temporal derivatives are evaluated at x and $x-\delta$. This means that the advective volume that is followed in the time discretization is the volume that at the beginning of the interval is at location $x-\delta$, and at the end of the interval is at location x. In order to improve the numerical efficiency, in this generalized method the temporal derivatives are evaluated centered around the solution point x, taking $x-(1-\alpha)\delta$ for time n and $x+\alpha\delta$ for time $n+1$ (Figure 2.16). That is, the advective volume considered for time discretization is the volume that at the beginning of the interval is at location $x-(1-\alpha)\delta$, and at the end of the interval is at location $x+\alpha\delta$. Note that if $\alpha=0$ one recovers the previous implicit scheme.

Once more, the first step consists on the time discretization of Eq. (2.83) along the characteristic, using the Finite Difference Method:

$$\begin{aligned}\rho c \frac{1}{\Delta t}\left(\phi^{n+1}\big|_{x+\alpha\delta} - \phi^{n}\big|_{[x-(1-\alpha)\delta]}\right) & \\ \approx \theta\left[\frac{\partial}{\partial x}\left(k^T\ \frac{\partial\phi}{\partial x}\right) - Q^T\right]^{n+1}\Bigg|_{x+\alpha\delta} & \\ + (1-\theta)\left[\frac{\partial}{\partial x}\left(k\ \frac{\partial\phi}{\partial x}\right) - Q^T\right]^{n}\Bigg|_{[x-(1-\alpha)\delta]} &\end{aligned} \tag{2.144}$$

The functions at $x-(1-\alpha)\delta$ and $x+\alpha\delta$ can be approximated using Taylor expansions as follows

$$\phi^n\big|_{[x-(1-\alpha)\delta]} \approx \phi^n - (1-\alpha)\delta\frac{\partial\phi^n}{\partial x} + \frac{(1-\alpha)^2\delta^2}{2}\frac{\partial^2\phi^n}{\partial x^2} + O(\Delta t^3) \tag{2.145}$$

$$\phi^{n+1}\big|_{(x+\alpha\delta\ )} \approx \phi^{n+1} + \alpha\delta\frac{\partial\phi^{n+1}}{\partial x} + \frac{(\alpha\delta)^2}{2}\frac{\partial^2\phi^{n+1}}{\partial x^2} + O(\Delta t^3) \tag{2.146}$$

$$\frac{\partial}{\partial x}\left(k^T\ \frac{\partial\phi}{\partial x}\right)^n\Bigg|_{[x-(1-\alpha)\delta]} \approx \frac{\partial}{\partial x}\left(k^T\ \frac{\partial\phi}{\partial x}\right)^n - (1-\alpha)\delta\frac{\partial}{\partial x}\left[\frac{\partial}{\partial x}\left(k^T\ \frac{\partial\phi}{\partial x}\right)^n\right] + O(\Delta t^2) \tag{2.147}$$

$$\frac{\partial}{\partial x}\left(k^T\ \frac{\partial\phi}{\partial x}\right)^{n+1}\Bigg|_{(x+\alpha\delta\ )} \approx \frac{\partial}{\partial x}\left(k^T\ \frac{\partial\phi}{\partial x}\right)^{n+1} + (\alpha\delta)\frac{\partial}{\partial x}\left[\frac{\partial}{\partial x}\left(k^T\ \frac{\partial\phi}{\partial x}\right)^{n+1}\right] + O(\Delta t^2) \tag{2.148}$$

$$Q^{T^n}\big|_{[x-(1-\alpha)\delta]} \approx Q^{T^n} - (1-\alpha)\delta\frac{\partial Q^{T^n}}{\partial x} + O(\Delta t^2) \tag{2.149}$$

$$Q^{T^{n+1}}\Big|_{(x+\alpha\delta\ )} \approx Q^{T^{n+1}} + (\alpha\delta\ )\frac{\partial Q^{T^{n+1}}}{\partial x} + O(\Delta t^2) \tag{2.150}$$

$$v^n\big|_{[x-(1-\alpha)\delta]} \approx v^n - (1-\alpha)\Delta t\ v^n\frac{\partial v^n}{\partial x} + O(\Delta t^2) \tag{2.151}$$

$$v^{n+1}\big|_{(x+\alpha\delta\ )} \approx v^{n+1} + \alpha\Delta t\ v^{n+1}\frac{\partial v^{n+1}}{\partial x} + O(\Delta t^2) \tag{2.152}$$

In previous expressions δ is the distance travelled by the particle during the time interval considered (Figure 2.16) and it can be expressed as

$$\delta = \bar{v}\Delta t \tag{2.153}$$

where $\bar{v}$ is the average value of velocity v along the characteristic, which in turn can be approximated leaving out the second term of Eqs. (2.151)-(2.152) by

$$\bar{v} = \frac{v^{n+1}\big|_{[x-(1-\alpha)\delta]} + v^{n}\big|_{(x+\alpha\delta)}}{2} \approx \frac{v^{n+1}+v^{n}}{2} \tag{2.154}$$

By substituting (2.154) in (2.153), the same expression as in the previous implicit formulation is obtained

$$\delta = \bar{v}\Delta t = \Delta t \frac{v^{n+1}+v^{n}}{2} = \Delta t\ v^{n+1/2} \tag{2.155}$$

Substituting the above approximations (2.145)-(2.155) into Eq. (2.144) and leaving out third-order terms the following is obtained:

$$\begin{aligned}
&\rho c \frac{1}{\Delta t}\left(\phi^{n+1}-\phi^{n}\right)\\
&\qquad = -(1-\alpha)\rho c\ v^{n+1/2}\frac{\partial \phi^{n}}{\partial x} + \frac{(1-\alpha)^2}{2}\rho c \Delta t\ v^{n+1/2}\ v^{n+1/2}\frac{\partial^2 \phi^{n}}{\partial x^2}\\
&\qquad - \alpha\rho c\ v^{n+1/2}\frac{\partial \phi^{n+1}}{\partial x} - \frac{\alpha^2}{2}\rho c \Delta t\ v^{n+1/2}\ v^{n+1/2}\frac{\partial^2 \phi^{n+1}}{\partial x^2}\\
&\qquad + \theta\left[\frac{\partial}{\partial x}\left(k^T\ \frac{\partial \phi}{\partial x}\right) - Q^T\right]^{n+1} + (1-\theta)\left[\frac{\partial}{\partial x}\left(k^T\ \frac{\partial \phi}{\partial x}\right) - Q^T\right]^{n}\\
&\qquad +\ (1-\theta)\left[\alpha\Delta t\ v^{n+1/2}\frac{\partial {Q^T}^{n}}{\partial x}\right] - \theta\left[(1-\alpha)\Delta t\ v^{n+1/2}\frac{\partial {Q^T}^{n+1}}{\partial x}\right]
\end{aligned} \tag{2.156}$$

Leaving out third order terms and performing the spatial discretization, applying the Theorem of the Divergence to the diffusion terms and using the FEM with the standard Galerkin weighting ($w = N^{(1)}, N^{(2)}, \ldots$) results in:

Summary 3 - Transient thermal equation for large advection in continuum media using the α-Implicit Characteristic Galerkin method.

$$\left(\frac{1}{\Delta t}\mathbf{C} + \alpha\mathbf{K}_{\mathbf{v}} + \frac{\alpha^2}{2}\mathbf{K}_{\mathbf{s}} + \theta\mathbf{K}\right)\Delta\phi = -\left[\mathbf{K} + \mathbf{K}_{\mathbf{v}} + \left(\frac{1}{2} - \alpha\right)\mathbf{K}_{\mathbf{s}}\right]\phi^n + \left(\mathbf{f}_{\mathrm{e}} + \mathbf{f}_{\mathbf{s},\mathrm{e}}\right) \tag{2.157}$$

where

$$\mathbf{C} = \rho c \int_\Omega [\mathbf{N}]^\top \mathbf{N}\,\mathrm{d}\Omega \tag{2.158}$$

$$\mathbf{K} = \int_\Omega \frac{\partial [\mathbf{N}]^\top}{\partial x_i} k_{ij}^T \frac{\partial \mathbf{N}}{\partial x_j}\,\mathrm{d}\Omega \tag{2.159}$$

$$\mathbf{K}_{\mathbf{v}} = \int_\Omega \rho c\, [\mathbf{N}]^\top v_i^{n+1/2} \frac{\partial \mathbf{N}}{\partial x_i}\,\mathrm{d}\Omega \tag{2.160}$$

$$\mathbf{K}_{\mathbf{s}} = \Delta t \int_\Omega \rho c\, \frac{\partial [\mathbf{N}]^\top}{\partial x_i} v_i^{n+1/2} v_j^{n+1/2} \frac{\partial \mathbf{N}}{\partial x_j}\,\mathrm{d}\Omega \tag{2.161}$$

$$\mathbf{f}_{\mathrm{e}} = (1-\theta)\int_\Omega [\mathbf{N}]^\top Q^{T^n}\, d\Omega \; + \theta \int_\Omega [\mathbf{N}]^\top Q^{T^{n+1/2}}\,\mathrm{d}\Omega + b.t. \tag{2.162}$$

$$\begin{aligned}\mathbf{f}_{\mathbf{s},\mathrm{e}} = (1-\theta)\alpha\Delta t &\int_\Omega [\mathbf{N}]^\top v_i^{n+1/2} \frac{\partial \mathbf{N}}{\partial x_i} Q^{T^n}\,\mathrm{d}\Omega \\ &- \theta(1-\alpha)\Delta \mathrm{t} \int_\Omega [\mathbf{N}]^\top v_i^{n+1/2} \frac{\partial \mathbf{N}}{\partial x_i} Q^{T^{n+1/2}}\,\mathrm{d}\Omega + b.t.\end{aligned} \tag{2.163}$$

It is important to note that the boundary condition defined by Eq. (2.54) must be added to the above formulation.

As in the implicit scheme presented in the previous section, the time-integration scheme is always stable when $0.5 \leq \theta \leq 1$. Additionally, the Courant (Eq. (2.117)) has to be satisfied, while the maximum time-increment that can be applied due to the advection effect is given by Eq. (2.143). Finally, the time-increment condition due to the diffusion (Eq. (2.118)) must also be satisfied.

Simple academic example 2: transient thermal conduction-advection in continuum medium using the α-Implicit Characteristic Method

The objective of this example is to compare the solutions between the standard Galerkin FEM method and the new α-ICG method and verify that latter one provides stable solutions when $Pe > 1$ in a 2-D simple example.

The geometry of this example consists of three horizontal layers in a domain of 400x250m (Figure 2.17.a). In order to observe the heat transport, a known and constant velocity field of magnitude $v = 0.32\ m/s$ (Figure 2.17.a) is imposed from the left to the right in the intermediate layer, as a preferential conduction layer throughout the continuous medium.

The initial state of the thermal problem is shown in Figure 2.17.b, which is the result of a steady-state problem where two values of temperature have been imposed on the left and right hand side of the domain, obtaining a linear distribution of temperatures for $t\ = 0$. The velocity field is imposed on the described initial state maintaining the Dirichlet boundary conditions used to reach the steady-state solution.

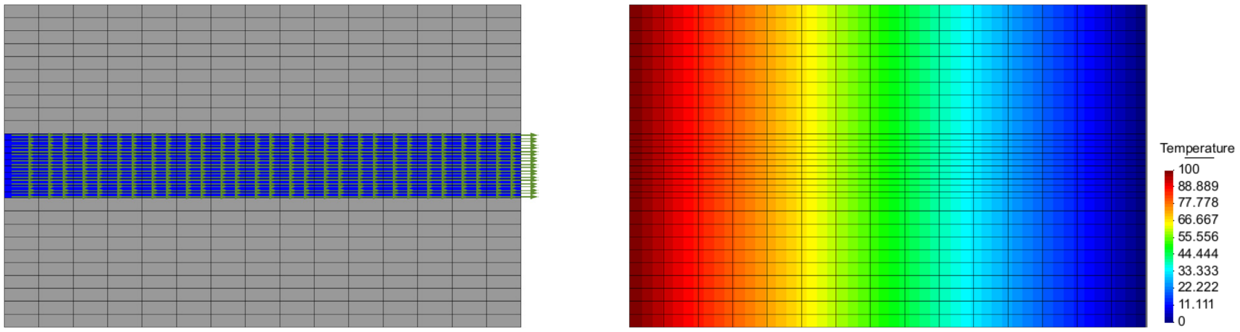

(a) *(b)*

Figure 2.17: (a) Imposed velocities in the intermediate layer and (b) steady-state temperature distribution at t=0 (after velocity application).

Figure 2.18 shows the results of the transient thermal problem with large advection ($Pe = 2.2$), first using the standard Galerkin weighting, which leads to oscillatory results, and then using the α-ICG method, which leads to the stable correct solution. In this case, it has been verified that the best result is reached for $\alpha\ =\ 0$, which corresponds to the Implicit Characteristic Galerkin Method. Note that the Courant number is smaller than 1 ($C\ = 0.72$), a necessary condition to obtain a stable solution.

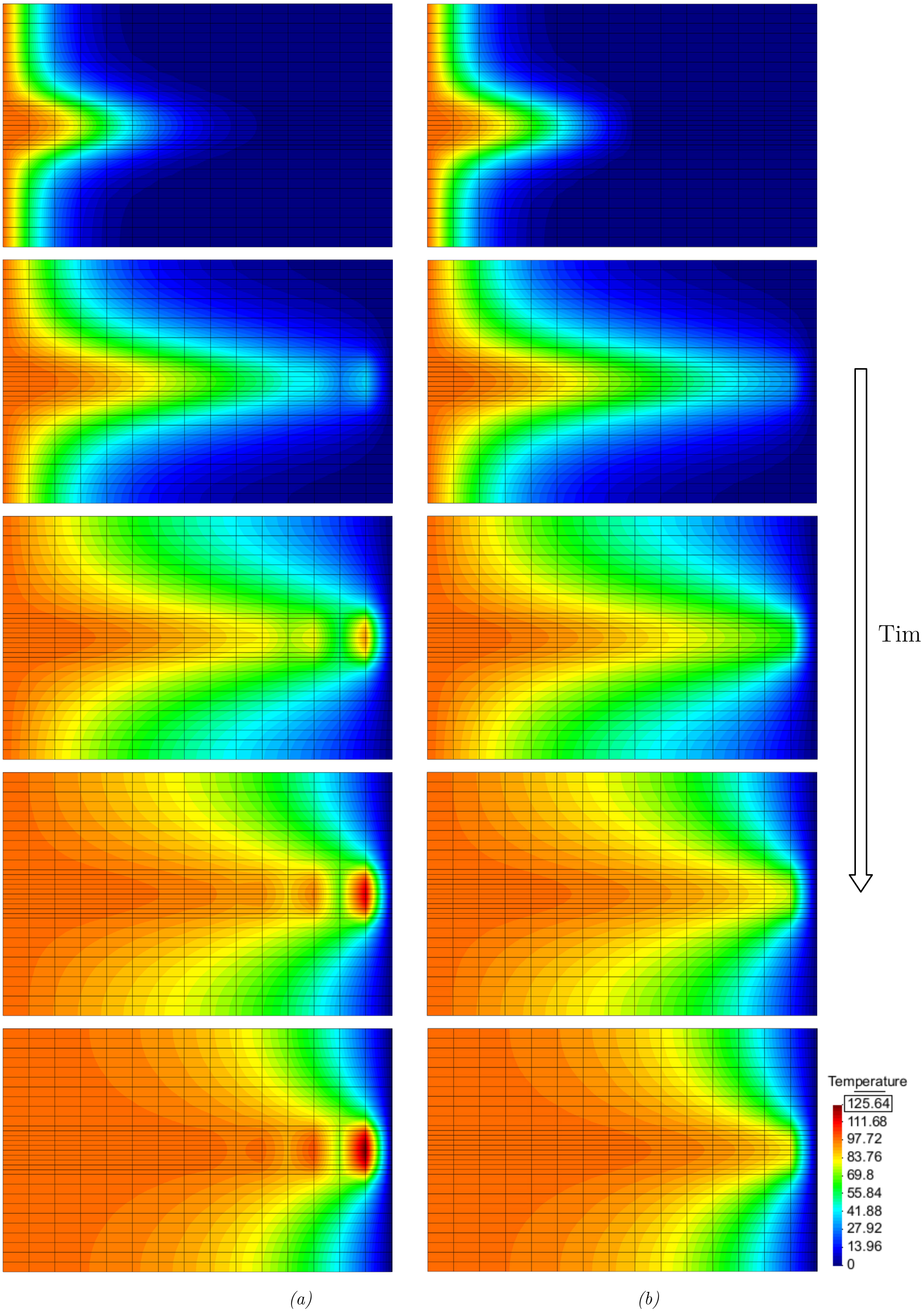

Figure 2.18: Transient thermal solution for Pe = 2.2. (a) Oscillatory results using the standard Galerkin weighting. (b) Correct solution using the new α-ICG method with $\alpha = 0$ for advective transport.

Simple academic example 3: transient pure advection in a continuum medium using the α-Implicit Characteristic Method

The geometry of this example consists of a horizontal domain of 400x80 meters with the initial temperature distribution shown in Figure 2.19. The transient problem is solved with a known uniform velocity field of magnitude $v = 0.75\ m/s$ from left to right. A correct solution consists of a temperature distribution moving from left to right with no oscillations. The FE mesh has 1377 nodes and 1280 continuum elements. Additionally, the thermal conductivity is equal to zero and the Péclet number tends to infinite.

The initial temperature distribution is moved to the right leading to oscillatory results using the standard Galerkin weighting (Figure 2.20) and to correct results using the new α-ICG method with $\alpha = 0.25$ (Figure 2.21). Comparison of both figures (taken at t = *100 s*) shows that the new method of characteristics used to solve the transient thermal problem with advection stabilizes the solution, leading to correct results.

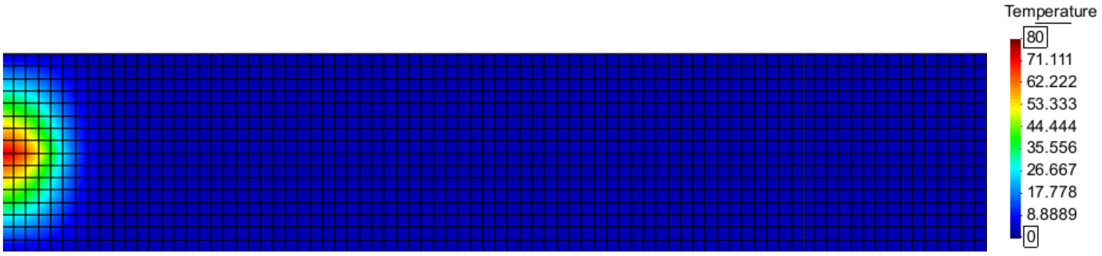

Figure 2.19: Mesh of the example and initial temperature distribution.

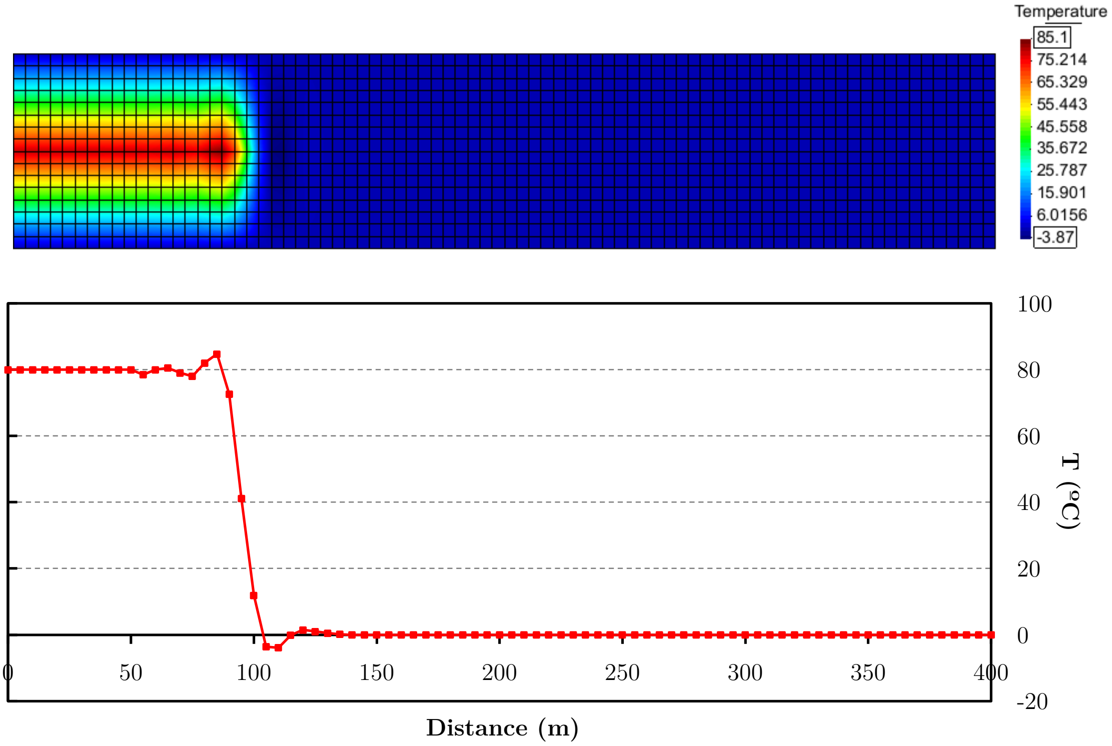

Figure 2.20: Transient thermal solution for Pe = ∞ using standard Galerkin weighting (t = 100 s). The plot shows the temperature distribution at the axis of symmetry.

In both cases the Courant number is less than 1 ($C = 0.75$), which is a necessary condition to obtain a non-oscillatory result using the method of characteristics. Similar results and conclusions can be reached at other times during the transient problem when comparing the standard Galerkin weighting method and the new method of characteristics. As in the previous example, the best solution in this case is reached for $\alpha =$ 0.25.

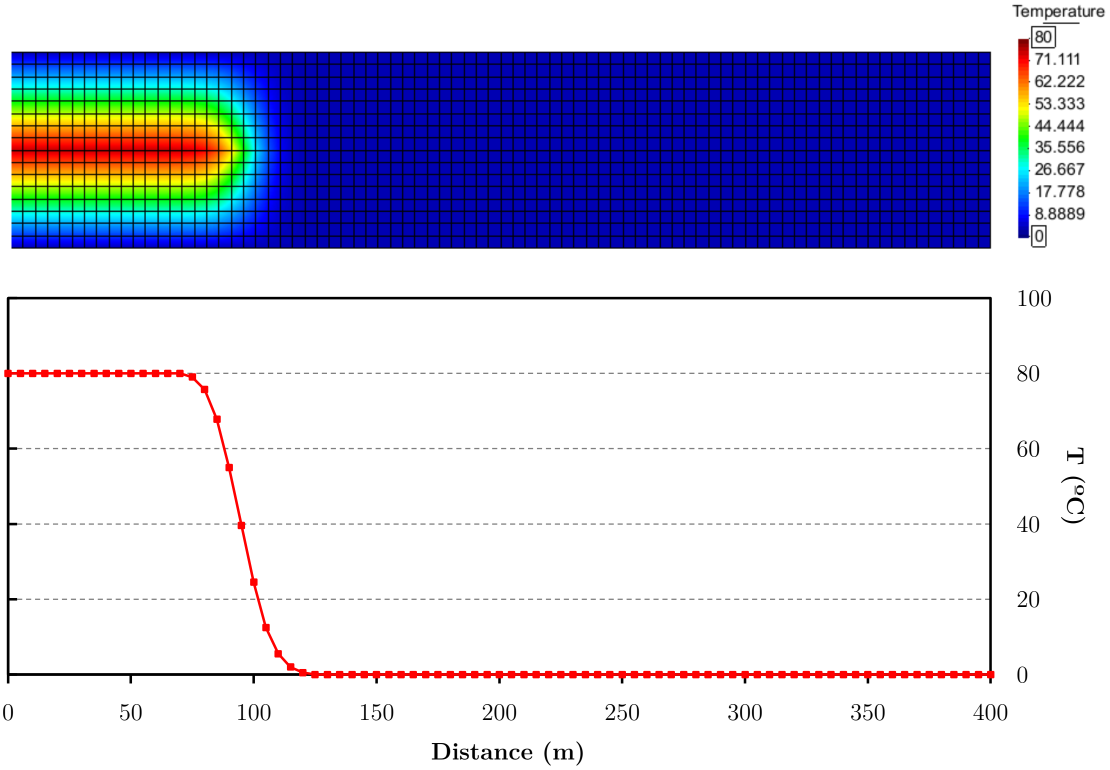

Figure 2.21: Transient thermal solution for Pe = ∞ using the implicit characteristic method for advective transport (t = 100 s). The plot shows the temperature distribution at the axis of symmetry.

Simple academic example 4: transient pure advection in a continuum medium using the α-Implicit Characteristic Method

The FE mesh of this example consists of a 2D horizontal domain of 1200x10 meters (Figure 2.22) composed of 480 continuum elements and 962 nodes. The initial distribution of temperatures of the thermal problem consists of a Gaussian distribution of temperatures, as shown in Figure 2.23. The transient problem is solved applying a known uniform velocity field of magnitude $v = 0.10\ m/s$ from left to right along the x-direction.

The thermal conductivity is assumed equal to zero and therefore the Péclet number tends to infinite (pure advection thermal problem). The Courant number in all the elements of the mesh is less than 1 ($C = 0.61$), which is a necessary condition to obtain a non-oscillatory result using the method of characteristics.

Figure 2.22: Mesh of the example (480 continuum elements and 962 nodes).

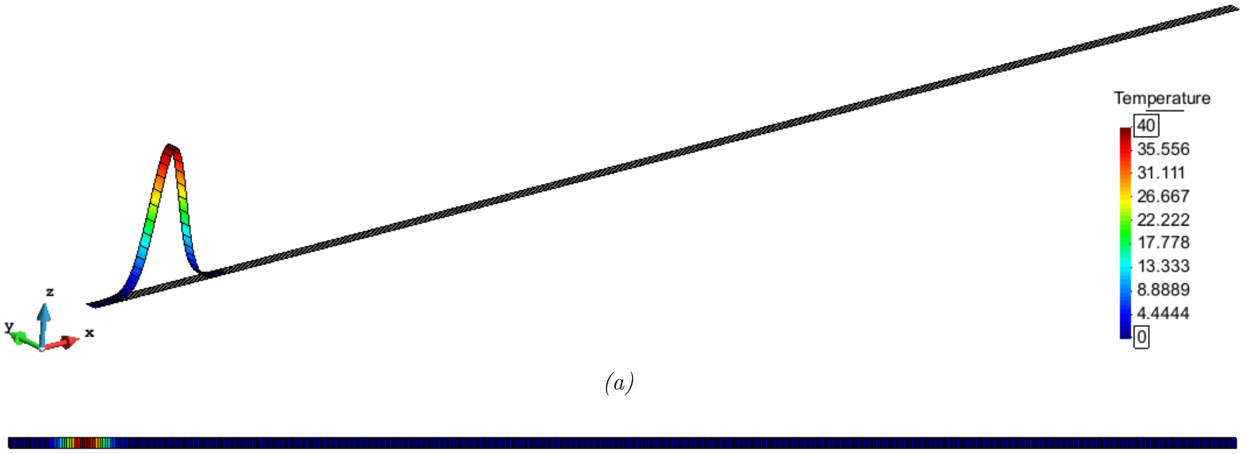

(a)

(b)

Figure 2.23: Initial distribution of temperatures: (a) 3-D profile; (b) 2-D profile.

As the time passes the initial temperature distribution has to move from left to right in the domain keeping the initial distribution profile. First, the analysis has been carried out with $\alpha = 1/10$ (Figure 2.24). These figures show that the method maintains the initial distribution of temperatures with small oscillations of +/- 0.60℃ at the top of the "bell" and at the front of the temperature profile.

The analysis can be carried out using other values of α. However, it has been observed that the best results are obtained for $\alpha = 1/4$ and the solution becomes unstable for $\alpha > 1/2$ and for $\alpha < 0$. Figure 2.25 shows the results for $\alpha = 1/4$, so that the temporal derivatives are evaluated centred around the solution x (Figure 2.16.b). In this case it is observed that the method maintains the initial distribution of temperatures with small oscillations of ± 0.10℃, only at the top of the “bell”. Moreover, Figure 2.26 shows the results for $\alpha = 2/5$, where it is observed that the oscillations become larger (± 4℃).

Finally, Figure 2.27 shows the results using the standard Galerkin weighting method, with which the original shape of the temperature profile is not maintained, with the peak value decreasing significantly as the “bell” base becomes much wider as time progresses.

Another test has been carried out with more refined meshes. In this case, the oscillations that appear in the front of the temperature profile become smaller and the solution improves significantly, producing lower loss of height of the temperature profile for both using the standard Galerkin weighting method and the α-Implicit Characteristic Galerkin method for all α-values.

It can be concluded that the α-Implicit Characteristic Galerkin method leads to better solutions than the standard Galerkin weighting on FEM, and that the best solution is achieved for a value of α=1/4. Meanwhile, the standard Galerkin weighting leads to solutions that have no relation to the real phenomenon in pure advective problems.

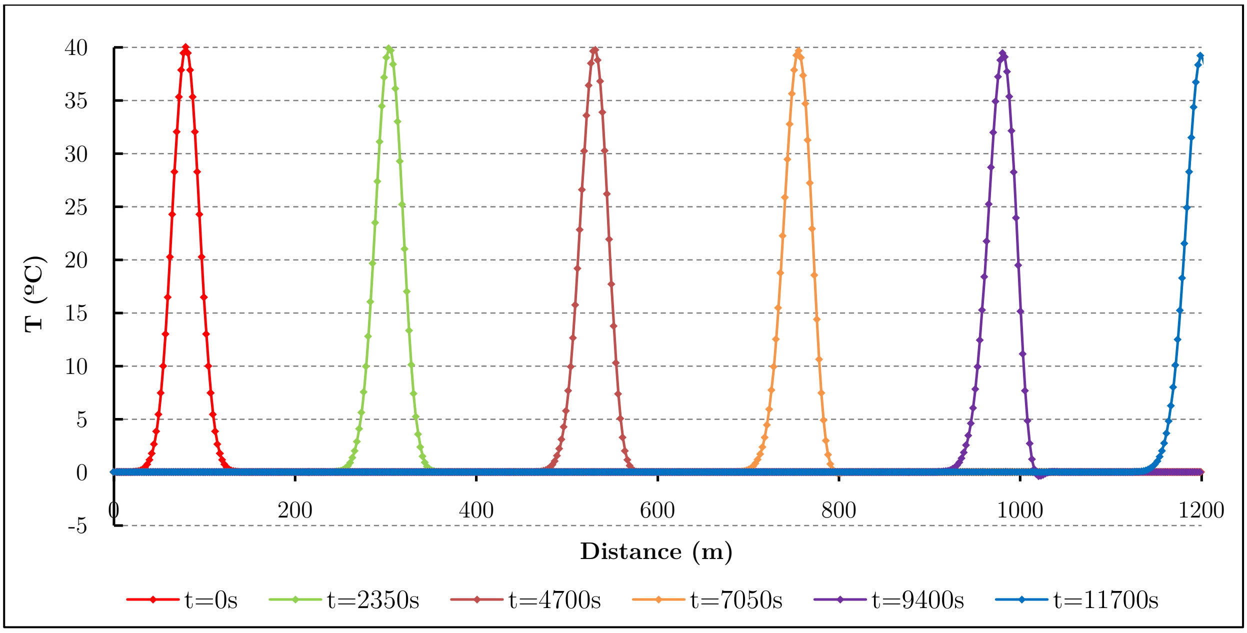

Figure 2.24: Distribution of temperatures using the α-ICG Method for different times ($\alpha = 1/10$).

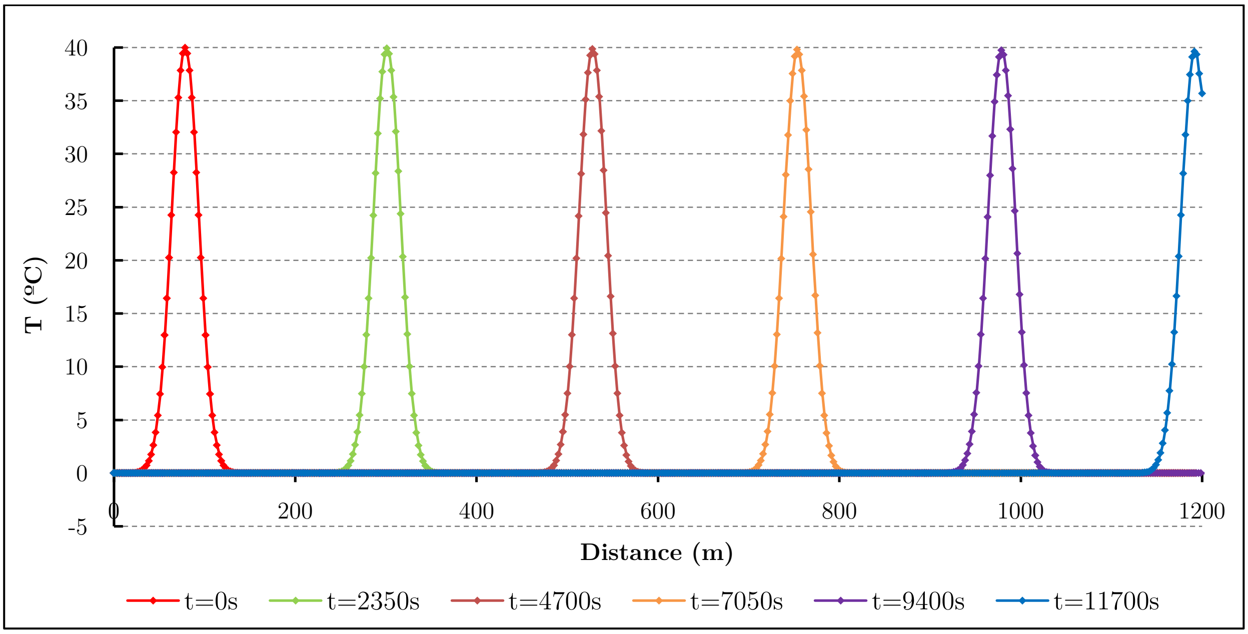

Figure 2.25: Distribution of temperatures using the α-ICG Method for different times ($\alpha = 1/4$).

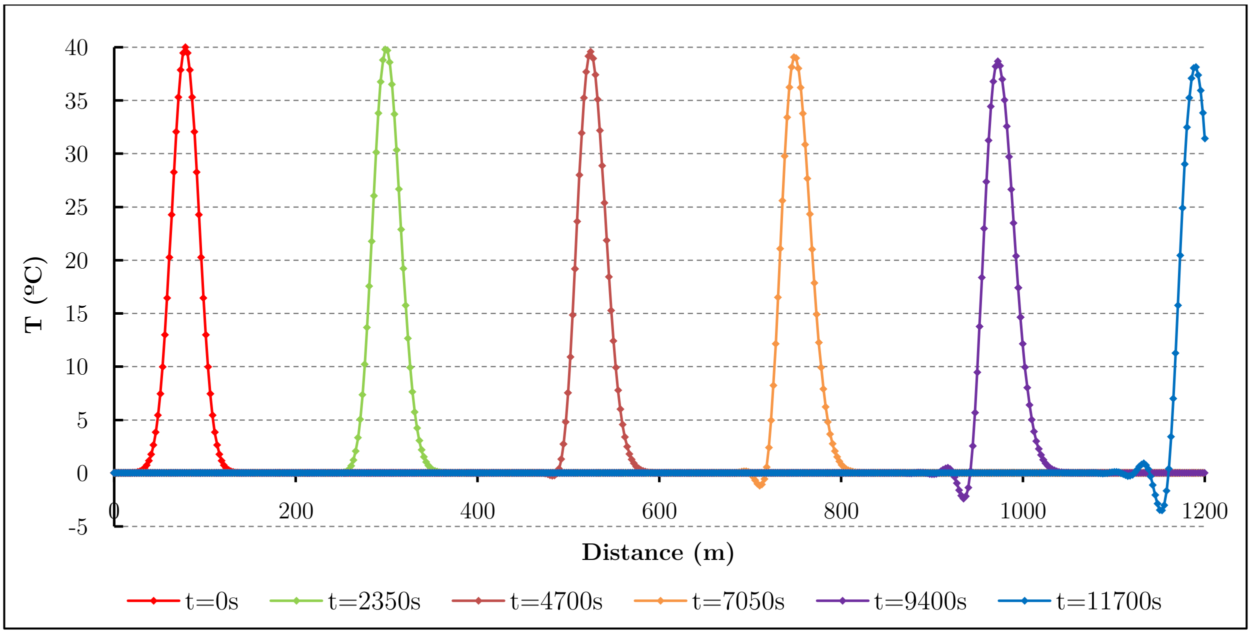

Figure 2.26: Distribution of temperatures using the α-ICG Method for different times ($\alpha = 2/5$).

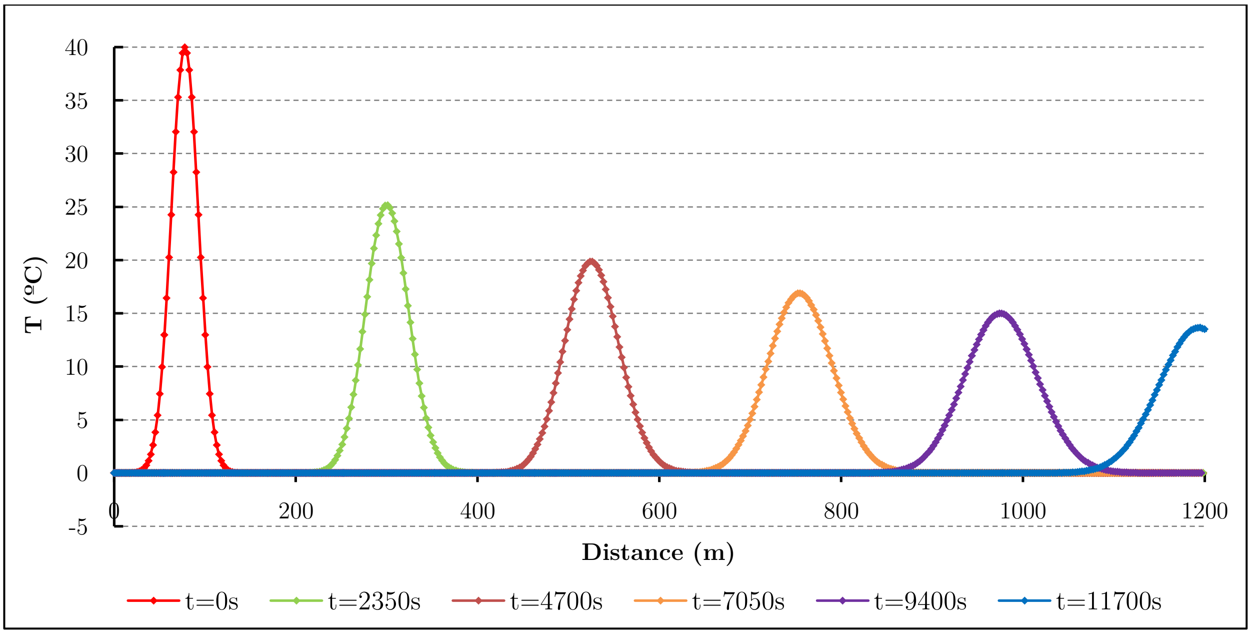

Figure 2.27: Distribution of temperatures for different times (Standard Galerkin Weighting).

Simple academic example 5: transient pure advection in a continuum medium using the α-Implicit Characteristic Method

The FE mesh of this example is the same as in the previous example (Figure 2.22) and consists of a 2D horizontal domain of 1200×10 meters composed of 480 continuum elements and 962 nodes. The initial distribution of temperatures of the thermal problem consists of a trapezoidal distribution of temperatures, as shown in Figure 2.23. The transient problem is solved by applying a known uniform velocity field of magnitude $v = 0.10\ m/s$ from the left to the right along the x-direction.

The thermal conductivity it is also assumed equal to zero and therefore the Péclet number tends to infinite (pure advection thermal problem). The Courant number in all the elements of the mesh is less than 1 ($C = 0.61$), which is a necessary condition to obtain a non-oscillatory result using the method of characteristics.

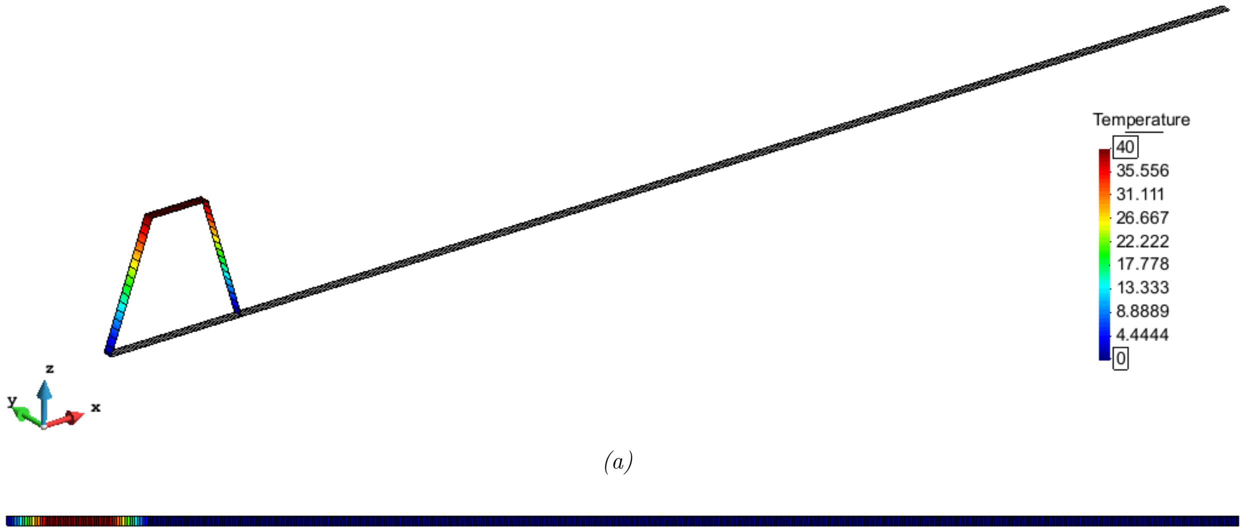

(a)

(b)

Figure 2.28: Initial distribution of temperatures: (a) 3-D profile; (b) 2-D profile.

As the time passes the initial temperature distribution has to move from the left to the right of the domain keeping the initial distribution profile. First, the analysis has been carried out with $\alpha = 1/10$ (Figure 2.29). The figure shows that, in this case, the method is not able to maintain the initial distribution of temperatures and leads to oscillations of +/- 2.40℃ at the top of the "platform" and at the front of the temperature profile.

The analysis can be carried out using other values of α. However, it has been observed that the best results are obtained for $\alpha = 1/4$ and the solution becomes unstable for $\alpha > 1/2$ and for $\alpha < 0$. Figure 2.30 shows the results for $\alpha = 1/4$, where it is observed that the method maintains the initial distribution of temperatures with small oscillations of ±0.40℃, at the top of the "platform" and at the front of the temperature profile. Moreover, Figure 2.31 shows the results for $\alpha = 1/2$, where it is observed that the oscillations become larger (±1.80℃) and the initial distribution of temperatures is not maintained.

In this case, the shape of the initial distribution of temperatures strongly influences the obtained results. The reason lies on the two nodes of the distribution where the temperature undergoes a sudden change. Thus, the main oscillations appear around these “jump” nodes, leading to the known Gibbs phenomenon.

Finally, Figure 2.32 shows the results using the standard Galerkin weighting method, with which the original shape of the temperature profile is not maintained, with the peak value decreasing significantly as the “platform” base becomes much wider as time progresses.

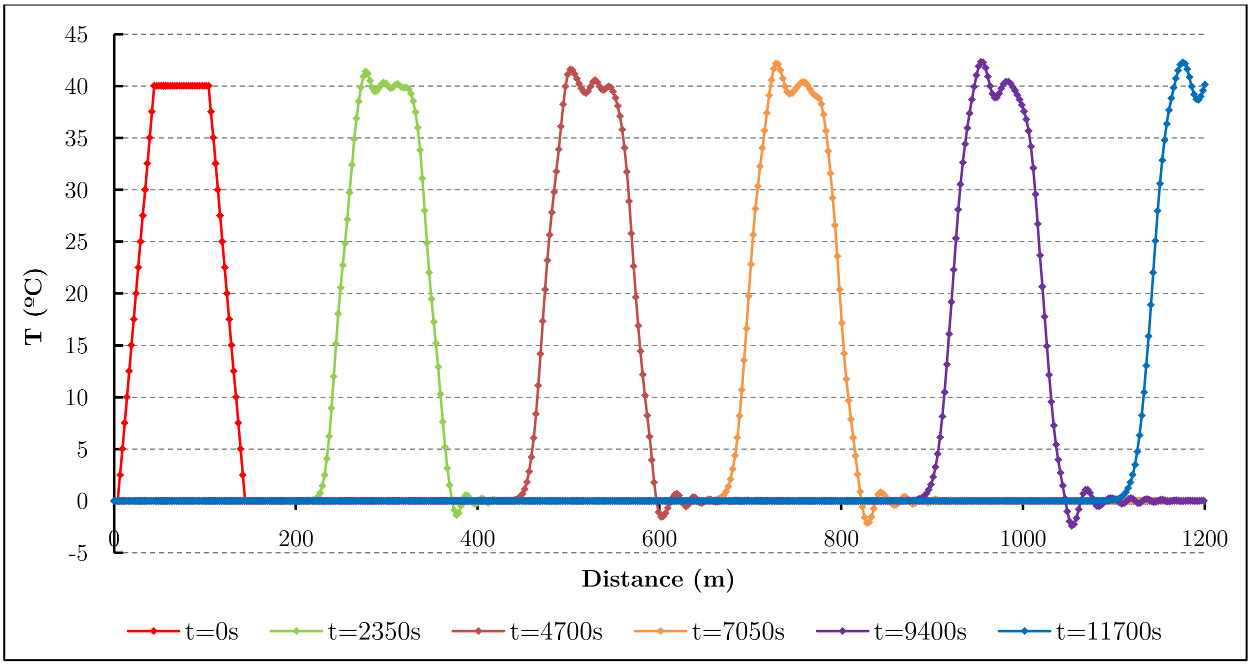

Figure 2.29: Distribution of temperatures using the α-ICG Method for different times ($\alpha = 1/10$).

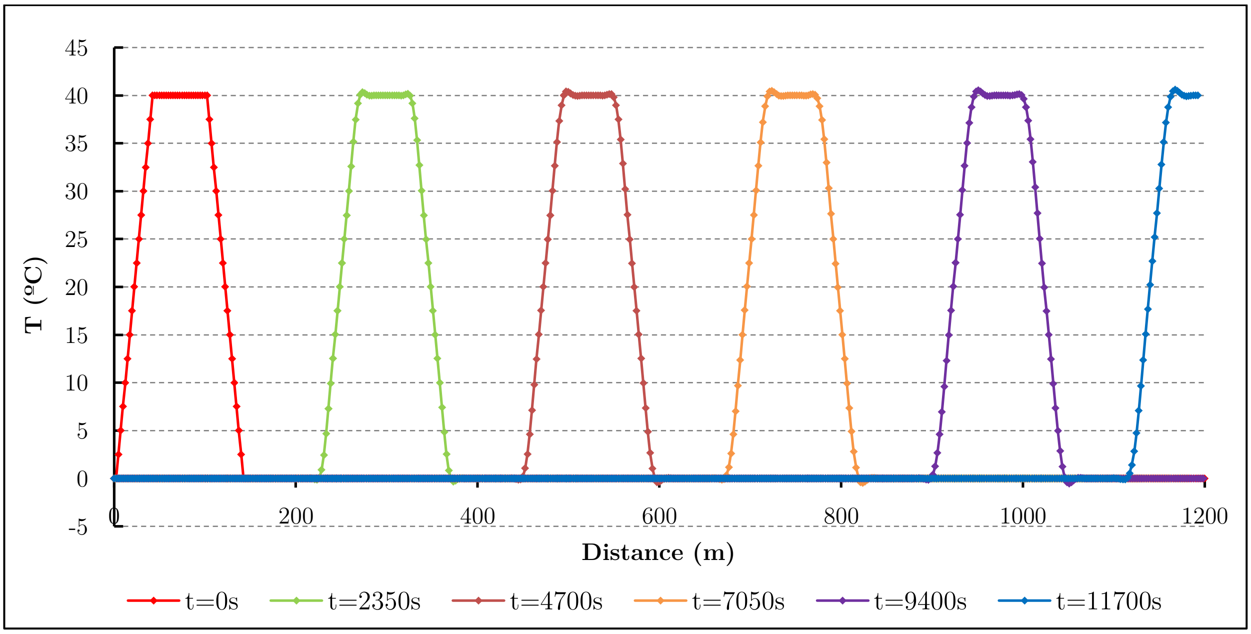

Figure 2.30: Distribution of temperatures using the α-ICG Method for different times ($\alpha = 1/4$).

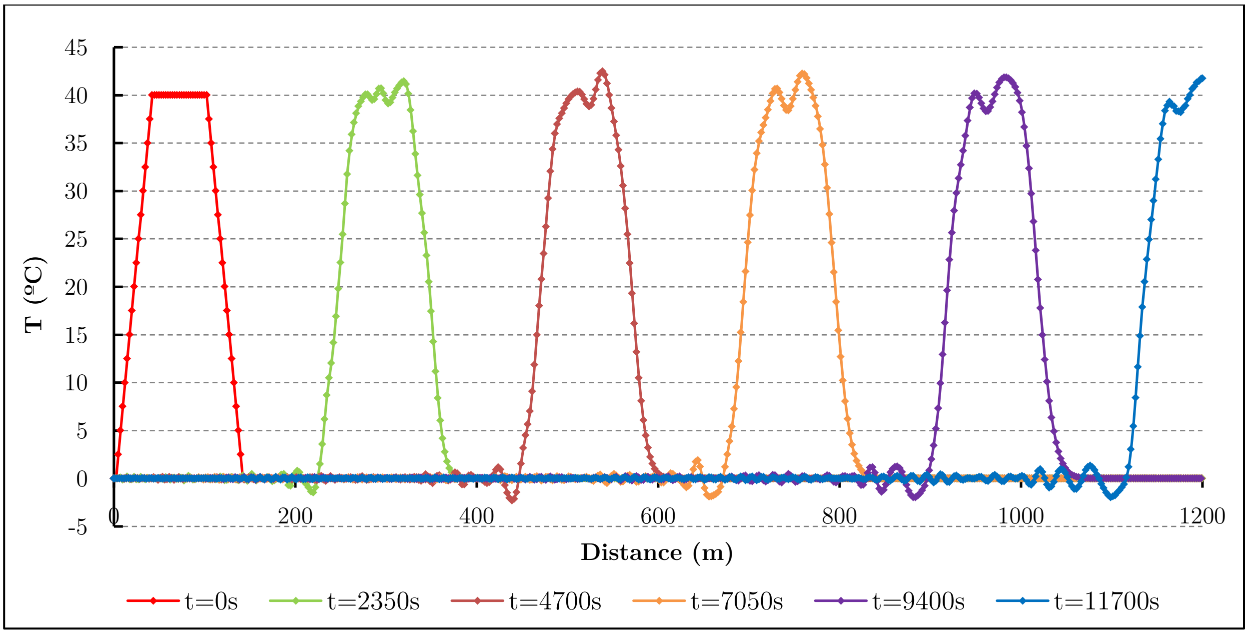

Figure 2.31: Distribution of temperatures using the α-ICG Method for different times ($\alpha = 1/2$).

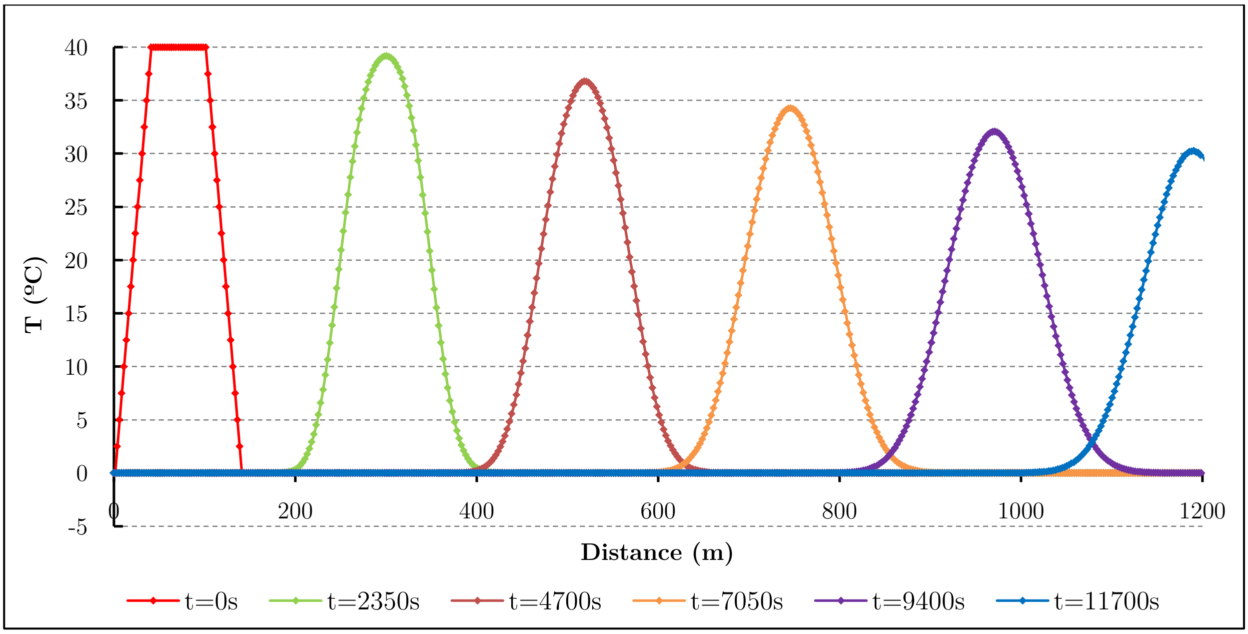

Figure 2.32: Distribution of temperatures using the α-ICG Method for different times (Standard Galerkin Weighting).

Simple academic example 6: transient pure advection in a continuum medium using the α-Implicit Characteristic Method

The FE mesh of this example is shown in Figure 2.33 and consists of a 2D mesh composed of 3000 continuum elements and 3311 nodes. In order to obtain a velocity field for the advective problem, the steady-state hydraulic problem is solved with the boundary conditions shown in Figure 2.35, which leads to the radial distribution of velocities with decreasing value which is shown in the same figure. These velocities, which vary from 0.60 to 1.80 m/s, are applied to the transient thermal problem, with the initial distribution of temperatures shown in Figure 2.34. The thermal conductivity is equal to zero and the Péclet number tends to infinite (pure advection thermal problem). The Courant number varies between 0.21 and 0.63 over the mesh (Figure 2.36).

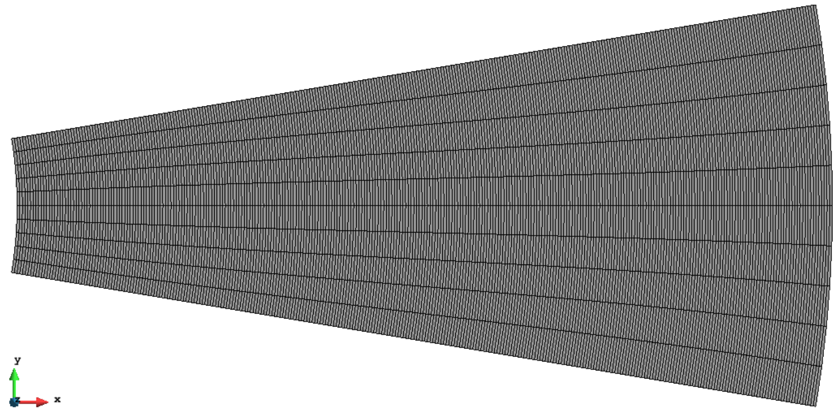

Figure 2.33: Mesh of the example (3000 continuum elements and 3311 nodes).

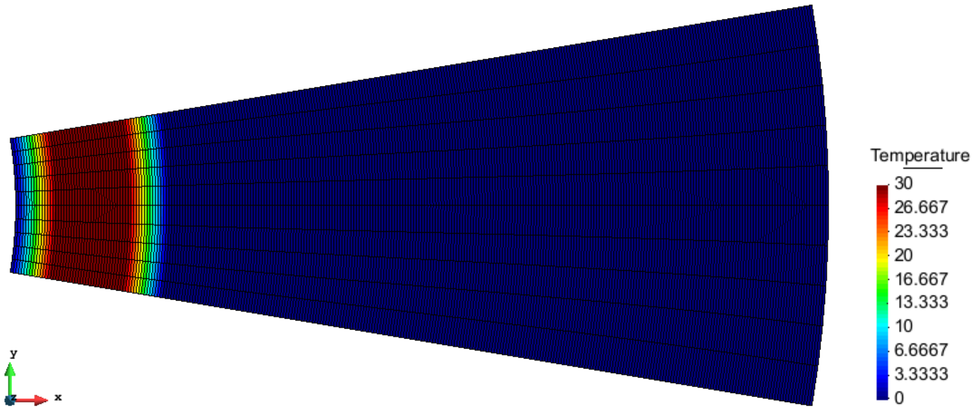

(a)

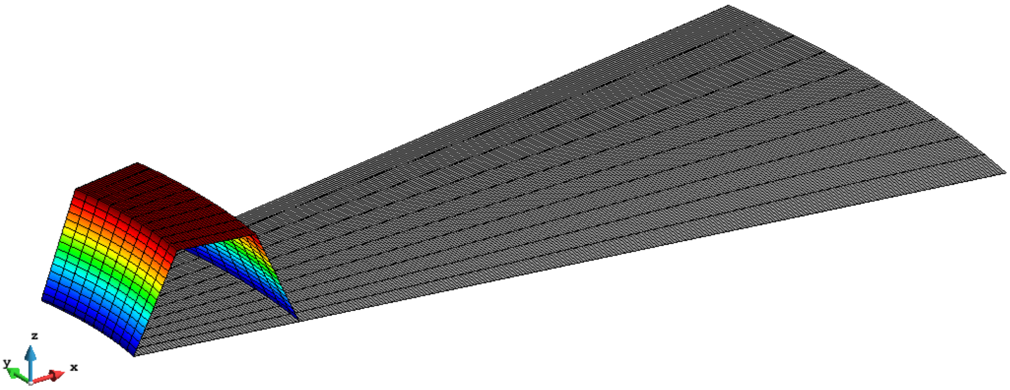

(b)

Figure 2.34: Initial distribution of temperatures: (a) 2-D profile; (b) 3-D profile.

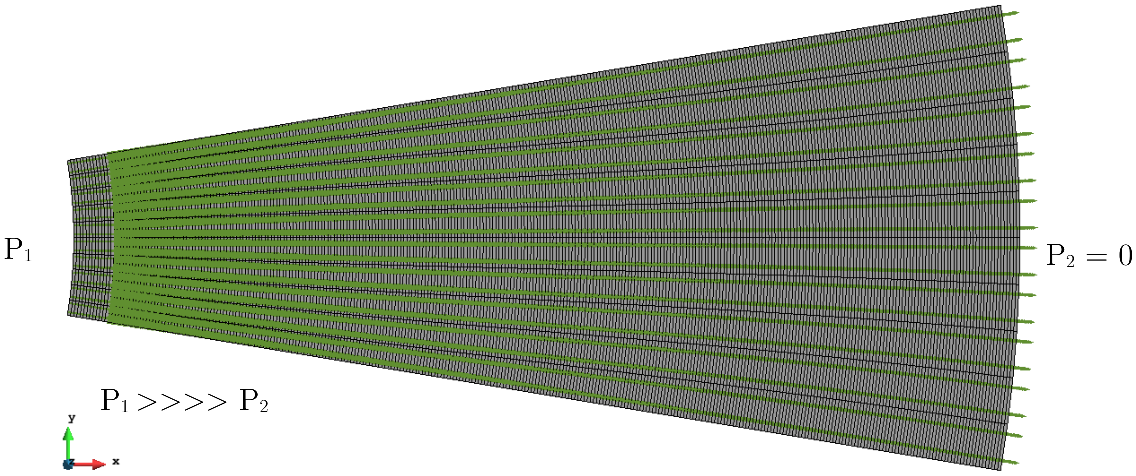

Figure 2.35: Boundary conditions of the hydraulic problem (imposed pressures) and the velocities obtained from the analysis. The velocities decrease towards the right of the domain. P_1 and P_2 are the imposed pressures of the problem.

The analysis has been carried out using the new α-Implicit Characteristic Galerkin method, first assuming $\alpha = 1/4$, which is, as described in the previous examples, the best value to stabilize the solution. The results for $\alpha = 1/4$ are presented in Figure 2.37. The figure shows that, as times progresses, the temperature distribution becomes narrower in the direction of velocities (x), and the maximum value of the temperatures remains constant, complying with the principle of heat preservation (the "volume" of the temperature field remains constant and because of that also the total amount of heat). Figure 2.38 shows the temperature distribution on the axis of simmetry of the domain. Small oscillations with values around ±0.5℃ can be perceived.

Moreover, the analysis has been carried out for other different values of α. Figure 2.39 shows the results using $\alpha = 0$, which is coincident with the Implicit Carachteristic Galerkin method. In this case the oscillations become bigger with values around ±1.2℃. Finally, Figure 2.40 shows the results using $\alpha = 0.50$. In this case the oscillations become bigger with values around ±1.7℃.

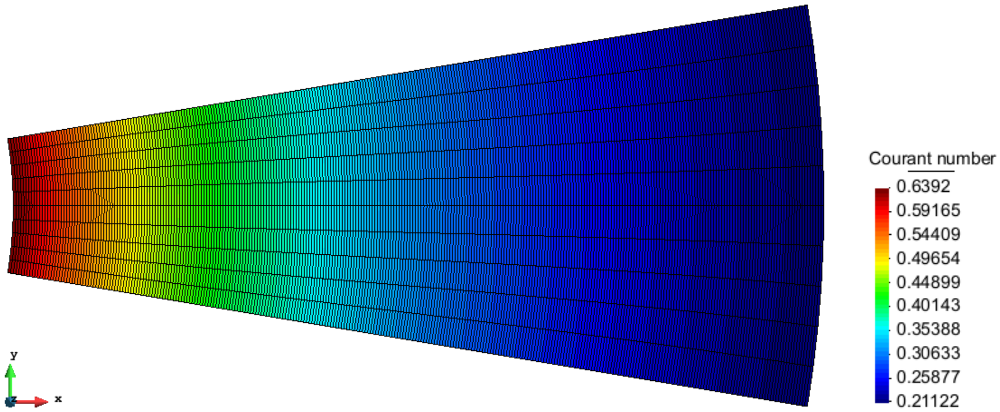

Figure 2.36: Courant number over the FEM mesh.

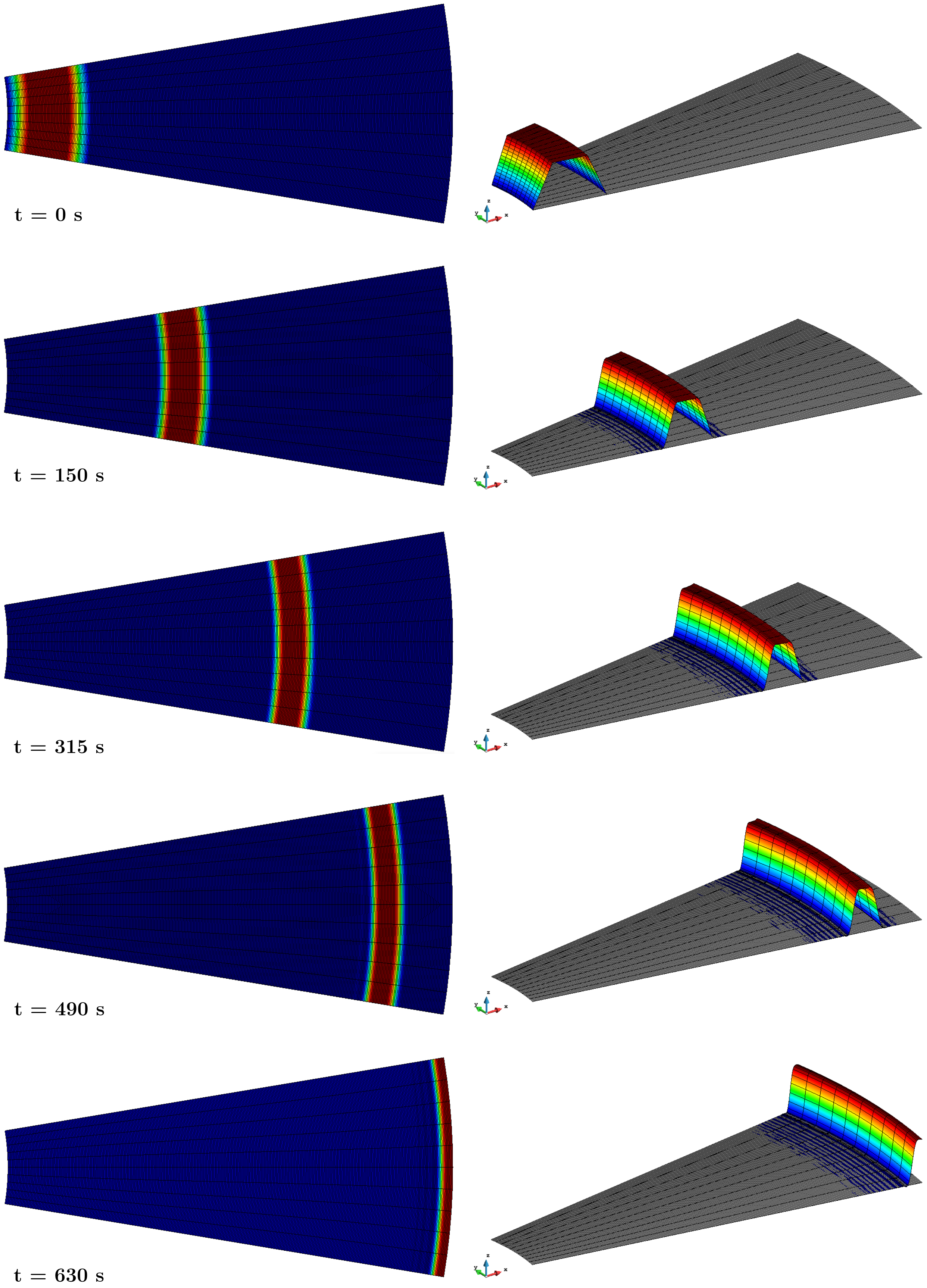

Figure 2.37: Distribution of temperatures for different times using the α-ICG method with $\alpha = 1/4$. Legend in figure Figure 2.34.a.

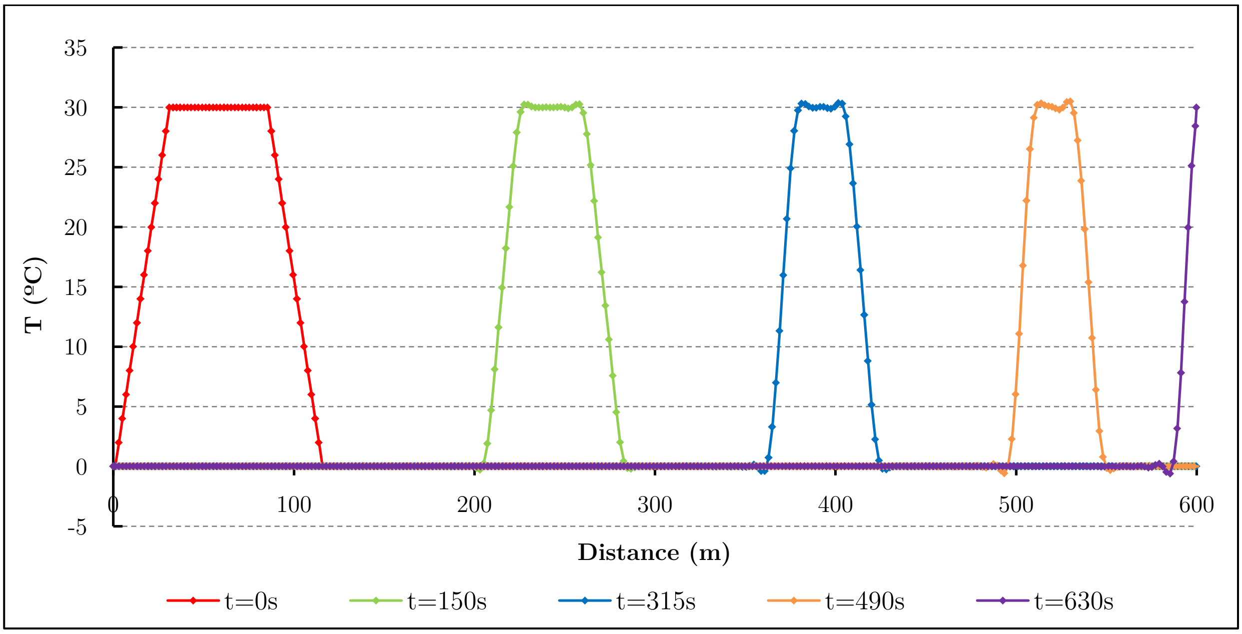

Figure 2.38: Distribution of temperatures for different times (axis of symmetry) for $\alpha = 1/4$.

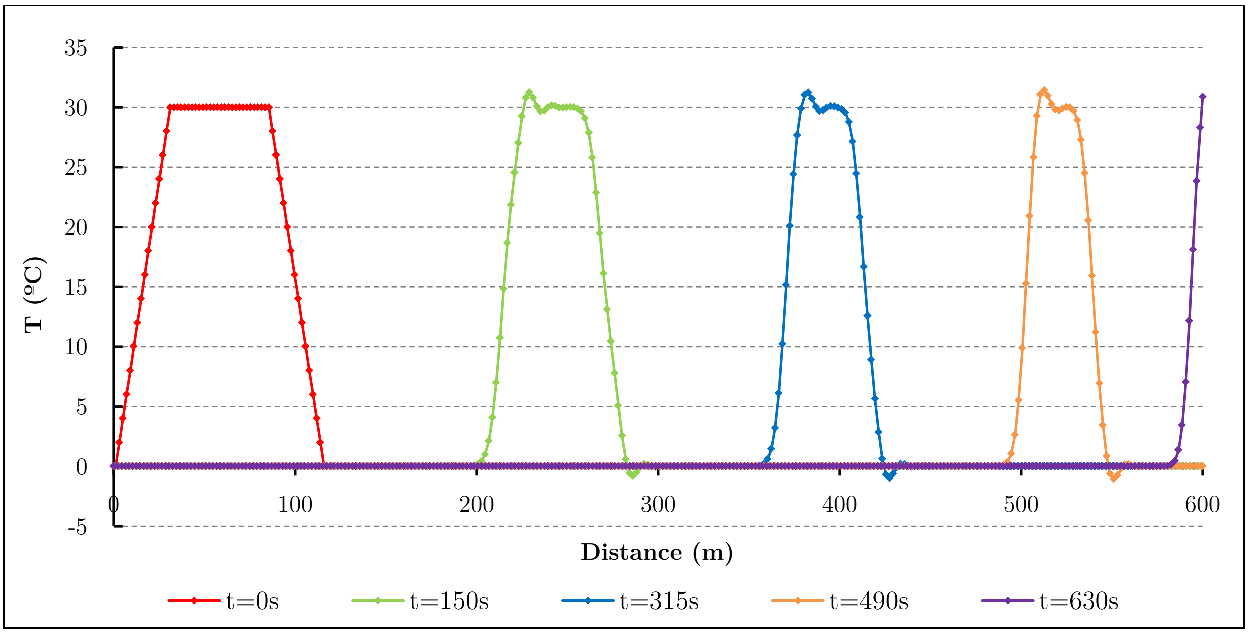

Figure 2.39: Distribution of temperatures for different times (axis of symmetry) for $\alpha = 0$.

Finally, Figure 2.41 shows the results using the standard Galerkin weighting method with which the original shape of the temperature profile is not maintained, and the peak value decreases significantly as the base becomes much wider. This effect is the same observed in the previous examples.

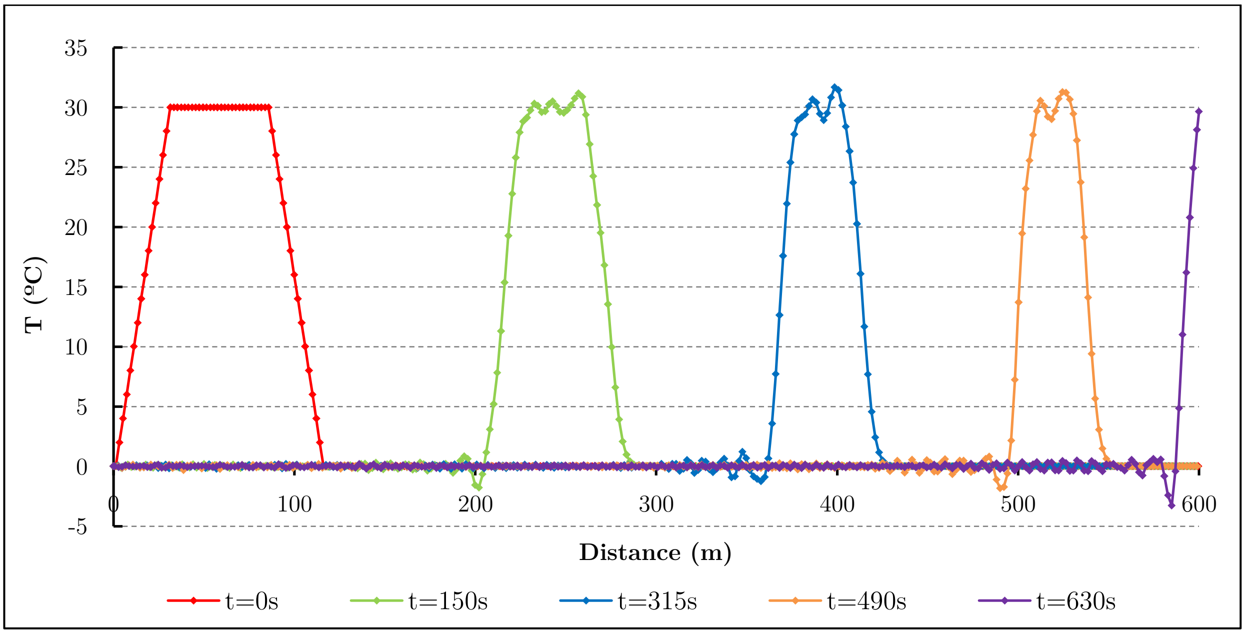

Figure 2.40: Distribution of temperatures for different times (axis of symmetry) for $\alpha = 1/2$.

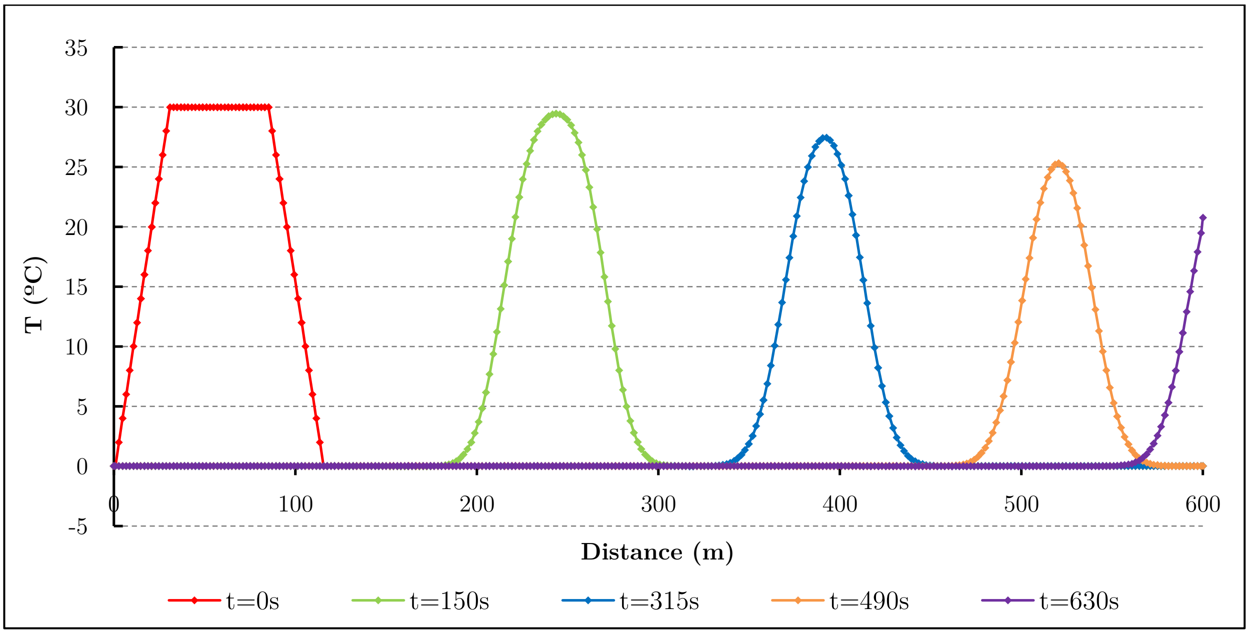

Figure 2.41: Distribution of temperatures for different times (axis of symmetry) (Standard Galerkin Weighting).

Simple academic example 7: transient pure advection in a continuum medium using the α-Implicit Characteristic Method

The FE mesh of this example consists of a quadrangular 500×500m domain with a 2D regular mesh composed of 10000 continuum quadrilateral elements and 10201 nodes. The initial distribution of temperatures of the thermal problem is trapezoidal, as shown in Figure 2.42. The thermal conductivity coefficient is assumed equal to zero and therefore the Péclet number tends to infinite (pure advection thermal problem). During the transient thermal analysis a circular velocity field ($\omega = 5 \cdot 10^{-04}$ rad/s) around the geometric centre of the domain is applied. Therefore, the physical solution of the problem consists of the initial temperature distribution rotating unaltered around the domain center. The Courant number varies between 0 (centre of the domain) and 0.50 (corners of the domain).

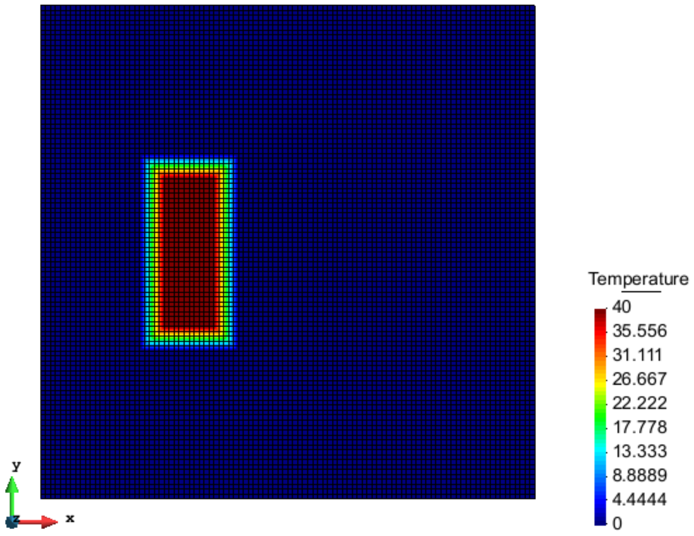

(a)

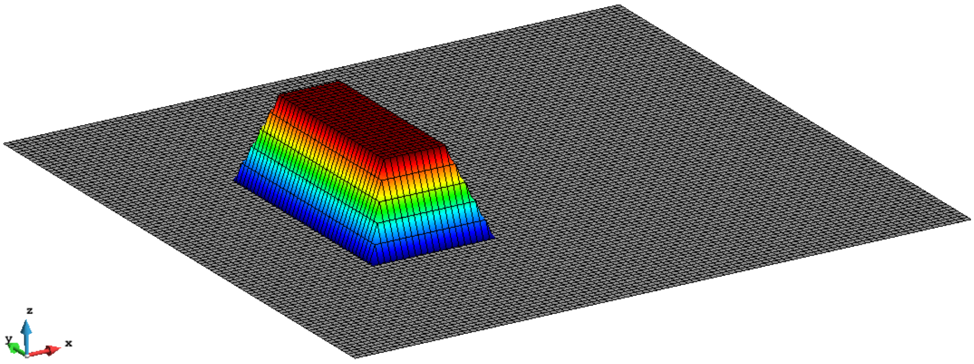

(b)

Figure 2.42: Initial distribution of temperatures. (a) 2-D profile; (b) 3-D profile.

The analysis can be carried out using the α-ICG method for different values of α. However, as in the previous examples, it has been observed that the best results are obtained for $\alpha = 1/4$ and the solution becomes unstable for $\alpha > 1/2$ and for $\alpha < 0$.

Figure 2.43 shows the results for $\alpha = 1/4$, where it is observed that the method maintains well the initial distribution of temperatures with small oscillations of ± 1.3℃ , mainly at the top of the "platform". However, a few small residual waves appear around the domain with the movement of the platform, which have small values ($\pm 5 \cdot 10^{-3}$℃), as shown in Figure 2.44.

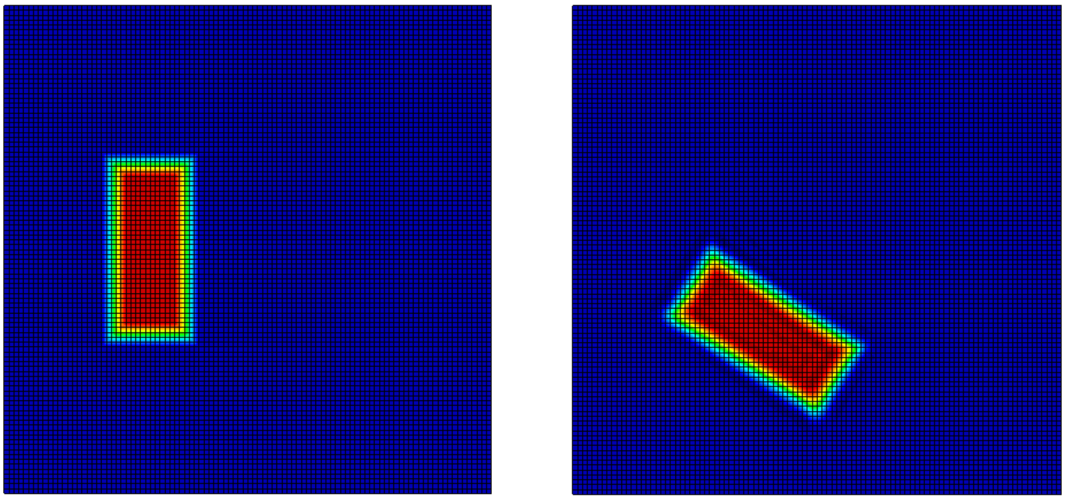

(a) $t = 0$ s. (b) $t = 1000$ s.

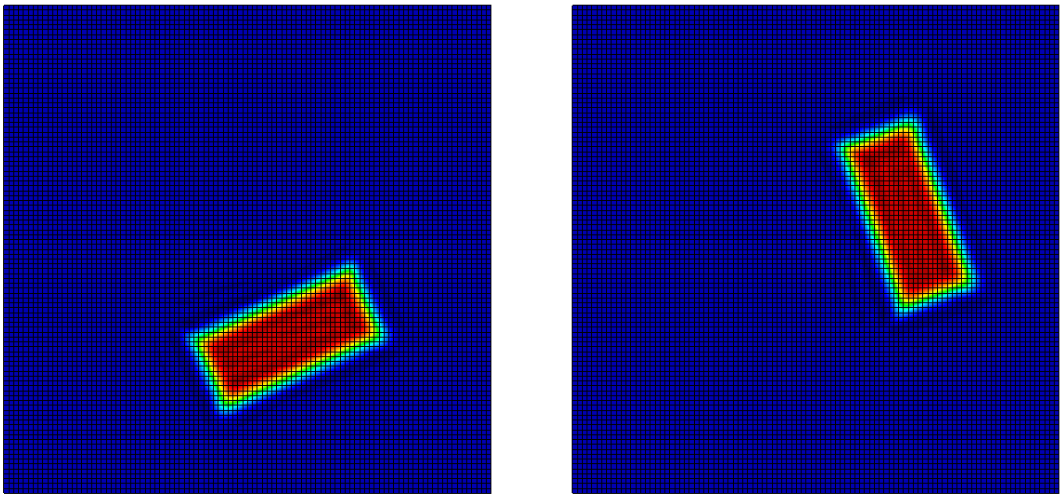

(c) $t = 2000$ s. (d) $t = 3500$ s.

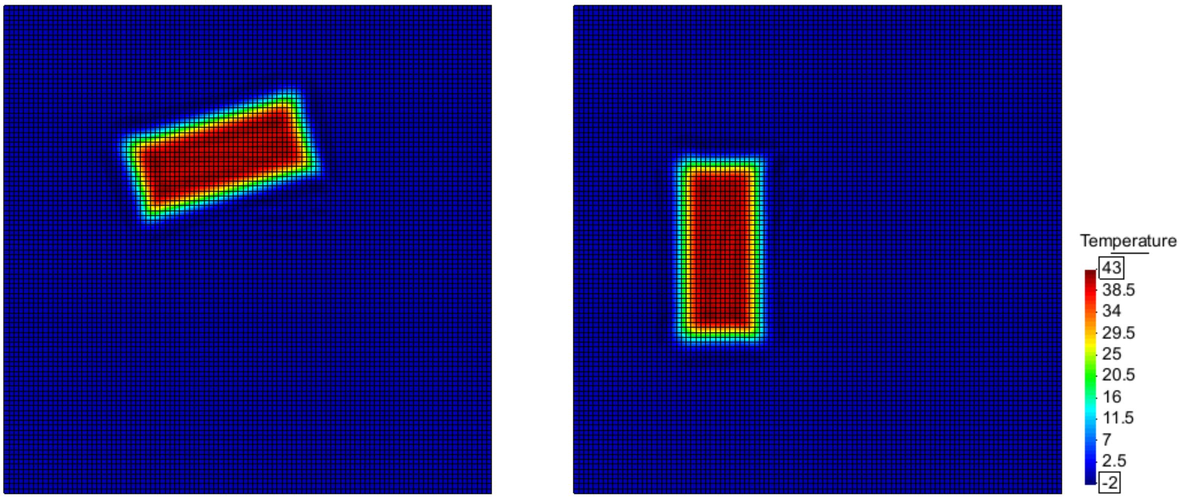

(e) $t = 5000$ s. (f) $t = 6300$ s.

Figure 2.43: Distribution of temperatures for different times using the α-ICG method with $\alpha = 1/4$.

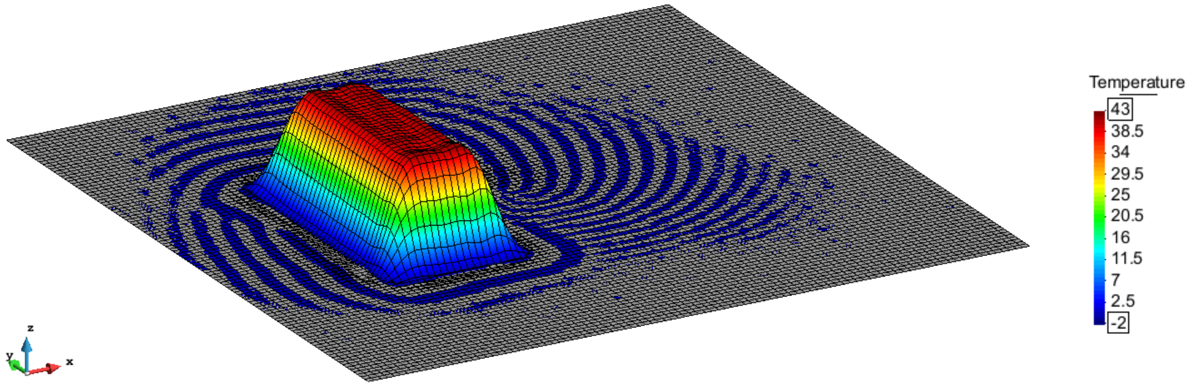

Figure 2.44: Distribution of temperatures after one complete rotation using the α*-ICG method with* $\alpha = 1/4$*. As it is observed, a few residual waves around the domain with values* $5 \cdot 10^{-3}$*ºC appear.*

Figure 2.45 shows the distribution of temperatures at the axis of the domain for the initial distribution, the distribution after a rotation of 180º and after 360º of rotation (Figure 2.43.f).

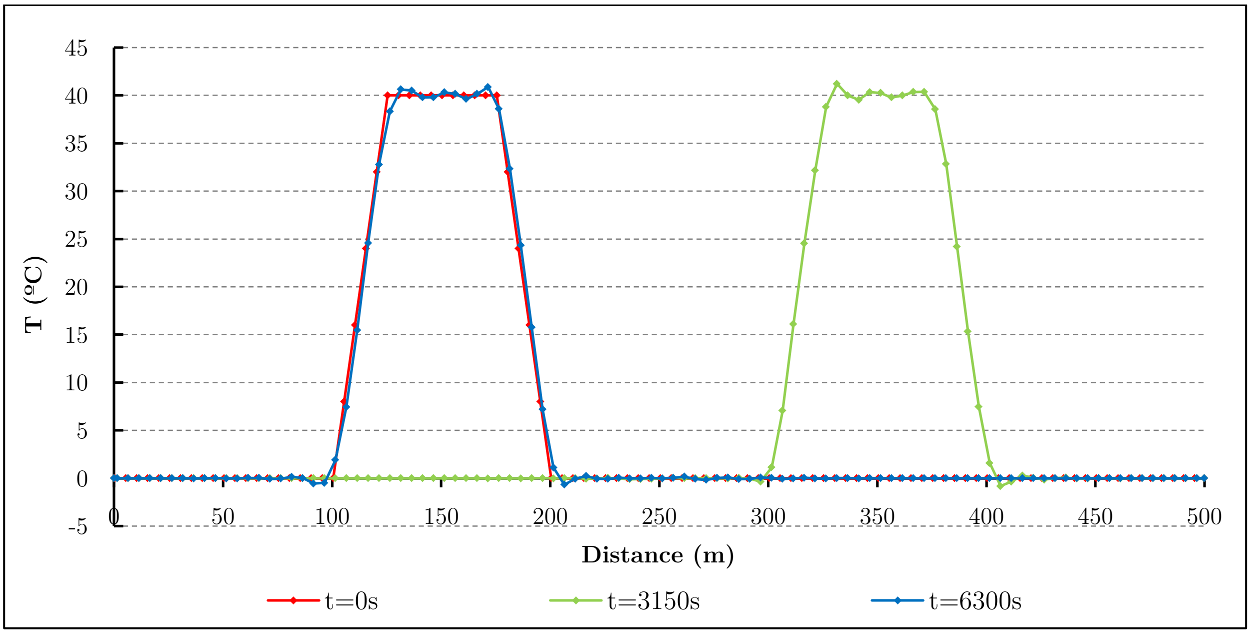

Figure 2.45: Distribution of temperatures for the initial distribution, after a rotation of 180º and after a rotation of 360º (axis of symmetry) using the α*-ICG method with* $\alpha = 1/4$*.*

Figure 2.46 and Figure 2.47 show the results using the standard Galerkin weighting method with which the original shape of the temperature profile is not maintained as the “platform” rotates around the centre of the domain.

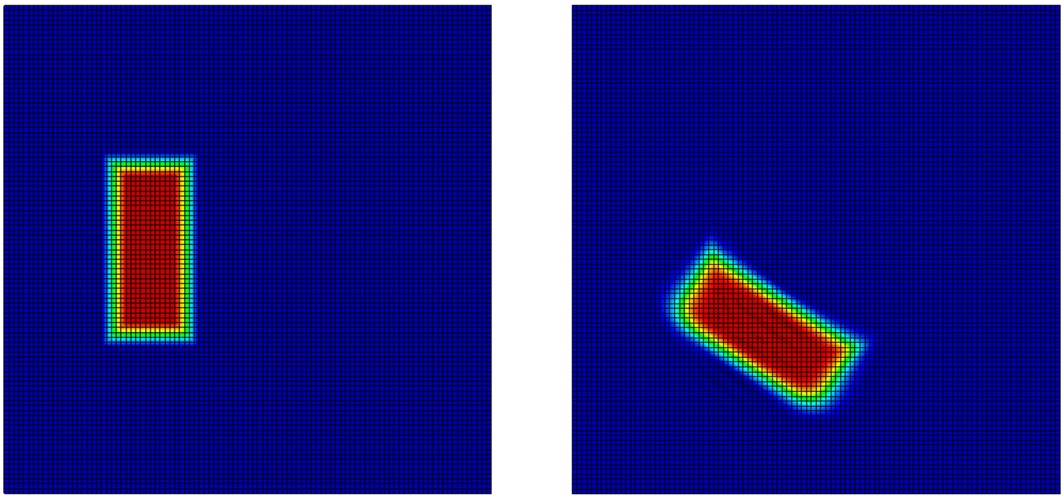

(a) $t = 0$ s. *(b) $t = 1000$ s.*

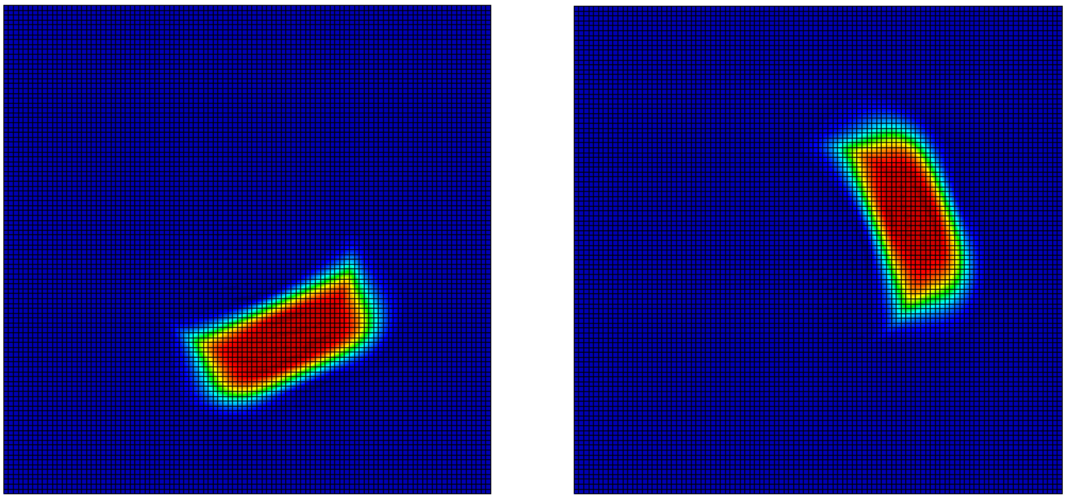

(c) $t = 2000$ s. *(d) $t = 3500$ s.*

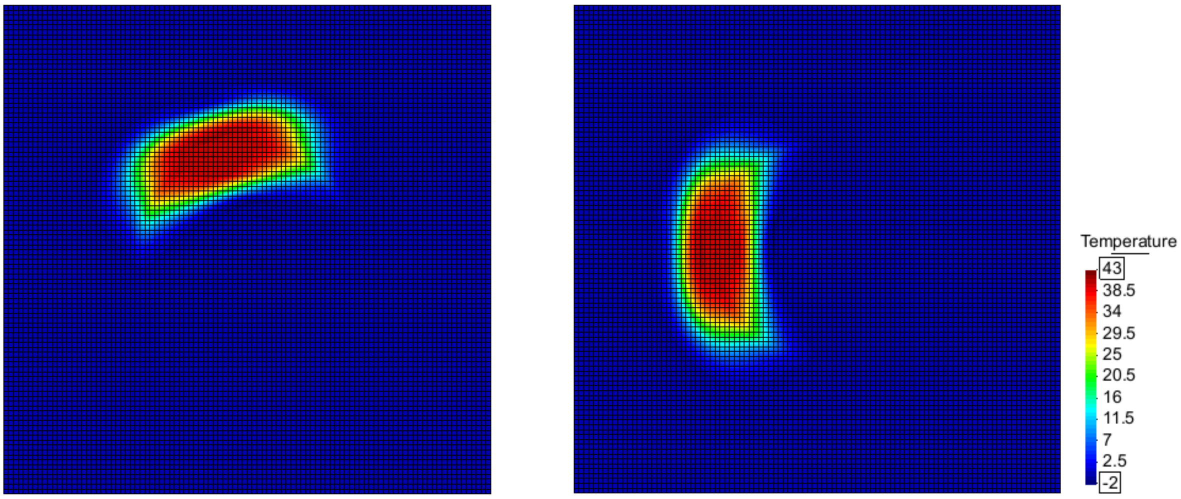

(e) $t = 5000$ s. *(f) $t = 6300$ s.*

Figure 2.46: Distribution of temperatures for different times (Standard Galerkin Weighting).

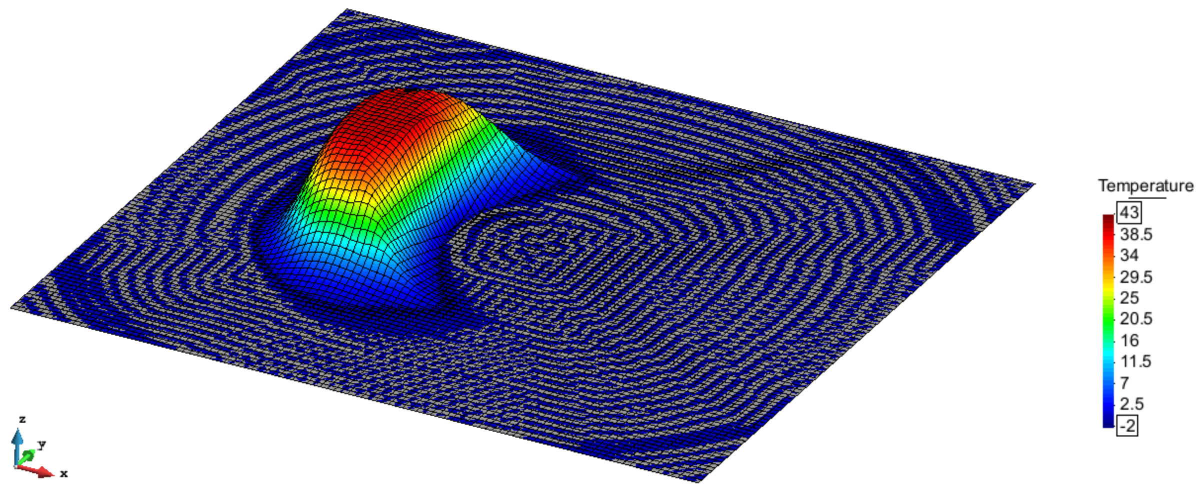

Figure 2.47: Distribution of temperatures after one complete rotation using the Standard Galerkin Weighting.

Simple academic example 8: transient pure advection in a continuum medium using the α-Implicit Characteristic Method

The FE mesh of this example consists of a circular domain (diameter 500m) with a 2D regular mesh composed of 12000 continuum elements (hexahedrons) and 12240 nodes. The initial distribution of temperatures of the thermal problem consists in a trapezoidal distribution of temperatures and a Gaussian distribution of temperatures, both separated 180º, as shown in Figure 2.48. The thermal conductivity coefficient is assumed equal to zero and therefore the Péclet number tends to infinite (pure advection thermal problem). During the transient thermal analysis, a circular velocity field ($\omega = 5 \cdot 10^{-04}$ rad/s) around the geometric centre of the domain is applied. Therefore, the physical solution of the problem consists of the initial temperature distribution rotating unaltered around the domain centre. The Courant number depends on the size of the element and the velocities and varies between 0.35 and 0.45.

The analysis can be carried out using the α-ICG method for different values of α. However, as in the previous examples, it has been observed that the best results are obtained for $\alpha = 1/4$ and the solution becomes unstable for $\alpha > 1/2$ and for $\alpha < 0$.

Figure 2.50 shows the results for $\alpha = 1/4$, where it is observed that the method maintains well the initial distribution of temperatures with small oscillations of ± 3.1℃, mainly at the base of the "platform", while the oscillations at the top of both distributions are around ± 0.2℃. Additionally, a few small residual waves appear around the domain with the movement of the temperature distributions, which have small values ($\pm 5 \cdot 10^{-3}$℃), as shown in Figure 2.49.

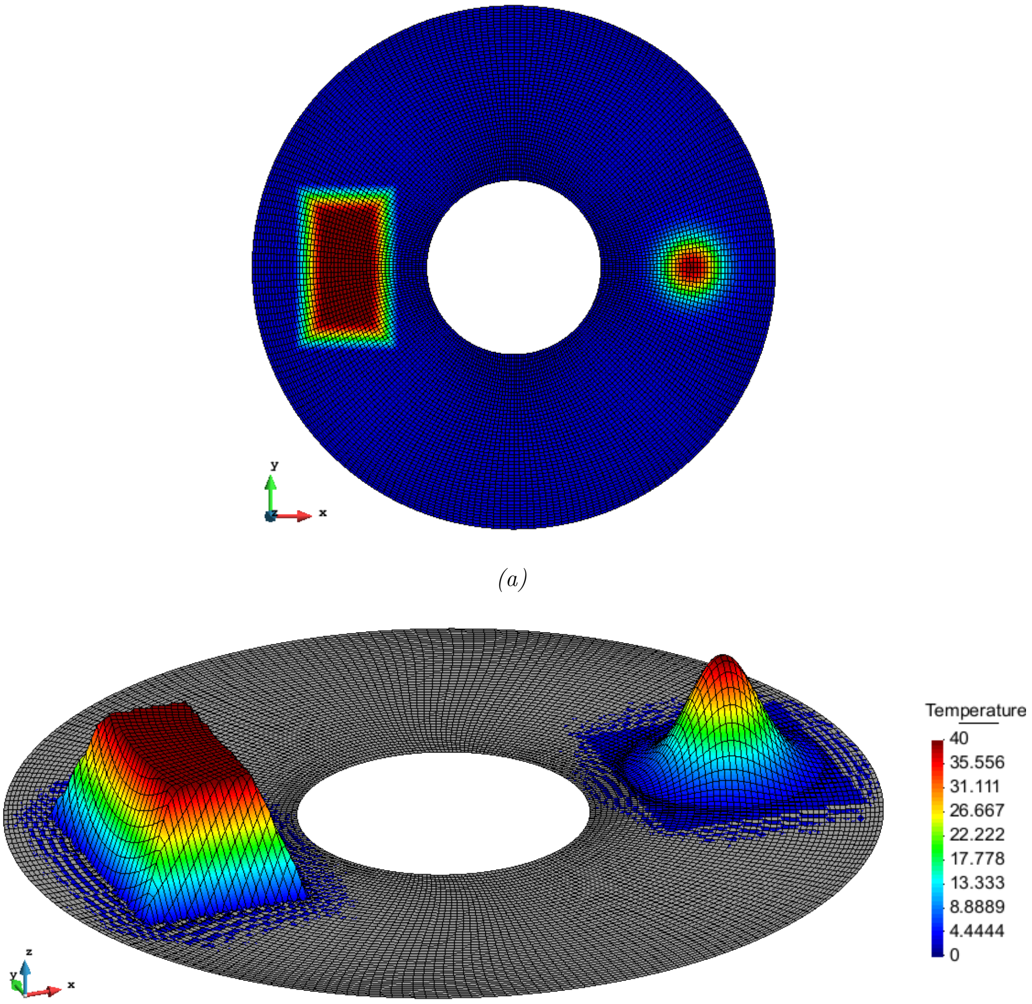

(a)

(b)

Figure 2.48: Initial distribution of temperatures. (a) 2-D profile; (b) 3-D profile.

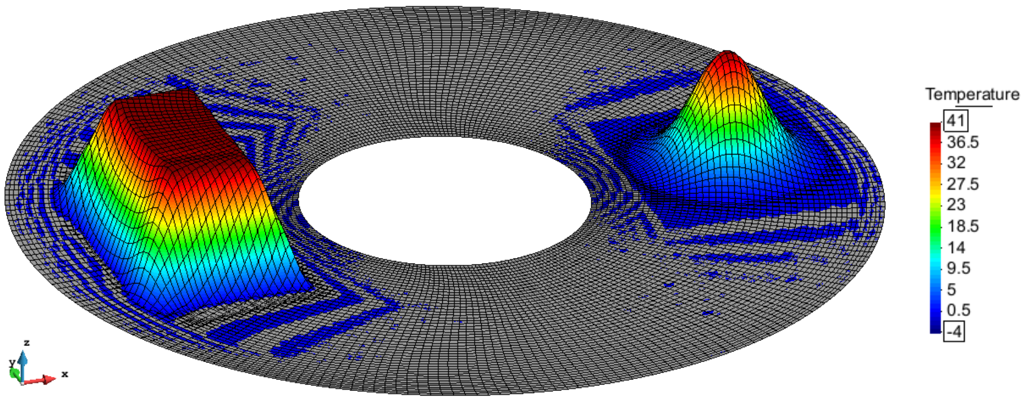

Figure 2.49: Distribution of temperatures after one complete rotation using the α-ICG method with $\alpha = 1/4$. As it is observed, a few residual waves around the domain with values $5 \cdot 10^{-3}$ºC appear.

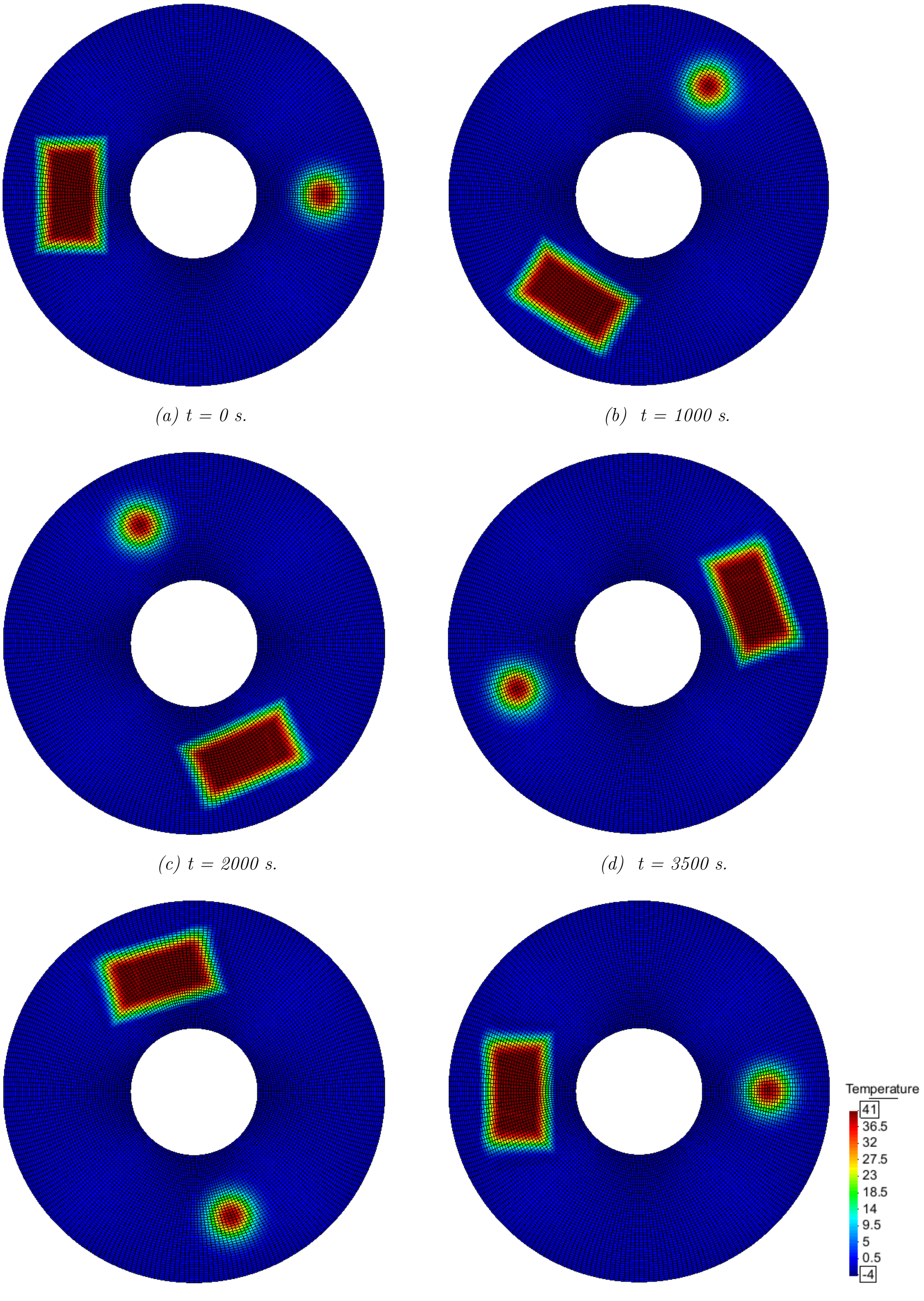
(a) t = 0 s.

(b) t = 1000 s.

(c) t = 2000 s.

(d) t = 3500 s.

(e) t = 5000 s.

(f) t = 6300 s.

Figure 2.50: Distribution of temperatures for different times using the α-ICG method with $\alpha = 1/4$.

Figure 2.51 shows the distribution of temperatures at the axis of the domain for the initial distribution and the distribution after a rotation of 360º (Figure 2.50.f).

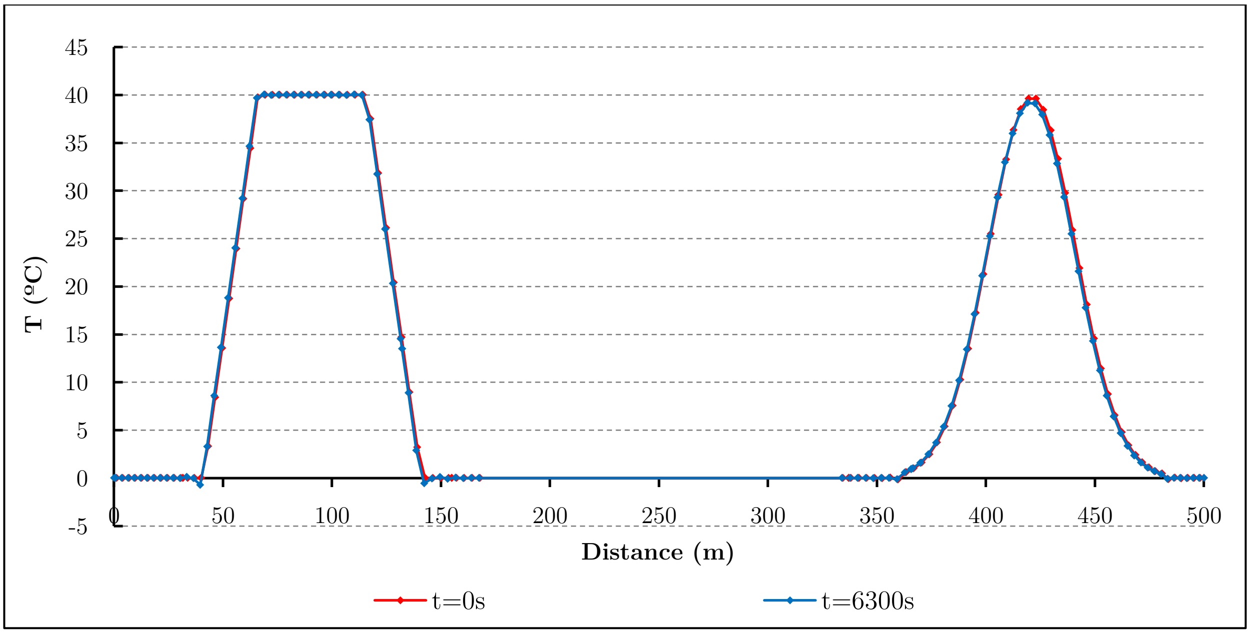

Figure 2.51: Distribution of temperatures for the initial distribution and after rotation of 360º (axis of symmetry) using the α-ICG method with $\alpha = 1/4$.

Finally, for comparison Figure 2.52 and Figure 2.53 show the results using the standard Galerkin weighting method with which the original shape of the temperature profile is not maintained as the "platform" rotates around the centre of the domain.

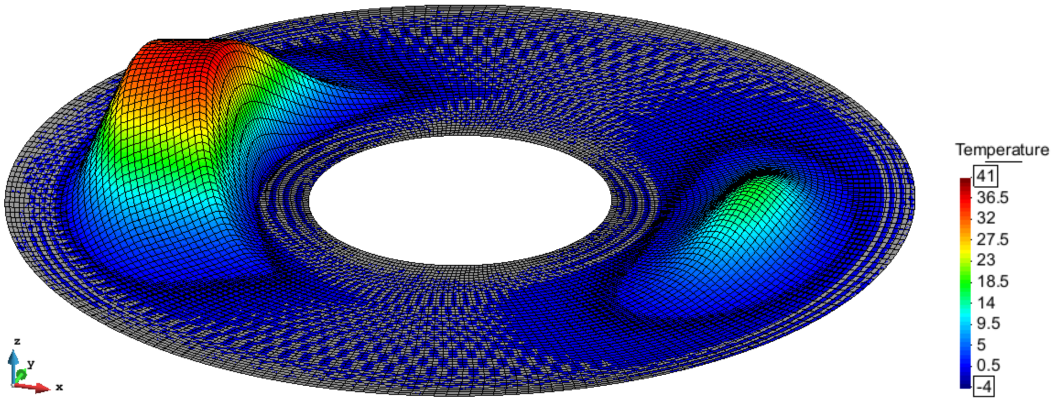

Figure 2.52: Distribution of temperatures after one complete rotation using the Standard Galerkin Weighting.

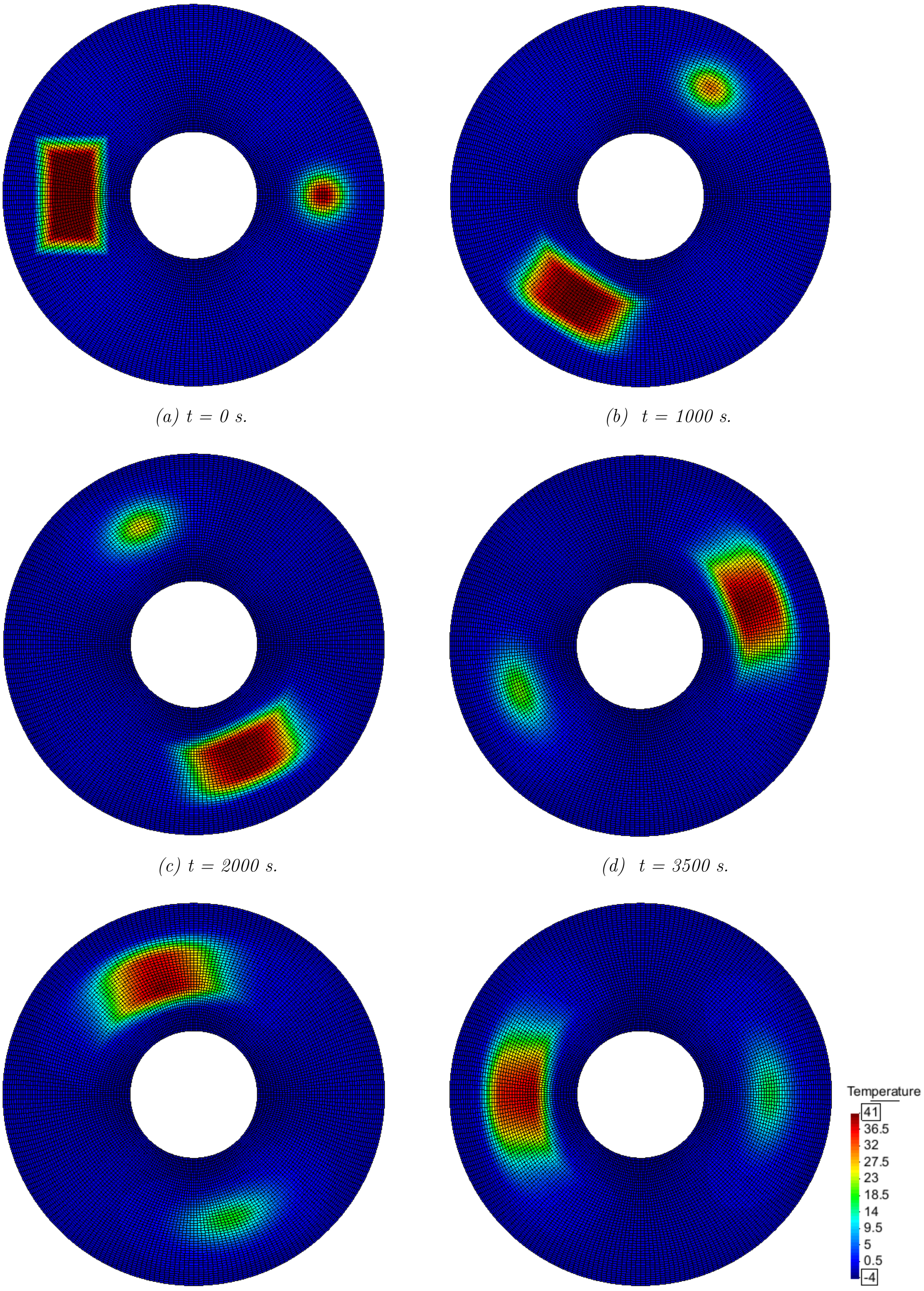

(a) t = 0 s.

(b) t = 1000 s.

(c) t = 2000 s.

(d) t = 3500 s.

(e) t = 5000 s.

(f) t = 6300 s.

Figure 2.53: Distribution of temperatures for different times (Standard Galerkin Weighting).

Chapter 3

Heat transfer with advection in zero-thickness interface elements

The main objective of this Chapter is to represent with a numerical model the advection phenomena that occur due to the hydraulic flow present in the discontinuities and the heat transport with the flow, assuming saturated conditions and incompressible fluid.

In modeling rock and quasi-brittle materials it is important to distinguish between the hydraulic behavior that occurs in the porous medium and through the discontinuities, both of them generating a double-permeability system. While the porous media provides a small permeability to the whole system, the discontinuities establish preferential flow paths and provide the main permeability of the same. Due to the high hydraulic velocities developed in the discontinuities, the main thermal transport may occur through them and the advection may be the dominant heat transfer mode. Thus, it is important to establish a numerical model to study the advection phenomena that differentiates the discontinuity network and the porous medium contributions.

When the fluid velocities are low the formulation and implementation of the additional advective term in the equations can be made by traditional FEM methods (Galerkin). However, when the fluid velocities are high enough, the standard Galerkin weighting leads to oscillatory results as it does in continuum elements, and consequently the advective term requires a special treatment to stabilize the numerical solution. However, this effect occurs typically only in fractures or discontinuities, and not in the continuum medium.

This Chapter follows the work of Segura (2007) and Garolera (2017), where the hydraulic flow for double-nodded zero-thickness interface elements was proposed in 2-D and 3-D, respectively. In this context, this Chapter presents the extension of this numerical approach in interfaces for thermal advective flow.

The first section of this Chapter presents a brief review of the different numerical approaches for the FEM modeling of discontinuities, concluding in the use of double-noded zero-thickness interface elements as the approach used in this thesis. The second section of this Chapter presents a classical FEM formulation to solve the conduction-advection problem for zero-thickness interface elements, only valid for small advection ($Pe \leq 1$). Finally, a third part presents the solution of the FEM problem considering stabilization methodologies in order to solve large advection problems ($Pe > 1$), already explained for continuum media in Chapter 2.

3.1. Numerical approach for discontinuities

The effect of the discontinuities may be studied using two different approaches (Figure 3.1). The first one is based in the discrete representation of individual joints and is known as discrete approach. The other one is the equivalent continuum method, in which the effect of existing discontinuities is studied by using an equivalent continuum material model. The discrete approach is in general used to describe the joint behavior in detail, while the equivalent continuum method is usually adopted when the problem involves a large number of discontinuities distributed with a certain homogeneity throughout a rock mass, defining an equivalent material in which the properties of the joint system are taken into account within the properties of the rock (Olofsson, 1985). The selection of the more appropriate approach depends on the scale of study of the considered problem.

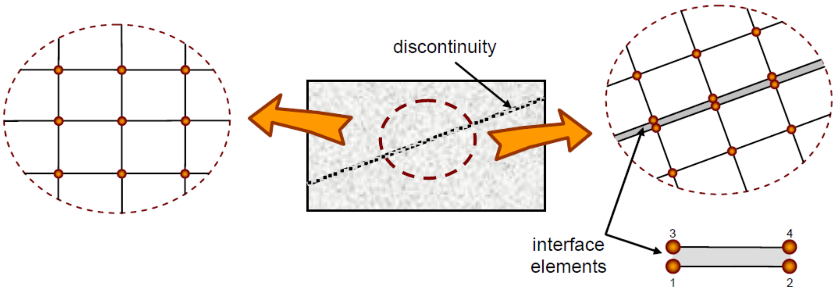

Figure 3.1: Equivalent continuum and discrete approaches for discontinuous media (Segura, 2007).

The discrete approach is based on the explicit representation of each discontinuity in an individualized manner by means of interface elements. In the FEM, the interface elements have been widely studied from the first works of Goodman, et al. (1968), Zienkiewicz, et al. (1970) and Ghaboussi, et al. (1973). In this context there are two major groups of interface elements: “thin-layer” and “zero-thickness” (Figure 3.2).

- The **“thin-layer”** interface elements consider the discontinuities as a thin continuum layer. In the FEM context these elements are standard continuum finite elements in which one of the dimensions is much smaller than the others and a constitutive model for continuum media is used. They were introduced by Desai, et al. (1984) and improved by Sharma & Desai (1992).

- The **"zero-thickness"** interface elements reduce the mechanical and diffusive formulations to the mid-plane of the joint. This type of element was originally developed by Goodman, et al. (1968) and their use is justified by the small thickness of the discontinuities in comparison with the dimensions of the problem. Since the 1980s, the "zero-thickness" interface models have been developed and applied to many practical problems in geomechanics and are nowadays well established, both in the mechanical and flow contexts. Section 4.4 presents the elasto-plastic mechanical constitutive law used in this thesis for zero-thickness interface elements, which is based in fracture mechanics and fracture energies.

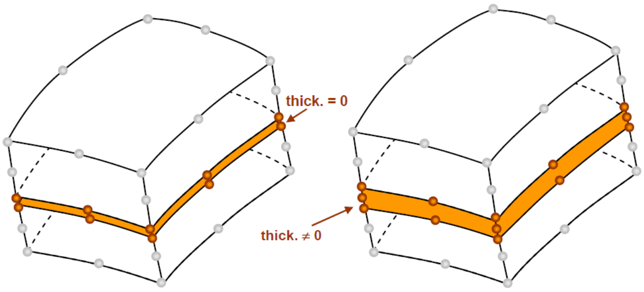

Figure 3.2: "Zero-thickness" and "thin-layer" interface elements inserted between two continuum finite elements (Segura, 2007).

In the diffusion context, the zero-thickness interface elements may be classified into single, double and triple-nodded (Figure 3.3). A detailed review of this type of elements is described in Segura (2007).

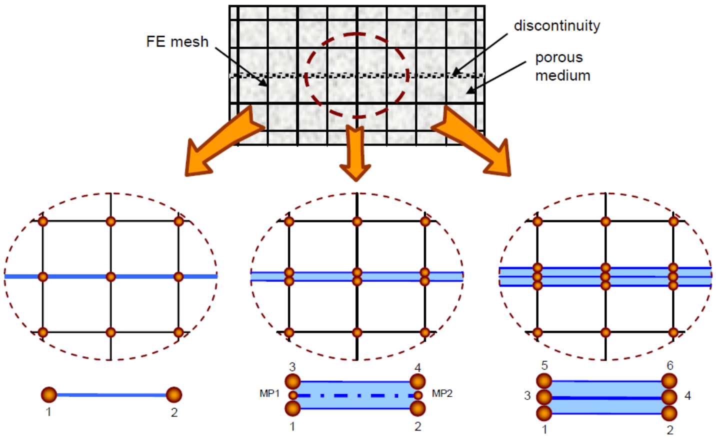

Figure 3.3: Single, double and triple node interfaces for diffusion analysis (Segura, 2007).

As the mechanical problem formulation is performed using zero-thickness double-nodded interface elements (Section 4.3), the more convenient strategy is to use the same kind of interface elements for the hydraulic and thermal problems. In this way, the same FEM mesh is used for the three problems, which is convenient in order to formulate the thermo-hydro-mechanical coupled problem in interface elements. Thus, the current thesis focuses on the study of the discontinuities from a discrete point of view by using double-nodded zero-thickness interface elements, which are pre-inserted along the FEM mesh before the calculations. This approach pre-establishes the possible paths of fracture, so it is important to determine a priori the main potential fracture paths of the problem and insert these interface elements in the most appropriate locations throughout the mesh.

It is important to note that the discontinuities can be classified in two groups: the pre-existing discontinuities and the new or developing ones. Pre-existing discontinuities in a rock mass are usually studied with Rock Mechanics, while the initiation and propagation is studied by Fracture Mechanics, which studies the crack propagation due to the existence of loads (mechanical, hydraulic or thermal). In this work, the interface elements are pre-inserted in the FEM mesh before the calculations, ant both types of discontinuities are treated indistinctly from the numerical point of view.

This thesis follows the definition of zero-thickness interface element proposed by Goodman, et al. (1968). In this type of elements one of the dimensions is collapsed and the integration is reduced one order; lines for 2D and surfaces for 3D problems (Figure 3.4).

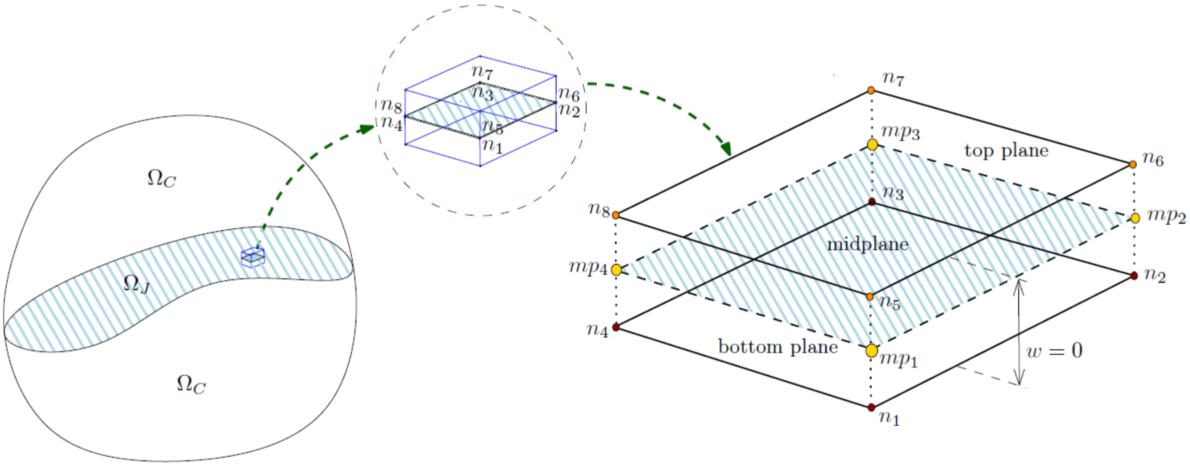

Figure 3.4: Double-nodded zero-thickness interface element. Example of a quadrilateral interface element, where n_i are the element nodes and mp_i the mid-plan nodes (Garolera, 2017).

The mechanic, hydraulic or thermal longitudinal (or in-plane) problem is formulated at the mid-plane surface, which is defined via isoparametric elements, such as lines, triangles or quadrangles, in the same manner as in the continuum medium (Figure 3.5). Once the results are obtained at the mid-plane, the temperatures at the nodes of the element are obtained assuming that the temperature at the mid-plane is the average of the temperature of the two original nodes of the interface.

Additional to the longitudinal flow, the existence of a discontinuity may also represent a resistance to the temperature flow in the transversal direction, which would result in a localized temperature drop across the interface, as it is explained in Section 3.2. In this case, also the thermal problem is formulated at the mid-plane nodes. However, in order to obtain the temperature values at the nodes of the element, it is assumed that the potential thermal drop at the mid-plane nodes is defined as the difference of potential between the two nodes of the interface, and not as an average of them as for the longitudinal flow.

One of the most important issues in the use of this kind of interface elements is to establish the appropriate local reference systems to carry out the calculations along the mid-plane of the elements, especially in 3-D problems, where the interfaces are represented as curved surfaces. In this context, two different reference systems are defined for each local point of the mid-plane:

- **Local coordinate system $(\boldsymbol{\xi}, \boldsymbol{\eta})$:** are the local coordinates defined along the mid-plane of the element, which corresponds to the one defined within the isoparametric element (Figure 3.5). This reference system does not satisfy the condition of orthonormality and can't be used for the calculations.
- **Local orthogonal coordinate system $(\boldsymbol{n}, \boldsymbol{l_1}, \boldsymbol{l_2})$:** since the local coordinate system does not satisfy the orthonormality condition, a new local basis is generated at each point of the mid-plane. For this, a tangent plane to each point of the mid-plane is defined. The first component of the new local basis is defined as the perpendicular unit vector to this plane, and the second and third components are contained in it, conforming an orthonormal basis with normal and tangential components. The calculations at each point of the interface elements are performed using this reference system.

Furthermore, the rotation matrices between these reference systems and the global system (x, y, z) must be also defined. More details of the variables and geometry aspects that involve the double-nodded zero-thickness interface elements formulation can be found in Section 2.2.2. of Garolera (2017).

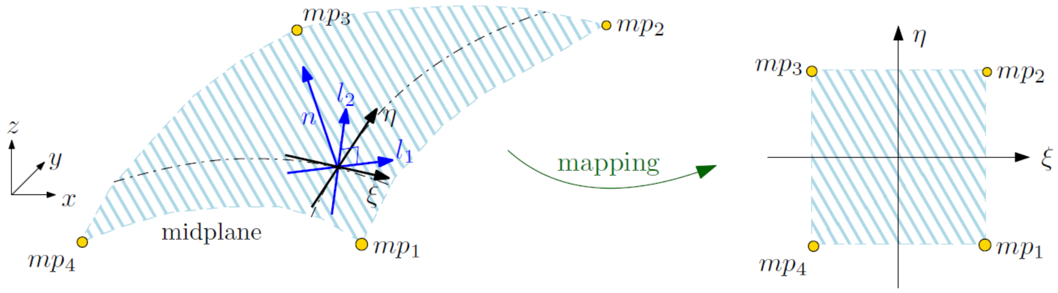

Physical element (mid-plane)

isoparametric element

Figure 3.5: Coordinate systems of a zero-thickness interface element. Global coordinate system (x, y, z), local element coordinate system (ξ, η) and local orthogonal coordinate system (n, l_1, l_2) (Garolera, 2017).

3.2. Formulation of the thermal problem with small advection in interfaces

This Section develops the formulation of the thermal problem with small advection using the zero-thickness interface elements presented in the previous Section 3. This approach follows the work of Segura & Carol (2004), which was the first in using this kind of interface elements applied to diffusion problems.

The formulation of this kind of elements is composed of two terms: the longitudinal flow along the interface and the transversal flow across the same, as described by Segura & Carol (2004), Segura (2007), Segura & Carol (2008a), Segura & Carol (2008b) and Garolera (2017).

A set of equations describing both longitudinal and transversal heat flow is developed in this section, assuming three-dimensional interface elements with a local orthogonal coordinate system $\{n, l_1, l_2\}$, where l_1 and l_2 are the local directions of the interface along the mid-plane.

It is also assumed that the discontinuity is surrounded by a continuum medium and, as in the hydraulic flow described by Segura (2007), the thermal flow can leak from the discontinuity to the continuum medium and vice versa.

Longitudinal flow

The longitudinal flow vector $\mathbf{q}_{\mathrm{L}}^{T}$ defined by the conduction-advection equation in the transient problem can be written from Eq. (2.11) as:

$$\mathbf{q}_{\mathrm{L}}^{T} = -k_{L}^{T}\ \boldsymbol{\nabla}_{J}\ \phi\ +\ \rho c \phi \mathbf{v}_{\mathrm{L}} \tag{3.1}$$

where k_{L}^{T} is the longitudinal thermal conductivity; $\boldsymbol{\nabla}_{J} = \left[\frac{\partial}{\partial l_1}\ \frac{\partial}{\partial l_2}\right]^{\top}$ is the partial differential operator for the local in-plane axis; $\mathbf{v}_{\mathrm{L}}$ is the longitudinal velocity (known) field at the mid-plane of the interface element; ϕ is the temperature field; and ρ and c are the density and the thermal capacity of the material filling the interface, respectively. In 3-D interfaces the longitudinal flow is the flow at the mid-plane of the interface, also known as in-plane flow.

The longitudinal heat transfer problem in a discontinuity is studied along the mid-plane of the interface (Figure 3.4). By imposing heat conservation in the longitudinal direction of a differential interface element (Figure 3.6) the continuity equation is obtained:

$$-[\boldsymbol{\nabla}_{J}]^{\top}\mathbf{Q}_{\mathrm{L}}^{T} = r_{N} \rho c \frac{\partial \phi}{\partial t} \tag{3.2}$$

where r_N is the interface aperture, source terms are left out for simplicity and $\mathbf{Q}_{\mathrm{L}}^{T}$ is the longitudinal heat flow rate derived from Darcy's law and Eq. (3.1) and can be written as:

$$\mathbf{Q}_{\mathrm{L}}^{T} = r_{N}\ \mathbf{q}_{\mathrm{L}}^{T} = -r_{N} k_{L}^{T} \boldsymbol{\nabla}_{J} \phi\ + r_{N} \rho c \phi \mathbf{v}_{\mathrm{L}} \tag{3.3}$$

Substituting (3.3) into (3.2) leads to:

$$r_N \rho c \left(\frac{\partial \phi}{\partial t} + [\mathbf{v}_\mathrm{L}]^\top \boldsymbol{\nabla}_J \phi \right) - r_N \ [\boldsymbol{\nabla}_J]^\top k_L^T \ \boldsymbol{\nabla}_J \phi = 0 \qquad \text{in} \qquad \Omega_J \tag{3.4}$$

where $\mathit{\Omega}_J$ is the local mid-plane longitudinal coordinate defined by the system $\{l_1, l_2, n\}$.

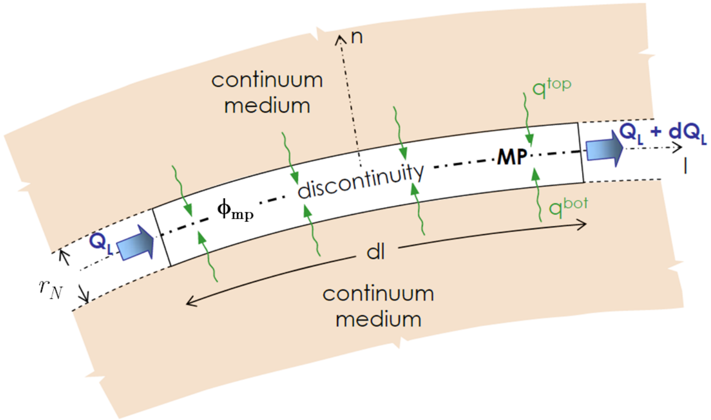

Figure 3.6: Thermal flow through a differential interface element (Segura, 2007).

There are two kinds of boundary conditions applicable to the transient conduction-advection differential equation. The first is the Dirichlet boundary condition, in which the temperature values are imposed on a boundary Γ_ϕ:

$$\phi = \bar{\phi}(x, y, x, t) \qquad \text{on} \qquad \Gamma_\phi \tag{3.5}$$

The second is the Neumann boundary condition, in which the normal heat flow is prescribed on a boundary Γ_q:

$$q_N^T = \bar{q}_N^T(x, y, z, t) \qquad \text{on} \qquad \Gamma_\mathrm{q} \tag{3.6}$$

where q_N^T is the heat flow normal to the boundary and $\bar{q}_N^T$ is the prescribed value of the heat flow. The heat flow q_N^T is calculated as the normal projection of the heat flow vector $\mathbf{Q}_\mathrm{L}^T$ on the boundary Γ_q. Using Eq. (3.1) this condition becomes:

$$q_N^T = [\mathbf{n}]^\top \mathbf{Q}_\mathrm{L}^T = -[\mathbf{n}]^\top r_N \ k_L^T \ \boldsymbol{\nabla}_J \phi \ + r_N \rho c \phi v_{L,N} \tag{3.7}$$

where $v_{L,N} = [\mathbf{n}]^\top \mathbf{v}_\mathrm{L}$ is the normal longitudinal component of the velocity at the boundary Γ_q. Using Eq. (3.6) and (3.7) the same equation may be finally written as:

$$-r_N \rho c \phi v_{L,N} + [\mathbf{n}]^\top r_N \ k_L^T \ \boldsymbol{\nabla}_J \phi \ + \bar{q}_N^T = 0 \qquad \text{on} \qquad \Gamma_\mathrm{q} \tag{3.8}$$

The term $\bar{q}_N^T$ may be a known normal heat flow applied to the boundary:

$$\bar{q}_N^T = \bar{q}^T \tag{3.9}$$

Substituting Eq. (3.9) into (3.8) results in the complete Neumann boundary condition of the conduction-advection heat transfer problem:

$$-r_N \rho c \phi v_{L,N} + [\mathbf{n}]^\top r_N \; k_L^T \; \boldsymbol{\nabla}_J \phi \; + \bar{q}^T \qquad \text{on} \qquad \Gamma_\mathrm{q} \tag{3.10}$$

Finally, the initial temperature condition for the transient problem can be written in the same form of Eq. (2.26).

Using the FEM to perform the spatial discretization of Eq. (3.4) along the mid-plane of the interface, the temperature can be written as:

$$\phi \cong \hat{\phi} = \sum_{i=1}^{m} N_J^{(a)} \; \phi_{mp}^{(a)} = \mathbf{N}_J \; \boldsymbol{\phi}_\mathrm{mp} \qquad a = 1{,}2{,}..m \tag{3.11}$$

where $\hat{\phi}$ is the approximate value of the temperature; $\phi_{mp}^{(a)}$ and $N_J^{(a)}$ are the value of the temperature and the shape function at the (a) mid-plane node respectively; and m is the number of mid-plane nodes of the interface element (equal to half of the nodes for double-node interface elements).

Eq. (3.4) represents the strong form of the governing differential equations of the problem and (3.5) and (3.10) the boundary conditions. Replacing the approximation $\hat{\phi}$ in (3.4) and (3.10) leads to:

$$r_N \rho c \left(\frac{\partial \hat{\phi}}{\partial t} + [\mathbf{v}_\mathrm{L}]^\top \boldsymbol{\nabla}_J \hat{\phi} \right) - r_N \; [\boldsymbol{\nabla}_J]^\top k_L^T \; \boldsymbol{\nabla}_J \hat{\phi} = r_{\Omega_J} \qquad \text{in} \qquad \Omega_J \tag{3.12}$$

$$-r_N \rho c \hat{\phi} v_{L,N} + [\mathbf{n}]^\top r_N k_L^T \; \boldsymbol{\nabla}_J \hat{\phi} \; + \bar{q}^T = r_\Gamma \qquad \text{on} \qquad \Gamma_\mathrm{q} \tag{3.13}$$

where r_{Ω_J} and r_Γ are the residuals from the finite element approximation. For the Dirichlet boundary conditions (3.5), it is assumed that the condition is satisfied exactly at prescribed nodes ($\hat{\phi} = \phi$).

Using the weighted residuals method to minimize r_{Ω_J} and r_Γ, the following integral expression is obtained:

$$\int_{\Omega_J} w \, r_{\Omega_J} \; \mathrm{d}\Omega_J + \int_{\Gamma_\mathrm{q}} \bar{w} \, r_\Gamma \; \mathrm{d}\Gamma = 0 \qquad a = 1{,}2{,}\dots m \tag{3.14}$$

where w and $\bar{w}$ are weight functions. Substituting Eqs. (3.12) and (3.13) in (3.14), considering the mid-plane nodes of the element and assuming $\bar{w} = -w$ on the boundary, the weak form of the problem is obtained:

$$\begin{aligned}\int_{\Omega_J} w\left[r_N\rho c\frac{\partial\hat{\phi}}{\partial t}+r_N\rho c\ [\mathbf{v}_{\mathrm{L}}]^{\top}\boldsymbol{\nabla}_J\hat{\phi}-r_N\ [\boldsymbol{\nabla}_J]^{\top}k_L^T\ \boldsymbol{\nabla}_J\hat{\phi}\right]\mathrm{d}\Omega_J&\\-\int_{\Gamma_{\mathrm{q}}} w\left(-r_N\rho c\hat{\phi}v_{L,N}+[\mathbf{n}]^{\top}r_N k_L^T\ \boldsymbol{\nabla}_J\hat{\phi}\ +\bar{q}^T\right)\,\mathrm{d}\Gamma=0&\end{aligned}\tag{3.15}$$

Using the standard Galerkin weighing $(w=N_J^{(a)}, a=1,\dots,m)$ the integral form is transformed into:

$$\begin{aligned}\int_{\Omega_J} N_J^{(a)}\left[r_N\rho c\frac{\partial\hat{\phi}}{\partial t}+r_N\rho c\ [\mathbf{v}_{\mathrm{L}}]^{\top}\boldsymbol{\nabla}_J\hat{\phi}-r_N\ [\boldsymbol{\nabla}_J]^{\top}k_L^T\ \boldsymbol{\nabla}_J\hat{\phi}\right]\mathrm{d}\Omega_J&\\-\int_{\Gamma_{\mathrm{q}}} N_J^{(a)}\left(-r_N\rho c\hat{\phi}v_{L,N}+[\mathbf{n}]^{\top}r_N k_L^T\ \boldsymbol{\nabla}_J\hat{\phi}\ +\bar{q}^T\right)\,\mathrm{d}\Gamma=0&\end{aligned}\tag{3.16}$$

where $N_J^{(a)}$ is each of the mid-plane shape functions of the interface element.

Applying the spatial discretization defined by Eq. (3.11) and the Theorem of the Divergence to the first term of Eq. (3.16) the final expression is obtained:

$$\mathbf{Q}_{\mathrm{L_{mp}}}=\mathbf{K}_{\mathrm{L_{mp}}}\boldsymbol{\phi}_{\mathrm{mp}}\ +\mathbf{C}_{\mathrm{L_{mp}}}\ \dot{\boldsymbol{\phi}}_{\mathrm{mp}}\tag{3.17}$$

where

$$\begin{aligned}\mathbf{K}_{\mathrm{L_{mp}}}=r_N\rho c\int_{\Omega_J}\left([\mathbf{N}_J]^{\top}\ \mathbf{v}_{\mathrm{L}}\ \ \mathbf{B}_J\right)\mathrm{d}\Omega_J+r_N\int_{\Omega_J}\left([\mathbf{B}_J]^{\top}\ k_L^T\ \mathbf{B}_J\right)\mathrm{d}\Omega_J&\\-\,r_N\rho c\int_{\Gamma_{\mathrm{q}}}\left([\mathbf{N}_J]^{\top}\ v_{L,N}\ \ \mathbf{N}_J\right)\mathrm{d}\Gamma&\end{aligned}\tag{3.18}$$

$$\mathbf{C}_{\mathbf{L}_{\mathrm{mp}}}=\ r_N\rho c\int_{\Omega_J}[\mathbf{N}_J]^{\top}\ \mathbf{N}_J\ \ \mathrm{d}\Omega_J\tag{3.19}$$

and

$$\mathbf{B}_J=\boldsymbol{\nabla}_J\mathbf{N}_J\tag{3.20}$$

$$\boldsymbol{\phi}_{\mathrm{mp}}=\left[\phi_{mp}^{(1)}\ \ \phi_{mp}^{(2)}\ \ \dots\ \ \phi_{mp}^{(m)}\right]^{\top}\qquad\qquad\mathbf{v}_{\mathrm{L}}=\left[v_L^{(1)}\ \ v_L^{(2)}\ \ \dots\ \ v_L^{(m)}\right]^{\top}\tag{3.21}$$

In order to obtain the final FEM formulation related to the nodes of the mesh (and not to the mid-plane nodes), an additional assumption is necessary:

$$\phi_{mp}^{(a)}\ =\frac{\phi_{top}^{(a)}+\phi_{bot}^{(a)}}{2}\qquad\qquad a=1,2,\dots m\tag{3.22}$$

where ϕ_{top} and ϕ_{bot} are the temperatures at each side of the discontinuity. That means that the temperature at the mid-plane is the average of the temperature at the corresponding nodes of the element. The temperature at the mid-plane of the interface can be written in terms of the element's nodal temperatures (see Figure 3.4) as:

$$\boldsymbol{\phi}_{\mathrm{mp}} = \frac{1}{2}\,[\mathbf{I}_m \;\; \mathbf{I}_m]\;\boldsymbol{\phi}_{\mathrm{e}} = \widetilde{\mathbb{T}}_{\mathrm{L}}\;\boldsymbol{\phi}_{\mathrm{e}} \tag{3.23}$$

where $\widetilde{\mathbb{T}}_{\mathrm{L}} = \frac{1}{2}\,[\mathbf{I}_m \;\; \mathbf{I}_m]$ is the longitudinal transference matrix, $\mathbf{I}_m$ is the $m \times m$ identity matrix and the element's temperature vector is defined by:

$$\boldsymbol{\phi}_{\mathrm{e}} = [\phi^{(1)} \quad \phi^{(2)} \;\dots\; \phi^{(2m)}]^{\top} \tag{3.24}$$

For two-dimensional interfaces Eq. (3.23) may be written as:

$$\boldsymbol{\phi}_{\mathrm{mp}} = \begin{bmatrix} \phi_{mp}^{(1)} \\ \phi_{mp}^{(2)} \end{bmatrix} = \begin{bmatrix} \dfrac{\phi^{(1)} + \phi^{(3)}}{2} \\ \dfrac{\phi^{(2)} + \phi^{(4)}}{2} \end{bmatrix} = \frac{1}{2}\,[\mathbf{I}_m \;\; \mathbf{I}_m]\;\boldsymbol{\phi}_{\mathrm{e}} = \widetilde{\mathbb{T}}_{\mathrm{L}}\;\boldsymbol{\phi}_{\mathrm{e}} \tag{3.25}$$

Additionally, using the Principle of Virtual Work (PVW) in a discrete form,

$$[\delta\boldsymbol{\phi}_{\mathrm{e}}]^{\top}\;\mathbf{Q}_{\mathrm{L_e}} = [\delta\boldsymbol{\phi}_{\mathrm{mp}}]^{\top}\;\mathbf{Q}_{\mathrm{L_{mp}}} \tag{3.26}$$

$$\mathbf{Q}_{\mathrm{L_e}} = \left[\widetilde{\mathbb{T}}_{\mathrm{L}}\right]^{\top}\mathbf{Q}_{\mathrm{L_{mp}}} \tag{3.27}$$

that is, a dual relation to Eq. (3.23) is obtained to relate the "thermal force" (heat discharge) element vector $\mathbf{Q}_{\mathrm{L_e}}$ (which is thermodynamically dual to the temperature element vector $\boldsymbol{\phi}_{\mathrm{e}}$) to the mid-point vector $\mathbf{Q}_{\mathrm{L_{mp}}}$ (which is thermodynamically dual to the mid-point vector $\boldsymbol{\phi}_{\mathrm{mp}}$). Note that this relation involves the rectangular matrix $\widetilde{\mathbb{T}}_{\mathrm{L}}$ which appears transposed in comparison to the dual expression in Eq. (3.23).

All the matrices and vectors defined at the mid-plane of the interface have to be transformed using the transference matrix, in order to obtain the similar relations between full element vectors including the pairs of nodes that appear in the FEM mesh. Substituting Eqs. (3.23) and (3.27) into Eq. (3.17) those relations are obtained as follows:

$$\mathbf{Q}_{\mathrm{L_e}} = \mathbf{C}_{\mathrm{L_e}}\;\dot{\boldsymbol{\phi}}_{\mathrm{e}} + \mathbf{K}_{\mathrm{L_e}}\;\boldsymbol{\phi}_{\mathrm{e}} \tag{3.28}$$

where

$$\mathbf{C}_{\mathrm{L_e}} = \left[\widetilde{\mathbb{T}}_{\mathrm{L}}\right]^{\top}\mathbf{C}_{\mathrm{L_{mp}}}\;\widetilde{\mathbb{T}}_{\mathrm{L}} \tag{3.29}$$

$$\mathbf{K}_{\mathrm{L_e}} = \left[\widetilde{\mathbb{T}}_{\mathrm{L}}\right]^{\top}\mathbf{K}_{\mathrm{L_{mp}}}\;\widetilde{\mathbb{T}}_{\mathrm{L}} \tag{3.30}$$

Transversal flow

Additional to the longitudinal flow, the existence of a discontinuity may also represent a resistance to the temperature flow in the transversal direction, which would result in a localized temperature drop across the interface (Figure 3.4). With double-node interface elements the temperature drop is natural to occur across the discontinuity, and it is assumed that this temperature drop $\breve{\phi}_N$ is related to the transverse heat flow q_N^T by a simple discrete version of Fick's law, in which the temperature drop plays the role of the temperature gradient:

$$q_N^T \ = \breve{k}_N^T \ \ \breve{\phi}_N \tag{3.31}$$

In this equation, $\breve{k}_N^T$ is the transversal thermal conductivity of the interface. The potential thermal drop across the discontinuity is defined by the temperature difference between the two surfaces of the interface as follows:

$$\breve{\phi}_N = \ \phi_{bot} - \phi_{top} \tag{3.32}$$

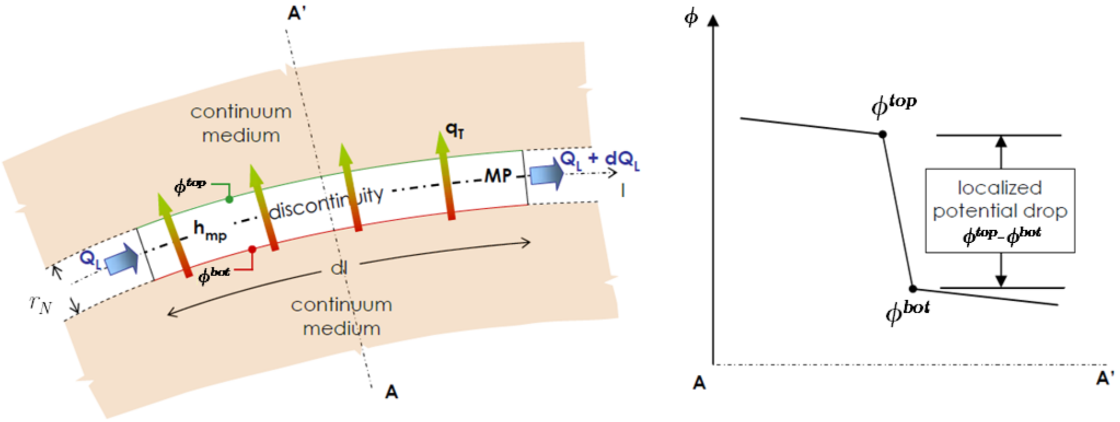

Figure 3.7: Scheme of the potential thermal drop across a differential interface element (Segura, 2007).

Performing the spatial discretization of the transversal jump $\breve{\phi}_N$ at the mid-plane nodes of the interface, yields:

$$\breve{\phi}_{N_{\mathrm{mp}}}(x,y,t) \cong \sum_{a=1}^{N} N_J^{(a)} \ \breve{\phi}_{N_{mp}}^{(a)} = \mathbf{N}_J \ \breve{\boldsymbol{\phi}}_{\mathrm{N_{mp}}} \tag{3.33}$$

where the unknown vector can be written as:

$$\breve{\boldsymbol{\phi}}_{\mathrm{N_{mp}}} = [-\mathbf{I}_m \ \ \mathbf{I}_m] \ \boldsymbol{\phi}_{\mathrm{e}} = \widetilde{\mathbb{T}}_{\mathrm{N}} \ \boldsymbol{\phi}_{\mathrm{e}} \tag{3.34}$$

where $\widetilde{\mathbb{T}}_{\mathrm{N}} = [-\mathbf{I}_m \ \ \mathbf{I}_m]$ is the transference transversal matrix. That means that the potential temperature drop at the mid-plane node is the difference of potential between the two actual nodes. This condition may be written for one-dimensional interface elements as:

$$\breve{\boldsymbol{\phi}}_{\mathrm{N_{mp}}} = \begin{bmatrix} \breve{\phi}_{N_{mp}}^{(1)} \\ \breve{\phi}_{N_{mp}}^{(2)} \end{bmatrix} = \begin{bmatrix} \phi^{(1)} - \phi^{(3)} \\ \phi^{(2)} - \phi^{(4)} \end{bmatrix} = [\mathbf{I}_m \ \ -\mathbf{I}_m] \ \boldsymbol{\phi}_{\mathrm{e}} = \widetilde{\mathbb{T}}_{\mathrm{N}} \ \boldsymbol{\phi}_{\mathrm{e}} \tag{3.35}$$

The FEM formulation for the mid-plane is obtained using the Principle of Virtual Work, which can be expressed for the transverse thermal flow problem as:

$$\left[\delta\breve{\boldsymbol{\phi}}_{\mathrm{N_{mp}}}\right]^{\top}\mathbf{Q}_{\mathrm{N_{mp}}} = \int_{\Omega_J} \delta\breve{\phi}_{\mathrm{N_{mp}}}\; q^{T}_{N_{\mathrm{mp}}}\; \mathrm{d}\Omega_J \qquad\qquad \forall\delta\breve{\boldsymbol{\phi}}_{\mathrm{N_{mp}}} \tag{3.36}$$

And substituting Eqs. (3.31) and (3.33) into (3.36),

$$\mathbf{Q}_{\mathrm{N_{mp}}} = \mathbf{K}_{\mathrm{N_{mp}}}\breve{\boldsymbol{\phi}}_{\mathrm{N_{mp}}} \tag{3.37}$$

$$\mathbf{K}_{\mathrm{N_{mp}}} = \int_{\Omega_J} \left[\mathbf{N}_J\right]^{\top} \breve{k}^{T}_{N}\; \mathbf{N}_J\; \mathrm{d}\Omega_J \tag{3.38}$$

where $\mathbf{K}_{\mathrm{N_{mp}}}$ is the transversal thermal conductivity matrix at the mid-plane. The vector of temperatures is defined by the same equation as in the longitudinal flow, Eq. (3.24).

Additionally, using the PVW in a discrete form,

$$\left[\delta\boldsymbol{\phi}_{\mathrm{e}}\right]^{\top}\mathbf{Q}_{\mathrm{N_e}} = \left[\delta\boldsymbol{\phi}_{\mathrm{mp}}\right]^{\top}\mathbf{Q}_{\mathrm{N_{mp}}} \tag{3.39}$$

$$\mathbf{Q}_{\mathrm{N_e}} = \left[\widetilde{\mathbb{T}}_{\mathrm{N}}\right]^{\top}\mathbf{Q}_{\mathrm{N_{mp}}} \tag{3.40}$$

As in the longitudinal case, all the matrices and vectors formulated at the mid-plane of the interface element have to be transformed using the transference matrix, to obtain the corresponding nodal values of the FEM mesh. Substituting Eqs. (3.39) and (3.40) into Eq. (3.37):

$$\mathbf{Q}_{\mathrm{N_e}} = \mathbf{K}_{\mathrm{N_e}}\;\boldsymbol{\phi}_{\mathrm{e}} \tag{3.41}$$

where $\mathbf{K}_{\mathrm{N_e}}$ is the transversal conductivity matrix of the element which, taking into account Eq. (3.34), can be written as:

$$\mathbf{K}_{\mathrm{N_e}} = \left[\widetilde{\mathbb{T}}_{\mathrm{N}}\right]^{\top}\mathbf{K}_{\mathrm{N_{mp}}}\widetilde{\mathbb{T}}_{\mathrm{N}} \tag{3.42}$$

Integrated formulation: longitudinal and transversal flow

To obtain an integrated conductivity matrix it is necessary to combine the longitudinal and the transversal flow as a sum of both:

$$\mathbf{Q}_{\mathrm{e}} = \mathbf{Q}_{\mathrm{L_e}} + \mathbf{Q}_{\mathrm{N_e}} = \mathbf{C}_{\mathrm{L_e}}\;\dot{\boldsymbol{\phi}}_{\mathrm{e}} + \mathbf{K}_{\mathrm{L_e}}\;\boldsymbol{\phi}_{\mathrm{e}} + \mathbf{K}_{\mathrm{N_e}}\;\boldsymbol{\phi}_{\mathrm{e}} \tag{3.43}$$

$$\mathbf{Q}_{\mathrm{e}} = \mathbf{C}_{\mathrm{L_e}}\;\dot{\boldsymbol{\phi}}_{\mathrm{e}} + \left(\mathbf{K}_{\mathrm{L_e}} + \mathbf{K}_{\mathrm{N_e}}\right)\;\boldsymbol{\phi}_{\mathrm{e}} \tag{3.44}$$

The last step in the solution of the transient problem is to perform the time integration of the system of Eqs. (3.44) using the FDM:

$$\left[\frac{1}{\Delta t}\mathbf{C}_{\mathrm{L_e}} + \theta\big(\mathbf{K}_{\mathrm{L_e}} + \mathbf{K}_{\mathrm{N_e}}\big)\right]\;\boldsymbol{\phi}_{\mathrm{e}}^{n+1} = 0 \tag{3.45}$$

Finally, the global matrices and vectors of the system of equation are obtained by the assembly of the contribution of each element of the mesh resulting in:

$$\left[\frac{1}{\Delta t}\mathbf{C} + \theta(\mathbf{K}_\mathrm{L} + \mathbf{K}_\mathrm{N})\right] \phi_\mathrm{e}^{n+1} = 0 \tag{3.46}$$

Final remarks

In order to obtain the steady-state formulation of the thermal advection problem for double-node interfaces it is sufficient to set $\mathbf{C}_{\mathrm{L}_\mathrm{e}} = 0$ in Eq. (3.44) and solve the following system of equations:

$$\mathbf{K}_\mathrm{e}\ \phi_\mathrm{e}^{n+1} = \mathbf{Q}_\mathrm{e} \tag{3.47}$$

On the other hand, to solve the thermal problem for double-node interfaces without advection (pure conduction) it is sufficient to set $\mathbf{v}_\mathrm{L} = 0$ in Eq. (3.18) and solve the system of Eq. (3.45) for the transient problem or solve the system of Eq. (3.47) for the steady-state problem.

Summary 4 - Thermal equation for small advection in zero-thickness interface elements.

$$\left[\frac{1}{\Delta t}\mathbf{C}_{\mathrm{L}_\mathrm{e}} + \theta\big(\mathbf{K}_{\mathrm{L}_\mathrm{e}} + \mathbf{K}_{\mathrm{N}_\mathrm{e}}\big)\right] \phi_\mathrm{e}^{n+1} = 0 \tag{3.48}$$

where ϕ_e^{n+1} is the nodal temperature vector of the element (unknown), $\mathbf{C}_{\mathrm{L}_\mathrm{e}}$ is the thermal capacity matrix of the element and $\mathbf{K}_{\mathrm{L}_\mathrm{e}}$ and $\mathbf{K}_{\mathrm{N}_\mathrm{e}}$ are the longitudinal and transversal thermal conduction-advection matrices of the element. Boundary conditions are left out for simplicity.

$$\begin{aligned}\mathbf{K}_{\mathrm{L}_\mathrm{e}} = \left[\widetilde{\mathbb{T}}_\mathrm{L}\right]^\top \Bigg(& r_N \rho c \int_{\Omega_J} \left([\mathbf{N}_J]^\top\ \mathbf{v}_\mathrm{L}\ \mathbf{B}_J\right) \mathrm{d}\Omega_J + r_N \int_{\Omega_J} \left([\mathbf{B}_J]^\top\ k_L^T\ \mathbf{B}_J\right) \mathrm{d}\Omega_J \\ & - r_N \rho c \int_{\Gamma} \left([\mathbf{N}_J]^\top\ v_{L,N}\ \mathbf{N}_J\right) \mathrm{d}\Gamma \Bigg) \widetilde{\mathbb{T}}_\mathrm{L}\end{aligned} \tag{3.49}$$

$$\mathbf{C}_{\mathrm{L}_\mathrm{e}} = \left[\widetilde{\mathbb{T}}_\mathrm{L}\right]^\top \left(r_N \rho c \int_{\Omega_J} [\mathbf{N}_J]^\top\ \mathbf{N}_J\, \mathrm{d}\Omega_J \right) \widetilde{\mathbb{T}}_\mathrm{L} \tag{3.50}$$

$$\mathbf{K}_{\mathrm{N}_\mathrm{e}} = \left[\widetilde{\mathbb{T}}_\mathrm{N}\right]^\top \left(\int_{\Omega_J} [\mathbf{N}_J]^\top\ k_N^T\ \mathbf{N}_J\ \mathrm{d}\Omega_J \right) \widetilde{\mathbb{T}}_\mathrm{N} \tag{3.51}$$

Finally, the global matrices of the system of Eq. (3.48) are obtained by the assembly of the contribution of each element of the mesh.

The *steady-state* problem is obtained as a particular case of the above formulation leaving out the transient terms. Moreover, the pure conduction formulation is obtained leaving out the advective terms ($\mathbf{v}_\mathrm{L} = 0$).

3.3. Formulation of the thermal problem with large advection in interfaces

As mentioned in the introduction of this chapter, the existence of discontinuities generate preferential paths where the hydraulic flow velocities are frequently much higher than in the porous medium and the advection tends to dominate the heat problem. Consequently, the standard Galerkin FEM method leads to oscillatory results in the interface elements as it does in the continuum elements and requires the use of stabilization methods.

This section presents the Streamline Upwind Petrov-Galerkin (SUPG) method to solve the steady-state problem and the new α-Implicit Characteristic-Galerkin Method (α-ICGM) to solve the transient problem, both developed previously for the continuum medium in Sections 2.2.2 and 2.2.3, respectively.

Also, it is assumed that the large advection affects only the longitudinal flow of the interfaces, while transversal flow remains unchanged from the formulation developed in previous Section 3.2.

3.3.1. Steady-state thermal problem with large advection in interfaces

In order to stabilize the numerical solution of the steady-state thermal problem with large advection in interfaces, the SUPG method presented in Section 2.2.2 is used as in the continuum medium. This method uses a different weighting function in the space discretization process ($w \neq N^{(1)}, N^{(2)}, \ldots$):

$$w = N^{(a)} + \frac{\alpha_{opt} h_{car}}{2} \frac{v_i}{|\mathbf{v}|} \frac{\partial N^{(a)}}{\partial x_i} \tag{3.52}$$

where $N^{(a)}$ are the usual shape functions, v_i is the velocity field, h_{car} is the characteristic length of the element (length of the element along the flow line) and α_{opt} is defined by Eq. (2.69) in order to obtain exact nodal values for any Péclet value.

Starting from the weak form defined by Eq. (3.15), leaving out the transient terms and using the SUPG weighing defined by Eq. (3.52) the integral form is transformed into:

$$\begin{aligned} &\int_{\Omega_J} \left(\mathbf{N}_J + \frac{\alpha_{opt} h_{car}}{2} \frac{\mathbf{v}_\mathrm{L}}{|\mathbf{v}_\mathrm{L}|} \boldsymbol{\nabla}_J \mathbf{N}_J \right) \left[r_N \rho c \, [\mathbf{v}_\mathrm{L}]^\top \boldsymbol{\nabla}_J \hat{\phi} - r_N \, [\boldsymbol{\nabla}_J]^\top k_L^T \, \boldsymbol{\nabla}_J \hat{\phi} \right] \mathrm{d}\Omega_J \\ &\qquad - \int_{\Gamma_\mathrm{q}} \left(\mathbf{N}_J + \frac{\alpha_{opt} h_{car}}{2} \frac{\mathbf{v}_\mathrm{L}}{|\mathbf{v}_\mathrm{L}|} \boldsymbol{\nabla}_J \mathbf{N}_J \right) \left(-r_N \rho c \hat{\phi} v_{L,N} + [\mathbf{n}]^\top r_N k_L^T \, \boldsymbol{\nabla}_J \hat{\phi} \right. \\ &\qquad \left. + \bar{q}^T \right) \mathrm{d}\Gamma = 0 \end{aligned} \tag{3.53}$$

Reordering terms leads to:

$$\begin{aligned}
& r_N \int_{\Omega_J} [\boldsymbol{\nabla}_J \mathbf{N}_J]^\top \, k_L^T \, \boldsymbol{\nabla}_J \hat{\phi} \, \mathrm{d}\Omega_J + r_N \int_{\Omega_J} \left(\frac{\alpha_{opt} h_{car}}{2} \frac{\mathbf{v}_\mathrm{L}}{|\mathbf{v}_\mathrm{L}|} \boldsymbol{\nabla}_J \mathbf{N}_J \right) [\boldsymbol{\nabla}_J]^\top \, k_L^T \, \boldsymbol{\nabla}_J \hat{\phi} \, \mathrm{d}\Omega_J \\
& \qquad - \, r_N \rho c \int_{\Omega_J} \mathbf{N}_J \, [\mathbf{v}_\mathrm{L}]^\top \boldsymbol{\nabla}_J \hat{\phi} \, \mathrm{d}\Omega_J \\
& \qquad - r_N \rho c \int_{\Omega_J} \left(\frac{\alpha_{opt} h_{car}}{2} \frac{\mathbf{v}_\mathrm{L}}{|\mathbf{v}_\mathrm{L}|} \boldsymbol{\nabla}_J \mathbf{N}_J \right) [\mathbf{v}_\mathrm{L}]^\top \boldsymbol{\nabla}_J \hat{\phi} \, \mathrm{d}\Omega_J \\
& \qquad + r_N \rho c \int_{\Gamma_\mathrm{q}} [\mathbf{N}_J]^\top \hat{\phi} v_{L,N} \, \mathrm{d}\Gamma \\
& \qquad + r_N \rho c \int_{\Gamma_\mathrm{q}} \left(\frac{\alpha_{opt} h_{car}}{2} \frac{\mathbf{v}_\mathrm{L}}{|\mathbf{v}_\mathrm{L}|} \boldsymbol{\nabla}_J \mathbf{N}_J \right) \hat{\phi} v_{L,N} \, \mathrm{d}\Gamma \\
& \qquad - r_N \int_{\Gamma_\mathrm{q}} [\mathbf{N}_J]^\top \, [\mathbf{n}]^\top k_L^T \, \boldsymbol{\nabla}_J \hat{\phi} \, \mathrm{d}\Gamma \\
& \qquad - r_N \int_{\Gamma_\mathrm{q}} \left(\frac{\alpha_{opt} h_{car}}{2} \frac{\mathbf{v}_\mathrm{L}}{|\mathbf{v}_\mathrm{L}|} \boldsymbol{\nabla}_J \mathbf{N}_J \right) [\mathbf{n}]^\top k_L^T \, \boldsymbol{\nabla}_J \hat{\phi} \, \mathrm{d}\Gamma = 0
\end{aligned} \tag{3.54}$$

Applying the Divergence Theorem to the diffusive terms and substituting Eq. (3.11) into (3.54) results in the following expression for the longitudinal flow along the mid-plane of a single element of the mesh:

$$\mathbf{Q}_{\mathrm{L_{mp}}} = \mathbf{K}_{\mathrm{L_{mp}}} \boldsymbol{\phi}_{\mathrm{mp}} \tag{3.55}$$

where

$$\mathbf{K}_{\mathrm{L_{mp}}} = \mathbf{K}_{\mathrm{L_{mp}}} + \mathbf{K}^{\mathrm{SUPG}}_{\mathrm{L_{mp}}} \tag{3.56}$$

$$\mathbf{K}_{\mathrm{L_{mp}}} = r_N \rho c \int_{\Omega_J} \mathbf{N}_J \, [\mathbf{v}_\mathrm{L}]^\top \, \mathbf{B}_J \, \mathrm{d}\Omega_J + \; r_N \int_{\Omega_J} ([\mathbf{B}_J]^\top \, k_L^T \, \mathbf{B}_J) \, \mathrm{d}\Omega_J \tag{3.57}$$

$$\begin{aligned}
\mathbf{K}^{\mathrm{SUPG}}_{\mathrm{L_{mp}}} &= r_N \rho c \int_{\Omega_J} \left(\frac{\alpha_{opt} h_{car}}{2|\mathbf{v}_\mathrm{L}|} \left[\mathbf{v}_\mathrm{L} \right]^\top \mathbf{B}_J \right) \left[\mathbf{v}_\mathrm{L} \right]^\top \mathbf{B}_J \, \mathrm{d}\Omega_J \\
&+ r_N \int_{\Omega_J} \left(\frac{\alpha_{opt} h_{car}}{2|\mathbf{v}_\mathrm{L}|} \left[\mathbf{v}_\mathrm{L} \right]^\top \boldsymbol{\nabla} \mathbf{B}_J \right) \; k_L^T \, \mathbf{B}_J \, \mathrm{d}\Omega_J
\end{aligned} \tag{3.58}$$

where $\mathbf{B}_J$, $\boldsymbol{\phi}_{\mathrm{mp}}$ and $\mathbf{v}_\mathrm{L}$ are defined by Eqs. (3.20) and (3.21). Note that the second integration term of Eq. (3.58) is cancelled for linear elements.

All the matrices and vectors defined at the mid-plane of the interface have to be transformed using the transference matrix to obtain the matrices and vectors defined at the nodes of the element, as described in Section 3.2 by Eqs. (3.22)-(3.30), obtaining finally the following relation for the longitudinal flow matrix:

$$\mathbf{K}_{\mathrm{L_e}} = \left[\widetilde{\mathbb{T}}_\mathrm{L} \right]^\top \mathbf{K}_{\mathrm{L_{mp}}} \widetilde{\mathbb{T}}_\mathrm{L} \tag{3.59}$$

As the large advection affects only the longitudinal flow, the transversal formulation is the same as presented in Section 3.2 by Eqs. (3.31)-(3.42). Additionally, the matrix assembly of both longitudinal and transversal flow is achieved in the same manner as presented in the same section by Eqs. (3.43) and (3.44). Leaving out the force terms, the global system of equations is obtained finally by the assembly of the contributions of each element, resulting the following simple expression:

$$\left(\mathbf{K}_\mathrm{L} + \mathbf{K}_\mathrm{L}^\mathrm{SUPG} + \mathbf{K}_\mathrm{T}\right) \boldsymbol{\phi}_\mathrm{e} \; = 0 \tag{3.60}$$

Summary 5 - Steady-state thermal equation for small advection in zero-thickness interface elements using the SUPG method.

$$\left(\mathbf{K}_{\mathrm{L}_\mathrm{e}} + \mathbf{K}_{\mathrm{L}_\mathrm{e}}^\mathrm{SUPG} + \mathbf{K}_{\mathrm{N}_\mathrm{e}}\right)\boldsymbol{\phi}_\mathrm{e} = 0 \tag{3.61}$$

where $\boldsymbol{\phi}_\mathrm{e}$ is the nodal temperature vector of the element (unknown), and $\mathbf{K}_{\mathrm{L}_\mathrm{e}}$, $\mathbf{K}_{\mathrm{L}_\mathrm{e}}^\mathrm{SUPG}$ and $\mathbf{K}_{\mathrm{N}_\mathrm{e}}$ are the longitudinal and transversal thermal conduction-advection matrices of the element. Boundary conditions are left out for simplicity.

$$\mathbf{K}_{\mathrm{L}_\mathrm{e}} = \left[\widetilde{\mathbb{T}}_\mathrm{L}\right]^\top \left(r_N \rho c \int_{\Omega_J} \mathbf{N}_J \, [\mathbf{v}_\mathrm{L}]^\top \, \mathbf{B}_J \, \mathrm{d}\Omega_J + \, r_N \int_{\Omega_J} \left([\mathbf{B}_J]^\top \, k_L^T \, \mathbf{B}_J\right) \mathrm{d}\Omega_J \right) \widetilde{\mathbb{T}}_\mathrm{L} \tag{3.62}$$

$$\begin{aligned} \mathbf{K}_{\mathrm{L}_\mathrm{e}}^\mathrm{SUPG} = \; & \left[\widetilde{\mathbb{T}}_\mathrm{L}\right]^\top \left(r_N \rho c \int_{\Omega_J} \left(\frac{\alpha_{opt} h_{car}}{2|\mathbf{v}_\mathrm{L}|} \left[\mathbf{v}_\mathrm{L}\right]^\top \mathbf{B}_J \right) \left[\mathbf{v}_\mathrm{L}\right]^\top \mathbf{B}_J \, \mathrm{d}\Omega_J \right. \\ & \left. + \, r_N \int_{\Omega_J} \left(\frac{\alpha_{opt} h_{car}}{2|\mathbf{v}_\mathrm{L}|} \left[\mathbf{v}_\mathrm{L}\right]^\top \boldsymbol{\nabla} \mathbf{B}_J \right) \, k_L^T \, \mathbf{B}_J \, \mathrm{d}\Omega_J \right) \widetilde{\mathbb{T}}_\mathrm{L} \end{aligned} \tag{3.63}$$

$$\mathbf{K}_{\mathrm{N}_\mathrm{e}} = \left[\widetilde{\mathbb{T}}_\mathrm{N}\right]^\top \left(\int_{\Omega_J} [\mathbf{N}_J]^\top \, \check{k}_N^T \, \mathbf{N}_J \, \mathrm{d}\Omega_J \right) \widetilde{\mathbb{T}}_\mathrm{N} \tag{3.64}$$

Finally, the global matrices of the system of Eq. (3.61) are obtained by the assembly of the contribution of each element of the mesh.

Simple academic example 9: steady-state large advection thermal problem in 2-D for interfaces using the SUPG method

The objective of this example is to compare the solutions between the standard Galerkin FEM method and the SUPG and verify that the last one provides stable solutions when $Pe > 1$ in a 2-D simple example using interfaces.

The geometry of this example consists of three horizontal layers with an interface at the symmetry axis (Figure 3.8.a), composed of 600 continuum elements and 20 interface elements. In order to visualize the heat transport, a known and constant velocity field from left to right (Figure 3.8.a) is imposed along the discontinuity, as a preferential path through the continuum medium.

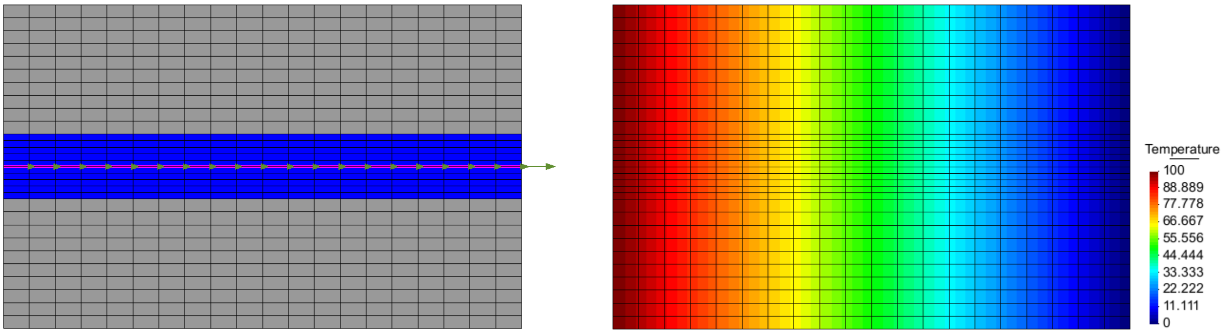

(a) *(b)*

Figure 3.8: (a) Imposed velocities along the discontinuity (b) steady-state temperature distribution at t=0 (after velocity application).

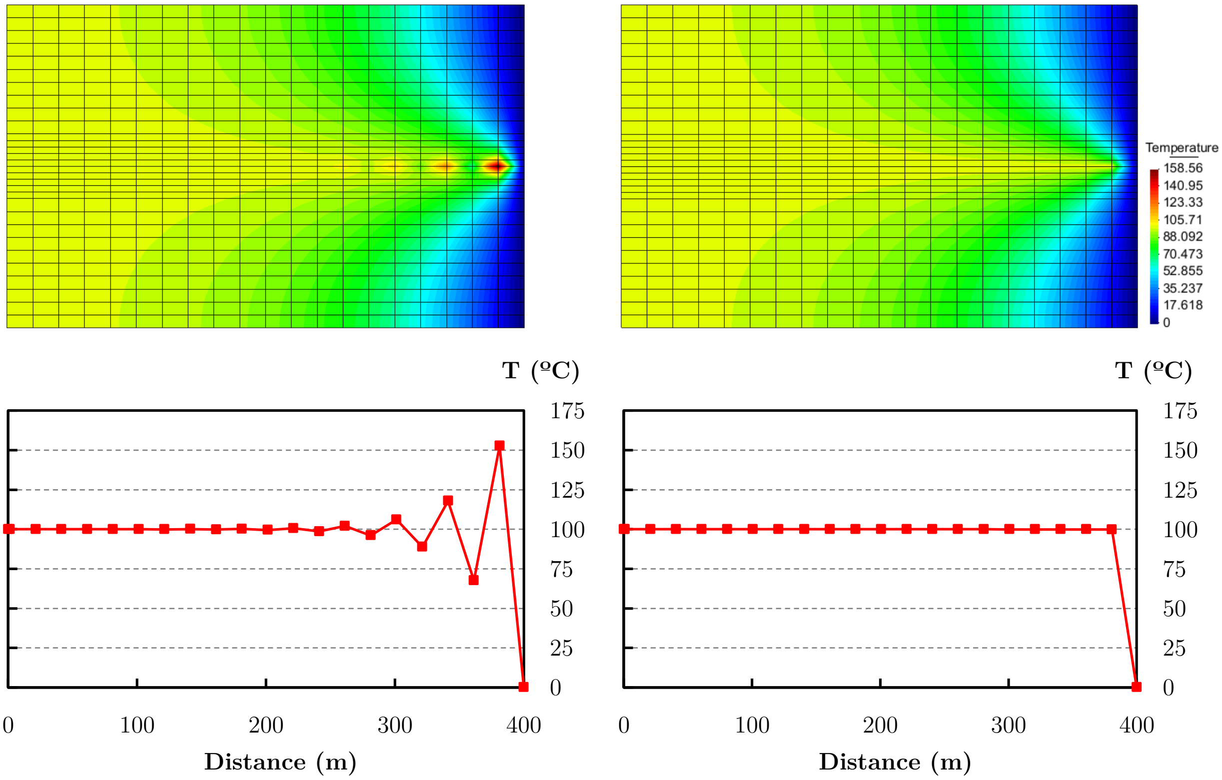

(a) *(b)*

Figure 3.9: (a) Oscillatory distribution of temperatures using the standard Galerkin weighting when Pe = 3.8 along the discontinuity (the rest of the domain Pe = 0). (b) Correct distribution of temperatures using SUPG method for the same problem. Graphs referred to the discontinuity of the problem.

The initial state of the thermal problem is shown in Figure 3.8.b, which is the result of a steady-state problem where two values of temperature have been imposed on the left and right hand side of the domain, obtaining a linear distribution of temperatures for $t = 0$. The velocity field is imposed on the described initial state.

In the first calculations the standard Galerkin weighting is used for a steady-state large advection problem ($Pe = 3.8$). As it is observed, the solution becomes purely oscillatory using the standard Galerkin weighting, as shown in Figure 3.9.a. However, using the new numerical solution (Petrov-Galerkin weighting, SUPG method), the steady-state solution is stabilized, as shown in Figure 3.9.b. In both cases the characteristic length of the element h_{car} is taken as the length of the element in the direction of the velocities.

3.3.2. Transient thermal problem with large advection in interfaces

In order to stabilize the numerical solution of the transient thermal problem with large advection in interfaces, the new Implicit Characteristic-Galerkin Method (α-ICGM) presented in Section 2.2.3 is used as in the continuum medium. Also, it is assumed that the large advection affects only the longitudinal flow of the interfaces, while transversal flow remains unchanged from the formulation developed in Section 3.2.

The differential equation for the one-dimensional transient problem in interfaces can be written from Eq. (3.4) as

$$\frac{\partial}{\partial l}\left(r_N\ k_L^T\ \frac{\partial \phi}{\partial l} - r_N \rho c \phi v_L\right) = r_N \rho c \frac{\partial \phi}{\partial t} \tag{3.65}$$

where l is the local coordinate system for the one-dimensional problem $\{l, n\}$. Considering a moving coordinate system l' defined by

$$dl' = dl - v_L\ dt \tag{3.66}$$

the differential equation becomes simply:

$$r_N \rho c \frac{\partial \phi}{\partial t} = \frac{\partial}{\partial l'}\left(r_N\ k_L^T\ \frac{\partial \phi}{\partial l'}\right) \tag{3.67}$$

where the advective term of the equation disappears and the new equation is evaluated *along the characteristics* (Section 2.2.3).

The first step of this procedure consists on the time discretization of Eq. (3.67) using the FDM. Following the α-ICG Method developed earlier (Section 2.2.3) for the continuum medium:

$$\begin{aligned} & r_N \rho c \frac{1}{\Delta t}\left(\phi^{n+1}\big|_{x+\alpha\delta} - \phi^{n}\big|_{(x-(1-\alpha)\delta)}\right) \approx \\ & \qquad \approx \theta \left[\frac{\partial}{\partial l}\left(r_N\ k_L^T\ \frac{\partial \phi}{\partial l}\right)\right]^{n+1}\Bigg|_{x+\alpha\delta} + (1-\theta)\left[\frac{\partial}{\partial l}\left(r_N\ k_L^T \frac{\partial \phi}{\partial l}\right)\right]^{n}\Bigg|_{(x-(1-\alpha)\delta)} \end{aligned} \tag{3.68}$$

Substituting Eqs. (2.145)-(2.155) into Eq. (3.68) and leaving out third-order terms results:

$$
\begin{aligned}
& r_N \rho c \frac{1}{\Delta t}\left(\phi^{n+1}-\phi^n\right)= \\
& \qquad =-(1-\alpha) r_N \rho c\ v_L^{n+1/2} \frac{\partial \phi^n}{\partial l}+\frac{(1-\alpha)^2}{2} r_N \rho c \Delta t\ v_L^{n+1/2}\ v_L^{n+1/2} \frac{\partial^2 \phi^n}{\partial l^2} \\
& \qquad -\alpha r_N \rho c\ v_L^{n+1/2} \frac{\partial \phi^{n+1}}{\partial l}-\frac{\alpha^2}{2} r_N \rho c \Delta t\ v_L^{n+1/2}\ v_L^{n+1/2} \frac{\partial^2 \phi^{n+1}}{\partial l^2} \\
& \qquad +\theta\left[\frac{\partial}{\partial l}\left(r_N\ k_L^T \frac{\partial \phi}{\partial l}\right)\right]^{n+1}+(1-\theta)\left[\frac{\partial}{\partial l}\left(r_N\ k_L^T \frac{\partial \phi}{\partial l}\right)\right]^n
\end{aligned}
\tag{3.69}
$$

Performing the spatial discretization of this equation along the mid-plane of the discontinuity, the temperature can be approximated as:

$$
\phi \cong \hat{\phi}=\sum_{a=1}^{m} N_J^{(a)} \phi_{mp}^{(a)} \tag{3.70}
$$

where $\hat{\phi}$ is the approximate value of the temperature, $\phi_{mp}^{(a)}$ is the value of the temperature at the (a) mid-plane node, $N_J^{(a)}$ is the shape function at the mid-plane node and m is the number of mid-plane nodes of the element.

The extension of the above formulation to 3D is automatic by considering a local coordinate system such as $\boldsymbol{l}_i=(l_1, l_2)$ and the corresponding nodes and mid-plane nodes depending on the type of element used (triangular or quadrangular interfaces).

Substituting Eq. (3.70) into (3.69), using the standard Galerkin weighting ($\mathrm{w}_i=N_i$) and applying the Theorem of the Divergence to the diffusive terms results in the following expression for the longitudinal flow along the mid-plane of a single element of the mesh:

$$
\mathbf{Q}_{\mathrm{L}_{\mathrm{mp}}}=\mathbf{C}_{\mathrm{L}_{\mathrm{mp}}} \dot{\boldsymbol{\phi}}_{\mathrm{mp}}+\left(\mathbf{K}_{\mathrm{L}_{\mathrm{mp}}}+\mathbf{K}_{\mathbf{v}, \mathrm{L}_{\mathrm{mp}}}+\mathbf{K}_{\mathbf{s}, \mathrm{L}_{\mathrm{mp}}}\right) \boldsymbol{\phi}_{\mathrm{mp}} \tag{3.71}
$$

where

$$
\mathbf{C}_{\mathrm{L}_{\mathrm{mp}}} = r_N \rho c \int_{\Omega_J}\left[\mathbf{N}_J\right]^{\top} \mathbf{N}_J \,\mathrm{d} \Omega_J \tag{3.72}
$$

$$
\mathbf{K}_{\mathrm{L}_{\mathrm{mp}}} = \int_{\Omega_J}\left(\left[\mathbf{B}_J\right]^{\top} r_N\ k_L^T\ \mathbf{B}_J\right) \mathrm{d} \Omega_J \tag{3.73}
$$

$$
\mathbf{K}_{\mathbf{v}, \mathrm{L}_{\mathrm{mp}}} = r_N \rho c \int_{\Omega_J}\left(\left[\mathbf{N}_J\right]^{\top} \mathbf{v}_{\mathrm{L}}\ \mathbf{B}_J\right) \mathrm{d} \Omega_J \tag{3.74}
$$

$$
\mathbf{K}_{\mathbf{s}, \mathrm{L}_{\mathrm{mp}}} = r_N \rho c\ \Delta t \int_{\Omega_J}\left(\left[\mathbf{B}_J\right]^{\top}\left[\mathbf{v}_{\mathrm{L}}\right]^{\top} \mathbf{v}_{\mathrm{L}}\ \mathbf{B}_J\right) \mathrm{d} \Omega_J \tag{3.75}
$$

where $\mathbf{B}_J$, $\boldsymbol{\phi}_{\mathrm{mp}}$ and $\mathbf{v}_{\mathrm{L}}$ are defined by Eqs. (3.20) and (3.21). Additionally, the boundary term of Eq. (3.18) must be added to the above formulation.

All the matrices and vectors defined at the mid-plane of the interface have to be transformed using the transference matrix to obtain the matrices and vectors defined at the nodes of the element, as described in Section 3.2 by Eqs. (3.22)-(3.30), obtaining finally the following relation for the longitudinal flow matrices:

$$\mathbf{C}_{\mathrm{L_e}} = \left[\widetilde{\mathbb{T}}_{\mathrm{L}}\right]^{\top} \mathbf{C}_{\mathrm{L_{mp}}} \widetilde{\mathbb{T}}_{\mathrm{L}} \tag{3.76}$$

$$\mathbf{K}_{\mathrm{L_e}} = \left[\widetilde{\mathbb{T}}_{\mathrm{L}}\right]^{\top} \mathbf{K}_{\mathrm{L_{mp}}} \widetilde{\mathbb{T}}_{\mathrm{L}} \tag{3.77}$$

$$\mathbf{K}_{\mathbf{v},\mathrm{L_e}} = \left[\widetilde{\mathbb{T}}_{\mathrm{L}}\right]^{\top} \mathbf{K}_{\mathbf{v},\mathrm{L_{mp}}} \widetilde{\mathbb{T}}_{\mathrm{L}} \tag{3.78}$$

$$\mathbf{K}_{\mathbf{s},\mathrm{L_e}} = \left[\widetilde{\mathbb{T}}_{\mathrm{L}}\right]^{\top} \mathbf{K}_{\mathbf{s},\mathrm{L_{mp}}} \widetilde{\mathbb{T}}_{\mathrm{L}} \tag{3.79}$$

It is important to note that, as the large advection affects only the longitudinal flow, the transversal formulation is the same as presented in Section 3.2 by Eqs. (3.31)-(3.42). Additionally, the matrix assembly of both longitudinal and transversal flow is achieved in the same manner as presented in the same section by Eqs. (3.43) and (3.44).

The last step in the solution of the transient problem is to perform the time integration of the system of Eqs. (3.71) using the FDM, resulting in the Eq. (3.80).

Summary 6 - Transient thermal equation for large advection in zero-thickness interface elements using the α-Implicit Characteristic Galerkin method.

$$\begin{gathered}\left(\frac{1}{\Delta t}\mathbf{C}_{\mathrm{L_e}} + \mathrm{\alpha}\mathbf{K}_{\mathbf{v},\mathrm{L_e}} + \frac{\alpha^2}{2}\mathbf{K}_{\mathbf{s},\mathrm{L_e}} + \theta\left(\mathbf{K}_{\mathrm{L_e}} + \mathbf{K}_{\mathrm{T_e}}\right)\right)\Delta\phi_{\mathrm{e}}^{n+1} \\ = -\left[\mathbf{K}_{\mathrm{L_e}} + \mathbf{K}_{\mathbf{v},\mathrm{L_e}} + \left(\frac{1}{2} - \mathrm{\alpha}\right)\mathbf{K}_{\mathbf{s},\mathrm{L_e}}\right]\phi_{\mathrm{e}}^{n}\end{gathered} \tag{3.80}$$

where $\Delta\phi_{\mathrm{e}}^{n+1}$ is the nodal increment temperature vector of the element (unknown), $\mathbf{C}_{\mathrm{L_e}}$ is the thermal capacity matrix of the element, $\mathbf{K}_{\mathrm{L_e}}$ and $\mathbf{K}_{\mathrm{N_e}}$ are the longitudinal and transversal thermal conduction matrices of the element, respectively, and $\mathbf{K}_{\mathbf{s},\mathrm{L_e}}$ and $\mathbf{K}_{\mathbf{v},\mathrm{L_e}}$are the longitudinal advective matrices. Boundary conditions are left out for simplicity.

$$\mathbf{K}_{\mathrm{L_e}} = \left[\widetilde{\mathbb{T}}_{\mathrm{L}}\right]^{\top}\left(r_N \int_{\Omega_J} \left([\mathbf{B}_J]^{\top}\ k_L^T\ \mathbf{B}_J\right) \mathrm{d}\Omega_J\right)\widetilde{\mathbb{T}}_{\mathrm{L}} \tag{3.81}$$

$$\mathbf{K}_{\mathbf{v},\mathrm{L_e}} = \left[\widetilde{\mathbb{T}}_{\mathrm{L}}\right]^{\top}\left(r_N \rho c \int_{\Omega_J} \left([\mathbf{N}_J]^{\top}\ \mathbf{v}_{\mathrm{L}}\ \mathbf{B}_J\right) \mathrm{d}\Omega_J\right)\widetilde{\mathbb{T}}_{\mathrm{L}} \tag{3.82}$$

$$\mathbf{K}_{\mathbf{s},\mathrm{L_e}} = \left[\widetilde{\mathbb{T}}_{\mathrm{L}}\right]^{\top}\left(r_N \rho c\ \Delta t \int_{\Omega_J} \left([\mathbf{B}_J]^{\top}\ [\mathbf{v}_{\mathrm{L}}]^{\top}\mathbf{v}_{\mathrm{L}}\ \mathbf{B}_J\right) \mathrm{d}\Omega_J\right)\widetilde{\mathbb{T}}_{\mathrm{L}} \tag{3.83}$$

$$\mathbf{C}_{\mathrm{L_e}} = \left[\widetilde{\mathbb{T}}_{\mathrm{L}}\right]^{\top} \left(r_N \rho c \int_{\Omega_J} [\mathbf{N}_J]^{\top}\, \mathbf{N}_J \, \mathrm{d}\Omega_J \right) \widetilde{\mathbb{T}}_{\mathrm{L}} \tag{3.84}$$

$$\mathbf{K}_{\mathrm{N_e}} = \left[\widetilde{\mathbb{T}}_{\mathrm{n}}\right]^{\top} \left(\int_{\Omega_J} [\mathbf{N}_J]^{\top}\, k_N^T \, \mathbf{N}_J \, \mathrm{d}\Omega_J \right) \widetilde{\mathbb{T}}_{\mathrm{n}} \tag{3.85}$$

Finally, the global matrices and vectors of the system of Eq. (3.48) are obtained by the assembly of the contribution of each element of the mesh.

Simple academic example 10: transient large advection thermal problem in 2-D for interfaces using the α-Implicit Characteristic Method

The objective of this example is to compare the solutions between the standard Galerkin FEM method and the α-Implicit Characteristic Method and verify that the last one provides stable solutions when $Pe > 1$ in a 2-D simple example with interfaces.

The geometry of this example consists in a domain of 400×250m of three horizontal layers with an interface at the symmetry axis (Figure 3.8.a), composed by 600 continuum elements and 20 interface elements. In order to observe the heat transport, a known and constant velocity field of $v_L = 0.19\ m/s$ from left to right (Figure 3.8.a) is imposed along the discontinuity, as a preferential path throughout the continuous medium.

The initial state of the thermal problem is shown in Figure 3.8.b, which is the result of a steady-state problem where two values of temperature have been imposed on the left and right hand side of the domain, obtaining a linear distribution of temperatures for $t = 0$. The velocity field is imposed on the described initial state solving the transient problem.

Figure 3.10 shows the results of the transient thermal problem with large advection ($Pe = 273$), first using the standard Galerkin weighting, which leads to oscillatory results, and then using the α-ICG method, which leads to the stable correct solution. In this case it has been verified that the best result is reached for $\alpha = 0.25$. Note that the Courant number is smaller than 1 ($C = 0.67$), a necessary condition to obtain a stable solution.

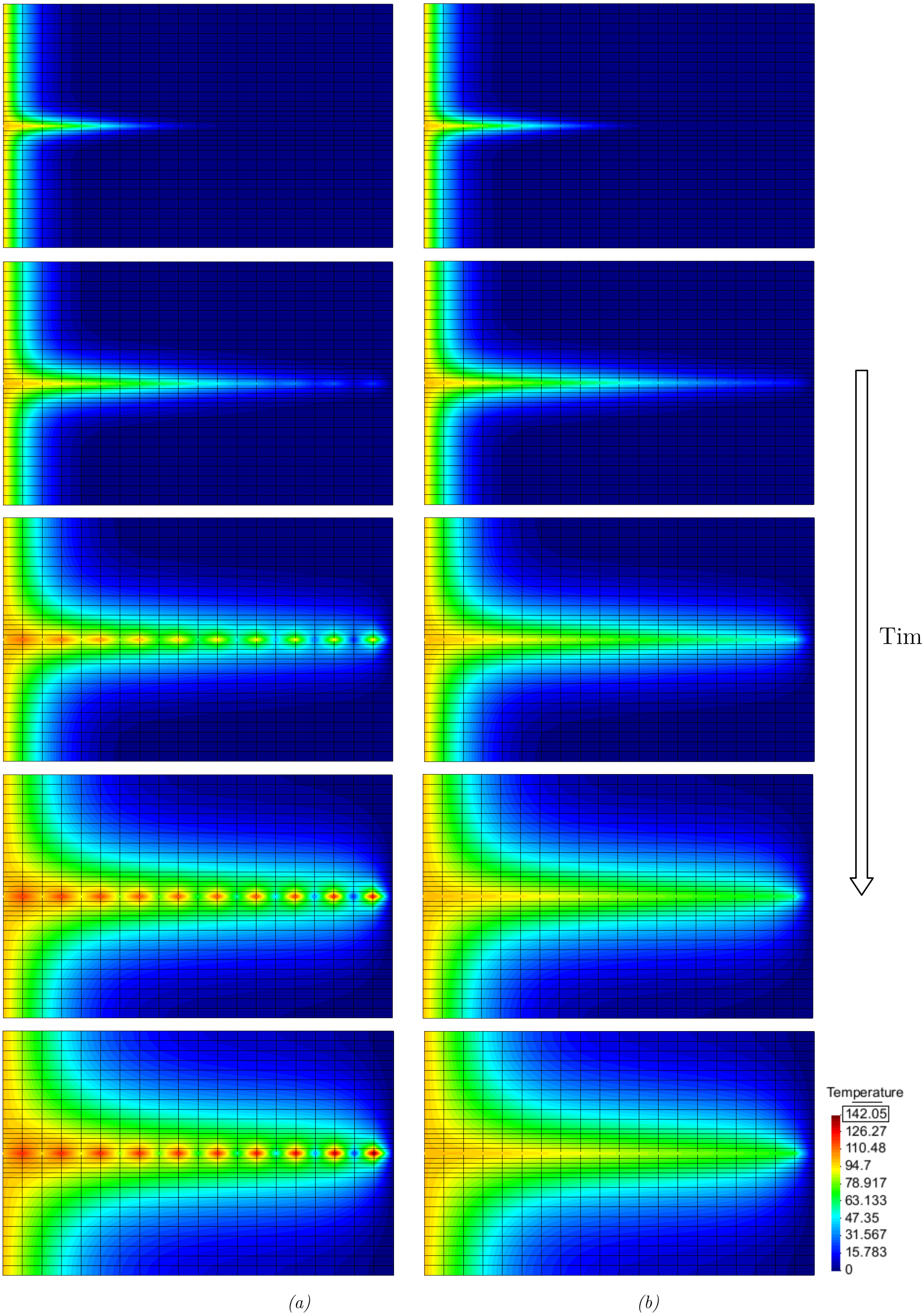

Figure 3.10: Transient thermal solution for Pe = 273. (a) Oscillatory results using the standard Galerkin weighting. (b) Correct solution using the new α-ICG method with $\alpha = 0$ for advective transport.

Simple academic example 11: transient pure advection problem in interfaces using the α-Implicit Characteristic Method

The FE mesh of the example is shown in Figure 3.11 and consists of a 2D mesh composed by 480 zero-thickness interface elements and 962 nodes. The imposed velocity field consists of a constant velocity field of $v_L = 0.1\ m/s$ from left to right along the x-direction. The thermal conductivity coefficient is assumed equal to zero and therefore the Péclet number tends to infinite (pure advection thermal problem). The Courant number in all the elements of the mesh is equal to 0.54.

The initial distribution of temperatures of the thermal problem consists of a Gaussian distribution of temperatures, as shown in Figure 3.11. This example is an analogy of the academic example 4 but using interfaces.

Figure 3.11: Mesh and initial distribution of temperatures along the interfaces.

Figure 3.12 shows the results for $\alpha = 0$, which corresponds to the Implicit Galerkin Characteristic method. In this case, the initial temperature distribution exhibits oscillations of ±0.25℃.

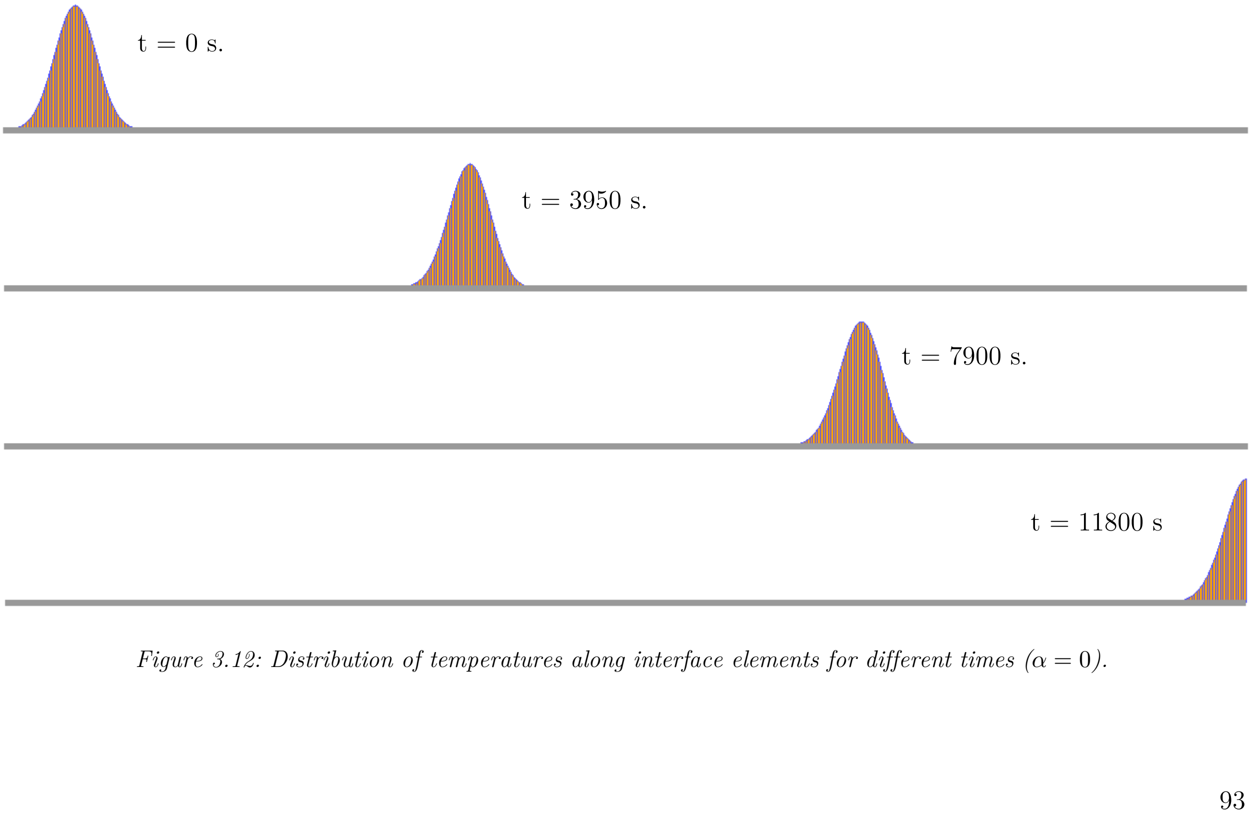

Figure 3.12: Distribution of temperatures along interface elements for different times ($\alpha = 0$).

Figure 3.13 shows the results for α = 1/4, with which the method maintains better the initial distribution of temperatures with small oscillations at the top of the bell of ±0.15℃.

Figure 3.14 shows the results for α = 1/2, with the temporal derivatives evaluated centred around the solution x (Figure 2.16.b). In this case, the initial distribution of temperatures exhibits oscillations of ±0.40℃.

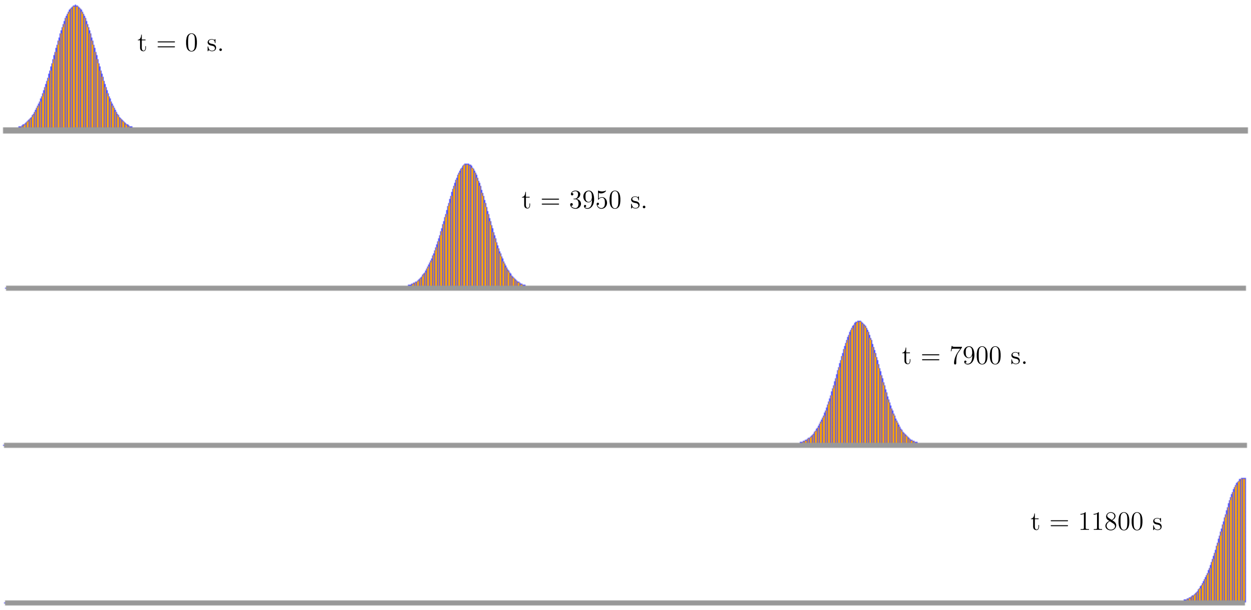

Figure 3.13: Distribution of temperatures along interface elements for different times (α = 1/4).

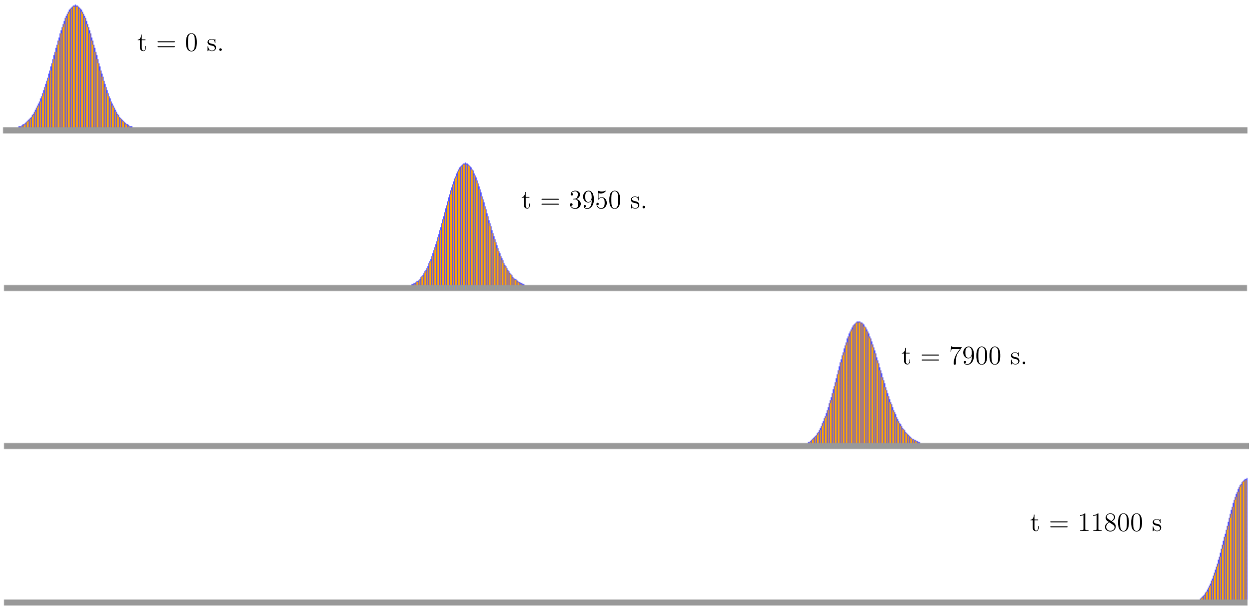

Figure 3.14: Distribution of temperatures along interface elements for different times (α = 1/2).

Finally, Figure 3.15 shows the results using the standard Galerkin weighting method. With this method, the original shape of the temperature profile is not maintained, and the peak value decreases significantly as the “bell” base becomes much wider.

The best solution of the problem using the α-ITCG Method is achieved again by using $\alpha = 1/4$.

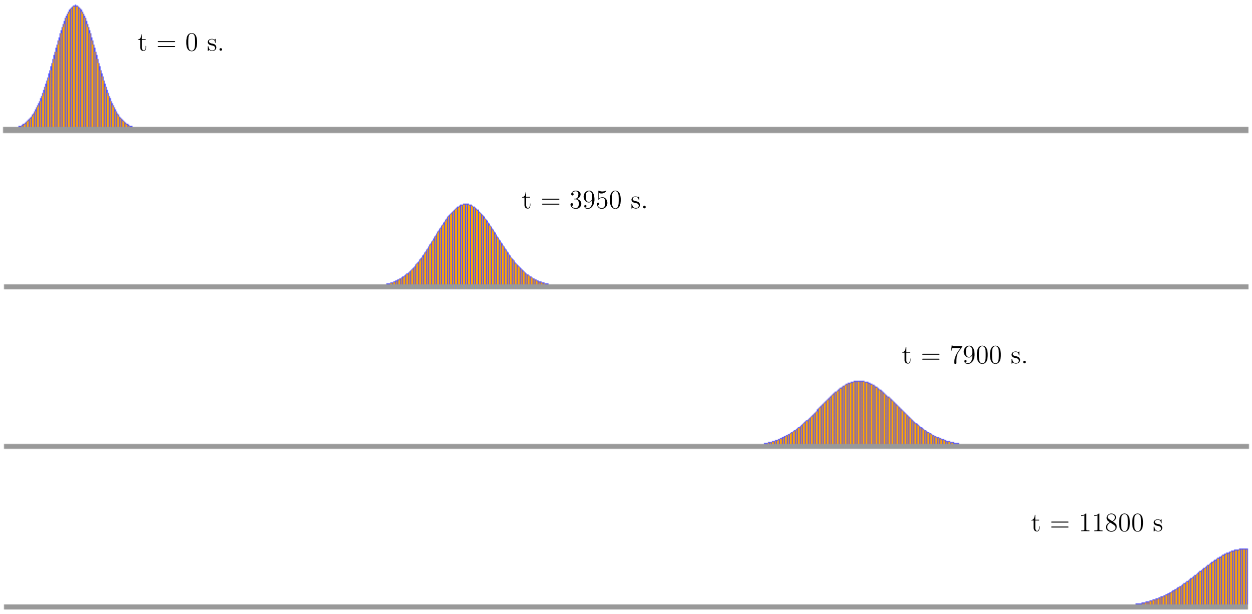

Figure 3.15: Distribution of temperatures along interface elements for different times (Standard Galerkin Weighting).

Simple academic example 12: transient pure advection problem in interfaces using the α-Implicit Characteristic Method

The FE mesh of this example is shown in Figure 3.16 and consists of a 2D mesh composed by 480 zero-thickness interface elements and 962 nodes. The imposed velocity field consists of a constant velocity field of $v_L = 0.10\ m/s$ from left to right along the x-direction. The thermal conductivity coefficient is assumed equal to zero and therefore the Péclet number tends to infinite (pure advection thermal problem). The Courant number in all the elements of the mesh is equal to 0.54.

The initial distribution of temperatures of the thermal problem is trapezoidal, as shown in Figure 3.16. This example is an analogy of the academic example 5 but using interfaces.

Figure 3.16: Mesh and initial distribution of temperatures along the interfaces.

Figure 3.17 shows the results for α = 1/4, with which the method maintains better the initial distribution of temperatures with small oscillations of ±0.5℃. Figure 3.18 shows the results obtained for α = 1/2, wich corresponds to the temporal derivatives evaluated centred around the solution x (Figure 2.16.b). In this case, the initial distribution of temperatures exhibits oscillations of ±2.2℃.

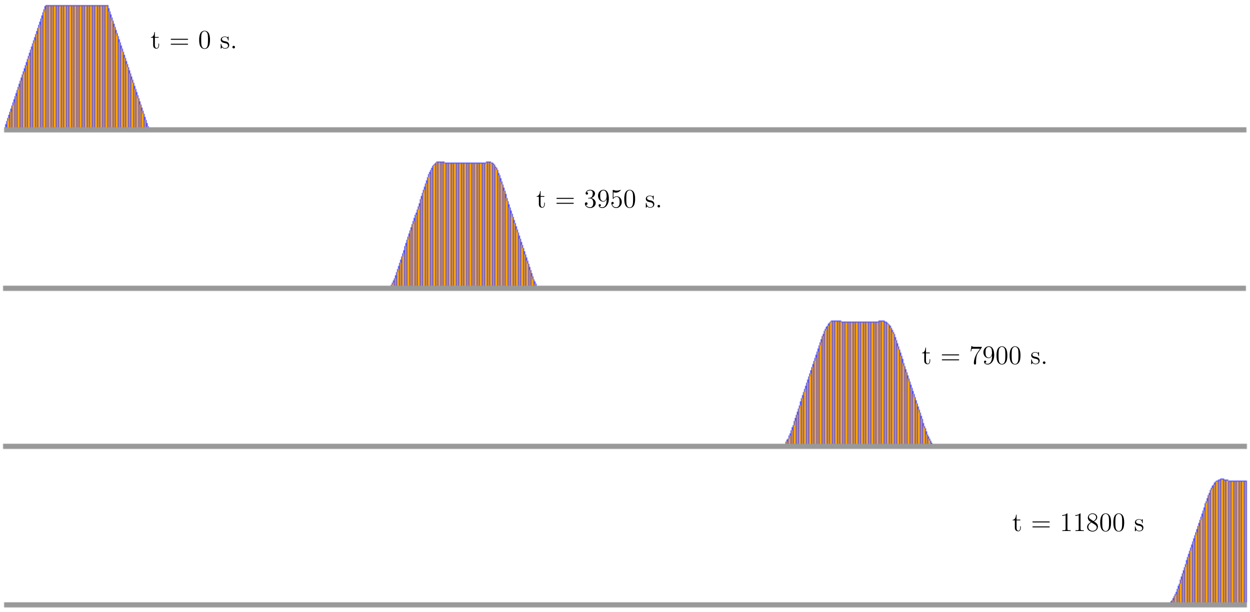

Figure 3.17: Distribution of temperatures along interface elements for different times (α = 1/4).

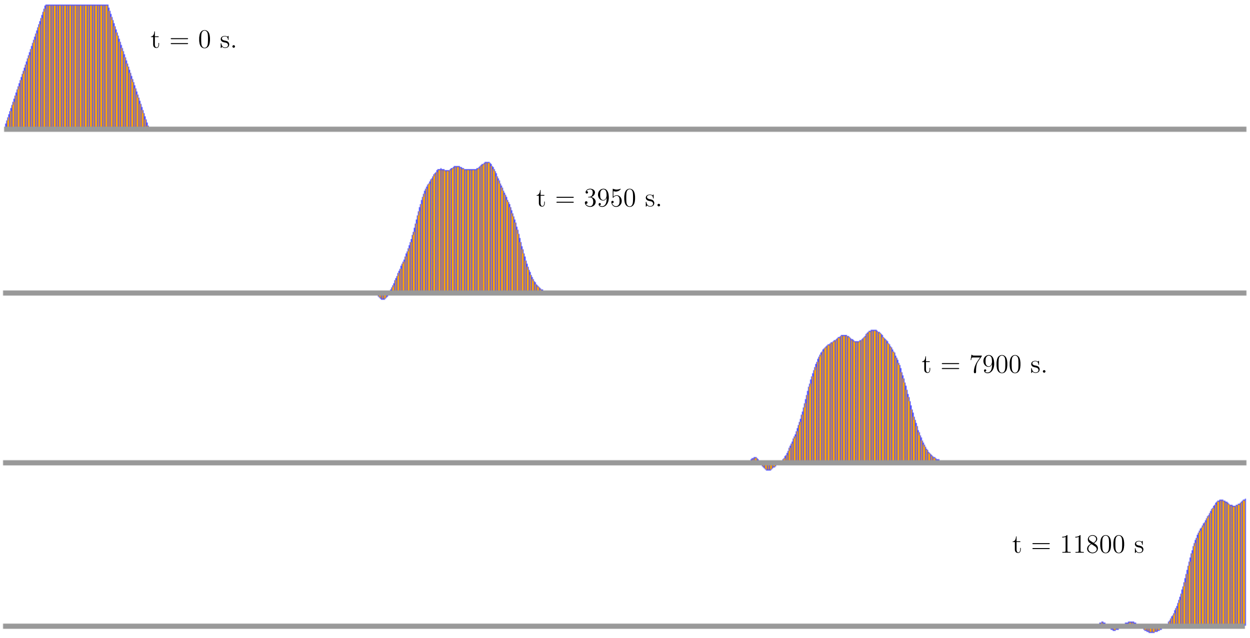

Figure 3.18: Distribution of temperatures along interfaces for different times (α = 1/2).

Finally, Figure 3.19 shows the results using the standard Galerkin weighting method. With this method, the original shape of the temperature profile is not maintained, and the peak value decreases significantly as the "bell" base becomes much wider.

The best solution of the problem is obtained, again, when using the α-ITCG Method with $\alpha = 1/4$.

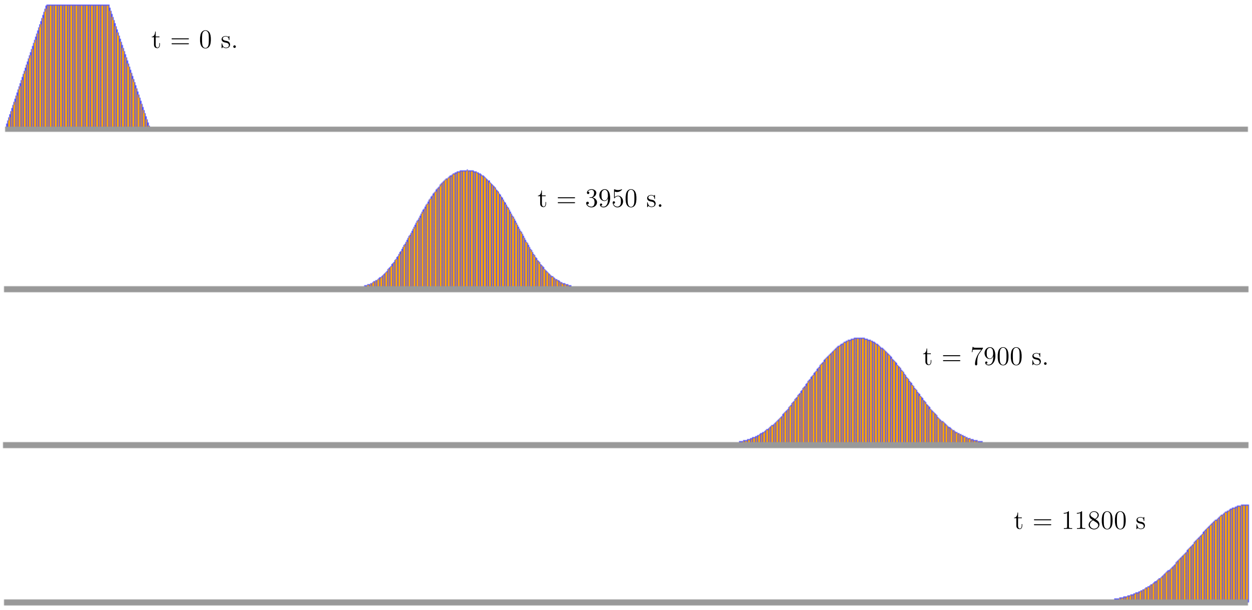

Figure 3.19: Distribution of temperatures along interfaces for different times (Standard Galerkin Weighting).

Chapter 4

Thermo-hydro-mechanical coupling with advection

Fully coupled approaches are not common in the thermo-hydro-mechanical (THM) analysis of discrete discontinuities. This chapter follows the work of Segura & Carol (2008a) and Garolera (2017), in which the hydro-mechanical (HM) coupled formulation for continuum media and zero-thickness interface elements (assuming saturated medium and incompressible fluid) were developed for 2D and 3D analysis, respectively. In their formulation, the mutual interaction between the fluid pressure and the solid deformation (with discontinuities) is achieved combining classic mechanical formulations and a diffusive flow model that introduces a transversal potential drop across the discontinuity, which causes also a drop in the effective stresses between its both sides. In fractured porous media, this mutual interaction may produce the fracture propagation due to the effect of fluid pressure. In their work all non-linear behaviour is assumed to occur at the interface elements, while poro-elasticity is assumed for the continuum porous medium. The method has been successfully applied to oil engineering in fractured reservoirs, in particular for the solution of fracture hydraulic problems.

The study of coupled THM processes with advection in discontinuities is important in problems with a certain degree of coupling between the mechanical, hydraulic and thermal behavior, and in which the hydraulic flow transports heat with a significant speed through the discontinuities. In this context, the 3D thermal advective formulations described in Chapter 2 and 3 are coupled with the HM formulation referenced before (Segura & Carol, 2008a; Garolera 2017).

This chapter describes two different approaches to solve the THM coupled problem with advection for saturated geomaterials, considering the continuum medium and the double-nodded zero-thickness interface elements introduced in Section 3. The first approach is the partitioned or staggered approach, which makes use of different codes, appropriately linked, to solve the THM advective problem. The second strategy is the fully coupled (i.e. monolithic) approach, which directly solves the whole THM system of equations using the Newton-Raphson iterative method. In both cases the solution is obtained by using the Finite Element Method (FEM).

From a mechanical point of view, the fluid pressure is introduced with the effective stress principle and the influence of the temperature by the solid (continuum) deformation as a function of the thermal expansion coefficient of the material. From a hydraulic point of view, the deformation produces changes in the fluid storage capacity and in the longitudinal conductivity of the interfaces. Finally, temperature changes modify the viscosity and density of the fluid, although in this thesis the variation of the fluid density with temperature is assumed negligible. Also, from a thermal point of view, the mechanical deformation of the interfaces influences their thermal storage capacity and longitudinal conductivity, while the fluid velocities (Darcy velocities) generates heat transport with the fluid.

In this thesis, the displacement of the solid phase, the fluid pressure and the temperature are considered as the main unknowns. Following continuum mechanics conventions, tension is assumed positive and compression negative. Then the relative displacements on the interface elements are positive in opening, and fluid pressures are negative and suctions are positive. Moreover, the zero-thickness interface elements used in the mechanical, hydraulic and thermal formulations are the same, and therefore, only a single FEM mesh is needed to solve the THM problem for both staggered and fully coupled approaches. The present formulation also assumes small strains, negligible inertial forces, saturated porous medium and incompressible fluid.

This chapter presents the THM advective coupled formulation for continuum medium and zero-thickness interface elements that can be numerically implemented following a fully coupled or a staggered strategy. It is divided in four sections: Section 4.1 describes the main couplings between the three THM fields; Section 4.2 describes the THM solution using a staggered coupled approach; Section 4.3 describes the monolithic THM formulation with advection for continuum medium and zero-interfaces; and Section 4.4 describes briefly the mechanical constitutive model for zero-thickness interface elements, which is based on fracture mechanics.

4.1. THM couplings

This section presents the different interactions between the thermal, hydraulic and thermal fields considering a saturated and fractured porous medium. This study, previous to the formulation and numerical implementation of the THM coupled problem, is essential to establish a framework and the main hypothesis about the interactions between the three fields.

4.1.1. Thermo-mechanical coupling

This section presents the two main phenomena that produce coupling between the thermal and mechanical fields. The first phenomenon is thermal expansion, which can be defined as the tendency of matter to change in shape, area or volume in response to a change of temperature. Thus, in the mechanical calculations, the change of volume due to the thermal effects may be considered as an induced strain that depends on the temperature increment and the coefficient of thermal expansion of the solid material:

$$\Delta \boldsymbol{\varepsilon}^T = \alpha_s^T \, \Delta T \tag{4.1}$$

where $\Delta \boldsymbol{\varepsilon}^T$ is the strain increment due to the thermal effects, α_s^T is the coefficient of thermal expansion of the solid material [°C^{-1}] and ΔT is the temperature increment that produces the thermal expansion. This phenomenon only affects the continuum porous medium and not the interfaces.

This thermal expansion of the solid material produces the variation of the total volume and, consequently, of the total pore volume, modifying the available space for the fluid in the porous medium. This change of the pore volume modifies the pressure distribution in the hydraulic problem and, due to the hydro-mechanical coupling, generates changes in the mechanical problem (effective stresses).

Additionally, the temperature variation affects the fluid that fills the pores or discontinuities, leading to volume changes of the fluid that are proportional to its coefficient of thermal expansion α_f^T. This change of the fluid volume modifies the pressure distribution in the hydraulic problem, and subsequently the effective stresses in the mechanical problem. However, this thermal expansion affects first the hydraulic problem, as explained in section 4.1.2.

The second phenomenon that produces coupling between the mechanical and thermal fields affects only the interfaces. The opening of the discontinuities may change the quantity of fluid that fills them (considering saturated medium), leading to a variation on the in-plane heat transmissivity, since the heat storage capacity depends on the quantity of fluid filling the discontinuities. Moreover, the transversal heat transmissivity may be also modified with the opening of the interfaces due to the volume change of the fluid in the transversal direction that the heat flow has to cross. As mentioned, this condition does not affect the continuum medium.

4.1.2. Hydro-thermal coupling

This section presents the two main phenomena that produce coupling between the thermal and hydraulic fields. The first consists on the variation of viscosity and density of the fluid due to the variation of temperature. This can also lead to volume changes of the fluid, modifying the pressure distribution in the hydraulic problem. In this thesis it is assumed that the fluid filling the pores and discontinuities is water. The variation of the water density and viscosity with temperature is well known (IAPWS, 2008; Huber et al. 2009) and is reproduce here in Figure 4.1.

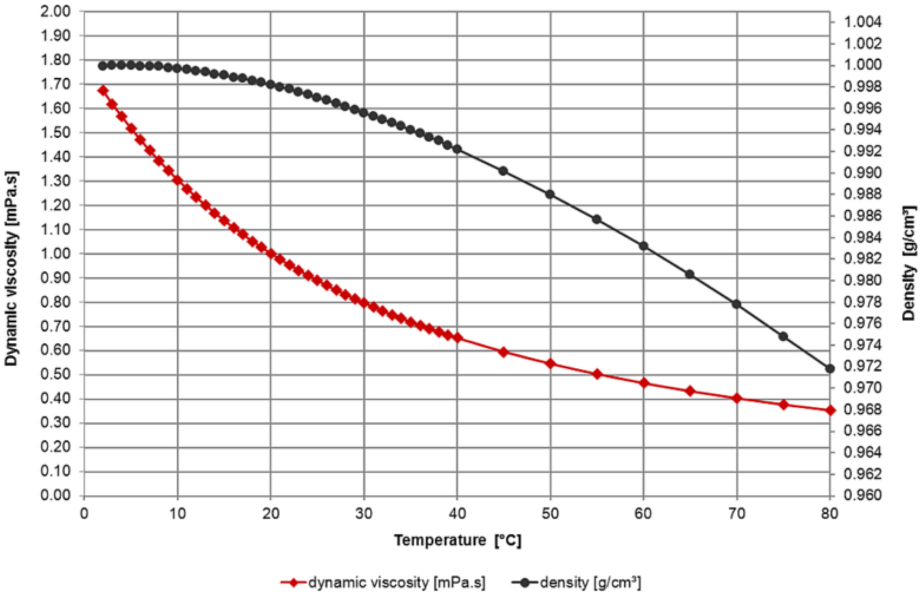

Figure 4.1: Variation of water density and dynamic viscosity with temperature.

The variation of viscosity and density with temperature can be modeled by interpolation of exponential functions to the data shown in Figure 4.1:

$$\mu(T) = \mathrm{a} \cdot \mathrm{e}^{-b\,T} = 2.1 \cdot \mathrm{e}^{-0.02\,T} \tag{4.2}$$

$$\rho^f(T) = \alpha \cdot \mathrm{e}^{-\beta\,T} = 1004 \cdot \mathrm{e}^{-0.0004\,T} \tag{4.3}$$

where μ [mPa $\cdot$ s] and ρ^f [kg/m^3] are the dynamic viscosity and density of the water and T is the temperature [℃].

Figure 4.1 shows that the variation of water density in the temperature range from 10 to 60℃, which is the range of temperature variation in the applications of interest in this thesis, is around 1.5%. For this reason, the variation of density of the fluid is left out in the THM formulation developed in this Chapter.

The variation of temperature modifies also the dynamic viscosity of the fluid and the hydraulic conductivity, leading to a variation of the fluid velocity field (Darcy velocities), which produces heat transport with the fluid and a variation of the distribution of temperatures obtained from the thermal analysis. This transport is known as advection and has been extensively discussed in Chapters 2 and 3 of this thesis, where the Darcy velocity appears directly in the conduction-advection equations (2.157)-(2.163) and (3.80)-(3.85). Thus, the variation of the dynamic viscosity changes the fluid velocity field and, subsequently, the distribution of temperatures in the thermal problem.

It is important to note that the advection affects mainly the discontinuities, because they are preferential paths for the hydraulic flow and heat can be transported along them with significant speed.

The second phenomenon is related with the volume changes produced due to the effect of thermal expansions, as explained in section 4.1.1. Both volume changes affect the fluid pressure distribution in the hydraulic problem, unless $\alpha_s^T = \alpha_f^T$, in which case both volumes are equal and variation of temperature does not affect the pressure distribution.

4.1.3. Hydro-mechanical coupling

The hydro-mechanical interaction is well known since the classical contributions of Terzaghi (1925) and Biot (1941) to consolidation analysis, and the FEM "u-p" formulation introduced by Zienkiewicz & Bettess (1982). This section follows the work of Segura (2007), where an extensive review of the HM coupling can be found.

In the analysis of saturated geomaterials it is assumed that the fluid fills the pores and the discontinuities of the fractured porous media. The resulting pressures of the hydraulic analysis and the deformations of the mechanical analysis are reciprocally affected. This mutual interaction is introduced by the effective stress principle:

$$\sigma' = \sigma + p \tag{4.4}$$

where σ is the total stress (positive in tension), p is the fluid pressure (positive in compression) and σ' is the effective stress. Thus, the pressure modifies the effective stress in the porous medium, leading to its deformation and may also produce propagation of the discontinuities.

In addition, from a hydraulic point of view, the interface opening modifies its hydraulic storage capacity and longitudinal conductivity, which depend on the aperture.

4.2. Coupled THM scheme based on a staggered approach

This section presents the solution of the THM advective coupled problem using a staggered scheme. In this type of scheme, two or more codes are sequentially used to reach the coupled solution by the introduction of the appropriate coupling loops between them. A driver must link these codes to handle the exchange of information between them at each iteration and check the convergence in order to decide whether to advance to the following time-step or to iterate again. The degree of coupling reached depends on the exchange of information between the codes involved in the staggered procedure.

This thesis has made use of the available code DRAC (Prat, et al., 1993), in which the HM fully coupled problem for continuum and interface elements proposed by Segura & Carol

(2008a) and Garolera (2017) was already implemented. In this context, the thermal problem with advection described in Chapters 2 and 3 has been implemented in a new code similar to DRAC (T-DRAC), so that the thermal problem may be solved independently.

Thus, in the staggered approach used here to solve the THM advective coupled problem, code DRAC solves the HM problem and code T-DRAC solves the thermal advective problem. In order to carry out this staggered scheme, some modifications have been introduced in both codes. In one hand, code DRAC generates three different files with the nodal displacements, the nodal pressures and the fluid Darcy velocities at Gauss points, and it reads the nodal temperature increments file generated by code T-DRAC. On the other hand, code T-DRAC generates a file with the nodal temperature increments and can read the files with nodal displacements and fluid Darcy velocities at Gauss points generated by code DRAC. Finally, a driver linking both codes has been programmed, which manages the exchange of information between codes DRAC and T-DRAC and is able to read the files with nodal temperatures, nodal pressures and nodal displacements of the current and previous staggered iterations in order to evaluate the convergence and perform the necessary iterations to reach a final solution.

In the staggered iterative process, when a solution with the HM code is obtained, the new estimate value of the nodal displacements, nodal pressures and fluid velocities can be introduced again in the thermal code. The same procedure is carried out with the new estimated value of the nodal temperatures obtained from the thermal code, which are applied to the HM code. This sequential procedure iterates from one code to the other until the results achieve a certain prefixed tolerance. The number of staggered iterations increases with the degree of coupling between the HM and T problems. In this case, as the advection produces a strong coupling between both problems, this may cause convergence inconveniences in THM staggered calculations.

Additionally, it is important to note that the HM and T formulations use the same double-nodded interface elements. Consequently, the same FE mesh can be used for both problems, which is an advantage for the exchange of information between both codes.

The staggered approach is schematically illustrated in Figure 4.2 and briefly summarized as follows:

a) The driver calls DRAC in order to solve the HM problem. Then code DRAC reads the nodal temperature increments file generated by code T-DRAC and solves the HM problem. In this solution, the thermo-mechanical (TM) coupling is achieved imposing the thermally-induced strains to the mechanical problem, which results from the multiplication of the nodal temperature increments by the coefficients of thermal expansion of each material. Additionally, the thermo-hydraulic (TH) coupling is achieved considering that the variation of the temperature produces variation of the viscosity of the fluid in the hydraulic problem and therefore modifies the conductivity of the fluid, the velocities and the pressure distribution of the hydraulic problem. Finally, at the end of the calculation, code DRAC generates three files with the resulting displacements and fluid pressures at all nodes in the domain and the fluid Darcy velocities at all Gauss points in the domain (continuum medium and interfaces).

b) The driver calls code T-DRAC in order to solve the thermal advective problem. Then code T-DRAC reads the files with nodal displacements and fluid Darcy velocities generated by code DRAC and solves the thermal advective problem. In this solution, the hydro-thermal (HT) coupling is achieved by the imposition of the Darcy velocities to the thermal problem, which involves heat transport with the fluid (formulation in Chapters 2 and 3) and leads to a variation on the distribution of temperatures of the thermal solution. Additionally, the mechanic-thermal (MT) coupling is achieved considering that the displacements of the mechanical problem cause the opening of the discontinuities, modifying the thermal storage capacity and the longitudinal conductivity of the interfaces (due to the variation in the amount of fluid filling them). At the end of the calculation, code T-DRAC generates a file with the resulting nodal temperatures at all nodes in the domain.

c) The driver reads the temperature, pressure and displacement files written by codes DRAC and T-DRAC, and evaluates the convergence from the increments of the variables between the current and the previous staggered iteration. If specified tolerances for temperatures, pressures and displacements are satisfied, the driver continues to the next time-step; otherwise, the driver performs the necessary iterations between the two codes for each time-step until convergence is reached.

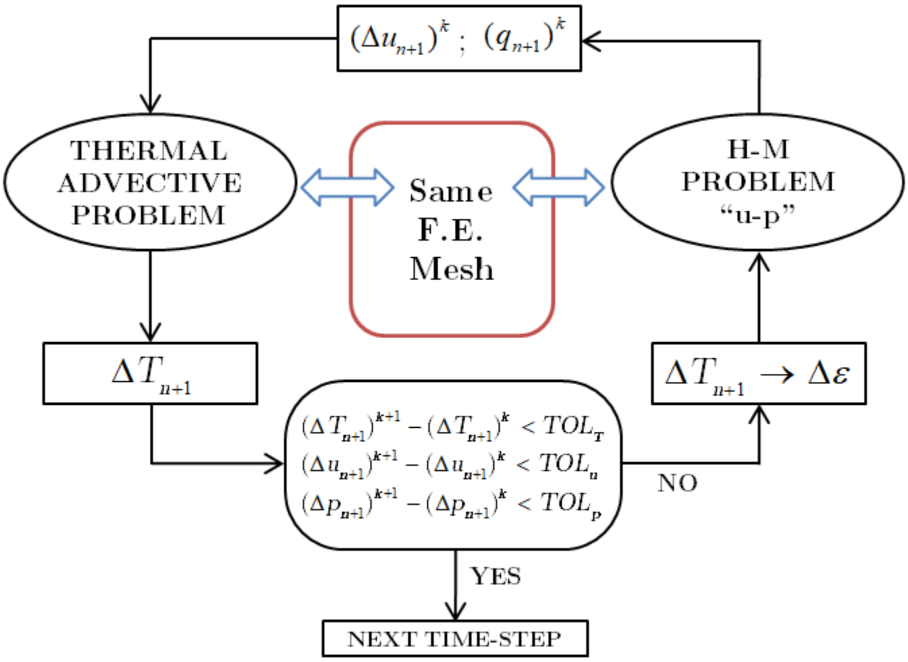

Figure 4.2: Scheme of the staggered approach for the THM coupling.

4.3. Thermo-Hydro-Mechanical fully coupled formulation

The monolithic or fully coupled scheme consists in a procedure that numerically solves simultaneously the whole system of coupled (thermal, hydro and mechanical) equations. Thus, the displacements, fluid pressures and temperatures at the nodes are obtained simultaneously.

This section presents the THM advective fully coupled formulation for continuum medium and zero-thickness interface elements using the FEM and the FDM for the spatial and time discretization, respectively.

4.3.1. THM formulation for continuum medium

In the following paragraphs, the THM advective fully coupled formulation for continuum media is presented, divided in four parts. The first three parts develop the mechanical, hydraulic and thermal formulations, respectively. The fourth part presents the solution of the non-linear THM fully coupled problem using a Newton-Raphson strategy.

Mechanical Formulation for continuum medium

The governing equation of the mechanical problem is the balance of linear momentum equation, which can be written, leaving out the acceleration terms, as follows:

$$[\mathbf{L}_{\mathbf{c}}^{u}]^{\top}\ \boldsymbol{\sigma} + \rho\ \mathbf{g} = 0 \tag{4.5}$$

where $\mathbf{L}_{\mathbf{c}}^{u}$ is a differential operator; $\boldsymbol{\sigma}$ is the total stresses tensor in Voigt notation; $\mathbf{g}$ is the gravity vector; ρ is the average density in which n is the porosity and ρ_s and ρ_f are the solid and fluid densities.

$$[\mathbf{L}_{\mathbf{c}}^{u}]^{\top} = \begin{pmatrix} \frac{\partial}{\partial x} & 0 & 0 & \frac{\partial}{\partial y} & 0 & \frac{\partial}{\partial z} \\ 0 & \frac{\partial}{\partial y} & 0 & \frac{\partial}{\partial x} & \frac{\partial}{\partial z} & 0 \\ 0 & 0 & \frac{\partial}{\partial z} & 0 & \frac{\partial}{\partial y} & \frac{\partial}{\partial x} \end{pmatrix} \tag{4.6}$$

$$\boldsymbol{\sigma} = (\sigma_x \quad \sigma_y \quad \sigma_z \quad \tau_{xy} \quad \tau_{yz} \quad \tau_{zx}\ )^{\top} \tag{4.7}$$

$$\mathbf{g} = (g_x \quad g_y \quad g_z\ )^{\top} \tag{4.8}$$

$$\rho = (1-n)\rho_s + n\ \rho_f \tag{4.9}$$

The boundary conditions associated with the linear momentum equation can be written as:

$$[\mathbf{n}_{\boldsymbol{\sigma}}]^{\top}\boldsymbol{\sigma} - \tilde{\mathbf{t}} = 0 \tag{4.10}$$

where $\tilde{\mathbf{t}}$ are the prescribed stress tractions on the boundary Γ_q and $\mathbf{n}_{\boldsymbol{\sigma}}$ is the operator defined as:

$$[\mathbf{n}_{\boldsymbol{\sigma}}]^\top = \begin{pmatrix} n_x & 0 & 0 & n_y & 0 & n_z \\ 0 & n_y & 0 & n_x & n_z & 0 \\ 0 & 0 & n_z & 0 & n_y & n_x \end{pmatrix} \tag{4.11}$$

where n_i are the components of the unit vector $\mathbf{n}$ normal to the boundary surface in the xyz system.

Performing the spatial discretization of Eq. (4.5) on the domain Ω by using the FEM, the nodal displacements can be approximated as:

$$u \cong \hat{u} = \sum_{a=1}^{n} N^{(a)}\ u^{(a)} = \mathbf{N}^u\ \mathbf{u} \tag{4.12}$$

where $\hat{u}$ is the approximate value of the nodal displacement, $u^{(a)}$ is the displacement value on the node (a), $N^{(a)}$ is the shape function value of the node (a) and n is the number of nodes of the element.

Eq. (4.5) represents the strong form of the governing differential equations of the problem and Eq. (4.10) the boundary conditions. Replacing the approximation $\hat{u}$ in Eqs. (4.5) and (4.10) leads to:

$$[\mathbf{L}_\mathbf{c}^u]^\top\ \widehat{\boldsymbol{\sigma}} + \rho\ \mathbf{g} = \boldsymbol{r}_{\boldsymbol{\Omega}} \qquad \text{on} \qquad \Omega \tag{4.13}$$

$$[\mathbf{n}_{\boldsymbol{\sigma}}]^\top\ \widehat{\boldsymbol{\sigma}} - \tilde{\mathbf{t}} = \boldsymbol{r}_{\boldsymbol{\Gamma}} \qquad \text{on} \qquad \Gamma_\mathrm{q} \tag{4.14}$$

where $\boldsymbol{r}_{\boldsymbol{\Omega}}$ and $\boldsymbol{r}_{\boldsymbol{\Gamma}}$ are the residuals from the finite element approximation and $\widehat{\boldsymbol{\sigma}}$ is the approximate value of the total stress tensor. For the Dirichlet boundary conditions it is assumed that the condition is satisfied on prescribed nodes ($\hat{u} = u$). Using the weighted residuals method to set $\boldsymbol{r}_{\boldsymbol{\Omega}}$ and $\boldsymbol{r}_{\boldsymbol{\Gamma}}$ to zero, the following integral expression is obtained:

$$\int_\Omega [\mathbf{w}]^\top \boldsymbol{r}_{\boldsymbol{\Omega}}\ \mathrm{d}\Omega + \int_{\Gamma_\mathrm{q}} [\overline{\mathbf{w}}]^\top \boldsymbol{r}_{\boldsymbol{\Gamma}}\ \mathrm{d}\Gamma = 0 \tag{4.15}$$

where $\mathbf{w}$ and $\overline{\mathbf{w}}$ are weight function vectors formed from the scalar weight functions as $\mathbf{w} = (w, w, w)$ and $\overline{\mathbf{w}} = (\overline{w}, \overline{w}, \overline{w})$. Substituting Eqs. (4.13) and (4.14) in (4.15), the weak form of the problem is obtained:

$$\int_\Omega [\mathbf{w}]^\top([\mathbf{L}_\mathbf{c}^u]^\top \boldsymbol{\sigma} + \rho\ \mathbf{g})\,\mathrm{d}\Omega + \int_{\Gamma_\mathrm{q}} [\overline{\mathbf{w}}]^\top\big([\mathbf{n}_{\boldsymbol{\sigma}}]^\top\ \boldsymbol{\sigma} - \tilde{\mathbf{t}}\big)\,\mathrm{d}\Gamma = 0 \tag{4.16}$$

Considering that the weight function is selected such that $\overline{\mathbf{w}} = -\mathbf{w}$**,** assuming that the unknown vector $\mathbf{u}$ is approximated by Finite Elements as shown in Eq. (4.12) and applying the Galerkin weighting repeatedly for $\mathbf{w}$ equal to each of the shape functions $N^{(a)}$, leads to:

$$\int_{\Omega} [\mathbf{N}^u]^\top ([\mathbf{L}_\mathbf{c}^u]^\top \boldsymbol{\sigma} + \rho\ \mathbf{g})\, \mathrm{d}\Omega - \int_{\Gamma_q} [\mathbf{N}^u]^\top \big([\mathbf{n}_{\boldsymbol{\sigma}}]^\top\ \boldsymbol{\sigma} - \tilde{\mathbf{t}}\big)\, \mathrm{d}\Gamma = 0 \tag{4.17}$$

And applying the Divergence Theorem described by Eq. (2.33) to the first term of the previous results:

$$-\int_{\Omega} [\mathbf{L}_\mathbf{c}^u\ \mathbf{N}^u]^\top\ \boldsymbol{\sigma}\ \ \mathrm{d}\Omega + \int_{\Omega} [\mathbf{N}^u]^\top\ \rho\ \mathbf{g}\ \ \mathrm{d}\Omega + \int_{\Gamma_q} [\mathbf{N}^u]^\top\ \tilde{\mathbf{t}}\ \ \mathrm{d}\Gamma = 0 \tag{4.18}$$

In order to consider the hydro-mechanical coupling, the efective stresses are written as:

$$\boldsymbol{\sigma} =\ \boldsymbol{\sigma}' - \alpha_{Biot}\ p\ \mathbf{m}_\mathbf{c} \tag{4.19}$$

where α_{Biot} is the Biot's Coefficient, p is the fluid pressure (negative in compression) and $\mathbf{m}_\mathbf{c}$ is the identity matrix in Voigt notation. Following the discretization made for the displacement field, the fluid preassure is approximated by:

$$p \cong \hat{p} = \sum_{a=1}^{n} N^{(a)}\ p^{(a)} = \mathbf{N}^p\ \mathbf{p} \tag{4.20}$$

where $\hat{p}$ is the approximate value of the nodal pressure, $p^{(a)}$ is the pressure value on the i node and $\mathbf{p}$ are the nodal pressures of the element.

Substituting Eqs. (4.19) and (4.20) into Eq. (4.18) and defining the deformation matrix ($\mathbf{B}^u = \mathbf{L}_\mathbf{c}^u\ \mathbf{N}^u$), results:

$$\int_{\Omega} [\mathbf{B}^u]^\top\ \boldsymbol{\sigma}'\, \mathrm{d}\Omega - \int_{\Omega} [\mathbf{B}^u]^\top \alpha_{Biot}\, \mathbf{N}^p\ \mathbf{p}\ \ [\mathbf{m}_\mathbf{c}]^\top\ \mathrm{d}\Omega = \int_{\Omega} [\mathbf{N}^u]^\top \rho\ \mathbf{g}\ \ \mathrm{d}\Omega + \int_{\Gamma_q} [\mathbf{N}^u]^\top\ \tilde{\mathbf{t}}\ \ \mathrm{d}\Gamma \tag{4.21}$$

which is the mechanic continuum equation.

In order to consider the thermo-mechanical coupling, the strain increment $\Delta\boldsymbol{\varepsilon}$ which is included in the stress tensor of the above equation has a thermal component and may be written as:

$$\Delta\boldsymbol{\varepsilon} = \Delta\boldsymbol{\varepsilon}^u - \Delta\boldsymbol{\varepsilon}^T \tag{4.22}$$

$$\Delta\boldsymbol{\varepsilon}^u = \mathbf{B}^u\ \Delta\mathbf{u} \tag{4.23}$$

$$\Delta\boldsymbol{\varepsilon}^T = \mathbf{m}_\mathbf{c}\ \alpha_s^T\ \Delta T \tag{4.24}$$

where α_s^T is the coefficient of thermal expansion of the solid [$^{\text{o}}C^{-1}$] and ΔT is temperature increment. Following the FEM discretization made for the displacement and pressure fields, the temperature increment is approximated by:

$$\mathit{\Delta} T \cong \mathit{\Delta}\hat{T} = \sum_{a=1}^{n} N^{(a)}\ \Delta T^{(a)} = \mathbf{N}^T\ \Delta\mathbf{T} \tag{4.25}$$

where $\Delta\hat{T}$ is the approximate value of the nodal pressure, $\Delta T^{(a)}$ is the pressure value on the node (a) and $\mathbf{\Delta T}$ are the nodal increment temperatures of the element.

Considering a linear elastic problem, the effective stress increment of Eq. (4.21) may be written as:

$$\Delta\boldsymbol{\sigma}' = \mathbf{D}_{tan}\Delta\boldsymbol{\varepsilon} = \mathbf{D}_{tan}\ \mathbf{B}^u\ \Delta\mathbf{u}\ - \mathbf{D}_{tan}\ \mathbf{m_c}\ \alpha_s^T\ \mathbf{N}^T\mathbf{\Delta T} \tag{4.26}$$

where $\mathbf{D}_{tan}$ is the tangent constitutive matrix for the considered increment.

The last step consists in the time discretization of the mechanical equation (4.21) using the FDM. The unknowns (x) are evaluated at time $(n+\theta)$ and the time derivatives are transformed into increments $(\Delta x_{n+\theta})$, assuming a linear variation of the unknowns within a time increment (Δt):

$$\begin{gathered} x_{n+\theta} = x_n + \theta\Delta x_n \\ \dot{x}_n = \frac{\Delta x_n}{\Delta t_{n+1}} \\ \Delta x_n = x_{n+\theta} - x_n \end{gathered} \tag{4.27}$$

Introducing the FDM time discretization defined by Eqs. (4.27) into Eq. (4.21) the final continuum mechanical equation (4.28) is reached:

Summary 7 - Mechanical continuum equation.

$$\int_\Omega [\mathbf{B}^u]^\top\ \boldsymbol{\sigma}'_{n+\theta}\ \mathrm{d}\Omega - \theta\ \mathbf{K_{up}}\ \Delta\mathbf{p}_{n+1} = \mathbf{f}^u_{\mathrm{e},n+\theta} + \mathbf{K_{up}}\ \mathbf{p}_n \tag{4.28}$$

where $\mathbf{K_{up}}$ is the hydro-mechanical coupling element matrix and $\mathbf{f^u_e}$ is the element vector of external forces:

$$\mathbf{K_{up}} = \int_\Omega [\mathbf{B}^u]^\top\ \alpha_{Biot}\ [\mathbf{m_c}]^\top\ \mathbf{N}^p\ \mathrm{d}\Omega \tag{4.29}$$

$$\mathbf{f}^u_\mathrm{e} = \int_\Omega [\mathbf{N}^u]^\top \rho\ \mathbf{g}\ \mathrm{d}\Omega + \int_{\Gamma_\mathrm{q}} [\mathbf{N}^u]^\top\ \tilde{\mathbf{t}}\ \mathrm{d}\Gamma \tag{4.30}$$

Hydraulic Formulation for continuum medium

The governing equation of the hydraulic problem is the fluid mass balance equation, which may be written for the HM coupled problem for porous medium (Garolera, 2017) in the following form:

$$\frac{1}{M^{Biot}}\frac{\partial p}{\partial t} + \alpha_{Biot}[\boldsymbol{\nabla}]^\top\mathbf{v}^s + [\boldsymbol{\nabla}]^\top\left[\frac{\mathbf{k}^p}{\mu}(-\boldsymbol{\nabla}p + \rho^f\ \mathbf{g})\right] = 0 \tag{4.31}$$

where p is the fluid pressure, M^{Biot} is the Biot's modulus, α_{Biot} is the Biot's coefficient, $\mathbf{k}^p$ is the hydraulic permeability, μ is the dynamic viscosity of the fluid, ρ^f is the fluid density, $\mathbf{g} = [0 \quad 0 \quad -9.8]^\top$ is the gravity vector, $\boldsymbol{\nabla} = \left[\frac{\partial}{\partial x} \quad \frac{\partial}{\partial y} \quad \frac{\partial}{\partial z}\right]^\top$, $\mathbf{v}^s$ is the solid velocity given in Eq. (4.33), $\mathbf{L}^u_\mathbf{c}$ is the differential operator given in Eq. (4.6), $\mathbf{m_c}$ is the identity matrix in Voigt notation, K^s is the compressibility modulus of the solid, K^f is the compressibility modulus of the fluid and n is the porosity.

$$\frac{1}{M^{Biot}} = \left(\frac{\alpha_{Biot} - n}{K^s} + \frac{n}{K^f}\right) \tag{4.32}$$

$$[\boldsymbol{\nabla}]^\top \mathbf{v}^s = [\mathbf{m_c}]^\top \frac{\partial \boldsymbol{\epsilon}}{\partial t} = [\mathbf{m_c}]^\top \ \mathbf{L}^u_\mathbf{c} \frac{\partial \mathbf{u}}{\partial t} \tag{4.33}$$

In saturated porous media it is important to consider the volume changes due to the effect of thermal expansions, which modify the available space for fluid storage, as explained in section 4.1.1. Under free thermal expansion, the volumetric strain increment of the solid due to thermal effects is:

$$\varepsilon^T_{v,solid} = \alpha^T_{v,s} \Delta T \tag{4.34}$$

where $\alpha^T_{v,s}$ is the volumetric coefficient of thermal expansion of the solid that, assuming small strains, may be obtained from the linear coefficient of thermal expansion as:

$$\alpha^T_{v,s} \approx 3\alpha^T_s \tag{4.35}$$

From this equation the volumetric strain rate in the solid may be written as:

$$\frac{\partial \varepsilon^T_{v,solid}}{\partial t} = \alpha^T_{v,s} \frac{\partial T}{\partial t} \tag{4.36}$$

Since the thermal deformation is considered to be homothetic, with equal thermal strains for the solid and the pores, it is assumed that the strain rate in the pores is the fraction of the corresponding strain rate in the solid according to the porosity:

$$\frac{\partial \varepsilon^T_{v,pores}}{\partial t} = n \frac{\partial \varepsilon^T_{v,solid}}{\partial t} = n \ \alpha^T_{v,s} \frac{\partial T}{\partial t} \tag{4.37}$$

If there are restrictions to free thermal expansion and the final deformation is equal to the result of the combination of thermal free deformations and the deformations due to the effective stress changes, the volumetric strain rate of the solid due to such stress changes may be expressed as:

$$\frac{\partial \varepsilon^M_{v,solid}}{\partial t} = \alpha_{Biot} \left([\boldsymbol{\nabla}]^\top \mathbf{v}^s - \alpha^T_{v,s} \frac{\partial T}{\partial t} \right) \tag{4.38}$$

The total variation of pore volume due to both simultaneous changes in temperature and stresses is the sum of Eqs. (4.37) and (4.38):

$$\frac{\partial \varepsilon_v^{T+M}}{\partial t} = n\ \alpha_{v,s}^T \frac{\partial T}{\partial t} + \alpha_{Biot} \left([\boldsymbol{\nabla}]^\top \mathbf{v}^s - \alpha_{v,s}^T \frac{\partial T}{\partial t} \right) \tag{4.39}$$

Additionally, it is important to consider the volume change of the fluid itself due to thermal effects. As the fluid is only present in the pores of the material, the volumetric strain rate of the fluid is:

$$\frac{\partial \varepsilon_{v,fluid}^T}{\partial t} = n\ \alpha_{v,f}^T \frac{\partial T}{\partial t} \tag{4.40}$$

where $\alpha_{v,f}^T$ is the volumetric coefficient of thermal expansion of the fluid filling the pores.

Finally, the combination of the volumetric strain rate of the pores, the solid and the fluid, defined by Eqs. (4.39) and (4.40), leads to the final volumetric strain rate due to thermal effects:

$$\frac{\partial \varepsilon_v^{T+M}}{\partial t} + \frac{\partial \varepsilon_{v,fluid}^T}{\partial t} = \{(n - \alpha_{Biot}\ )\alpha_{v,s}^T + n\ \alpha_{v,f}^T\} \frac{\partial T}{\partial t} + \alpha_{Biot} [\boldsymbol{\nabla}]^\top \mathbf{v}^s \tag{4.41}$$

where the second term of the right-hand side already existed in the traditional Biot formulation, and the new term due to temperature changes is:

$$\frac{\partial \varepsilon_v^T}{\partial t} = \alpha_{eq}^T \frac{\partial T}{\partial t} \tag{4.42}$$

where α_{eq}^T is an equivalent coefficient of thermal expansion for the hydraulic problem:

$$\alpha_{eq}^T = (n - \alpha_{Biot})\alpha_{v,s}^T + n\ \alpha_{v,f}^T \tag{4.43}$$

This term has to be added to the fluid mass balance equation (4.31), leading to the new fluid mass balance equation for the THM coupled problem in continuum porous medium:

$$\frac{1}{M^{Biot}} \frac{\partial p}{\partial t} + \alpha_{eq}^T \frac{\partial T}{\partial t} + \alpha_{Biot} [\boldsymbol{\nabla}]^\top \mathbf{v}^s + [\boldsymbol{\nabla}]^\top \left[\frac{\mathbf{k}^p}{\mu(T)} (-\boldsymbol{\nabla} p + \rho^f\ \mathbf{g}) \right] = 0 \tag{4.44}$$

where the dynamic viscosity of the fluid $\mu(T)$ also depends on the temperature and is given in Eq. (4.2) for water.

Eq. (4.44) is similar to Eq. 2.20 (pp45) of Lewis & Schrefler (1998) but considering saturated porous media, a single phase of water and constant fluid density.

There are two kinds of boundary conditions applicable to the transient Eq. (4.44). The first is the Dirichlet boundary condition, in which the values of pressure $\bar{p}$ are imposed on a boundary Γ_ϕ (Eq. (4.45)). The second is the Neumann boundary condition, in which a normal prescribed flow $\bar{q}_N^p$ is imposed on a boundary Γ_q (Eq. (4.46)).

$$p = \bar{p}(x, y, z, t) \qquad \text{on} \qquad \Gamma_\phi \tag{4.45}$$

$$[\mathbf{n}]^\top \frac{\mathbf{k}^p}{\mu(T)}(-\boldsymbol{\nabla} p + \rho^f \mathbf{g}) - \bar{q}_N^p = 0 \qquad \text{on} \qquad \Gamma_\mathrm{q} \tag{4.46}$$

Using the weighted residuals method to set r_Ω and r_Γ to zero, the following integral expression is obtained:

$$\int_\Omega w\, r_\Omega \; \mathrm{d}\Omega + \int_{\Gamma_\mathrm{q}} \overline{w}\, r_\Gamma \; \mathrm{d}\Gamma = 0 \tag{4.47}$$

where w and $\overline{w}$ are weight functions. Substituting Eqs. (4.45) and (4.46) in (4.47), the weak form of the problem is obtained:

$$\begin{aligned}
&\int_\Omega w \left(\frac{1}{M^{Biot}}\frac{\partial p}{\partial t}\right) \mathrm{d}\Omega + \int_\Omega w \left(\alpha_{eq}^T \frac{\partial T}{\partial t}\right) \mathrm{d}\Omega + \int_\Omega w \left(\alpha_{Biot}\; [\mathbf{m_c}]^\top\; \mathbf{L_c}^u \frac{\partial \mathbf{u}}{\partial t}\right) \mathrm{d}\Omega \\
&\qquad + \int_\Omega w \left([\boldsymbol{\nabla}]^\top \left[\frac{\mathbf{k}^p}{\mu(T)}(-\boldsymbol{\nabla} p + \rho^f \mathbf{g})\right]\right) \mathrm{d}\Omega \\
&\qquad + \int_{\Gamma_\mathrm{q}} \overline{w} \left([\mathbf{n}]^\top \frac{\mathbf{k}^p}{\mu(T)}(-\boldsymbol{\nabla} p + \rho^f \mathbf{g}) - \bar{q}_N^p\right) \mathrm{d}\Gamma = 0
\end{aligned} \tag{4.48}$$

Introducing the approximate values of nodal displacements, pressures and temperatures given by Eqs. (4.12), (4.20) and (4.25), applying the Divergence Theorem defined by Eq. (2.33) to the first term of the equation, applying the Galerkin weighting ($w = N^{p\,(1)}, N^{p\,(2)}, \ldots$) and considering that $w = 0$ on Γ_ϕ and $\overline{w} = -w$ on Γ_q, the following equation is obtained:

$$\begin{aligned}
&\int_\Omega [\boldsymbol{\nabla}]^\top \mathbf{N}^p \frac{\mathbf{k}^p}{\mu(T)} \boldsymbol{\nabla}\mathbf{N}^p\, \mathbf{p}\; \mathrm{d}\Omega + \int_\Omega \mathbf{N}^p \alpha_{Biot}\; [\mathbf{m_c}]^\top\; \mathbf{B}^u \frac{\partial \mathbf{u}}{\partial t}\; \mathrm{d}\Omega \\
&\qquad - \int_\Omega [\boldsymbol{\nabla}]^\top \mathbf{N}^p\; \mathbf{k}^p \frac{\rho^f}{\mu\,(T)}\; \mathbf{g}\, \mathrm{d}\Omega \; + \int_\Omega \mathbf{N}^p \frac{1}{M^{Biot}} [\mathbf{N}^p]^\top\; \frac{\partial \mathbf{p}}{\partial t} \mathrm{d}\Omega \\
&\qquad + \int_\Omega \mathbf{N}^T \alpha_{eq}^T [\mathbf{N}^T]^\top\; \frac{\partial \mathbf{T}}{\partial t} \mathrm{d}\Omega \; + \int_{\Gamma_\mathrm{q}} \mathbf{N}^p\; \bar{q}_N^p\, \mathrm{d}\Gamma = 0
\end{aligned} \tag{4.49}$$

where the fluid dynamic viscosity is approximated by:

$$\frac{1}{\mu(T)} = \frac{1}{\mu_0(T)}\; \mathrm{e}^{b\, \mathbf{N}^T \mathbf{T}} \tag{4.50}$$

where μ_0 and b are the coefficients defined in Eq. (4.2).

The last step consists in the time discretization of the hydraulic equation (4.49) using the FDM. Additionally, the linearization of Eq. (4.50) may be developed using the first term of the Taylor expansion, obtaining:

$$
\begin{aligned}
\frac{1}{\mu(T)} &= \frac{1}{\mu_0 \mathrm{e}^{-b\mathbf{N}^T\mathbf{T}_n}} \mathrm{e}^{b\theta\mathbf{N}^T\Delta\mathbf{T}_{n+1}} = \frac{1}{\mu_n}\mathrm{e}^{b\theta\mathbf{N}^T\Delta\mathbf{T}_{n+1}} \\
\frac{1}{\mu(T)} &\approx \frac{1}{\mu_n}(1+\mathrm{b}\theta\mathbf{N}^T\Delta\mathbf{T}_{n+1})
\end{aligned}
\tag{4.51}
$$

Finally, introducing the FDM time discretization defined in Eq. (4.27) into Eq. (4.49) and substituting Eq. (4.51) the final continuum hydraulic equation (4.52) is reached:

Summary 8 - Hydraulic continuum equation.

$$
\begin{aligned}
(\mathbf{S}_{\mathbf{p}} + \theta\Delta t_{n+1}\mathbf{K}_{\mathbf{pp}})\Delta\mathbf{p}_{n+1} + (\mathbf{S}_{\mathbf{pT}} + \theta\Delta t_{n+1}\mathbf{K}_{\mathbf{pT}})\Delta\mathbf{T}_{n+1} + [\mathbf{K}_{\mathbf{pu}}]^\top\Delta\mathbf{u}_{n+1} \\
= \Delta t_{n+1}\mathbf{f}^p_{\mathrm{e}} - \Delta t_{n+1}\mathbf{K}_{\mathbf{pp}}\,\mathbf{p}_n
\end{aligned}
\tag{4.52}
$$

where $\mathbf{K}_{\mathbf{pp}}$ is the element hydraulic diffusion matrix, $\mathbf{S}_{\mathbf{p}}$ is the element hydraulic capacity matrix, $\mathbf{K}_{\mathbf{pu}}$ is the element hydro-mechanical coupling matrix, $\mathbf{K}_{\mathbf{pT}}$ is the element thermo-hydraulic coupling matrix and $\mathbf{f}^p_{\mathrm{e}}$ is the element vector of external forces:

$$
\mathbf{S}_{\mathbf{p}} = \int_\Omega \mathbf{N}^p \frac{1}{M^{Biot}}[\mathbf{N}^p]^\top \,\mathrm{d}\Omega \tag{4.53}
$$

$$
\mathbf{K}_{\mathbf{pp}} = \int_\Omega [\boldsymbol{\nabla}]^\top\mathbf{N}^p \frac{\mathbf{k}^p}{\mu_n}\boldsymbol{\nabla}\mathbf{N}^p \;\mathrm{d}\Omega \tag{4.54}
$$

$$
\mathbf{S}_{\mathbf{pT}} = \int_\Omega \mathbf{N}^p\;\alpha^T_{eq}[\mathbf{N}^p]^\top \,\mathrm{d}\Omega \tag{4.55}
$$

$$
\mathbf{K}_{\mathbf{pT}} = b\int_\Omega [\boldsymbol{\nabla}]^\top\mathbf{N}^p\frac{\mathbf{k}^p}{\mu_n}\boldsymbol{\nabla}\mathbf{N}^p\mathbf{p}_n\;\mathbf{N}^T\,\mathrm{d}\Omega - b\int_\Omega [\boldsymbol{\nabla}]^\top\mathbf{N}^p\;\mathbf{k}^p\frac{\rho^f}{\mu_n}\mathbf{g}\;\mathbf{N}^T\,\mathrm{d}\Omega \tag{4.56}
$$

$$
\mathbf{K}_{\mathbf{pu}} = \int_\Omega [\mathbf{N}^p]^\top\alpha_{Biot}\,[\mathbf{m}_{\mathbf{c}}]^\top\;\mathbf{B}^u\;\mathrm{d}\Omega \tag{4.57}
$$

$$
\mathbf{f}^p_{\mathrm{e}} = \int_\Omega [\boldsymbol{\nabla}]^\top\mathbf{N}^p\;\mathbf{k}^p\frac{\rho^f}{\mu_n}\;\mathbf{g}\,\mathrm{d}\Omega - \int_{\Gamma_{\mathrm{q}}}\mathbf{N}^p\;\bar{q}^{\,p}_N\,\mathrm{d}\Gamma \tag{4.58}
$$

$$
\mu_n = \mu_0\;\mathrm{e}^{-b\;\mathbf{N}^T\mathbf{T}_n} \tag{4.59}
$$

Thermal Formulation for continuum medium

The thermal advective equation developed in Section 2.2.3 (α-Implicit Characteristic Galerkin method) may be written from Eq. (2.156) – leaving out source terms - as follows:

$$\begin{aligned}
&\rho c \frac{1}{\Delta t_{n+1}} (\Delta T_{n+1}) \\
&\qquad = -(1-\alpha)\rho c \left[\mathbf{q}^p_{n+1/2}\right]^\top \boldsymbol{\nabla} T_n \\
&\qquad + \frac{(1-\alpha)^2}{2}\rho c\ \Delta t_{n+1}\left[\mathbf{q}^p_{n+1/2}\right]^\top \mathbf{q}^p_{n+1/2}\boldsymbol{\nabla}^2 T_n - \alpha\rho c\ \left[\mathbf{q}^p_{n+1/2}\right]^\top \boldsymbol{\nabla} T_{n+1} \\
&\qquad - \frac{\alpha^2}{2}\rho c \Delta t_{n+1}\left([\boldsymbol{\nabla}]^\top \mathbf{q}^p_{n+1/2}\right)\left(\left[\mathbf{q}^p_{n+1/2}\right]^\top \boldsymbol{\nabla} T_{n+1}\right) + \theta\ [\boldsymbol{\nabla}]^\top(\mathbf{k}^T\ \boldsymbol{\nabla} T_{n+1}) \\
&\qquad + (1-\theta)[\boldsymbol{\nabla}]^\top(\mathbf{k}^T\ \boldsymbol{\nabla} T_n)
\end{aligned} \tag{4.60}$$

where T_n and T_{n+1} are the temperature values for times n and $n+1$, ρ, c and $\mathbf{k}^T$ are the density, the specific heat and the thermal conductivity of the medium where the heat transfer occurs (which may be defined in the same form as in Eq. (4.9)) and $\mathbf{q}^p_{n+1/2}$ are the Darcy's velocities from the hydraulic problem which may be written from Eq. (2.154) as:

$$\mathbf{q}^p_{n+1/2} \approx \bar{\mathbf{q}} = \mathbf{q}^p_n + \frac{1}{2}\Delta\mathbf{q}^p_{n+1} \tag{4.61}$$

where $\mathbf{q}^p_n$ is Darcy's velocity of the previous time-step (known) and $\Delta\mathbf{q}^p_{n+1}$ may be written from Eq. (4.31) as:

$$\Delta\mathbf{q}^p_{n+1} = \mathbf{k}^p\left\{\frac{1}{\mu_n}(-\boldsymbol{\nabla}\Delta p_{n+1}) + \frac{1}{\Delta\mu_{n+1}}(-\boldsymbol{\nabla}\Delta p_{n+1}) + \frac{1}{\Delta\mu_{n+1}}(-\boldsymbol{\nabla} p_n) + \frac{1}{\Delta\mu_{n+1}}\mathbf{g}\right\} \tag{4.62}$$

where Δp_{n+1} is the increment of fluid pressure for the current time-step, p_n is the fluid pressure of the previous time-step, $\mathbf{k}^p$ is the hydraulic permeability, μ_n is the dynamic viscosity at time n defined by Eq. (4.59) and $\Delta\mu_{n+1}$ is the increment of dynamic viscosity of the current time-step defined by Eq. (4.51).

Performing the spatial discretization of Eq. (4.60) using the FEM (Eq. (2.27)), applying the Divergence Theorem to the diffusion terms and the standard Galerkin weighting ($w = N^{T(1)}, N^{T(2)}, \ldots$) results in:

$$\begin{aligned}
&\left(\frac{1}{\Delta t_{n+1}}\mathbf{C_T} + \alpha\mathbf{K_v} + \frac{\alpha^2}{2}\mathbf{K_s} + \theta\mathbf{K_{TT-D}}\right)\Delta\mathbf{T}_{n+1} \\
&= -\left[\mathbf{K_{TT-D}} + \mathbf{K_v} + \left(\frac{1}{2} - \alpha\right)\mathbf{K_s}\right]\mathbf{T}_{\mathrm{e},n}
\end{aligned} \tag{4.63}$$

where $\mathbf{K_{TT-D}}$ is the element conductivity matrix, $\mathbf{C_T}$ is the element thermal capacity matrix, $\mathbf{K_v}$ is the element advective matrix and $\mathbf{K_s}$ is the element stabilization matrix which results from the aplication of the α-Implicit Characteristic Galerkin method, with components:

$$C_T^{(a,b)} = \int_\Omega \rho c \; N^{T(a)} N^{T(b)} \, \mathrm{d}\Omega \tag{4.64}$$

$$K_{TT-D}^{(a,b)} = \int_\Omega \left[\boldsymbol{\nabla} N^{T(a)}\right]^\top \mathbf{k}^T \; \boldsymbol{\nabla} N^{T(b)} \, \mathrm{d}\Omega \tag{4.65}$$

$$K_v^{(a,b)} = \int_\Omega \rho c \; N^{T(a)} \left[\mathbf{q}^p_{n+1/2}\right]^\top \boldsymbol{\nabla} N^{T(b)} \, \mathrm{d}\Omega \tag{4.66}$$

$$K_s^{(a,b)} = \Delta t_{n+1} \int_\Omega \rho c \left(\left[\mathbf{q}^p_{n+1/2}\right]^\top \boldsymbol{\nabla} N^{T(a)} \right) \left(\left[\mathbf{q}^p_{n+1/2}\right]^\top \boldsymbol{\nabla} N^{T(b)} \right) \mathrm{d}\Omega \tag{4.67}$$

The spatial and time discretization (using the FEM and the FDM, respectively) must be applied to Eq. (4.62), resulting in:

$$\begin{aligned} \Delta \mathbf{q}^p_{n+1} = & -\frac{\mathbf{k}^p}{\mu_n} \boldsymbol{\nabla} N^{p(c)} \Delta p_{n+1}^{(c)} - b\theta \; \frac{\mathbf{k}^p}{\mu_n} \boldsymbol{\nabla} N^{p(e)} N^{T(d)} \Delta p_{n+1}^{(e)} \Delta T_{n+1}^{(d)} \\ & + \theta \; b \frac{\mathbf{k}^p}{\mu_n} \left\{ -\boldsymbol{\nabla} N^{p(c)} p_n^{(c)} + \rho^f \mathbf{g} \right\} N^{T(d)} \Delta T_{n+1}^{(d)} \end{aligned} \tag{4.68}$$

where b is defined in Eq. (4.2) and μ_n is the fluid viscosity at the previous time-step defined in Eq. (4.59). Introducing Eqs. (4.61) and (4.68) into Eq. (4.66) and leaving out the second-order terms $\Delta p_{\mathrm{n+1}} \Delta T_{\mathrm{n+1}}$ of Eq. (4.66) results in the following expression for the right-hand side of Eq. (4.63):

$$\begin{aligned} K_v^{(a,b)} T_n^{(b)} = & \int_\Omega \rho c \; N^{T(a)} \left[\mathbf{q}^p_n + \frac{1}{2} \Delta \mathbf{q}^p_{n+1} \right]^\top \boldsymbol{\nabla} N^{T(b)} \, \mathrm{d}\Omega \; T_n^{(b)} \\ = & \int_\Omega \rho c \; N^{T(a)} \; \left[\mathbf{q}^p_n\right]^\top \; \boldsymbol{\nabla} N^{T(b)} \, \mathrm{d}\Omega \; T_n^{(b)} \\ & - \frac{1}{2} \int_\Omega \rho c \; N^{T(a)} \left[\boldsymbol{\nabla} N^{T(b)} T_n^{(b)} \right]^\top \frac{\mathbf{k}^p}{\mu_n} \boldsymbol{\nabla} N^{p(c)} \, \mathrm{d}\Omega \; \Delta p_{n+1}^{(c)} \\ & + \frac{\theta}{2} \int_\Omega \rho c \; N^{T(a)} \left[\boldsymbol{\nabla} N^{T(b)} T_n^{(b)} \right]^\top \frac{\mathbf{k}^p}{\mu_n} b \Big\{ -\boldsymbol{\nabla} N^{p(c)} p_n^{(c)} \\ & + \rho^f \mathbf{g} \Big\} N^{T(d)} \mathrm{d}\Omega \; \Delta T_{n+1}^{(d)} \end{aligned} \tag{4.69}$$

and the following expression for the left-hand side of Eq. (4.63):

$$\begin{aligned} K_v^{(a,b)} \Delta T_{n+1}^{(b)} = & \int_\Omega \rho c \; N^{T(a)} \left[\mathbf{q}^p_n + \frac{1}{2} \Delta \mathbf{q}^p_{n+1} \right]^\top \boldsymbol{\nabla} N^{T(b)} \, \mathrm{d}\Omega \; \Delta T_{n+1}^{(b)} \\ = & \int_\Omega \rho c \; N^{T(a)} \; \left[\mathbf{q}^p_n\right]^\top \; \boldsymbol{\nabla} N^{T(b)} \, \mathrm{d}\Omega \; \Delta T_{n+1}^{(b)} \end{aligned} \tag{4.70}$$

where the second-order terms $\Delta T_{\mathrm{n+1}} \; \Delta p_{\mathrm{n+1}}$ have been left out.

In order to introduce the hydro-thermal coupling into Eq. (4.67) the subsequent development must be made:

$$\begin{aligned}\mathbf{q}^p_{n+1/2}\,\left[\mathbf{q}^p_{n+1/2}\right]^\top &= \left[\mathbf{q}^p_n + \frac{1}{2}\Delta\mathbf{q}^p_{n+1}\right]\left[\mathbf{q}^p_n + \frac{1}{2}\Delta\mathbf{q}^p_{n+1}\right]^\top \\ &= \mathbf{q}^p_n\,[\mathbf{q}^p_n]^\top + \frac{1}{2}\mathbf{q}^p_n[\Delta\mathbf{q}^p_{n+1}]^\top + \frac{1}{2}\Delta\mathbf{q}^p_{n+1}[\mathbf{q}^p_n]^\top + \frac{1}{4}\Delta\mathbf{q}^p_{n+1}[\Delta\mathbf{q}^p_{n+1}]^\top\end{aligned} \tag{4.71}$$

where the last term of the above expansion is of second-order and can be left out. Introducing Eqs. (4.61) and (4.68) into Eq. (4.67) results in the following expression for the right-hand side of Eq. (4.63):

$$\begin{aligned}K_{\mathrm{s}}^{(a,b)}T_n^{(b)} = \Delta t_{n+1}\int_\Omega \rho c\left(\left[\mathbf{q}^p_n + \frac{1}{2}\Delta\mathbf{q}^p_{n+1}\right]^\top \boldsymbol{\nabla}N^{T(a)}\right)\Bigg(\Bigg[\mathbf{q}^p_n \\ + \frac{1}{2}\Delta\mathbf{q}^p_{n+1}\Bigg]^\top \boldsymbol{\nabla}N^{T(b)}\Bigg)\,\mathrm{d}\Omega\;T_n^{(b)} \\ = \Delta t_{n+1}\int_\Omega \rho c\left([\mathbf{q}^p_n]^\top\boldsymbol{\nabla}N^{T(a)}\right)\left([\mathbf{q}^p_n]^\top\boldsymbol{\nabla}N^{T(b)}T_n^{(b)}\right)\mathrm{d}\Omega \\ -\frac{1}{2}\Delta t_{n+1}\int_\Omega \rho c\left(\left[\boldsymbol{\nabla}N^{T(a)}\right]^\top\frac{\mathbf{k}^p}{\mu_n}\boldsymbol{\nabla}N^{p(c)}\right)\left([\mathbf{q}^p_n]^\top\boldsymbol{\nabla}N^{T(b)}T_n^{(b)}\right)\mathrm{d}\Omega\;\Delta p_{n+1}^{(c)} \\ +\frac{\theta}{2}\Delta t_{n+1}\int_\Omega \rho c\Bigg(\left[\boldsymbol{\nabla}N^{T(a)}\right]^\top\frac{\mathbf{k}^p}{\mu_n}b\Big\{-\boldsymbol{\nabla}N^{p(c)}p_n^{(c)} \\ +\rho^f\mathbf{g}\Big\}N^{T(d)}\Bigg)\left([\mathbf{q}^p_n]^\top\boldsymbol{\nabla}N^{T(b)}T_n^{(b)}\right)\mathrm{d}\Omega\;\Delta T_{n+1}^{(d)} \\ -\frac{1}{2}\Delta t_{n+1}\int_\Omega \rho c\left([\mathbf{q}^p_n]^\top\boldsymbol{\nabla}N^{T(b)}T_n^{(b)}\right)\left(\left[\boldsymbol{\nabla}N^{T(a)}\right]^\top\frac{\mathbf{k}^p}{\mu_n}\boldsymbol{\nabla}N^{p(c)}\right)\mathrm{d}\Omega\;\Delta p_{n+1}^{(c)} \\ +\frac{\theta}{2}\Delta t_{n+1}\int_\Omega \rho c\left([\mathbf{q}^p_n]^\top\boldsymbol{\nabla}N^{T(b)}T_n^{(b)}\right)\Bigg(\left[\boldsymbol{\nabla}N^{T(a)}\right]^\top\frac{\mathbf{k}^p}{\mu_n}b\Big\{-\boldsymbol{\nabla}N^{p(c)}p_n^{(c)} \\ +\rho^f\mathbf{g}\Big\}N^{T(d)}\Bigg)\mathrm{d}\Omega\;\Delta T_{n+1}^{(d)}\end{aligned} \tag{4.72}$$

and the following expression for the left-hand side of Eq. (4.63):

$$K_s^{(a,b)}\Delta T_{n+1}^{(b)} = \Delta t_{n+1}\int_\Omega \rho c\left([\mathbf{q}^p_n]^\top\boldsymbol{\nabla}N^{T(a)}\right)\left([\mathbf{q}^p_n]^\top\boldsymbol{\nabla}N^{T(b)}\right)\mathrm{d}\Omega\;\Delta T_{n+1}^{(b)} \tag{4.73}$$

where the second-order terms $\Delta p_{n+1}\Delta T_{n+1}$ are left out in the last equation.

Finally, substituting Eqs. (4.69)-(4.73) into Eq. (4.63) and leaving out the second-order terms $\Delta p_{n+1}\Delta T_{n+1}$, the final continuum thermal equation (4.74) is reached:

Summary 9 - Thermal continuum equation with advection (α-ICG method).

$$\begin{aligned}&\left[\frac{1}{\Delta t_{n+1}}\mathbf{C_T} + \alpha\mathbf{K_{TT-A}} + \frac{\alpha^2}{2}\mathbf{K_{TT-S}} + \theta\mathbf{K_{TT-D}} + \mathbf{K_{TT-A2}}\right.\\ &\qquad\left. + \left(\frac{1}{2} - \alpha\right)\mathbf{K_{TT-S2}}\right]\Delta\mathbf{T}_{n+1} + \left[\mathbf{K_{Tp-A}} + \left(\frac{1}{2} - \alpha\right)\mathbf{K_{Tp-S}}\right]\Delta\mathbf{p}_{n+1}\\ &\qquad = -\left[\mathbf{K_{TT-D}} + \mathbf{K_{TT-A}} + \left(\frac{1}{2} - \alpha\right)\mathbf{K_{TT-S}}\right]\mathbf{T}_n\end{aligned} \tag{4.74}$$

where $\mathbf{K_{TT-D}}$ is the thermal conductivity matrix, $\mathbf{C_T}$ is the thermal capacity matrix, $\mathbf{K_{TT-A}}$ is the advective matrix, $\mathbf{K_{TT-S}}$ is the stabilization matrix (which results from the aplication of the α-ICG method) and $\mathbf{K_{Tp-A}}$, $\mathbf{K_{Tp-S}}$, $\mathbf{K_{TT-A2}}$ and $\mathbf{K_{TT-S2}}$ are the hydro-thermal coupling matrices, with components:

$$C_T^{(a,b)} = \int_\Omega \rho c\; N^{T(a)} N^{T(b)}\,\mathrm{d}\Omega \tag{4.75}$$

$$K_{TT-D}^{(a,b)} = \int_\Omega \boldsymbol{\nabla} N^{T(a)}\;\mathbf{k}^T\;\boldsymbol{\nabla} N^{T(b)}\,\mathrm{d}\Omega \tag{4.76}$$

$$K_{TT-A}^{(a,b)} = \int_\Omega \rho c\; N^{T(a)}\;[\mathbf{q}_n^p]^\top\;\boldsymbol{\nabla} N^{T(b)}\,\mathrm{d}\Omega \tag{4.77}$$

$$K_{TT-S}^{(a,b)} = \Delta t_{n+1}\int_\Omega \rho c\left([\mathbf{q}_n^p]^\top\boldsymbol{\nabla} N^{T(a)}\right)\left([\mathbf{q}_n^p]^\top\boldsymbol{\nabla} N^{T(b)}\right)\mathrm{d}\Omega \tag{4.78}$$

$$K_{Tp-A}^{(a,c)} = -\frac{1}{2}\int_\Omega \rho c\; N^{T(a)}\left[\boldsymbol{\nabla} N^{T(b)} T_n^{(b)}\right]^\top\frac{\mathbf{k}^p}{\mu_n}\boldsymbol{\nabla} N^{p(c)}\,\mathrm{d}\Omega \tag{4.79}$$

$$K_{TT-A2}^{(a,d)} = \frac{\theta}{2}\int_\Omega \rho c\; N^{T(a)}\left[\boldsymbol{\nabla} N^{T(b)} T_n^{(b)}\right]^\top\frac{\mathbf{k}^p}{\mu_n} b\left\{-\boldsymbol{\nabla} N^{p(c)} p_n^{(c)} + \rho^f\mathbf{g}\right\}N^{T(d)}\mathrm{d}\Omega \tag{4.80}$$

$$\begin{aligned}K_{Tp-S}^{(a,c)} = -\frac{1}{2}\Delta t_{n+1}&\left[\int_\Omega \rho c\left(\left[\boldsymbol{\nabla} N^{T(a)}\right]^\top\frac{\mathbf{k}^p}{\mu_n}\boldsymbol{\nabla} N^{p(c)}\right)\left([\mathbf{q}_n^p]^\top\boldsymbol{\nabla} N^{T(b)} T_n^{(b)}\right)\mathrm{d}\Omega\right.\\ &\left. + \int_\Omega \rho c\left([\mathbf{q}_n^p]^\top\boldsymbol{\nabla} N^{T(b)} T_n^{(b)}\right)\left(\left[\boldsymbol{\nabla} N^{T(a)}\right]^\top\frac{\mathbf{k}^p}{\mu_n}\boldsymbol{\nabla} N^{p(c)}\right)\mathrm{d}\Omega\right]\end{aligned} \tag{4.81}$$

$$\begin{aligned}K_{TT-S2}^{(a,d)} = \frac{\theta}{2}\Delta t_{n+1}&\left[\int_\Omega \rho c\left(\left[\boldsymbol{\nabla} N^{T(a)}\right]^\top\frac{\mathbf{k}^p}{\mu_n} b\left\{-\boldsymbol{\nabla} N^{p(c)} p_n^{(c)}\right.\right.\right.\\ &\left.\left. + \rho^f\mathbf{g}\right\}N^{T(d)}\right)\left([\mathbf{q}_n^p]^\top\boldsymbol{\nabla} N^{T(b)} T_n^{(b)}\right)\mathrm{d}\Omega\\ &+ \int_\Omega \rho c\left([\mathbf{q}_n^p]^\top\boldsymbol{\nabla} N^{T(b)} T_n^{(b)}\right)\left(\left[\boldsymbol{\nabla} N^{T(a)}\right]^\top\frac{\mathbf{k}^p}{\mu_n} b\left\{-\boldsymbol{\nabla} N^{p(c)} p_n^{(c)}\right.\right.\\ &\left.\left.\left. + \rho^f\mathbf{g}\right\}N^{T(d)}\right)\mathrm{d}\Omega\;\right]\end{aligned} \tag{4.82}$$

$$\mu_n = \mu_0\;\mathrm{e}^{-b\,\mathbf{N}^T\mathbf{T}_n} \tag{4.83}$$

Fully coupled solution for continuum medium

The final fully-coupled THM system of equations for continuum medium may be written from Eqs. (4.28), (4.52) and (4.74) as follows:

Summary 10 - Fully-coupled THM system of equations in continuum medium.

$$-\int_{\Omega}[\mathbf{B}^u]^\top\boldsymbol{\sigma}'_{n+\theta}\,\mathrm{d}\Omega+\theta\,\mathbf{K}_{\mathbf{up}}\,\Delta\mathbf{p}_{n+1}+\mathbf{f}^u_{\mathrm{e},n+\theta}+\mathbf{K}_{\mathbf{up}}\,\mathbf{p}_n=0$$

$$\begin{aligned}&(\mathbf{S}_{\mathbf{p},n+\theta}+\theta\Delta t_{n+1}\mathbf{K}_{\mathbf{pp},n+\theta})\Delta\mathbf{p}_{n+1}+(\mathbf{S}_{\mathbf{pT}}+\theta\Delta t_{n+1}\mathbf{K}_{\mathbf{pT}})\Delta\mathbf{T}_{n+1}\\&\quad+[\mathbf{K}_{\mathbf{pu}}]^\top\,\Delta\mathbf{u}_{n+1}-\Delta t_{n+1}\mathbf{f}^p_{\mathrm{e},n+\theta}+\Delta t_{n+1}\mathbf{K}_{\mathbf{pp},n+\theta}\,\mathbf{p}_n=0\end{aligned}$$

$$\begin{aligned}&\left[\frac{1}{\Delta t_{n+1}}\mathbf{C}_{n+\theta}+\alpha\mathbf{K}_{\mathbf{TT-A},n}+\frac{\alpha^2}{2}\mathbf{K}_{\mathbf{TT-S},n}+\theta\mathbf{K}_{\mathbf{TT-D},n+\theta}+\mathbf{K}_{\mathbf{TT-A2},n+\theta}\right.\\&\qquad\left.+\left(\frac{1}{2}-\alpha\right)\mathbf{K}_{\mathbf{TT-S2},n+\theta}\right]\Delta\mathbf{T}_{n+1}\\&\qquad+\left[\mathbf{K}_{\mathbf{Tp-A},n+\theta}+\left(\frac{1}{2}-\alpha\right)\mathbf{K}_{\mathbf{Tp-S},n+\theta}\right]\Delta\mathbf{p}_{n+1}\\&\qquad+\left[\mathbf{K}_{\mathbf{TT-D},n+\theta}+\mathbf{K}_{\mathbf{TT-A},n}+\left(\frac{1}{2}-\alpha\right)\mathbf{K}_{\mathbf{TT-S},n}\right]\Delta\mathbf{T}_n=0\end{aligned}\tag{4.84}$$

Due to the non-linearity of this system of equations, the Newton-Raphson (NR) iterative procedure is proposed in order to solve the THM fully-coupled problem. This method is well known and is described in detail in Zienkiewicz & Taylor (2000a, 2000b), or Smith & Griffths (2004). Moreover, Segura (2007) describes in detail the NR implementation for the fully-coupled hydro-mechanical problem.

The first step consists in the grouping of the nodal variables $(\mathbf{u},\mathbf{p},\mathbf{T})$ in a single vector of nodal variables $(\mathbf{x})$, both knows $\mathbf{x}_n$ and unknowns $\Delta\mathbf{x}_{n+1}$. The system of equations to be solved may be represented as the residual in the following form:

$$\boldsymbol{\Psi}_{n+\theta}(\mathbf{x}_n,\Delta\mathbf{x}_{n+1})=\begin{pmatrix}\boldsymbol{\Psi}^u_{n+\theta}\\\boldsymbol{\Psi}^p_{n+\theta}\\\boldsymbol{\Psi}^T_{n+\theta}\end{pmatrix}\tag{4.85}$$

$$\mathbf{x}_{\mathbf{n}}=\begin{pmatrix}\mathbf{u}\\\mathbf{p}\\\mathbf{T}\end{pmatrix}\qquad\qquad\Delta\boldsymbol{x}_{n+1}=\begin{pmatrix}\Delta\mathbf{u}\\\Delta\mathbf{p}\\\Delta\mathbf{T}\end{pmatrix}\tag{4.86}$$

This method develops the operator $\boldsymbol{\Psi}_{n+\theta}$, which is the residual defined in Eqs. (4.84), in a first order Taylor expansion around an estimate solution ${}^{i}\Delta\mathbf{x}_{n+1}$ as follows:

$$\boldsymbol{\Psi}_{n+\theta}(\mathbf{x}_n,{}^{i+1}\Delta\mathbf{x}_{n+1})\approx\boldsymbol{\Psi}_{n+\theta}(\mathbf{x}_n,{}^{i}\Delta\mathbf{x}_{n+1})+\mathbf{J}_{n+\theta}(\mathbf{x}_n,{}^{i}\Delta\mathbf{x}_{n+1})\,{}^{i+1}\delta\Delta\mathbf{x}_{n+1}\tag{4.87}$$

where

$$^{i+1}\Delta\mathbf{x}_{n+1} = {}^{i}\Delta\mathbf{x}_{n+1} + {}^{i+1}\delta\Delta\mathbf{x}_{n+1} \tag{4.88}$$

and $\mathbf{J}_{n+\theta}$ is the Jacobian matrix:

$$\mathbf{J}_{n+\theta}(\mathbf{x}_n, {}^{i}\Delta\mathbf{x}_{n+1}) = \left.\frac{\partial\boldsymbol{\Psi}_{n+\theta}}{\partial\Delta\mathbf{x}}\right|_{\mathbf{x}_n,{}^{i}\Delta\mathbf{x}_{n+1}} = \left.\begin{pmatrix} \dfrac{\partial\boldsymbol{\Psi}^u_{n+\theta}}{\partial\Delta\mathbf{u}} & \dfrac{\partial\boldsymbol{\Psi}^u_{n+\theta}}{\partial\Delta\mathbf{p}} & \dfrac{\partial\boldsymbol{\Psi}^u_{n+\theta}}{\partial\Delta\mathbf{T}} \\ \dfrac{\partial\boldsymbol{\Psi}^p_{n+\theta}}{\partial\Delta\mathbf{u}} & \dfrac{\partial\boldsymbol{\Psi}^p_{n+\theta}}{\partial\Delta\mathbf{p}} & \dfrac{\partial\boldsymbol{\Psi}^p_{n+\theta}}{\partial\Delta\mathbf{T}} \\ \dfrac{\partial\boldsymbol{\Psi}^T_{n+\theta}}{\partial\Delta\mathbf{u}} & \dfrac{\partial\boldsymbol{\Psi}^T_{n+\theta}}{\partial\Delta\mathbf{p}} & \dfrac{\partial\boldsymbol{\Psi}^T_{n+\theta}}{\partial\Delta\mathbf{T}} \end{pmatrix}\right|_{\mathbf{x}_n,{}^{i}\Delta\mathbf{x}_{n+1}} \tag{4.89}$$

The objective is to obtain a value of the unknowns so that the residual at the next iteration is zero. Consequently, $\boldsymbol{\Psi}_{n+\theta}(\mathbf{x}_n, {}^{i+1}\Delta\mathbf{x}_{n+1}) = 0$ is imposed, obtaining:

$$\mathbf{J}_{n+\theta}(\mathbf{x}_n, {}^{i}\Delta\mathbf{x}_{n+1})^{i+1}\delta\Delta\mathbf{x}_{n+1} = -\boldsymbol{\Psi}_{n+\theta}(\mathbf{x}_n, {}^{i}\Delta\mathbf{x}_{n+1}) \tag{4.90}$$

Therefore, given an initial estimate ${}^{0}\Delta\mathbf{x}_{n+1}$, the algorithm solves Eq. (4.90) until a certain tolerance is satisfied in ${}^{i+1}\delta\Delta\mathbf{x}_{n+1}$ or $\boldsymbol{\Psi}_{n+\theta}(\mathbf{x}_n, {}^{i}\Delta\mathbf{x}_{n+1})$, while the residual $\boldsymbol{\Psi}_{n+\theta}$ is the solution of Eq. (4.84) at the previous iteration (or the initial estimator at the first iteration).

It is important to note that the Jacobian matrix is obtained by using the linearized residual defined in Eqs. (4.84), while the residual is evaluated by using the non-linearized Eqs. (4.28), (4.49) and (4.63).

Finally, the components of the Jacobian matrix defined in Eq. (4.89) may be obtained as follows:

a) *Partial derivative of the mechanical equation with respect to the displacement increment*

$$\mathbf{J}_{\mathbf{uu}} = \frac{\partial\boldsymbol{\Psi}^u_{n+\theta}}{\partial\Delta\mathbf{u}} = \frac{\partial}{\partial\Delta\mathbf{u}}\left\{-\frac{1}{\theta}\int_\Omega [\mathbf{B}^u]^\top\ {}^{i}\boldsymbol{\sigma}'_{n+\theta}\ \mathrm{d}\Omega\right\} \tag{4.91}$$

Decomposing the stresses in its incremental form:

$${}^{i}\boldsymbol{\sigma}'_{n+\theta} = \boldsymbol{\sigma}'_n + \theta\ {}^{i}\boldsymbol{\sigma}'_{n+1} \tag{4.92}$$

and considering the tangent constitutive matrix ${}^{i}\mathbf{D}_{n+1}$ the stress increment may be developed as:

$${}^{i}\Delta\boldsymbol{\sigma}'_{n+1} = {}^{i}\mathbf{D}_{n+1}{}^{i}\Delta\boldsymbol{\varepsilon}_{n+1} = {}^{i}\mathbf{D}_{n+1}({}^{i}\Delta\boldsymbol{\varepsilon}^u_{n+1} - {}^{i}\Delta\boldsymbol{\varepsilon}^T_{n+1}) \tag{4.93}$$

$${}^{i}\Delta\boldsymbol{\sigma}'_{n+1} = {}^{i}\mathbf{D}_{n+1}\ \mathbf{B}^u\ {}^{i}\Delta\mathbf{u}_{n+1} - {}^{i}\mathbf{D}_{n+1}\mathbf{m_c}\ \alpha^T_s\ \mathbf{N}^T\ {}^{i}\Delta\mathbf{T}_{n+1} \tag{4.94}$$

Substituting Eqs. (4.92) and (4.93) into Eq. (4.91) the following is obtained:

$$\begin{aligned}\mathbf{J_{uu}} = \frac{\partial \mathbf{\Psi}^u_{n+\theta}}{\partial \Delta \mathbf{u}} = \frac{\partial}{\partial \Delta \mathbf{u}} \Bigg\{ & \left(-\int_\Omega [\mathbf{B}^u]^\top \, {}^i\mathbf{D}_{n+1} \, \mathbf{B}^u \, \mathrm{d}\Omega \right) {}^i\Delta \mathbf{u}_{n+1} \\ & + \left(\int_\Omega [\mathbf{B}^u]^\top \, {}^i\mathbf{D}_{n+1} \, \mathbf{m_c} \, \alpha_s^T \, \mathbf{N}^T \, \mathrm{d}\Omega \right) {}^i\Delta \mathbf{T}_{n+1} \Bigg\} = -{}^i\mathbf{K}_{\mathbf{uu},n+\theta}\end{aligned} \tag{4.95}$$

where

$${}^i\mathbf{K}_{\mathbf{uu},n+\theta} = \int_\Omega [\mathbf{B}^u]^\top \, {}^i\mathbf{D}_{n+1} \, \mathbf{B}^u \, \mathrm{d}\Omega \tag{4.96}$$

b) Partial derivative of the mechanical equation with respect to the fluid pressure increment

$$\mathbf{J_{up}} = \frac{\partial \mathbf{\Psi}^u_{n+\theta}}{\partial \Delta \mathbf{p}} = \mathbf{K_{up}} \tag{4.97}$$

c) Partial derivative of the mechanical equation with respect to the temperature increment

$$\mathbf{J_{ut}} = \frac{\partial \mathbf{\Psi}^u_{n+\theta}}{\partial \Delta \mathbf{T}} = {}^i\mathbf{K}_{\mathbf{uT},n+\theta} \tag{4.98}$$

where

$${}^i\mathbf{K}_{\mathbf{uT},n+\theta} = \int_\Omega [\mathbf{B}^u]^\top \, {}^i\mathbf{D}_{n+1} \, \mathbf{m_c} \, \alpha_s^T \, \mathbf{N}^T \, \mathrm{d}\Omega \tag{4.99}$$

d) Partial derivative of the hydraulic equation with respect to the displacement increment

$$\mathbf{J_{pu}} = \frac{\partial \mathbf{\Psi}^p_{n+\theta}}{\partial \Delta \mathbf{u}} = [\mathbf{K_{pu}}]^\top \tag{4.100}$$

e) Partial derivative of the hydraulic equation with respect to the fluid pressure increment

$$\mathbf{J_{pp}} = \frac{\partial \mathbf{\Psi}^p_{n+\theta}}{\partial \Delta \mathbf{p}} = {}^i\mathbf{S}_{\mathbf{p},n+\theta} + \theta \Delta t_{n+1} \, {}^i\mathbf{K_{pp}}_{n+\theta} \tag{4.101}$$

f) Partial derivative of the hydraulic equation with respect to the temperature increment

$$\mathbf{J_{pT}} = \frac{\partial \mathbf{\Psi}^p_{n+\theta}}{\partial \Delta \mathbf{T}} = {}^i\mathbf{S_{pT}} + \theta \Delta t_{n+1} \, {}^i\mathbf{K}_{\mathbf{pT},n+\theta} \tag{4.102}$$

g) Partial derivative of the thermal equation with respect to the displacement increment

$$\mathbf{J_{Tu}} = \frac{\partial \mathbf{\Psi}^T_{n+\theta}}{\partial \Delta \mathbf{u}} = 0 \tag{4.103}$$

h) Partial derivative of the thermal equation with respect to the fluid pressure increment

$$\mathbf{J}_{\mathbf{Tp}} = \frac{\partial \mathbf{\Psi}^{T}_{n+\theta}}{\partial \Delta \mathbf{p}} = {}^{i}\mathbf{K}_{\mathbf{Tp-A},n+\theta} + \left(\frac{1}{2} - \alpha\right) {}^{i}\mathbf{K}_{\mathbf{Tp-S},n+\theta} \tag{4.104}$$

i) Partial derivative of the thermal equation with respect to the temperature increment

$$\begin{aligned} \mathbf{J}_{\mathbf{TT}} = \frac{\partial \mathbf{\Psi}^{T}_{n+\theta}}{\partial \Delta \mathbf{T}} = \mathbf{C}_{n+\theta} + \alpha {}^{i}\mathbf{K}_{\mathbf{TT-A},n} + \frac{\alpha^2}{2} {}^{i}\mathbf{K}_{\mathbf{TT-S},n} + \theta {}^{i}\mathbf{K}_{\mathbf{TT-D},n+\theta} \\ + {}^{i}\mathbf{K}_{\mathbf{TT-A2},n+\theta} + \left(\frac{1}{2} - \alpha\right) {}^{i}\mathbf{K}_{\mathbf{TT-S2},n+\theta} \end{aligned} \tag{4.105}$$

4.3.2. THM formulation for zero-thickness interface elements

Next the THM advective fully-coupled formulation for double-nodded zero-thickness interface elements is presented in four parts. The first three parts develops the mechanical, hydraulic and thermal formulations, respectively. The fourth part presents the solution of the non-linear THM fully-coupled system using a Newton-Raphson strategy.

Mechanical Formulation for interfaces

As described for continuum media, the stress form of the mechanical problem follows the effective stress principle of Terzaghi as follows:

$$\boldsymbol{\sigma}'_J = \boldsymbol{\sigma}_J + \alpha_{Biot}\, \mathbf{m}_J\, \bar{p} \tag{4.106}$$

where α_{Biot} is the Biot's coefficient, $\bar{p}$ is the average fluid pressure at the mid-plane (negative in compression) and $\boldsymbol{\sigma}_J$ is the stress tensor at the mid-plane of the interfaces in the local orthogonal system $\{n, l_1, l_2\}$, which contains the normal and tangential components:

$$\boldsymbol{\sigma}_J = (\sigma_N, \tau_{l1}, \tau_{l2})^{\top} \tag{4.107}$$

It is important to note that, in interfaces, as the fluid pressure only affects the volumetric component, only the normal term of the stress tensor is affected. Thus, the identity matrix in *Voigt* notation $\mathbf{m}_J$ can be written as:

$$\mathbf{m}_J = (1 \quad 0 \quad 0)^{\top} \tag{4.108}$$

Moreover, the average fluid pressure at the mid-plane, considering the spatial discretization described in Eq. (3.11) may be written as:

$$\bar{p} = \mathbf{N}^{p}_{J}\, \widetilde{\mathbb{T}}^{p}_{\mathrm{L}} \mathbf{p}_{\mathrm{e}} \tag{4.109}$$

where $\mathbf{N}_J^p$ are the mid-plane shape functions of the interface element and $\widetilde{\mathbb{T}}_{\mathrm{L}}^p$ is the in-plane transference matrix, which assumes that the pressure at the mid-plane is the average of the pressure at the corresponding nodes of the element and may be written as:

$$\widetilde{\mathbb{T}}_{\mathrm{L}}^p = \frac{1}{2}\,[\mathbf{I}_m \;\; \mathbf{I}_m] \tag{4.110}$$

where m is the number of mid-plane nodes of the interface element and $\mathbf{I}_m$ is the $m \times m$ identity matrix.

In the interface elements used, the effective stress $\boldsymbol{\sigma}'_J$ and the relative displacements $\mathbf{r} = (r_N, r_{l1}, r_{l2})^\top$ are related with the mechanical constitutive law and in consequence, with the mechanical stiffness matrix $\mathbf{D}_J^u$. Due to the non-linear constitutive law used for the interface elements (Section 4.4), this relationship is written in incremental form:

$$d\boldsymbol{\sigma}'_J = \mathbf{D}_J^u \, d\mathbf{r} \tag{4.111}$$

where the increment of relative displacements $d\mathbf{r}$ can be written as:

$$d\mathbf{r} = \mathbf{R}_J \, \mathbf{N}_J^u \, \widetilde{\mathbb{T}}^u \, d\mathbf{u}_{\mathrm{e}} = \mathbf{B}_J \, d\mathbf{u}_{\mathrm{e}} \tag{4.112}$$

where $d\mathbf{u}_{\mathrm{e}}$ is the variation of nodal displacements of the interface element, $\mathbf{N}_J^u$ are the mid-plane shape functions of the interface element, $\widetilde{\mathbb{T}}^u$ is the transference matrix which converts the nodal displacements into jumps at the mid-plane nodes of the interface element, $\mathbf{R}_J$ is the rotation matrix that relates the xyz system with the local orthogonal system nl_1l_2 and $\mathbf{B}_J$ is the matrix that relates the relative displacements with the nodal displacements of the interface.

$$\mathbf{N}_J^u = \left(N_{mp}^{(1)} \;\; N_{mp}^{(2)} \; \ldots \; N_{mp}^{(m)}\right) \otimes \mathbf{I}_d \tag{4.113}$$

$$\widetilde{\mathbb{T}}^u = [-\mathbf{I}_m \;\; \mathbf{I}_m] \otimes \mathbf{I}_m \tag{4.114}$$

where $\mathbf{I}_d$ is the $d \times d$ identity matrix with $d = 2$ for 2-D problems and $d = 3$ for 3-D problems.

In order to perform the spatial discretization the PVW is applied. Considering that the work of the external forces with the virtual nodal displacements $\delta\mathbf{u}_{\mathrm{e}}$ is equivalent to the internal work of the internal forces with the relative displacements $\delta\mathbf{r}$ over the mid-plane of the interface the following expression may be used:

$$\delta\mathbf{u}_{\mathrm{e}} \; \mathbf{f}_{\mathrm{e}}^u = \int_{\Omega_J} [\delta\mathbf{r}]^\top \boldsymbol{\sigma}_J \; \mathrm{d}\Omega_J \tag{4.115}$$

Since the equation has to be satisfied for any value of the virtual displacements ($\delta\mathbf{u}_{\mathrm{e}}$) the following is obtained:

$$\mathbf{f}_{\mathrm{e}}^{u} = \left[\widetilde{\mathbb{T}}^{u}\right]^{\top} \int_{\Omega_J} [\mathbf{N}_J^u]^{\top} [\mathbf{R}_J]^{\top} \boldsymbol{\sigma}_J \, \mathrm{d}\Omega_J \tag{4.116}$$

Substituting the effective stress principle from Eq. (4.106) into Eq. (4.116) and adding the fluid average pressure from Eq. (4.109):

$$\begin{aligned} \mathbf{f}_{\mathrm{e}}^{u} = \left[\widetilde{\mathbb{T}}^{u}\right]^{\top} & \int_{\Omega_J} [\mathbf{N}_J^u]^{\top} [\mathbf{R}_J]^{\top} \boldsymbol{\sigma}'_J \; \mathrm{d}\Omega_j \\ & - \left[\widetilde{\mathbb{T}}^{u}\right]^{\top} \left(\int_{\Omega_J} [\mathbf{N}_J^u]^{\top} [\mathbf{R}_J]^{\top} \alpha_{Biot} \, \mathbf{m}_J \, [\mathbf{N}_J^p]^{\top} \, \mathrm{d}\Omega_j \right) \widetilde{\mathbb{T}}_{\mathrm{L}}^{p} \mathbf{p}_{\mathrm{e}} \end{aligned} \tag{4.117}$$

Summary 11 - Mechanical zero-thickness interface equation.

$$\int_{\Omega_J} [\mathbf{B}_J^u]^{\top} \boldsymbol{\sigma}'_{J,n+\theta} \, \mathrm{d}\Omega_J - \mathbf{K}_{\mathbf{up}} \, \mathbf{p}_{\mathrm{e},n+\theta} = 0 \tag{4.118}$$

where $\mathbf{K}_{\mathbf{up}}$ is the hydro-mechanical coupling matrix:

$$\mathbf{K}_{\mathbf{up}} = \left[\widetilde{\mathbb{T}}^{u}\right]^{\top} \left(\int_{\Omega_J} [\mathbf{N}_J^u]^{\top} [\mathbf{R}_J]^{\top} \, \alpha_{Biot} \, \mathbf{m}_J \, [\mathbf{N}_J^p]^{\top} \, \mathrm{d}\Omega_J \right) \widetilde{\mathbb{T}}_{\mathrm{L}}^{p} \tag{4.119}$$

Hydraulic Formulation for interfaces

According to Segura & Carol (2004) and Garolera (2017), the flow in the interfaces is composed of two terms: longitudinal (or in-plane) along the interface and transversal across it.

A set of equations describing both longitudinal and in-plane heat flow is developed in this section, assuming three-dimensional interface elements with a local orthogonal coordinate system $\{n, l_1, l_2\}$, where l_1 and l_2 are the local directions of the interface along the mid-plane.

It is also assumed that the discontinuity is surrounded by a continuum medium and, as described by Segura (2007), the hydraulic flow can leak from the discontinuity to the continuum medium and vice-versa.

The in-plane hydraulic problem is studied along the mid-plane of the interface. The first fundamental equation is derived from Darcy's Law, from which the average in-plane flow vector across the discontinuity $\mathbf{q}_{\mathrm{L}}^{p}$ may be written as:

$$\mathbf{q}_{\mathrm{L}}^{p} = -\frac{\mathbf{k}_{\mathrm{L}}^{p} \, \gamma^f}{\mu} \, \boldsymbol{\nabla}_J \left(\frac{\bar{p}}{\gamma^f} + z \right) \tag{4.120}$$

where $\mathbf{k}_{\mathrm{L}}^{p}$ is the longitudinal hydraulic permeability; $\bar{p}$ is the average pressure at the mid-plane, γ^f and μ are the specific weight and the dynamic viscosity of the fluid filling the discontinuity, respectively, and $\boldsymbol{\nabla}_J = \left(\frac{\partial}{\partial l_1} \quad \frac{\partial}{\partial l_2} \right)^{\top}$ is the partial differential operator for the local in-plane axis.

Then, by imposing mass conservation in the longitudinal direction of a differential interface element, the fluid mass balance equation for the HM coupled problem may be written as:

$$[\boldsymbol{\nabla}_J]^{\top}\ \mathbf{Q}_{\mathrm{L}}^{p} + \frac{1}{M^{Biot}}\frac{\partial \bar{p}}{\partial t} + \alpha_{Biot}\frac{\partial r_N}{\partial t} = 0 \tag{4.121}$$

where M^{Biot} is the Biot's modulus, α_{Biot} is the Biot's coefficient, r_N is the opening of the interface (normal relative displacement) and $\mathbf{Q}_{\mathrm{L}}^{p}$ is the discharge per unit width defined by:

$$\mathbf{Q}_{\mathrm{L}}^{p} = r_N \mathbf{q}_{\mathrm{L}}^{p} = -\mathbf{K}_{\mathrm{L}}^{p}\ \boldsymbol{\nabla}_J\left(\frac{\bar{p}}{\gamma^f} + z\right) \tag{4.122}$$

where $\mathbf{K}_{\mathrm{L}}^{p}$ is the longitudinal transmissivity, which may be defined in terms of the local mid-plane axis as:

$$\mathbf{K}_{\mathrm{L}}^{p} = r_N \frac{\mathbf{k}_{\mathrm{L}}^{p}\ \gamma^f}{\mu} = \begin{pmatrix} K_{L_{1,1}} & K_{L_{1,2}} \\ K_{L_{2,1}} & K_{L_{2,2}} \end{pmatrix} \tag{4.123}$$

Eq. (4.123) defines the general expression of the transmissivity. However, it is assumed here that there is no preferential flow direction along the mid-plane and in consequence the terms of the diagonal are equal. Additionally, the cross-terms are left out and Eq. (4.123) can be transformed into:

$$\mathbf{K}_{\mathrm{L}}^{p} = K_L^p \begin{pmatrix} 1 & 0 \\ 0 & 1 \end{pmatrix} \tag{4.124}$$

Moreover, as described by Segura (2007) and Garolera (2017), the value of K_L^p may be defined by means of a cubic law (Poiseuille Law), which considers a non-linear relation of the transmissivity depending on the opening of the interface element (r_N). This cubic law, defined in Witherspoon, et al. (1980) and Oron & Berkowitz (1998) may be written as:

$$K_L^p = \frac{\gamma^f}{12\mu} r_N^3 \tag{4.125}$$

It must to be noted that, in the thermal coupling context of this thesis, the value of μ depends on the value of the temperature.

Additionally, it is important to consider the volume change of the fluid due to thermal effects. As the fluid is fills the discontinuity, the volumetric strain rate of the fluid is defined as:

$$\frac{\partial \varepsilon_{v,fluid}^{T}}{\partial t} = r_N\ \alpha_{v,f}^{T}\frac{\partial T}{\partial t} \tag{4.126}$$

where $\alpha_{v,f}^{T}$ is the volumetric coefficient of thermal expansion of the fluid.

Substituting Eqs. (4.122) and (4.126) into (4.121) the governing equation of the in-plane flow is obtained:

$$[\boldsymbol{\nabla}_J]^\top \left(-\mathbf{K}_\mathrm{L}^p\ \boldsymbol{\nabla}_J \left(\frac{\bar{p}}{\gamma^f}+z\right)\right)+\frac{1}{M^{Biot}}\frac{\partial \bar{p}}{\partial t}+r_N\ \alpha_{v,f}^T\frac{\partial T}{\partial t}+\alpha_{Biot}\frac{\partial r_N}{\partial t}=0 \tag{4.127}$$

where the rate of the normal displacements can be related to the rate of relative displacement in *xyz* coordinates as follows:

$$\frac{\partial r_N}{\partial t}=[\mathbf{m}_J]^\top\ \frac{\partial \mathbf{r}}{\partial t} \tag{4.128}$$

There are two kinds of boundary conditions applicable to the transient Eq. (4.127). The first is the Dirichlet boundary condition, in which the pressure p values are imposed on a boundary Γ_ϕ (Eq. (4.129)). The second is the Neumann boundary condition, in which a normal prescribed flow $\bar{Q}_N^p$ is imposed on a boundary Γ_q (Eq. (4.130)).

$$p=\bar{p}(x,y,x,t) \qquad \text{on} \qquad \Gamma_\phi \tag{4.129}$$

$$-[\mathbf{n}]^\top\ \mathbf{K}_\mathrm{L}^p\ \boldsymbol{\nabla}_J\left(\frac{\bar{p}}{\gamma^f}+z\right)-\bar{Q}_N^p=0 \qquad \text{on} \qquad \Gamma_\mathrm{q} \tag{4.130}$$

Using the weighted residuals method defined by equation (4.47) the follow integral form is obtained:

$$\begin{aligned}\mathbf{Q}_{\mathrm{L}_\mathrm{mp}}^p=\int_{\Omega_J} w &\left[[\boldsymbol{\nabla}_J]^\top\left(-\mathbf{K}_\mathrm{L}^p\ \boldsymbol{\nabla}_J\left(\frac{\bar{p}}{\gamma^f}+z\right)\right)+\frac{1}{M^{Biot}}\frac{\partial \bar{p}}{\partial t}+r_N\alpha_{v,f}^T\frac{\partial T}{\partial t}\right.\\ &\left.+\alpha_{Biot}\frac{\partial r_N}{\partial t}\right]\mathrm{d}\Omega_J+\int_{\Gamma_\mathrm{q}^p}\overline{w}\left[-[\mathbf{n}]^\top\mathbf{K}_\mathrm{L}^p\ \boldsymbol{\nabla}_J\left(\frac{\bar{p}}{\gamma^f}+z\right)-\bar{Q}_N^p\right]\mathrm{d}\Gamma^p=0\end{aligned} \tag{4.131}$$

Applying the Galerkin weighting $\left(w=N_J^{p\,(1)},N_J^{p\,(2)},\ldots\right)$, assuming $\overline{w}=w$, applying the Divergence Theorem to the first term of the above equation and performing the spatial discretization of Eq. (4.131) on the domain Ω_J by using the FEM and approximating the nodal displacements, pressures and temperatures by Eqs. (4.12), (4.20) and (4.25), the following is obtained:

$$\begin{aligned}\mathbf{Q}_{\mathrm{L}_\mathrm{mp}}^p=&-\int_{\Omega_J}[\boldsymbol{\nabla}_J]^\top\mathbf{N}_J^p\ \frac{\mathbf{K}_\mathrm{L}^p(T)}{\gamma^f}\ \boldsymbol{\nabla}_J\mathbf{N}_J^p\,\mathrm{d}\Omega_J\ \mathbf{p}_\mathrm{mp}+\int_{\Omega_J}\boldsymbol{\nabla}_J[\mathbf{N}_J^p]^\top\mathbf{K}_\mathrm{L}^p(T)\ \rho^f\boldsymbol{\nabla}_J z\,\mathrm{d}\Omega_J\\ &+\int_{\Omega_J}[\mathbf{N}_J^p]^\top\frac{1}{M^{Biot}}\mathbf{N}_J^p\,\mathrm{d}\Omega_J\ \frac{\partial \mathbf{p}_\mathrm{mp}}{\partial t}+\int_{\Omega_J}[\mathbf{N}_J^T]^\top\ r_N\alpha_{v,f}^T\ \mathbf{N}_J^T\,\mathrm{d}\Omega_J\ \frac{\partial \mathbf{T}_\mathrm{mp}}{\partial t}\\ &+\int_{\Omega_J}[\mathbf{N}_J^p]^\top\ \alpha_{Biot}\ [\mathbf{m}_J]^\top\ \mathbf{R}_J\ \mathbf{N}_J^u\,\mathrm{d}\Omega_J\ \frac{\partial \mathbf{r}}{\partial t}-\int_{\Gamma_\mathrm{q}^p}[\mathbf{N}_J^p]^\top\ \bar{Q}_N^p\ \mathrm{d}\Gamma^p=0\end{aligned} \tag{4.132}$$

where $\mathbf{K}_\mathrm{L}^p$, according to Eq. (4.50), depends on the temperature, leading to:

$$K_L^p(T) = \frac{\gamma^f}{12\ \mu(T)} r_N^3 = \frac{\gamma^f}{12\ \mu_0} r_N^3\ \mathrm{e}^{b\ \mathbf{N}_J^T\ \mathbf{T}_{\mathrm{mp}}} \tag{4.133}$$

where μ_0 and b are coefficients defined in Eq. (4.2).

In addition, the term $\boldsymbol{\nabla}_J z$ of Eq. (4.132) is the gravity vector in local system nl_1l_2 of the interface, given by:

$$\boldsymbol{\nabla}_J z = \mathbf{g}_{nl_1l_2} = \ \mathbf{g}\ \mathbf{R}_J \tag{4.134}$$

where $\mathbf{R}_J$ is the rotation matrix that relates the xyz system with the local orthogonal system nl_1l_2 and $\mathbf{g}$ is the gravity vector in the xyz system defined by Eq. (4.8).

Moreover, the average fluid pressure at the mid-plane, considering the spatial discretization described in Eq. (3.11), may be written as:

$$\mathbf{p}_{\mathrm{mp}} = \widetilde{\mathbb{T}}_{\mathrm{L}}^{p}\ \mathbf{p}_{\mathrm{e}} \tag{4.135}$$

where $\widetilde{\mathbb{T}}_{\mathrm{L}}^{p}$ is the transference matrix, in which it is assumed that the pressure at the mid-plane is the average of the pressure at the corresponding nodes of the element, Eq. (4.110). Now the PVW is applied leading to:

$$\delta\mathbf{p}_{\mathrm{e}}\mathbf{Q}_{\mathrm{L_e}}^{p} = \int_{\Omega_J} \delta\mathbf{p}_{\mathrm{mp}}\ \mathbf{Q}_{\mathrm{L_{mp}}}^{p}\ \mathrm{d}\Omega_J \tag{4.136}$$

Since the equation has to be satisfied for any value of the virtual pressures ($\delta\mathbf{p}_{\mathrm{e}}$) the following equation is reached:

$$\mathbf{Q}_{\mathrm{L_e}}^{p} = \left[\widetilde{\mathbb{T}}_{\mathrm{L}}^{p}\right]^{\top} \mathbf{Q}_{\mathrm{L_{mp}}}^{p} \tag{4.137}$$

Substituting Eqs. (4.135) and (4.137) into Eqs. (4.132) and (4.133), the in-plane hydraulic equation related to the nodes of the interface element is obtained as follows:

$$
\begin{aligned}
\mathbf{Q}^p_{\mathrm{L_e}} = &- \left[\widetilde{\mathbb{T}}^{p}_{\mathrm{L}}\right]^\top \int_{\Omega_J} [\boldsymbol{\nabla}_J]^\top \mathbf{N}^p_J \; \frac{\mathbf{K}^p_{\mathrm{L}}(T)}{\gamma^f} \; \boldsymbol{\nabla}_J \mathbf{N}^p_J \; \widetilde{\mathbb{T}}^{p}_{\mathrm{L}} \mathbf{p}_{\mathrm{e}} \; \mathrm{d}\Omega_J \\
&+ \left[\widetilde{\mathbb{T}}^{p}_{\mathrm{L}}\right]^\top \int_{\Omega_J} [\boldsymbol{\nabla}_J]^\top \mathbf{N}^p_J \; \mathbf{K}^p_{\mathrm{L}}(T) \; \rho^f \mathbf{g}_{nl_1 l_2} \; \mathrm{d}\Omega_J \\
&+ \left[\widetilde{\mathbb{T}}^{p}_{\mathrm{L}}\right]^\top \int_{\Omega_J} [\mathbf{N}^p_J]^\top \frac{1}{M^f_J} \mathbf{N}^p_J \, \widetilde{\mathbb{T}}^{p}_{\mathrm{L}} \; \frac{\partial \mathbf{p}_{\mathrm{e}}}{\partial t} \; \mathrm{d}\Omega_J \\
&+ \left[\widetilde{\mathbb{T}}^{p}_{\mathrm{L}}\right]^\top \int_{\Omega_J} [\mathbf{N}^T_J]^\top \; r_N \alpha^T_{v,f} \; \mathbf{N}^T_J \, \widetilde{\mathbb{T}}^{T}_{\mathrm{L}} \; \frac{\partial \mathbf{T}_{\mathrm{e}}}{\partial t} \; \mathrm{d}\Omega_J \\
&+ \left[\widetilde{\mathbb{T}}^{p}_{\mathrm{L}}\right]^\top \int_{\Omega_J} [\mathbf{N}^p_J]^\top \; \alpha_{Biot} \; [\mathbf{m}_J]^\top \; \mathbf{B}^u_J \; \frac{\partial \mathbf{u}_{\mathrm{e}}}{\partial t} \; \mathrm{d}\Omega_J \\
&- \left[\widetilde{\mathbb{T}}^{p}_{\mathrm{L}}\right]^\top \int_{\Gamma^p_{\mathrm{q}}} [\mathbf{N}^p_J]^\top \, \bar{Q}^{\,p}_N \; \mathrm{d}\Gamma^p = 0
\end{aligned}
\tag{4.138}
$$

where $\mathbf{B}^u_J$ is defined by Eq. (4.112). Performing the spatial discretization of the transmissivity given in Eq. (4.133), this equation is further transformed into:

$$
K^p_L(T) = \frac{\gamma^f}{12\;\mu(T)} r^3_N = \frac{\gamma^f}{12\;\mu_0} r^3_N \; \mathrm{e}^{b\;\mathbf{N}^T_J \, \widetilde{\mathbb{T}}^{T}_{\mathrm{L}} \mathbf{T}_{\mathrm{e}}}
\tag{4.139}
$$

Additional to the in-plane flow, the existence of a discontinuity may also represent a resistance to the hydraulic flow in the transversal direction, which would result in a localized pressure drop across the interface. As defined for temperatures (section 3.2), the transversal flow may be defined as:

$$
q^p_N = \breve{K}^p_N \; \breve{p}
\tag{4.140}
$$

where $\breve{K}^p_N$ is the transverse hydraulic coefficient and relates the transverse fluid flow q^p_N with the transversal pressure drop $\breve{p}$. Using the PVW in a discrete form,

$$
[\delta \breve{p}_{\mathrm{e}}]^\top \; \mathbf{Q}^p_{\mathrm{N_e}} \; = [\delta \breve{p}_{\mathrm{mp}}]^\top \; \mathbf{Q}^p_{\mathrm{N_{mp}}}
\tag{4.141}
$$

$$
\mathbf{Q}^p_{\mathrm{N_e}} = \left[\widetilde{\mathbb{T}}^{p}_{\mathrm{N}}\right]^\top \mathbf{Q}^p_{\mathrm{N_{mp}}}
\tag{4.142}
$$

where $\widetilde{\mathbb{T}}^{p}_{\mathrm{N}}$ is the transference transversal matrix defined in Eqs. (3.34) and (3.35). Finally, performing the spatial discretization of Eq. (4.140) using the FEM and using Eqs. (4.135) and (4.142) the following equation is reached:

$$
\mathbf{Q}^p_{\mathrm{N_e}} = \left[\widetilde{\mathbb{T}}^{p}_{\mathrm{N}}\right]^\top \int_{\Omega_J} [\mathbf{N}^p_J]^\top \breve{K}^p_N \; \mathbf{N}^p_J \; \widetilde{\mathbb{T}}^{p}_{\mathrm{N}} \; \mathbf{p}_{\mathrm{e}} \; \mathrm{d}\Omega_J
\tag{4.143}
$$

To obtain an integrated conductivity matrix it is necessary to combine the longitudinal and the transversal flow as a sum of both:

$$\mathbf{Q}^p_{\mathrm{e}} = \mathbf{Q}^p_{\mathrm{L_e}} + \mathbf{Q}^p_{\mathrm{N_e}} \tag{4.144}$$

Substituting Eqs. (4.138) and (4.143) into Eq. (4.144) the following expression is obtained:

$$\begin{aligned}
\mathbf{Q}^p_{\mathrm{e}} = &- \left[\widetilde{\mathbb{T}}^p_{\mathrm{L}}\right]^\top \left(\int_{\Omega_J} [\boldsymbol{\nabla}_J]^\top \mathbf{N}^p_J \frac{\mathbf{K}^p_{\mathrm{L}}(T)}{\gamma^f} \; \boldsymbol{\nabla}_J \mathbf{N}^p_J \, \mathrm{d}\Omega_J \right) \widetilde{\mathbb{T}}^p_{\mathrm{L}} \; \mathbf{p}_{\mathrm{e}} \\
&+ \left[\widetilde{\mathbb{T}}^p_{\mathrm{N}}\right]^\top \left(\int_{\Omega_J} [\mathbf{N}^p_J]^\top \check{K}^p_N \; \mathbf{N}^p_J \; \mathrm{d}\Omega_J \right) \widetilde{\mathbb{T}}^p_{\mathrm{N}} \; \mathbf{p}_{\mathrm{e}} \\
&+ \left[\widetilde{\mathbb{T}}^p_{\mathrm{L}}\right]^\top \left(\int_{\Omega_J} [\boldsymbol{\nabla}_J]^\top \mathbf{N}^p_J \; \mathbf{K}^p_{\mathrm{L}}(T) \; \rho^f \mathbf{g}_{nl_1 l_2} \; \mathrm{d}\Omega_J \right) \\
&+ \left[\widetilde{\mathbb{T}}^p_{\mathrm{L}}\right]^\top \left(\int_{\Omega_J} [\mathbf{N}^p_J]^\top \frac{1}{M^{Biot}} \mathbf{N}^p_J \, \mathrm{d}\Omega_J \right) \widetilde{\mathbb{T}}^p_{\mathrm{L}} \; \frac{\partial \mathbf{p}_{\mathrm{e}}}{\partial t} \\
&+ \left[\widetilde{\mathbb{T}}^p_{\mathrm{L}}\right]^\top \left(\int_{\Omega_J} [\mathbf{N}^T_J]^\top \; r_N \alpha^T_{v,f} \; \mathbf{N}^T_J \, \mathrm{d}\Omega_J \right) \widetilde{\mathbb{T}}^T_{\mathrm{L}} \; \frac{\partial \mathbf{T}_{\mathrm{e}}}{\partial t} \\
&+ \left[\widetilde{\mathbb{T}}^p_{\mathrm{L}}\right]^\top \left(\int_{\Omega_J} [\mathbf{N}^p_J]^\top \; \alpha_{Biot} \; [\mathbf{m}_J]^\top \; \mathbf{R}_J \; \mathbf{N}^u_J \, \mathrm{d}\Omega_J \right) \widetilde{\mathbb{T}}^u \; \frac{\partial \mathbf{u}_{\mathrm{e}}}{\partial t} \\
&- \left[\widetilde{\mathbb{T}}^p_{\mathrm{L}}\right]^\top \int_{\Gamma^p_{\mathrm{q}}} [\mathbf{N}^p_J]^\top \, \bar{Q}^p_N \; \mathrm{d}\Gamma^p = 0
\end{aligned} \tag{4.145}$$

The last step consists in the time discretization of the hydraulic equation (4.145) using the FDM. Additionally, the linearization of Eq. (4.139) may be developed using the first term of the Taylor expansion, obtaining:

$$\begin{aligned}
\frac{1}{\mu(T)} &= \frac{1}{\mu_0 \; \mathrm{e}^{-b \, \mathbf{N}^T_J \, \widetilde{\mathbb{T}}^T_{\mathrm{L}} \mathbf{T}_{\mathrm{e},n}}} \mathrm{e}^{b\theta \mathbf{N}^T_J \, \widetilde{\mathbb{T}}^T_{\mathrm{L}} \Delta \mathbf{T}_{\mathrm{e},n+1}} = \frac{1}{\mu_n} \mathrm{e}^{b\theta \mathbf{N}^T_J \, \widetilde{\mathbb{T}}^T_{\mathrm{L}} \Delta \mathbf{T}_{\mathrm{e},n+1}} \\
\frac{1}{\mu(T)} &\approx \frac{1}{\mu_n} \left(1 + b\theta \mathbf{N}^T_J \; \widetilde{\mathbb{T}}^T_{\mathrm{L}} \Delta \mathbf{T}_{\mathrm{e},n+1} \right)
\end{aligned} \tag{4.146}$$

Finally, introducing the FDM time discretization defined in Eq. (4.27) into Eq. (4.145) and substituting Eq. (4.146) the final hydraulic equation for zero-thickness interface elements (4.147) is reached.

Summary 12 - Hydraulic zero-thickness interface equation.

$$\begin{aligned}(\mathbf{S}_{\mathbf{p}} + \theta\Delta t_{n+1}\mathbf{K}_{\mathbf{pp}})\Delta\mathbf{p}_{\mathrm{e},n+1} + (\mathbf{S}_{\mathbf{pT}} + \theta\Delta t_{n+1}\mathbf{K}_{\mathbf{pT}})\Delta\mathbf{T}_{\mathrm{e},n+1} + [\mathbf{K}_{\mathbf{pu}}]^\top\Delta\mathbf{u}_{\mathrm{e},n+1} \\ = \Delta t_{n+1}\mathbf{f}^p_{\mathrm{e}} - \Delta t_{n+1}\mathbf{K}_{\mathbf{pp}}\ \mathbf{p}_{\mathrm{e},n}\end{aligned} \tag{4.147}$$

where $\mathbf{K}_{\mathbf{pp}}$ is the element hydraulic diffusion matrix, $\mathbf{S}_{\mathbf{p}}$ is the element hydraulic capacity matrix, $\mathbf{K}_{\mathbf{ppu}}$ is the element hydro-mechanical coupling matrix, $\mathbf{K}_{\mathbf{pT}}$ is the element thermo-hydraulic coupling matrices and $\mathbf{f}^p_{\mathrm{e}}$ is the element vector of external forces:

$$\mathbf{S}_{\mathbf{p}} = \left[\widetilde{\mathbb{T}}^p_{\mathrm{L}}\right]^\top \left(\int_{\Omega_J} [\mathbf{N}^p_J]^\top \frac{1}{M^{Biot}} \mathbf{N}^p_J \,\mathrm{d}\Omega_J\right) \widetilde{\mathbb{T}}^p_{\mathrm{L}} \tag{4.148}$$

$$\begin{aligned}\mathbf{K}_{\mathbf{pp}} = \left[\widetilde{\mathbb{T}}^p_{\mathrm{L}}\right]^\top \left(\int_{\Omega_J} [\boldsymbol{\nabla}_J]^\top \mathbf{N}^p_J \ \frac{\mathbf{K}^p_{\mathrm{L}}(T_n)}{\gamma^f} \boldsymbol{\nabla}_J \mathbf{N}^p_J \,\mathrm{d}\Omega_J\right) \widetilde{\mathbb{T}}^p_{\mathrm{L}} \\ + \widetilde{\mathbb{T}}^{p\ \top}_{\mathrm{N}} \left(\int_{\Omega_J} [\mathbf{N}^p_J]^\top \check{K}^p_N \ \mathbf{N}^p_J \ \mathrm{d}\Omega_J\right) \widetilde{\mathbb{T}}^{\ p}_{\mathrm{N}}\end{aligned} \tag{4.149}$$

$$\mathbf{S}_{\mathbf{pT}} = \left[\widetilde{\mathbb{T}}^p_{\mathrm{L}}\right]^\top \left(\int_{\Omega_J} [\mathbf{N}^T_J]^\top \ r_N \alpha^T_f \ \mathbf{N}^T_J \,\mathrm{d}\Omega_J\right) \widetilde{\mathbb{T}}^T_{\mathrm{L}} \tag{4.150}$$

$$\begin{aligned}\mathbf{K}_{\mathbf{pT}} = \left[\widetilde{\mathbb{T}}^p_{\mathrm{L}}\right]^\top \left(b \int_{\Omega_J} [\boldsymbol{\nabla}_J]^\top \mathbf{N}^p_J \ \frac{\mathbf{K}^p_{\mathrm{L}}(T_n)}{\gamma^f} \ \boldsymbol{\nabla}_J \mathbf{N}^p_J \widetilde{\mathbb{T}}^p_{\mathrm{L}} \mathbf{p}_{\mathrm{e},n} \ \mathbf{N}^T_J \,\mathrm{d}\Omega_J\right) \widetilde{\mathbb{T}}^T_{\mathrm{L}} \\ - \left[\widetilde{\mathbb{T}}^p_{\mathrm{L}}\right]^\top \left(b \int_{\Omega_J} [\boldsymbol{\nabla}_J]^\top \mathbf{N}^p_J \ \mathbf{K}^p_{\mathrm{L}}(T_n) \ \mathbf{N}^T_J \ \rho^f \mathbf{g}_{nl_1 l_2} \ \mathrm{d}\Omega_J\right) \widetilde{\mathbb{T}}^T_{\mathrm{L}}\end{aligned} \tag{4.151}$$

$$\mathbf{K}_{\mathbf{pu}} = \left[\widetilde{\mathbb{T}}^p_{\mathrm{L}}\right]^\top \left(\int_{\Omega_J} [\mathbf{N}^p_J]^\top \ \alpha_{Biot} \ [\mathbf{m}_J]^\top \ \mathbf{R}_J \ \mathbf{N}^u_J \,\mathrm{d}\Omega_J\right) \widetilde{\mathbb{T}}^{\,u} \tag{4.152}$$

$$\mathbf{f}^p_{\mathrm{e}} = \left[\widetilde{\mathbb{T}}^p_{\mathrm{L}}\right]^\top \left(-\int_{\Omega_J} [\boldsymbol{\nabla}_J]^\top \mathbf{N}^p_J \ \mathbf{K}^p_{\mathrm{L}}(T_n) \ \rho^f \mathbf{g}_{nl_1 l_2} \ \mathrm{d}\Omega_J + \int_{\Gamma^p_{\mathrm{q}}} [\mathbf{N}^p_J]^\top \ \bar{Q}^{\ p}_N \ \mathrm{d}\Gamma^p\right) \tag{4.153}$$

$$K^p_L(T_n) = \frac{\gamma^f}{12\mu_n} r^3_N \tag{4.154}$$

$$\mu_n = \mu_0 \ \mathrm{e}^{-b\ \mathbf{N}^T_J \ \widetilde{\mathbb{T}}^T_{\mathrm{L}} \mathbf{T}_{\mathrm{e},n}} \tag{4.155}$$

Thermal Formulation for interfaces

The thermal advective equation for zero-thickness interface elements at the mid-plane developed in Section 2.2.3 (α-Implicit Characteristic Galerkin method) may be written from Eq. (3.69) as follows:

$$
\begin{aligned}
\mathrm{Q}^{T}_{\mathrm{L_{mp}}} &= r_N \rho c \frac{1}{\Delta t_{n+1}} \left(\Delta T_{\mathrm{mp},n+1}\right) \\
&= -(1-\alpha) r_N \rho c \left[\mathbf{q}^{p}_{\mathrm{L},n+1/2}\right]^{\top} \boldsymbol{\nabla}_J T_{\mathrm{mp},n} \\
&+ \frac{(1-\alpha)^2}{2} r_N \rho c \Delta t_{n+1} \Big([\boldsymbol{\nabla}_J]^{\top}\, \mathbf{q}^{p}_{\mathrm{L},n+1/2} \Big) \Big(\left[\mathbf{q}^{p}_{\mathrm{L},n+1/2}\right]^{\top} \boldsymbol{\nabla}_J T_{\mathrm{mp},n} \Big) \\
&- \alpha r_N \rho c \left[\mathbf{q}^{p}_{\mathrm{L},n+1/2}\right]^{\top} \boldsymbol{\nabla}_J T_{\mathrm{mp},n+1} \\
&- \frac{\alpha^2}{2} r_N \rho c \Delta t_{n+1} \Big([\boldsymbol{\nabla}_J]^{\top}\, \mathbf{q}^{p}_{\mathrm{L},n+1/2} \Big) \Big(\left[\mathbf{q}^{p}_{\mathrm{L},n+1/2}\right]^{\top} \boldsymbol{\nabla}_J T_{\mathrm{mp},n+1} \Big) \\
&+ \theta [\boldsymbol{\nabla}_J]^{\top} \left(r_N\, \mathbf{k}^{T}_{\mathrm{L}}\, \boldsymbol{\nabla}_J T_{\mathrm{mp},n+1} \right) + (1-\theta) [\boldsymbol{\nabla}_J]^{\top} \left(r_N\, \mathbf{k}^{T}_{\mathrm{L}}\, \boldsymbol{\nabla}_J T_{\mathrm{mp},n} \right)
\end{aligned}
\tag{4.156}
$$

where $T_{\mathrm{mp},n}$ and $T_{\mathrm{mp},n+1}$ are the values of temperature at the mid-plane for times n and $n+1$, ρ, c and $\mathbf{k}^{T}_{\mathrm{L}}$ are the density, the specific heat and the thermal conductivity of the medium where the heat transfer occurs (e.g. fluid), r_N is the normal interface opening and $\mathbf{q}^{p}_{\mathrm{L},n+1/2}$ are the average Darcy's velocities across the discontinuity aperture from the hydraulic problem, which may be written from Eq. (2.154) as:

$$
\mathbf{q}^{p}_{\mathrm{L},n+1/2} \approx \bar{\mathbf{q}}^{p}_{\mathrm{L}} = \mathbf{q}^{p}_{\mathrm{L},n} + \frac{1}{2} \Delta \mathbf{q}^{p}_{\mathrm{L},n+1}
\tag{4.157}
$$

where $\mathbf{q}^{p}_{\mathrm{L},n}$ is the Darcy's velocity of the previous time-step (known) and $\Delta \mathbf{q}^{p}_{\mathrm{L},n+1}$ may be written from Eq. (4.120) as:

$$
\Delta \mathbf{q}^{p}_{\mathrm{L},n+1} = \mathbf{k}^{p}_{\mathrm{L}} \left\{ \frac{1}{\mu_n} \left(-\boldsymbol{\nabla}_J \Delta \bar{p}_{n+1}\right) + \frac{1}{\Delta \mu_{n+1}} \left(-\boldsymbol{\nabla}_J \bar{p}_n\right) + \frac{1}{\Delta \mu_{n+1}} \rho^f \mathbf{g}_{n l_1 l_2} \right\}
\tag{4.158}
$$

where $\Delta \bar{p}_{n+1}$ is the increment of fluid pressure at the mid-plane for the current time-step, $\bar{p}_n$ is the fluid pressure at the mid-plane for the previous time-step, $\mathbf{k}^{p}_{\mathrm{L}}$ is the in-plane hydraulic permeability, μ_n is the dynamic viscosity at time n defined in Eq. (4.155) and $\Delta \mu_{n+1}$ is the increment of dynamic viscosity of the current time-step defined by Eq. (4.146). In order to avoid second-order products $\Delta \bar{p}_{n+1} \Delta \bar{T}_{n+1}$, the term $\frac{\mathbf{k}^{p}_{\mathrm{L}}}{\Delta \mu_{n+1}} \left(-\boldsymbol{\nabla} \Delta \bar{p}_{n+1}\right)$ has been left out in Eq. (4.158). Additionally, considering a cubic law for the interfaces, the components of the hydraulic permeability matrix may be written as:

$$
k^{p}_{\mathrm{L}} = \frac{r_N^2}{12}
\tag{4.159}
$$

Performing the spatial discretization of Eq. (4.156) using the FEM (Eq. (2.27)), applying the Divergence Theorem to the diffusion terms, considering $\overline{\mathbf{w}} = \mathbf{w}$ on Γ_{q}, and applying the standard Galerkin weighting ($\mathbf{w} = \mathbf{N}^{T}_{J}$) results in the following system of equations at the mid-plane of the interface:

$$\begin{aligned}\left(\frac{1}{\Delta t_{n+1}}\mathbf{C}+\alpha\mathbf{K_v}+\frac{\alpha^2}{2}\mathbf{K_s}+\theta\mathbf{K_{TT-D}}\right)\Delta\mathbf{T}_{\mathrm{mp},n+1}&\\=-\left[\mathbf{K_{TT-D}}+\mathbf{K_v}+\left(\frac{1}{2}-\alpha\right)\mathbf{K_s}\right]\mathbf{T}_{\mathrm{mp},n}&\end{aligned}\tag{4.160}$$

where $\mathbf{K_{TT-D}}$ is the element conductivity matrix, $\mathbf{C}$ is the element capacity matrix, $\mathbf{K_v}$ is the element advective matrix and $\mathbf{K_s}$ is the element stabilization matrix which results from the aplication of the α-Implicit Characteristic Galerkin method, with components:

$$\mathrm{C}^{(a,b)}=\int_{\Omega_J}r_{N,n+1}\;\rho c\;N_J^{T(a)}N_J^{T(b)}\,\mathrm{d}\Omega_J\tag{4.161}$$

$$\mathrm{K}_{\mathrm{TT-D}}^{(a,b)}=\int_{\Omega_J}r_{N,n+1}\left[\boldsymbol{\nabla}_J N_J^{T(a)}\right]^{\top}\mathbf{k}_{\mathrm{L}}^{T}\;\boldsymbol{\nabla}_J N_J^{T(b)}\,\mathrm{d}\Omega_J\tag{4.162}$$

$$\mathrm{K}_{\mathrm{v}}^{(a,b)}=\int_{\Omega_J}r_{N,n+1}\;\rho c\;N_J^{T(a)}\left[\mathbf{q}_{\mathrm{L},n+1/2}^{p}\right]^{\top}\boldsymbol{\nabla}_J N_J^{T(b)}\,\mathrm{d}\Omega_J\tag{4.163}$$

$$\mathrm{K}_{\mathrm{s}}^{(a,b)}=\;\Delta t_{n+1}\int_{\Omega_J}r_{N,n+1}\;\rho c\left(\left[\mathbf{q}_{\mathrm{L},n+1/2}^{p}\right]^{\top}\boldsymbol{\nabla}_J N_J^{T(a)}\right)\left(\left[\mathbf{q}_{\mathrm{L},n+1/2}^{p}\right]^{\top}\boldsymbol{\nabla}_J N_J^{T(b)}\right)\mathrm{d}\Omega_J\tag{4.164}$$

The spatial and time discretization (using the FEM and the FDM, respectively) must be applied to Eq. (4.158), obtaining:

$$\begin{aligned}\Delta\mathbf{q}_{\mathrm{L},n+1}^{p}=&-\frac{\mathbf{k}_{\mathrm{L}}^{p}}{\mu_n}\boldsymbol{\nabla}_J N_J^{p(c)}\Delta p_{\mathrm{mp},n+1}^{(c)}\\&+\theta\;\frac{\mathbf{k}_{\mathrm{L}}^{p}}{\mu_n}b\left\{-\boldsymbol{\nabla}_J N_J^{p(c)}p_{\mathrm{mp},n}^{(c)}+\rho^f\mathbf{g}_{nl_1l_2}\right\}N_J^{T(d)}\Delta T_{\mathrm{mp},n+1}^{(d)}\end{aligned}\tag{4.165}$$

where b is defined in Eq. (4.2) and μ_n is the fluid viscosity at the previous time-step defined in Eq. (4.155). Introducing Eq. (4.165) into Eq. (4.163) results in the following expression for the right-hand side of Eq. (4.160):

$$\begin{aligned}\mathrm{K}_{\mathrm{v}}^{(a,b)}T_{\mathrm{mp},n}^{(b)}=&\int_{\Omega_J}r_{N,n+1}\;\rho c\;N_J^{T(a)}\left[\mathbf{q}_{\mathrm{L},n}^{p}+\frac{1}{2}\Delta\mathbf{q}_{\mathrm{L},n+1}^{p}\right]^{\top}\boldsymbol{\nabla}_J N_J^{T(b)}\,\mathrm{d}\Omega_J\;T_{\mathrm{mp},n}^{(b)}\\=&\int_{\Omega_J}r_{N,n+1}\;\rho c\;N_J^{T(a)}\;\left[\mathbf{q}_{\mathrm{L},n}^{p}\right]^{\top}\;\boldsymbol{\nabla}_J N_J^{T(b)}\,\mathrm{d}\Omega_J\;T_{\mathrm{mp},n}^{(b)}\\&-\frac{1}{2}\int_{\Omega_J}\rho c\;N_J^{T(a)}\left[\boldsymbol{\nabla}_J N_J^{T(b)}T_{\mathrm{mp},n}^{(b)}\right]^{\top}r_{N,n+1}\frac{\mathbf{k}_{\mathrm{L}}^{p}}{\mu_n}\boldsymbol{\nabla}_J N_J^{p(c)}\,\mathrm{d}\Omega_J\;\Delta p_{\mathrm{mp},n+1}^{(c)}\\&+\frac{\theta}{2}\int_{\Omega_J}\rho c\;N_J^{T(a)}\left[\boldsymbol{\nabla}_J N_J^{T(b)}T_{\mathrm{mp},n}^{(b)}\right]^{\top}r_{N,n+1}\frac{\mathbf{k}_{\mathrm{L}}^{p}}{\mu_n}b\left\{-\boldsymbol{\nabla}_J N_J^{p(c)}p_{\mathrm{mp},n}^{(c)}\right.\\&\left.+\rho^f\mathbf{g}_{nl_1l_2}\right\}N_J^{T(d)}\mathrm{d}\Omega_J\;\Delta T_{\mathrm{mp},n+1}^{(d)}\end{aligned}\tag{4.166}$$

and the following expression for the left-hand side of Eq. (4.160):

$$\begin{aligned} \mathrm{K}_{\mathrm{v}}^{(a,b)} \Delta T_{\mathrm{mp},n+1}^{(b)} &= \int_{\Omega_J} r_{N,n+1}\ \rho c\ N_J^{T(a)} \left[\mathbf{q}_{\mathrm{L},n}^{p} + \frac{1}{2}\Delta\mathbf{q}_{\mathrm{L},n+1}^{p}\right]^{\top} \boldsymbol{\nabla}_J N_J^{T(b)}\, \mathrm{d}\Omega_J\ \Delta T_{\mathrm{mp},n+1}^{(b)} \\ &= \int_{\Omega_J} r_{N,n+1}\ \rho c\ N_J^{T(a)}\ \left[\mathbf{q}_{\mathrm{L},n}^{p}\right]^{\top} \boldsymbol{\nabla}_J N_J^{T(b)}\, \mathrm{d}\Omega_J\ \Delta T_{\mathrm{mp},n+1}^{(b)} \end{aligned} \tag{4.167}$$

where the second-order terms $\Delta p_{n+1}\Delta T_{n+1}$ are left out in the last equation and $r_N \frac{\mathbf{k}_{\mathrm{L}}^{p}}{\mu_n}$ can be replaced by the hydraulic transmissivity divided by the fluid specific weight of the previous time-step, and using the cubic law defined in Eq. (4.159), leads to:

$$\frac{\mathbf{K}_{\mathrm{L},n}^{p}}{\gamma^f} = r_N \frac{\mathbf{k}_{\mathrm{L}}^{p}}{\mu_n} \tag{4.168}$$

where $\mathbf{K}_{\mathrm{L},n}^{p}$ is the longitudinal transmissivity defined by:

$$\mathbf{K}_{\mathrm{L},n}^{p} = K_{L,n}^{p} \begin{pmatrix} 1 & 0 \\ 0 & 1 \end{pmatrix} \tag{4.169}$$

whit components:

$$K_{L,n}^{p} = \frac{\gamma^f}{12\mu_n} r_{N,n}^{3} \tag{4.170}$$

In order to introduce the hydro-thermal coupling into Eq. (4.164) the subsequent development must be made:

$$\begin{aligned} \mathbf{q}_{\mathrm{L},n+1/2}^{p} \left[\mathbf{q}_{\mathrm{L},n+1/2}^{p}\right]^{\top} &= \left[\mathbf{q}_{\mathrm{L},n}^{p} + \frac{1}{2}\Delta\mathbf{q}_{\mathrm{L},n+1}^{p}\right] \left[\mathbf{q}_{\mathrm{L},n}^{p} + \frac{1}{2}\Delta\mathbf{q}_{\mathrm{L},n+1}^{p}\right]^{\top} \\ &= \mathbf{q}_{\mathrm{L},n}^{p} \left[\mathbf{q}_{\mathrm{L},n}^{p}\right]^{\top} + \frac{1}{2}\mathbf{q}_{\mathrm{L},n}^{p} \left[\Delta\mathbf{q}_{\mathrm{L},n+1}^{p}\right]^{\top} + \frac{1}{2}\Delta\mathbf{q}_{\mathrm{L},n+1}^{p} \left[\mathbf{q}_{\mathrm{L},n}^{p}\right]^{\top} \\ &+ \frac{1}{4}\Delta\mathbf{q}_{\mathrm{L},n+1}^{p} \left[\Delta\mathbf{q}_{\mathrm{L},n+1}^{p}\right]^{\top} \end{aligned} \tag{4.171}$$

where the last term of the above expansion is second-order and can be left out. Introducing Eq. (4.165) into Eq. (4.164) results in the following expression for the right-hand side of Eq. (4.160):

$$
\begin{aligned}
&\mathrm{K}_{\mathrm{s}}^{(a,b)} T_{\mathrm{mp},n}^{(b)} \\
&= \Delta t_{n+1} \int_{\Omega_J} r_{N,n+1}\, \rho c \left(\left[\mathbf{q}_{\mathrm{L},n}^{p} + \frac{1}{2} \Delta \mathbf{q}_{\mathrm{L},n+1}^{p} \right]^{\top} \boldsymbol{\nabla}_J N_J^{T(a)} \right) \left(\left[\mathbf{q}_{\mathrm{L},n}^{p} \right.\right. \\
&\left.\left. + \frac{1}{2} \Delta \mathbf{q}_{\mathrm{L},n+1}^{p} \right]^{\top} \boldsymbol{\nabla}_J N_J^{T(b)} \right) \mathrm{d}\Omega_J \; T_{\mathrm{mp},n}^{(b)} \\
&= \Delta t_{n+1} \int_{\Omega_J} r_{N,n+1}\, \rho c \left(\left[\mathbf{q}_{\mathrm{L},n}^{p} \right]^{\top} \boldsymbol{\nabla}_J N_J^{T(a)} \right) \left(\left[\mathbf{q}_{\mathrm{L},n}^{p} \right]^{\top} \boldsymbol{\nabla}_J N_J^{T(b)} \; T_{\mathrm{mp},n}^{(b)} \right) \mathrm{d}\Omega_J \\
&- \frac{1}{2} \Delta t_{n+1} \int_{\Omega_J} \rho c \left(\left[\boldsymbol{\nabla}_J N_J^{T(a)} \right]^{\top} r_{N,n+1} \frac{\mathbf{k}_{\mathrm{L}}^{p}}{\mu_n} \boldsymbol{\nabla}_J N_J^{p(c)} \right) \left(\left[\mathbf{q}_{\mathrm{L},n}^{p} \right]^{\top} \boldsymbol{\nabla}_J N_J^{T(b)} T_{\mathrm{mp},n}^{(b)} \right) \mathrm{d}\Omega_J \Delta p_{\mathrm{mp},n+1}^{(c)} \\
&+ \frac{\theta}{2} \Delta t_{n+1} \int_{\Omega_J} \rho c \left(\left[\boldsymbol{\nabla}_J N_J^{T(a)} \right]^{\top} r_{N,n+1} \frac{\mathbf{k}_{\mathrm{L}}^{p}}{\mu_n} b \Big\{ - \boldsymbol{\nabla}_J N_J^{p(c)} p_{\mathrm{mp},n}^{(c)} \right. \\
&\left. + \rho^f \mathbf{g}_{n l_1 l_2} \Big\} N_J^{T(d)} \right) \left(\left[\mathbf{q}_{\mathrm{L},n}^{p} \right]^{\top} \boldsymbol{\nabla}_J N_J^{T(b)} T_{\mathrm{mp},n}^{(b)} \right) \mathrm{d}\Omega_J \; \Delta T_{\mathrm{mp},n+1}^{(d)} \\
&- \frac{1}{2} \Delta t_{n+1} \int_{\Omega_J} \rho c \left(\left[\mathbf{q}_{\mathrm{L},n}^{p} \right]^{\top} \boldsymbol{\nabla}_J N_J^{T(b)} T_{\mathrm{mp},n}^{(b)} \right) \left(\left[\boldsymbol{\nabla}_J N_J^{T(a)} \right]^{\top} r_{N,n+1} \frac{\mathbf{k}_{\mathrm{L}}^{p}}{\mu_n} \boldsymbol{\nabla}_J N_J^{p(c)} \right) \mathrm{d}\Omega_J \Delta p_{\mathrm{mp},n+1}^{(c)} \\
&+ \frac{\theta}{2} \Delta t_{n+1} \int_{\Omega_J} \rho c \left(\left[\boldsymbol{\nabla}_J N_J^{T(a)} \right]^{\top} r_{N,n+1} \frac{\mathbf{k}_{\mathrm{L}}^{p}}{\mu_n} b \Big\{ - \boldsymbol{\nabla}_J N_J^{p(c)} p_{\mathrm{mp},n}^{(c)} \right. \\
&\left. + \rho^f \mathbf{g}_{n l_1 l_2} \Big\} N_J^{T(d)} \right) \left(\left[\mathbf{q}_{\mathrm{L},n}^{p} \right]^{\top} \boldsymbol{\nabla}_J N_J^{T(b)} T_{\mathrm{mp},n}^{(b)} \right) \mathrm{d}\Omega_J \; \Delta T_{\mathrm{mp},n+1}^{(d)}
\end{aligned}
\tag{4.172}
$$

and the following expression for the left-hand side of Eq. (4.164):

$$
\begin{aligned}
&\mathrm{K}_{\mathrm{s}}^{(a,b)} \Delta T_{\mathrm{mp},n+1}^{(b)} \\
&= \Delta t_{n+1} \int_{\Omega_J} r_{N,n+1}\, \rho c \left(\left[\mathbf{q}_{\mathrm{L},n}^{p} \right]^{\top} \boldsymbol{\nabla}_J N_J^{T(a)} \right) \left(\left[\mathbf{q}_{\mathrm{L},n}^{p} \right]^{\top} \boldsymbol{\nabla}_J N_J^{T(b)} \right) \mathrm{d}\Omega_J \; \Delta T_{\mathrm{mp},n+1}^{(b)}
\end{aligned}
\tag{4.173}
$$

where the second-order terms $\Delta p_{n+1} \Delta T_{n+1}$ are left out in the last equation and $r_N \frac{\mathbf{k}_{\mathrm{L}}^{p}}{\mu_n}$ can be replaced by the hydraulic transmissivity divided by the fluid specific weight of the previous time-step, as defined in Eqs. (4.168)-(4.170).

Similar to Eq. (4.135) for the hydraulic problem, the temperature values at the mid-plane have to be referred to the nodes of the element. Moreover, the same consideration has to be made in account to the flows, as described in Eq. (4.137). From these equations the following is obtained:

$$
\mathbf{T}_{\mathrm{mp}} = \widetilde{\mathbb{T}}_{\mathrm{L}}^{T} \, \mathbf{T}_{\mathrm{e}}
\tag{4.174}
$$

$$
\mathbf{Q}_{\mathrm{L}_{\mathrm{e}}}^{T} = \left[\widetilde{\mathbb{T}}_{\mathrm{L}}^{T} \right]^{\top} \mathbf{Q}_{\mathrm{L}_{\mathrm{mp}}}^{T}
\tag{4.175}
$$

Additional to the longitudinal flow, the existence of a discontinuity may also represent a resistance to the thermal flow in the transversal direction, which would result in a localized temperature drop across the interface. As defined for the hydraulic problem, the transversal flow may be defined as:

$$q_N^T = \check{K}_N^T \; \check{T}_J \tag{4.176}$$

where $\check{K}_N^T$ is the transverse thermal coefficient and relates the transverse flow q_N^T to the transversal temperature drop $\check{T}$. Using the PVW in a discrete form,

$$\left[\delta \check{T}_\mathrm{e}\right]^\top \mathbf{Q}^T_{\mathrm{N_e}} = \left[\delta \check{T}_\mathrm{mp}\right]^\top \; \mathbf{Q}^T_{\mathrm{N_{mp}}} \tag{4.177}$$

$$\mathbf{Q}^T_{\mathrm{N_e}} = \left[\widetilde{\mathbb{T}}^T_\mathrm{N}\right]^\top \mathbf{Q}^T_{\mathrm{N_{mp}}} \tag{4.178}$$

where $\widetilde{\mathbb{T}}^T_\mathrm{N}$ transference transversal matrix defined in Eqs. (3.34) and (3.35). Finally, performing the spatial discretization of Eq. (4.176) using the FEM and considering Eqs. (4.174) and (4.178) the following equation is reached:

$$\mathbf{Q}^T_{\mathrm{N_e}} = \left[\widetilde{\mathbb{T}}^T_\mathrm{N}\right]^\top \int_{\Omega_J} [\mathbf{N}_J^T]^\top \check{K}_N^T \, \mathbf{N}_J^T \, \mathbf{T}_\mathrm{e} \, \mathrm{d}\Omega_J \; \widetilde{\mathbb{T}}^T_\mathrm{N} \tag{4.179}$$

To obtain an integrated conductivity matrix it is necessary to combine the in-plane and the transversal flow as a sum of both:

$$\mathbf{Q}^T_\mathrm{e} = \mathbf{Q}^T_{\mathrm{L_e}} + \mathbf{Q}^T_{\mathrm{N_e}} \tag{4.180}$$

Substituting Eqs. (4.166), (4.167), (4.172) and (4.173) into Eq. (4.160), considering the Eqs. (4.174) and (4.175) to obtain the equations referred to the nodes of the element and considering the transversal flow defined in Eq. (4.179), the final thermal equation for zero-thickness interface elements (4.181) is reached.

Summary 13 - Thermal zero-thickness interface equation with advection (α-ICG method).

$$\begin{aligned}
&\left[\frac{1}{\Delta t_{n+1}}\mathbf{C} + \alpha\mathbf{K_{TT-A}} + \frac{\alpha^2}{2}\mathbf{K_{TT-S}} + \theta\mathbf{K_{TT-D}} + \mathbf{K_{TT-A2}}\right. \\
&\qquad \left. + \left(\frac{1}{2} - \alpha\right)\mathbf{K_{TT-S2}}\right]\Delta\mathbf{T}_{\mathrm{e},n+1} + \left[\mathbf{K_{Tp-A}} + \left(\frac{1}{2} - \alpha\right)\mathbf{K_{Tp-S}}\right]\Delta\mathbf{p}_{\mathrm{e},n+1} \\
&\qquad = -\left[\mathbf{K_{TT-D}} + \mathbf{K_{TT-A}} + \left(\frac{1}{2} - \alpha\right)\mathbf{K_{TT-S}}\right]\mathbf{T}_{\mathrm{e},n}
\end{aligned} \tag{4.181}$$

where $\mathbf{K_{TT-D}}$ is the element thermal conductivity matrix, $\mathbf{C}$ is the element thermal capacity matrix, $\mathbf{K_{TT-A}}$ is the element advective matrix with the velocities of the previous time-step, $\mathbf{K_{TT-S}}$ is the element stabilization matrix with the velocities of the previous time-step (which results from the aplication of the α-ICG method) and $\mathbf{K_{Tp-A}}$, $\mathbf{K_{Tp-S}}$, $\mathbf{K_{TT-A2}}$

and $\mathbf{K}_{\mathbf{TT-S2}}$ are the hydro-thermal coupling matrices, with components:

$$\mathrm{C}^{(a,b)} = \left[\widetilde{\mathbb{T}}_{\mathrm{L}}^{T}\right]^{\top} \left(\int_{\Omega_J} r_{N,n+1}\ \rho c\ N_J^{T(a)} N_J^{T(b)}\, \mathrm{d}\Omega_J \right) \widetilde{\mathbb{T}}_{\mathrm{L}}^{T} \tag{4.182}$$

$$\begin{aligned}\mathrm{K}_{\mathrm{TT-D}}^{(a,b)} = &\left[\widetilde{\mathbb{T}}_{\mathrm{L}}^{T}\right]^{\top} \left(\int_{\Omega_J} r_{N,n+1} \left[\boldsymbol{\nabla}_J N_J^{T(a)}\right]^{\top} \mathbf{k}_{\mathrm{L}}^{T}\ \boldsymbol{\nabla}_J N_J^{T(b)}\, \mathrm{d}\Omega_J \right) \widetilde{\mathbb{T}}_{\mathrm{L}}^{T} \\ &+ \left[\widetilde{\mathbb{T}}_{\mathrm{N}}^{T}\right]^{\top} \left(\int_{\Omega_J} N_J^{T(a)} \check{K}_N^{T}\ N_J^{T(b)}\, \mathrm{d}\Omega_J \right) \widetilde{\mathbb{T}}_{\mathrm{N}}^{T}\end{aligned} \tag{4.183}$$

$$\mathrm{K}_{\mathrm{TT-A}}^{(a,b)} = \left[\widetilde{\mathbb{T}}_{\mathrm{L}}^{T}\right]^{\top} \left(\int_{\Omega_J} r_{N,n+1}\ \rho c\ N_J^{T(a)} \left[\mathbf{q}_{\mathrm{L},n}^{p}\right]^{\top} \boldsymbol{\nabla}_J N_J^{T(b)}\, \mathrm{d}\Omega_J \right) \widetilde{\mathbb{T}}_{\mathrm{L}}^{T} \tag{4.184}$$

$$\mathrm{K}_{\mathrm{TT-S}}^{(a,b)} = \Delta t_{n+1} \left[\widetilde{\mathbb{T}}_{\mathrm{L}}^{T}\right]^{\top} \left(\int_{\Omega_J} r_{N,n+1}\ \rho c \left(\left[\mathbf{q}_{\mathrm{L},n}^{p}\right]^{\top} \boldsymbol{\nabla}_J N_J^{T(a)} \right) \left(\left[\mathbf{q}_{\mathrm{L},n}^{p}\right]^{\top} \boldsymbol{\nabla}_J N_J^{T(b)} \right) \mathrm{d}\Omega_J \right) \widetilde{\mathbb{T}}_{\mathrm{L}}^{T} \tag{4.185}$$

$$\mathrm{K}_{\mathrm{Tp-A}}^{(a,c)} = \left[\widetilde{\mathbb{T}}_{\mathrm{L}}^{T}\right]^{\top} \left(-\frac{1}{2} \int_{\Omega_J} \rho c\ N_J^{T(a)} \left[\boldsymbol{\nabla}_J N_J^{T(b)} \widetilde{\mathbb{T}}_{\mathrm{L}}^{T} T_{\mathrm{e},n}^{(b)}\right]^{\top} \frac{\mathbf{K}_{\mathrm{L}.n}^{p}}{\gamma^f} \boldsymbol{\nabla}_J N_J^{p(c)}\, \mathrm{d}\Omega_J \right) \widetilde{\mathbb{T}}_{\mathrm{L}}^{p} \tag{4.186}$$

$$\begin{aligned}&\mathrm{K}_{\mathrm{Tp-S}}^{(a,b)} \\ &= -\frac{1}{2} \Delta t_{n+1} \left[\widetilde{\mathbb{T}}_{\mathrm{L}}^{T}\right]^{\top} \left(\int_{\Omega_J} \rho c \left(\left[\boldsymbol{\nabla}_J N_J^{T(a)}\right]^{\top} \frac{\mathbf{K}_{\mathrm{L},n}^{p}}{\gamma^f} \boldsymbol{\nabla}_J N_J^{p(c)} \right) \left(\left[\mathbf{q}_{\mathrm{L},n}^{p}\right]^{\top} \boldsymbol{\nabla}_J N_J^{T(b)} \widetilde{\mathbb{T}}_{\mathrm{L}}^{T} T_{\mathrm{e},n}^{(b)} \right) \mathrm{d}\Omega_J \right. \\ &\left. + \int_{\Omega_J} \rho c \left(\left[\mathbf{q}_{\mathrm{L},n}^{p}\right]^{\top} \boldsymbol{\nabla}_J N_J^{T(b)} \widetilde{\mathbb{T}}_{\mathrm{L}}^{T} T_{\mathrm{e},n}^{(b)} \right) \left(\left[\boldsymbol{\nabla}_J N_J^{T(a)}\right]^{\top} \frac{\mathbf{K}_{\mathrm{L},n}^{p}}{\gamma^f} \boldsymbol{\nabla}_J N_J^{p(c)} \right) \mathrm{d}\Omega_J \right) \widetilde{\mathbb{T}}_{\mathrm{L}}^{P}\end{aligned} \tag{4.187}$$

$$\begin{aligned}\mathrm{K}_{\mathrm{TT-A2}}^{(a,b)} = &\left[\widetilde{\mathbb{T}}_{\mathrm{L}}^{T}\right]^{\top} \left(\frac{\theta}{2} \int_{\Omega_J} \rho c\ N_J^{T(d)} \left[\boldsymbol{\nabla}_J N_J^{T(a)} \widetilde{\mathbb{T}}_{\mathrm{L}}^{T} T_{\mathrm{e},n}^{(d)}\right]^{\top} \frac{\mathbf{K}_{\mathrm{L},n}^{p}}{\gamma^f} b \left\{ -\boldsymbol{\nabla}_J N_J^{p(c)} \widetilde{\mathbb{T}}_{\mathrm{L}}^{p} p_{\mathrm{e},n}^{(c)} \right. \right. \\ &\left. \left. + \rho^f \mathbf{g}_{nl_1 l_2} \right\} N_J^{T(b)} \mathrm{d}\Omega_J \right) \widetilde{\mathbb{T}}_{\mathrm{L}}^{T}\end{aligned} \tag{4.188}$$

$$\begin{aligned}\mathrm{K}_{\mathrm{TT-S2}}^{(a,b)} = \frac{\theta}{2} \Delta t_{n+1} \left[\widetilde{\mathbb{T}}_{\mathrm{L}}^{T}\right]^{\top} &\left[\int_{\Omega_J} \rho c \left(\left[\boldsymbol{\nabla}_J N_J^{T(a)}\right]^{\top} \frac{\mathbf{K}_{\mathrm{L},n}^{p}}{\gamma^f} b \left\{ -\boldsymbol{\nabla}_J N_J^{p(c)} \widetilde{\mathbb{T}}_{\mathrm{L}}^{p} p_{\mathrm{e},n}^{(c)} \right. \right. \right. \\ &\left. \left. + \rho^f \mathbf{g}_{nl_1 l_2} \right\} N_J^{T(d)} \right) \left(\left[\mathbf{q}_{\mathrm{L},n}^{p}\right]^{\top} \boldsymbol{\nabla}_J N_J^{T(b)} \widetilde{\mathbb{T}}_{\mathrm{L}}^{T} T_{\mathrm{e},n}^{(b)} \right) \mathrm{d}\Omega_J \\ &+ \int_{\Omega_J} \rho c \left(\left[\boldsymbol{\nabla}_J N_J^{T(a)}\right]^{\top} \frac{\mathbf{K}_{\mathrm{L},n}^{p}}{\gamma^f} b \left\{ -\boldsymbol{\nabla}_J N_J^{p(c)} \widetilde{\mathbb{T}}_{\mathrm{L}}^{p} p_{\mathrm{e},n}^{(c)} \right. \right. \\ &\left. \left. \left. + \rho^f \mathbf{g}_{nl_1 l_2} \right\} N_J^{T(d)} \right) \left(\left[\mathbf{q}_{\mathrm{L},n}^{p}\right]^{\top} \boldsymbol{\nabla}_J N_J^{T(b)} \widetilde{\mathbb{T}}_{\mathrm{L}}^{T} T_{\mathrm{e},n}^{(b)} \right) \mathrm{d}\Omega_J \right] \widetilde{\mathbb{T}}_{\mathrm{L}}^{T}\end{aligned} \tag{4.189}$$

$$K_{L.n}^{p} = \frac{\gamma^f}{12 \mu_n} r_{N,n}^{3} \tag{4.190}$$

$$\mu_n = \mu_0\ \mathrm{e}^{-b\ \mathbf{N}_J^{T}\ \widetilde{\mathbb{T}}_{\mathrm{L}}^{T} \mathbf{T}_{\mathrm{e},n}} \tag{4.191}$$

Fully coupled solution for zero-thickness interface elements

The final fully-coupled THM system of equations for zero-thickness interface elements may be written from Eqs. (4.118), (4.147) and (4.181) as follows:

Summary 14 - Fully-coupled THM system of equations for zero-thickness interface elements.

$$\begin{aligned}
&-\left[\widetilde{\mathbb{T}}_{\mathrm{L}}^{u}\right]^{\top}\frac{1}{\theta}\int_{\Omega_J}[\mathbf{B}_J^u]^{\top}\,\boldsymbol{\sigma}'_{J,n+\theta}\,\mathrm{d}\Omega_J+\mathbf{K}_{\mathbf{up}}\;\mathbf{p}_{\mathrm{e},n}+\mathbf{K}_{\mathbf{up}}\;\Delta\mathbf{p}_{\mathrm{e},n+1}=0\\[2ex]
&(\mathbf{S}_{\mathbf{p},n+\theta}+\theta\Delta t_{n+1}\mathbf{K}_{\mathbf{pp},n+\theta})\Delta\mathbf{p}_{\mathrm{e},n+1}+(\mathbf{S}_{\mathbf{pT},n+\theta}+\theta\Delta t_{n+1}\mathbf{K}_{\mathbf{pT},n+\theta})\Delta\mathbf{T}_{\mathrm{e},n+1}\\
&\qquad+[\mathbf{K}_{\mathbf{pu}}]^{\top}\;\Delta\mathbf{u}_{\mathrm{e},n+1}-\Delta t_{n+1}\mathbf{f}^{\mathbf{p}}_{\mathrm{e},n+\theta}+\Delta t_{n+1}\mathbf{K}_{\mathbf{pp},n+\theta}\;\mathbf{p}_{\mathrm{e},n}=0\\[2ex]
&\Bigg[\frac{1}{\Delta t_{n+1}}\mathbf{C}_{n+\theta}+\alpha\mathbf{K}_{\mathbf{TT-A},n}+\frac{\alpha^2}{2}\mathbf{K}_{\mathbf{TT-S},n}+\theta\mathbf{K}_{\mathbf{TT-D},n+\theta}+\mathbf{K}_{\mathbf{TT-A2},n+\theta}\\
&\qquad+\left(\frac{1}{2}-\alpha\right)\mathbf{K}_{\mathbf{TT-S2},n+\theta}\Bigg]\,\Delta\mathbf{T}_{\mathrm{e},n+1}\\
&\qquad+\left[\mathbf{K}_{\mathbf{Tp-A},n+\theta}+\left(\frac{1}{2}-\alpha\right)\mathbf{K}_{\mathbf{Tp-S},n+\theta}\right]\Delta\mathbf{p}_{\mathrm{e},n+1}\\
&\qquad+\left[\mathbf{K}_{\mathbf{TT-D},n+\theta}+\mathbf{K}_{\mathbf{TT-A},n}+\left(\frac{1}{2}-\alpha\right)\mathbf{K}_{\mathbf{TT-S},n}\right]\mathbf{T}_{\mathrm{e},n}=0
\end{aligned}\tag{4.192}$$

Similar to the fully-coupled solution of the continuum problem and due to the non-linearity of the system of equations (4.192), the solution of the fully-coupled problem is carried out by using the Newton-Raphson (NR) iterative procedure. As described, the system to be solved is:

$$\mathbf{J}_{n+\theta}(\mathbf{x}_n,{}^{i}\Delta\mathbf{x}_{n+1})=\left.\frac{\partial\boldsymbol{\Psi}_{n+\theta}}{\partial\Delta\mathbf{x}}\right|_{\mathbf{x}_n,{}^{i}\Delta\mathbf{x}_{n+1}}=\left.\begin{pmatrix}\dfrac{\partial\boldsymbol{\Psi}^u_{n+\theta}}{\partial\Delta\mathbf{u}} & \dfrac{\partial\boldsymbol{\Psi}^u_{n+\theta}}{\partial\Delta\mathbf{p}} & \dfrac{\partial\boldsymbol{\Psi}^u_{n+\theta}}{\partial\Delta\mathbf{T}}\\ \dfrac{\partial\boldsymbol{\Psi}^p_{n+\theta}}{\partial\Delta\mathbf{u}} & \dfrac{\partial\boldsymbol{\Psi}^p_{n+\theta}}{\partial\Delta\mathbf{p}} & \dfrac{\partial\boldsymbol{\Psi}^p_{n+\theta}}{\partial\Delta\mathbf{T}}\\ \dfrac{\partial\boldsymbol{\Psi}^T_{n+\theta}}{\partial\Delta\mathbf{u}} & \dfrac{\partial\boldsymbol{\Psi}^T_{n+\theta}}{\partial\Delta\mathbf{p}} & \dfrac{\partial\boldsymbol{\Psi}^T_{n+\theta}}{\partial\Delta\mathbf{T}}\end{pmatrix}\right|_{\mathbf{x}_n,{}^{i}\Delta\mathbf{x}_{n+1}}\tag{4.193}$$

As explained for the fully-coupled resolution of the continuum problem and due to the non-linearity of the above system of equations, the resolution of the fully-coupled problem is carried out by using the Newton-Raphson (NR) iterative procedure. As described, the system to be solved is:

$$\mathbf{J}_{n+\theta}(\mathbf{x}_n,{}^{i}\Delta\mathbf{x}_{n+1})^{i+1}\delta\Delta\mathbf{x}_{n+1}=-\boldsymbol{\Psi}_{n+\theta}(\mathbf{x}_n,{}^{i}\Delta\mathbf{x}_{n+1})\tag{4.194}$$

where $\mathbf{J}_{n+\theta}$ is the Jacobian matrix defined as:

$$\mathbf{J}_{n+\theta}(\mathbf{x}_n, {}^i\Delta\mathbf{x}_{n+1}) = \left.\frac{\partial \boldsymbol{\Psi}_{n+\theta}}{\partial \Delta \mathbf{x}}\right|_{\mathbf{x}_n, {}^i\Delta\mathbf{x}_{n+1}} = \left.\begin{pmatrix} \dfrac{\partial \boldsymbol{\Psi}^u_{n+\theta}}{\partial \Delta \mathbf{u}} & \dfrac{\partial \boldsymbol{\Psi}^u_{n+\theta}}{\partial \Delta \mathbf{p}} & \dfrac{\partial \boldsymbol{\Psi}^u_{n+\theta}}{\partial \Delta \mathbf{T}} \\ \dfrac{\partial \boldsymbol{\Psi}^p_{n+\theta}}{\partial \Delta \mathbf{u}} & \dfrac{\partial \boldsymbol{\Psi}^p_{n+\theta}}{\partial \Delta \mathbf{p}} & \dfrac{\partial \boldsymbol{\Psi}^p_{n+\theta}}{\partial \Delta \mathbf{T}} \\ \dfrac{\partial \boldsymbol{\Psi}^T_{n+\theta}}{\partial \Delta \mathbf{u}} & \dfrac{\partial \boldsymbol{\Psi}^T_{n+\theta}}{\partial \Delta \mathbf{p}} & \dfrac{\partial \boldsymbol{\Psi}^T_{n+\theta}}{\partial \Delta \mathbf{T}} \end{pmatrix}\right|_{\mathbf{x}_n, {}^i\Delta\mathbf{x}_{n+1}} \tag{4.195}$$

where $\boldsymbol{\Psi}_{n+\theta}$ is the linearized residual defined by Eqs. (4.192). However, the residual is evaluated using the non-linearized Eqs. (4.118), (4.145) and (4.160). Finally, the components of $\mathbf{J}_{n+\theta}$ may be obtained as follows:

a) Partial derivative of the mechanical equation with respect to the displacement increment

$$\mathbf{J}_{\mathbf{uu}} = \frac{\partial \boldsymbol{\Psi}^u_{n+\theta}}{\partial \Delta \mathbf{u}} = \frac{\partial}{\partial \Delta \mathbf{u}} \left\{ - \left[\widetilde{\mathbb{T}}^u_{\mathrm{L}}\right]^\top \frac{1}{\theta} \int_{\Omega_J} [\mathbf{B}^u_J]^\top \ \boldsymbol{\sigma}'_{J,n+\theta} \, \mathrm{d}\Omega_J \right\} \tag{4.196}$$

Decomposing the stresses in its incremental form:

$${}^i\boldsymbol{\sigma}'_{J,n+\theta} = \boldsymbol{\sigma}'_{J,n} + \theta\, {}^i\Delta\boldsymbol{\sigma}'_{J,n+\theta} \tag{4.197}$$

and considering the tangent constitutive matrix ${}^i\mathbf{D}_{n+1}$ the stress increment may be developed as:

$${}^i\Delta\boldsymbol{\sigma}'_{J,n+1} = {}^i\mathbf{D}_{n+1}\, {}^i\Delta\boldsymbol{\varepsilon}_{n+1} = {}^i\mathbf{D}_{n+1} \mathbf{B}^u_J \ {}^i\Delta\mathbf{u}_{\mathrm{mp},n+1} \tag{4.198}$$

Substituting Eqs. (4.92) and (4.93) into Eq. (4.91) the following is obtained:

$$\begin{aligned} \mathbf{J}_{\mathbf{uu}} = \frac{\partial \boldsymbol{\Psi}^u_{n+\theta}}{\partial \Delta \mathbf{u}} &= \frac{\partial}{\partial \Delta \mathbf{u}} \left\{ \left[\widetilde{\mathbb{T}}^u_{\mathrm{L}}\right]^\top \left(- \int_{\Omega_J} [\mathbf{B}^u_J]^\top\, {}^i\mathbf{D}_{n+1} \mathbf{B}^u_J \, \mathrm{d}\Omega_J \right) \widetilde{\mathbb{T}}^u_{\mathrm{L}} \ {}^i\Delta\mathbf{u}_{\mathrm{e},n+1} \right\} \\ &= -\,{}^i\mathbf{K}_{\mathbf{uu},n+\theta}\, {}^i\Delta\mathbf{u}_{\mathrm{e},n+1} \end{aligned} \tag{4.199}$$

b) Partial derivative of the mechanical equation with respect to the fluid pressure increment

$$\mathbf{J}_{\mathbf{up}} = \frac{\partial \boldsymbol{\Psi}^u_{n+\theta}}{\partial \Delta \mathbf{p}} = \mathbf{K}_{\mathbf{up}} \tag{4.200}$$

c) Partial derivative of the mechanical equation with respect to the temperature increment

$$\mathbf{J}_{\mathbf{uT}} = \frac{\partial \boldsymbol{\Psi}^u_{n+\theta}}{\partial \Delta \mathbf{T}} = 0 \tag{4.201}$$

d) *Partial derivative of the hydraulic equation with respect to the displacement increment*

$$\begin{aligned}
\mathbf{J}_{\mathbf{pu}} &= \frac{\partial \boldsymbol{\Psi}^{p}_{n+\theta}}{\partial \Delta \mathbf{u}} = \Delta t_{n+1} \frac{\partial \mathbf{K}_{\mathbf{pp},n+\theta}}{\partial \Delta \mathbf{u}} \mathbf{p}_{\mathrm{e},n+\theta} + [\mathbf{K}_{\mathbf{pu}}]^{\top} \\
&= \Delta t_{n+1} \frac{\partial}{\partial \Delta \mathbf{u}} (\mathbf{K}_{\mathbf{pp},n+\theta}) \mathbf{p}_{\mathrm{e},n+\theta} + [\mathbf{K}_{\mathbf{pu}}]^{\top} \\
&= \Delta t_{n+1} \left\{ \left[\widetilde{\mathbb{T}}^{p}_{\mathrm{L}}\right]^{\top} \left(\int_{\Omega_J} [\boldsymbol{\nabla}_J \mathbf{N}^{p}_{J}]^{\top} \frac{1}{\gamma^f} \frac{\partial \mathbf{K}^{p}_{\mathrm{L}}(T_n)}{\partial \Delta \mathbf{u}} \, \boldsymbol{\nabla}_J \mathbf{N}^{p}_{J} \, \mathrm{d}\Omega_J \right) \widetilde{\mathbb{T}}^{p}_{\mathrm{L}} \right\} \mathbf{p}_{\mathrm{e},n+\theta} + [\mathbf{K}_{\mathbf{pu}}]^{\top}
\end{aligned} \tag{4.202}$$

where

$$\begin{aligned}
\frac{\partial \mathbf{K}^{p}_{\mathrm{L}}(T_n)}{\partial \Delta \mathbf{u}} &= \frac{\partial}{\partial \Delta \mathbf{u}} \left(\frac{\gamma^f}{12\mu_n} r^{3}_{N,n+1} \right) = \frac{\partial}{\partial \Delta \mathbf{u}} \left(\frac{\gamma^f}{12\mu_n} ([\mathbf{m}_J]^{\top} \mathbf{B}^{u}_{J} \mathbf{u}_{\mathrm{mp},n+1})^{3} \right) \\
&= \frac{\gamma^f}{4\mu_n} ([\mathbf{m}_J]^{\top} \mathbf{B}^{u}_{J} \mathbf{u}_{\mathrm{mp},n+1})^{2} [\mathbf{m}_J]^{\top} \mathbf{B}^{u}_{J} = \frac{\gamma^f}{4\mu_n} r^{2}_{N,n+1} [\mathbf{m}_J]^{\top} \mathbf{B}^{u}_{J}
\end{aligned} \tag{4.203}$$

And substituting Eq. (4.203) in Eq. (4.202) leads to:

$$\begin{aligned}
\mathbf{J}_{\mathbf{pu}} = \Delta t_{n+1} &\left\{ \left[\widetilde{\mathbb{T}}^{p}_{\mathrm{L}}\right]^{\top} \left(\int_{\Omega_J} [\boldsymbol{\nabla}_J \mathbf{N}^{p}_{J}]^{\top} \; [\mathbf{m}_J]^{\top} \mathbf{B}^{u}_{J} \frac{r^{2}_{N,n+1}}{4\mu_n} \; \boldsymbol{\nabla}_J \mathbf{N}^{p}_{J} \, \mathrm{d}\Omega_J \right) \widetilde{\mathbb{T}}^{p}_{\mathrm{L}} \right\} \mathbf{p}_{\mathrm{e},n+\theta} \\
&+ [\mathbf{K}_{\mathbf{pu}}]^{\top}
\end{aligned} \tag{4.204}$$

The same development is carried out for $\mathbf{f}^{p}_{\mathrm{e}}$ term of the hydraulic equation where $\mathbf{K}^{p}_{\mathrm{L}}(T_n)$ appears.

e) *Partial derivative of the hydraulic equation with respect to the fluid pressure increment*

$$\mathbf{J}_{\mathbf{pp}} = \frac{\partial \boldsymbol{\Psi}^{p}_{n+\theta}}{\partial \Delta \mathbf{p}} = {}^{i}\mathbf{S}_{\mathbf{p},n+\theta} + \theta \Delta t_{n+1} \, {}^{i}\mathbf{K}_{\mathbf{pp},n+\theta} \tag{4.205}$$

f) *Partial derivative of the hydraulic equation with respect to the temperature increment*

$$\mathbf{J}_{\mathbf{pT}} = \frac{\partial \boldsymbol{\Psi}^{p}_{n+\theta}}{\partial \Delta \mathbf{T}} = {}^{i}\mathbf{S}_{\mathbf{pT},n+\theta} + \theta \Delta t_{n+1} \, {}^{i}\mathbf{K}_{\mathbf{pT},n+\theta} \tag{4.206}$$

g) *Partial derivative of the thermal equation with respect to the displacement increment*

$$
\begin{aligned}
\mathbf{J}_{\mathbf{Tu}} = \frac{\partial \boldsymbol{\Psi}^T_{n+\theta}}{\partial \Delta \mathbf{u}} &= \frac{\partial\left(\left[\mathbf{K}_{\mathbf{TT-D},n+\theta} + \mathbf{K}_{\mathbf{TT-A},n} + (\frac{1}{2} - \alpha)\mathbf{K}_{\mathbf{TT-S},n}\right]\right)}{\partial \Delta \mathbf{u}} \mathbf{T}_{\mathrm{e},n} \\
&= \left[\widetilde{\mathbb{T}}_{\mathrm{L}}^{T}\right]^{\top} \left(\int_{\Omega_J} [\mathbf{m}_J]^{\top} B_J^{u\,(a)} \left[\boldsymbol{\nabla}_J N_J^{T(c)}\right]^{\top} \mathbf{k}_{\mathrm{L}}^{T}\ \boldsymbol{\nabla}_J N_J^{T(b)}\, \mathrm{d}\Omega_J \right. \\
&+ \int_{\Omega_J} \rho c\, [\mathbf{m}_J]^{\top}\ B_J^{u\,(a)} N_J^{T(c)} \left[\mathbf{q}^{p}_{\mathrm{L},n}\right]^{\top} \boldsymbol{\nabla}_J N_J^{T(b)}\, \mathrm{d}\Omega_J \\
&+ \left. \int_{\Omega_J} \rho c\, [\mathbf{m}_J]^{\top} B_J^{u\,(a)} \left(\left[\mathbf{q}^{p}_{\mathrm{L},n}\right]^{\top} \boldsymbol{\nabla}_J N_J^{T(c)}\right) \left(\left[\mathbf{q}^{p}_{\mathrm{L},n}\right]^{\top} \boldsymbol{\nabla}_J N_J^{T(b)}\right) \mathrm{d}\Omega_J \right) \widetilde{\mathbb{T}}_{\mathrm{L}}^{T} T_{\mathrm{e},n}^{(b)}
\end{aligned}
\tag{4.207}
$$

h) *Partial derivative of the thermal equation with respect to the fluid pressure increment*

$$
\mathbf{J}_{\mathbf{Tp}} = \frac{\partial \boldsymbol{\Psi}^T_{n+\theta}}{\partial \Delta \mathbf{p}} = {}^{i}\mathbf{K}_{\mathbf{Tp-A},n+\theta} + \left(\frac{1}{2} - \alpha\right) {}^{i}\mathbf{K}_{\mathbf{Tp-S},n+\theta}
\tag{4.208}
$$

i) *Partial derivative of the thermal equation with respect to the temperature increment*

$$
\begin{aligned}
\mathbf{J}_{\mathbf{TT}} = \frac{\partial \boldsymbol{\Psi}^T_{n+\theta}}{\partial \Delta \mathbf{T}} &= \frac{1}{\Delta t_{n+1}} \mathbf{C}_{n+\theta} + \alpha\, {}^{i}\mathbf{K}_{\mathbf{TT-A},n} + \frac{\alpha^2}{2}\, {}^{i}\mathbf{K}_{\mathbf{TT-S},n} + \theta\, {}^{i}\mathbf{K}_{\mathbf{TT-D},n+\theta} \\
&+ {}^{i}\mathbf{K}_{\mathbf{TT-A2},n+\theta} + \left(\frac{1}{2} - \alpha\right) {}^{i}\mathbf{K}_{\mathbf{TT-S2},n+\theta}
\end{aligned}
\tag{4.209}
$$

4.4. Mechanical constitutive law for interfaces

The mechanical constitutive law for interfaces used in this work is presented in this section.

4.4.1. Constitutive model definition

The mechanical constitutive law for interfaces used in this thesis is an elasto-plastic law based in fracture mechanics, which was originally proposed by Carol & Prat (1990, 1995) and subsequently modified by Carol, et al. (1997, 2001), and López (1999) for 2D analysis and extended to 3D by Caballero, et al. (2008). This model has been successfully applied to 2D (Carol et al. 2001, Garolera et al. 2005, López 1999, Roa et al. 2002, Segura 2007, Idiart et al. 2011) and 3D analysis (Caballero, et al., 2008. Pérez 2013 and Riera 2016),

The constitutive law establishes the relation between deformations and stresses, and, in the particular case of the double-nodded zero-thickness interface elements described in Section 3.1, the constitutive law is formulated in terms of the normal and the two tangential components of stress ($\boldsymbol{\sigma}_J$) and the corresponding relative displacements ($\mathbf{r}$) at the mid-plane of the interface using a local orthogonal reference system (Figure 4.3).

$$\boldsymbol{\sigma}_J = (\sigma \quad \tau_1 \quad \tau_2) \tag{4.210}$$

$$\mathbf{r} = (r_1 \quad r_{l_1} \quad r_{l_2}) \tag{4.211}$$

In continuum model formulations the displacements could be usually obtained by integrating the strain over length ($u = \int \epsilon \; ds$). However, by definition, the interface elements have no thickness, and therefore $ds = 0$. To avoid this inconsistency, the constitutive model is formulated in terms of stresses and relative displacements.

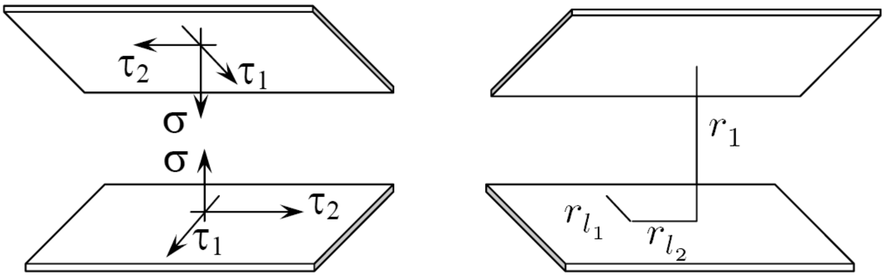

Figure 4.3: Definition of stress variables and conjugate strain variables (relative displacements) for the interface (Caballero, 2005).

4.4.2. Cracking surface

As the constitutive model is based in the theory of the plasticity, the material behaviour is controlled by a yield surface that in this case is a fracture surface. F, which is defined by:

$$F = F(\boldsymbol{\sigma}, \kappa) \tag{4.212}$$

where $\boldsymbol{\sigma}$ is the stress field and κ is a generic variable which contains the necessary parameters to define F. As for the classic theory of plasticity, this fracture surface delimits the state of any current stress situation, which can be divided in: (a) when $F = 0$ the stress $\boldsymbol{\sigma}$ is on F and (b) when $F < 0$ the stress $\boldsymbol{\sigma}$ is inside F. The situation $F > 0$ is not admissible. Cracking begins when the mid-plane stresses of the interface reaches the condition $F = 0$, while the behaviour is linear elastic for $F < 0$.

The cracking surface of this model is defined by the following three-parameter hyperboloid proposed by Carol & Prat (1990):

$$F\big(\boldsymbol{\sigma}, \mathbf{p}(W^{cr})\big) = |\tau|^2 - (c - \sigma \; \tan\phi)^2 + (c - \chi \; \tan\phi)^2 \tag{4.213}$$

This hyperbola was modified by Caballero, et al. (2008) in order to avoid numerical problems caused by double solution inherent to hyperbola's equation, obtaining finally:

$$F\big(\boldsymbol{\sigma}, \mathbf{p}(W^{cr})\big) = \sigma \; \tan\phi + \sqrt{\tau^2 + (c - \chi \; \tan\phi)^2} - c \tag{4.214}$$

where τ is the modulus of the shear stresses $\left(\tau = \|\boldsymbol{\tau}\| = \sqrt{\tau_1^2 + \tau_2^2}\right)$, σ is the normal stress, χ is the vertex of the hyperbola representing the tensile strength, c is the apparent cohesion (intersection point between τ and the asymptote) and tanϕ is the slope of the asymptote, which physically represents an asymptotic friction angle (Figure 4.4).

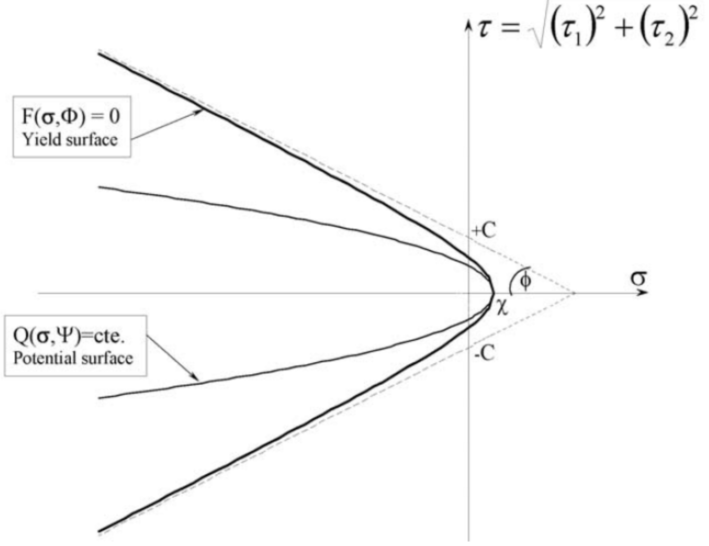

Figure 4.4: Graphic representation of the hyperbolic yield surface (F) and plastic potential (Q). (Caballero, 2005)

4.4.3. Plastic potential (dilatancy)

The classical theory of the plasticity assumes that the total strain may be decomposed in the sum of elastic and plastic (or non-recoverable) strains. However, as the cracking surface, the model must be expressed in terms of the relative displacements of the interface elements. Thus, the total relative displacements ($\mathbf{r}$) contains an elastic part ($d\mathbf{r}^e$) and a plastic or fracture component ($d\mathbf{r}^{cr}$):

$$d\mathbf{r} = d\mathbf{r}^e + d\mathbf{r}^{cr} \tag{4.215}$$

with:

$$d\mathbf{r}^{cr} = d\lambda \frac{\partial Q}{\partial \boldsymbol{\sigma}_\mathbf{J}} = d\lambda\ \boldsymbol{m}_Q \tag{4.216}$$

where Q is the plastic potential (or fracture potential), $d\lambda$ is the fracture multiplier and $\boldsymbol{m}_Q$ is the gradient of Q.

The history variable is the work spent during the fracture process, which can be written in its incremental form as follows:

$$dW^{cr} = \begin{cases} \boldsymbol{\sigma}_J \cdot d\mathbf{r}^{cr} = d\lambda\ \boldsymbol{\sigma}_J \cdot \boldsymbol{m}_Q & \text{if } \sigma \geq 0 \quad (\textit{tension}) \\ (|\tau| + \sigma\ \tan\phi)|d\mathbf{r}_l^{cr}| & \text{if } \sigma < 0 \quad (\textit{compresion}) \end{cases} \tag{4.217}$$

where $d\mathbf{r}_l^{cr}$ is the increment of relative crack opening displacements in the tangential direction defined by:

$$d\mathbf{r}_l^{cr} = \sqrt{d\mathbf{r}_{l_1}^{cr2} + d\mathbf{r}_{l_2}^{cr2}} \tag{4.218}$$

From the preceding equations it may be deduced that, in tension, all plastic work dissipated is used for the formation of the crack, while for compression, the work dissipated also includes a significant contribution of frictional processes (heat) that does not contribute to W^{cr} (Caballero, 2005).

In heterogeneous materials, such as rocks or concrete, the cracking paths exhibit some roughness due to their tendency to propagate along the weakest areas of the material (e.g. particle-matrix contacts). Thus, under a constant normal stress level, the shear phenomena will in general produce shear strains and also normal crack opening of the interfaces (dilatancy). Using the theory of the plasticity, the direction of dilatancy (direction of the fracture deformation vector at each point) is perpendicular to the cracking potential Q (flow rule) and the dilatancy angle can be interpreted as the angle between the gradient of Q and the shear axis τ. Consequently, a direction parallel to the shear axis indicates no dilatancy, while a direction parallel to the normal stress axis indicates a fracture opening without tangential displacement (e.g. pure tension test). Some experimental results for quasi-brittle materials, such as rocks or concrete, show that dilatancy diminishes as the compression stress increases and finally disappears for levels of compressive stress larger than a certain value (Amadei, et al., 1989). In addition, as observed by Pande, et al. (1990), the joint dilatancy decreases with its degradation.

In order to reproduce the dilatancy phenomenon the constitutive model must be non-associated ($Q \neq F$), and the fracture potential Q (Figure 4.4) can be defined depending on the fracture surface by using the following expressions:

$$\boldsymbol{m}_Q = \frac{\partial Q}{\partial \boldsymbol{\sigma}_J} = \mathbf{A}\ \mathbf{n} \tag{4.219}$$

$$\boldsymbol{n} = \frac{\partial F}{\partial \boldsymbol{\sigma}_J} = \begin{pmatrix} \dfrac{\partial F}{\partial \sigma} \\ \dfrac{\partial F}{\partial \tau_1} \\ \dfrac{\partial F}{\partial \tau_2} \end{pmatrix} = \begin{pmatrix} \tan\phi \\ \dfrac{\tau_1}{\sqrt{|\tau|^2 + (c + \chi\ \tan\phi)^2}} \\ \dfrac{\tau_2}{\sqrt{|\tau|^2 + (c + \chi\ \tan\phi)^2}} \end{pmatrix} \tag{4.220}$$

$$\mathbf{A} = \begin{pmatrix} f_c^{dil} f_\sigma^{dil} & 0 & 0 \\ 0 & 1 & 0 \\ 0 & 0 & 1 \end{pmatrix} \tag{4.221}$$

where f_c^{dil} and f_σ^{dil} are defined in the following section. It must be noticed that if $\mathbf{A}$ is equal to the identity tensor, then the constitutive model becomes associated ($Q = F$).

4.4.4. Evolution Law

The evolution of the fracture surface and the fracture potential is defined by the reduction of the parameters that defines the fracture surface (Eq. (4.214)): tensile strength (χ), cohesion (c) and friction angle (tanϕ), in function of the work spent (W^{cr}) during the fracture process (Eq.(4.217)).

Starting from an initial fracture surface (Figure 4.4), the final configuration will depend on the mode of fracture taking place. For pure tension (Mode I) a completed developed crack requires the total separation of the two sides of the interface, obtaining a final fracture surface defined by a hyperbola with vertex at the origin (curve 2 in Figure 4.5). For a situation under shear and very high compression with no dilatancy (Mode IIa), the final fracture surface is defined by a pair of straight lines representing pure frictional behaviour (curve 4 of Figure 4.6). The evolution of the fracture surface results in its shrinkage, as shown in Figure 4.5 and Figure 4.6. The parameters that control the two fracture modes are the classical fracture energy in Mode I (G_F^I, pure tension), and the Mode IIa energy (G_F^{IIa}, shear under high compression).

The mentioned parameters of the hyperbola decrease from their initial values depending on the work spent during the fracture process (W^{cr}), following a scale function S defined by Carol & Prat (1990):

$$S(\xi, \alpha) = \frac{e^{-\alpha}\xi}{1 + (e^{-\alpha} - 1)\xi} \tag{4.222}$$

where ξ is the generic property to be scaled and α is the scaling factor. The evolution of the parameters χ, c and tanϕ are defined by the following paragraphs.

Evolution of χ

The tensile strength decreases from its initial value (χ_0) as W^{cr} increases, becoming zero when $W^{cr} = G_I^F$. The scaling function $S(\xi_\chi, \alpha_\chi)$ defined in Eq. (4.222) is applied taking $\xi_\chi = W^{cr}/G_I^F$ and $\alpha = \alpha_\chi$ (Figure 4.8). The evolution is given by the following expression:

$$\chi = \begin{cases} \chi_0 \left(1 - S(\xi_\chi, \alpha_\chi)\right) & \text{if } W^{cr} < G_I^F \\ 0 & \text{if } W^{cr} \geq G_I^F \end{cases} \tag{4.223}$$

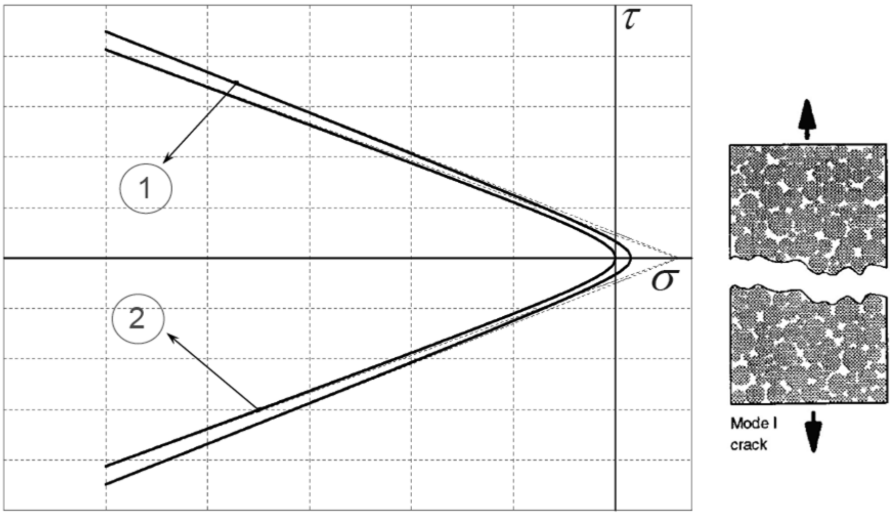

Figure 4.5: Evolution of the fracture surface from the initial state (1) to the final state (2) after exhausting the pure tensile strength of the material (fracture Mode I). (Caballero, 2005)

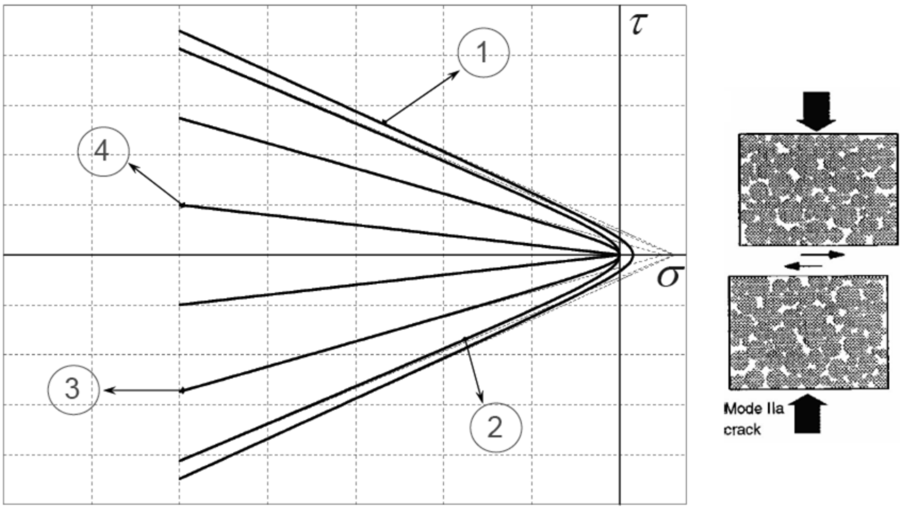

Figure 4.6: Evolution of the fracture surface from the initial state (1) to the final state after exhausting the pure tensile strength of the material (curve 2) and after applying the load in Mode IIa, resulting in a final state with residual pure shear (4). (Caballero, 2005)

Evolution of c

The reduction of the cohesion can be calculated by using χ, tanϕ and a new parameter "a" representing the horizontal distance between the vertex of the hyperbola and its asymptotes:

$$c = (\chi + a)\tan\phi \tag{4.224}$$

Then, assuming that the parameter "a" changes from its initial value (obtained from Eq. (4.224) by using the initial values of c, χ and tanϕ) to zero when $W^{cr} = G^{F}_{IIa}$, the parameters of the scaling function $S(\xi_a, \alpha_a)$ are $\xi_a = W^{cr}/G^F_{IIa}$ and $\alpha = \alpha_a$ (Figure 4.8). The evolution is given by the following expression:

$$\chi = \begin{cases} c_0 \left(1 - S(\xi_a, \alpha_a) - \dfrac{\chi_0}{c_0} \tan\phi (S(\xi_\chi, \alpha_\chi) - S(\xi_a, \alpha_a))\right) & \text{if } W^{cr} < G^F_{IIa} \\ 0 & \text{if } W^{cr} \geq G^F_{IIa} \end{cases} \tag{4.225}$$

Evolution of tanϕ

The friction angle decreases from its initial value tanϕ_0) as W^{cr} increases, becoming the residual friction angle tanϕ_{res} when $W^{cr} = G^F_{IIa}$. The scaling function $S(\xi_\phi, \alpha_\phi)$ defined in Eq. (4.222) is applied taking $\xi_\phi = W^{cr}/G^F_{IIa}$ and $\alpha = \alpha_\phi$ (Figure 4.8). The evolution is given by the following expression:

$$\tan\phi = \begin{cases} \tan\phi_0 - (\tan\phi_0 - \tan\phi_{res}) S(\xi_\phi, \alpha_\phi) & \text{if } W^{cr} < G^F_{IIa} \\ \tan\phi_{res} & \text{if } W^{cr} \geq G^F_{IIa} \end{cases} \tag{4.226}$$

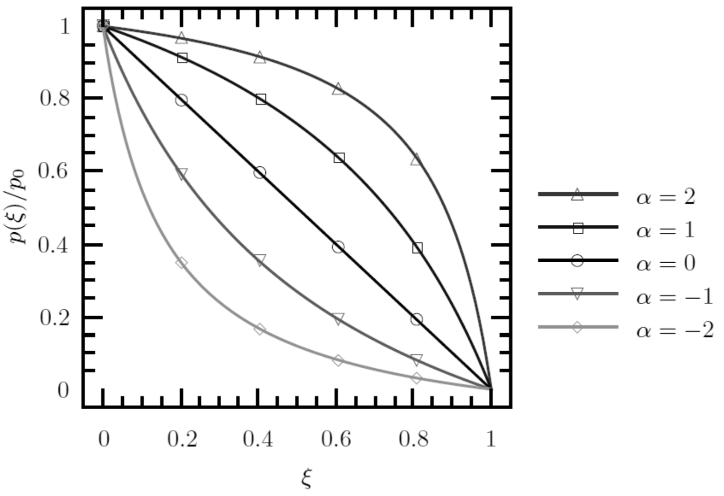

Figure 4.7: Evolution law (Garolera, 2017).

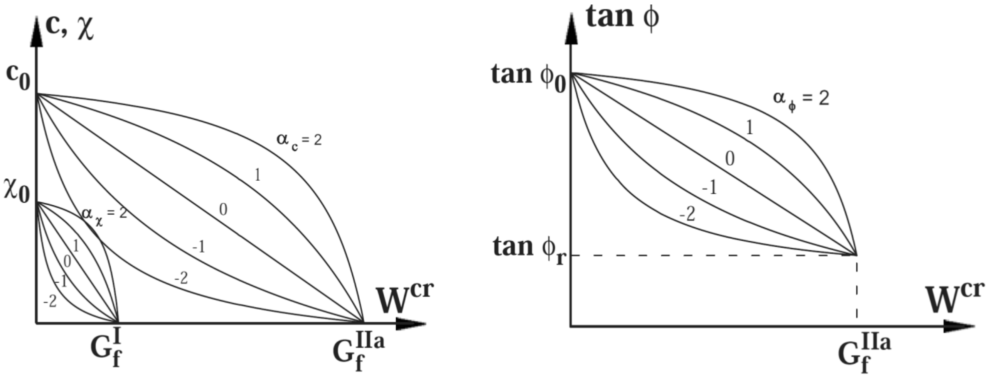

Figure 4.8: Evolution of the tensile strength (χ), the cohesion (c) and the friction angle ($tan\phi$) with the work spent by the fracture process W^{cr} (López, 1999).

Evolution of f_c^{dil} and f_σ^{dil}

As discussed in Section 4.4.3, the effects of dilatancy are introduced by reducing the normal component of matrix **A** using the parameters f_c^{dil} and f_σ^{dil}. Both parameters vary depending on the different parameters involved in the fracture process.

First, dilatancy varies with the intensity of the compressive stress, and it is cancelled when the compression reaches the pre-defined value σ_{dil}, that is the value of the normal compression stress for which the dilatancy is zero. The function decreases from 1 to 0 (Figure 4.9) following the expression:

$$f_\sigma^{dil} = 1 - S\left(\frac{\sigma}{\sigma_{dil}}, \alpha_{\sigma_{dil}}\right) \tag{4.227}$$

Finally, dilatancy decreases as the interface suffers degradation, and it is cancelled when the surface F reaches its state of residual friction (curve 4 in Figure 4.6):

$$f_c^{dil} = 1 - S\left(\frac{W^{cr}}{G_{IIa}^F}, \alpha_{c_{dil}}\right) \tag{4.228}$$

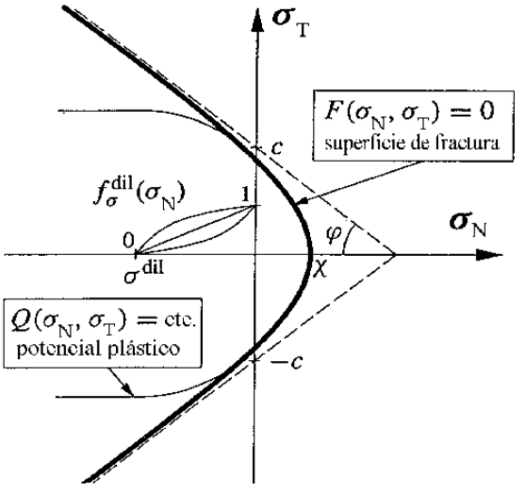

Figure 4.9: Graphic representation of the hyperbolic yield surface (F) and plastic potential (Q) (López, 1999).

4.4.5. Constitutive integration

The integration of the constitutive model is performed using an implicit integration algorithm (backward Euler) with substepping (López, 1999), where the system is solved taking into account the stresses ($\boldsymbol{\sigma}_J$), the history variable (W^{cr}) and the plastic multiplier (λ), as it is explained in detail by Caballero (2005), based on the previous work of Pérez-Foguet, et al. (2001).

In addition, a more accurately description of the interface constitutive law can be found in Carol, et al. (1997, 2001) or López (1999), and details of its numerical implementation in Caballero, et al. (2008).

Chapter 5

THM model verification and practical applications

In the preceding chapter a THM fully-coupled model with large advection for porous medium and zero-thickness interface elements has been developed. This chapter presents the verification of the numerical model and a practical application. The first section deals with the numerical verification of the THM model by means of several academic examples. The second section focuses in the numerical solution of hydraulic fracture problems using the THM model, its comparison with results from a HM numerical analysis and a performance parallelization analysis.

5.1. THM model verification examples

This section presents verification examples of the THM fully-coupled model with large advection developed in Chapter 4 for the continuum medium and for zero-thickness interface elements.

5.1.1. THM model verification examples for continuum medium

Six verification examples of the THM fully-coupled model with large advection developed in Chapter 4 for the continuum medium are discussed in the following paragraphs. Summarizing, the main verifications focus on:

1) the mechanical effects due to thermal expansions (thermo-mechanical coupling),
2) the advective heat transport with the hydraulic flow using the α-Implicit Characteristic Galerkin Method (hydro-thermal coupling) and,

3) the influence of thermal variations in a porous medium, in particular the influence of the solid and fluid expansions, the pressure and stress-strain variations and the generated fluxes (thermo-hydro-mechanical coupling).

Verification example 1: Thermo-Mechanical coupling in continuum medium

The objective of this example is to verify the thermo-mechanical coupling of the model (thermal expansion), comparing the numerical and analytical solutions.

The geometry consists of a domain of 20×5m (Figure 5.1), discretized with 100 quadrilateral continuum elements, where a temperature is applied at the left-hand side of the domain –as a Dirichlet condition– and with no mechanical restriction preventing the free thermal expansion of the material. The boundary conditions and the material parameters of the numerical analysis are shown in Figure 5.1.

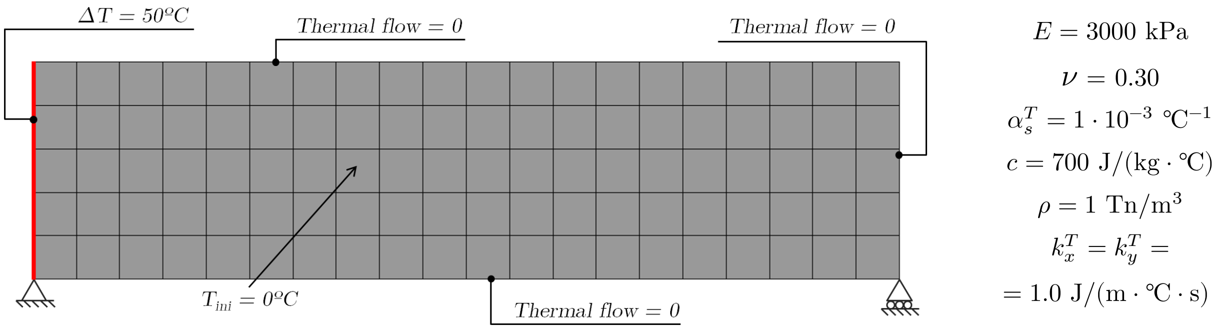

Figure 5.1: Mesh, boundary conditions and material properties of the TM verification example.

The transient analysis takes place under plane stress conditions with a linear elastic material and the effect of the gravity is omitted. Additionally, since there is no coupling with the hydraulic problem, the heat transfer mode is pure conduction.

Figure 5.2 shows the advance of temperature with time in a deformed mesh until reaching steady-state conditions, when the temperature of the full domain is the same as the imposed at the left-hand side. At this point, the maximum displacements obtained with the analysis are: $\Delta u_{max,x} = 1.00$ m and $\Delta u_{max,y} = 0.25$ m.

On the other hand, the analytical solution of the problem, considering that the material can expand freely during the analysis, gives the following results:

$$\Delta \varepsilon^T = \alpha_s^T \; \Delta T = 0.05 \tag{5.1}$$

$$\Delta u_{max,x} = \Delta \varepsilon^T \; L_x = 0.05 \times 20 \text{ m} = 1.00 \text{ m} \tag{5.2}$$

$$\Delta u_{max,y} = \Delta \varepsilon^T \; L_y = 0.05 \times 5 \text{ m} = 0.25 \text{ m} \tag{5.3}$$

These results show that the numerical and the analytical solutions match successfully. Additionally, the stress field remains constant and equal to zero during the analysis as expected for a free thermal expansion problem.

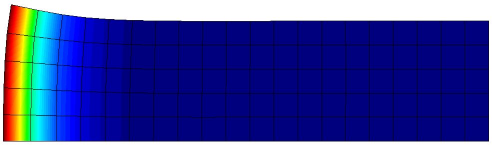

(a) t = 17 min.

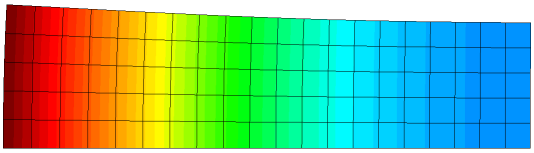

(b) t = 1017 min.

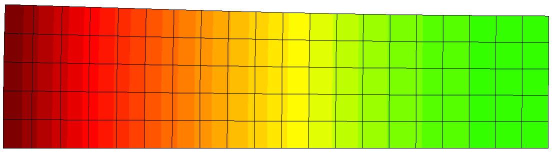

(c) t = 2017 min.

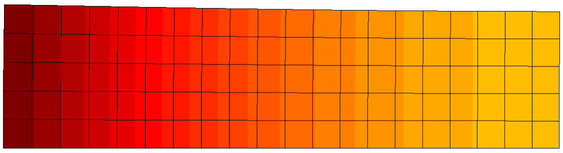

(d) t = 3017 min.

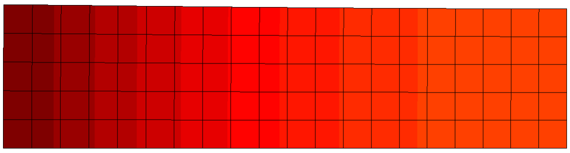

(d) t = 4017 min.

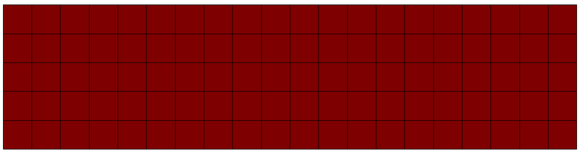

(d) t → ∞ (Steady-state)

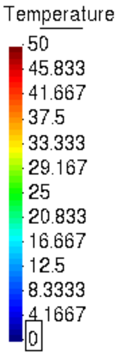

Figure 5.2: Temperature distribution (°C) for different times and deformed mesh (×4).

The numerical analysis has been computed under plane strain conditions, obtaining a final displacement (t → ∞) of $\Delta u_{max,x} = 1.25$ and $\Delta u_{max,y} = 0.3125$, that corresponds with a strain of $\Delta \varepsilon^T = 0.0625$, and an out-of-plane stresses equal to $\Delta\sigma_z = -150$ kPa, that matches the values obtained analytically:

$$\Delta\varepsilon^T = (1+\nu)\alpha_s^T\ \Delta T = 0.0625 \tag{5.4}$$

$$\Delta\sigma_z = -E'\alpha_s^T\Delta T = -3000\ \text{kPa}\cdot 0.001℃^{-1}\cdot 50℃ = -150\ \text{kPa} \tag{5.5}$$

Moreover, the plane stress analysis has been carried out considering that the displacements are prescribed at the four boundaries of the domain ($u_x = u_y = 0$), so that it cannot expand due to the thermal changes, and subsequently leads to thermal stresses that may be calculated analytically (assuming plane stress conditions) as:

$$\Delta\sigma^T = -\frac{E}{1-\nu^2}\Delta\varepsilon^T(1+\nu) \tag{5.6}$$

Considering the steady-state distribution of temperatures ($t\ \rightarrow \infty$) and the induced thermal strains from Eq. (5.1), the following stress increment due to the prevented thermal expansion is obtained:

$$\Delta\sigma^T = -\frac{3000\ \text{kPa}}{1-0.25^2}0.05(1+0.25) = -200\ \text{kPa} \tag{5.7}$$

that matches the result obtained in the numerical analysis. Therefore, it can be concluded that the TM model leads to correct solutions.

Verification example 2: Hydro-Thermal coupling in continuum medium without fluid thermal expansion and constant fluid viscosity

The objective of this example is to verify the hydro-thermal coupling of the model, in particular the stability of the advection phenomenon that occurs due to the existence of the fluid flow and its correct velocity transport. For simplicity, the following assumptions are made: pure advection, constant fluid viscosity, no volume change of the fluid due to thermal effects ($\alpha_f^T = 0$) and gravity omitted for the hydraulic problem.

The geometry consists of a domain of 450×10m, discretized with 180 quadrilateral continuum elements, as shown in Figure 5.3 with the material parameters of the numerical analysis.

$K^f = 3\cdot 10^{12}$ kPa

$\gamma^f = 10$ kN/m^3

$\mu^f = 1\cdot 10^{-11}$kPa · s

$\alpha_f^T = 0℃^{-1}$

$c = 700$ J/(kg · ℃)

$\rho = 2000$ kg/m^3

$k_x^T = k_y^T = 0$ J/(m · ℃ · s)

$k_x^p = k_y^p = 9\cdot 10^{-13}$ m^2

$\alpha_{ICG} = 0.25$

Figure 5.3: Mesh and material properties of the HT verification example.

In a first step the temperature of the domain is equal to zero and the steady-state hydraulic problem is solved considering the boundary conditions shown in Figure 5.4. The results of this step are shown in Figure 5.5 (lineal distribution of pressures). The Darcy velocity obtained from the numerical analysis is 0.006 m/s (from the left to the right), which matches the analytical solution:

$$q_x^p = -\frac{k_x^p}{\mu^f}\left(\frac{\Delta p}{L}\right) = -\frac{9 \cdot 10^{-13}\ \mathrm{m}^2}{1 \cdot 10^{-11}\ \mathrm{kPa/s}}\left(\frac{20 - 50\ \mathrm{kPa}}{450\ \mathrm{m}}\right) = 0.006\ \mathrm{m/s} \tag{5.8}$$

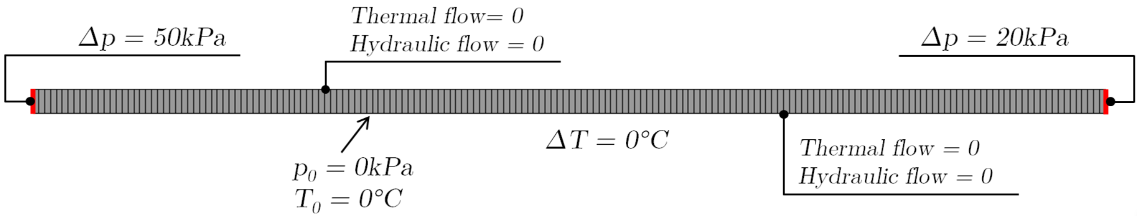

Figure 5.4: Boundary conditions for the first step of the HT verification example.

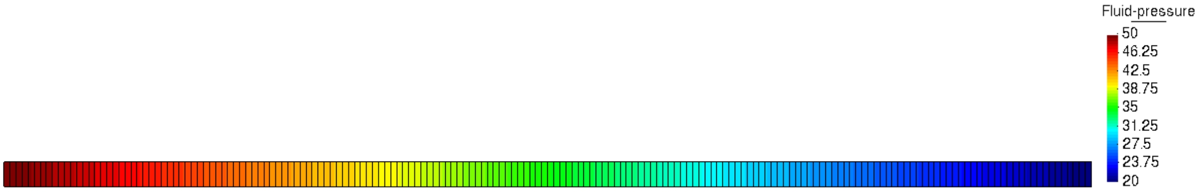

Figure 5.5: Fluid pressure distribution for the first step of the HT verification example.

In a second step, a Gaussian distribution of temperatures is applied as a Dirichlet condition (Figure 5.6) while the fluid flow remains constant (Figure 5.7).

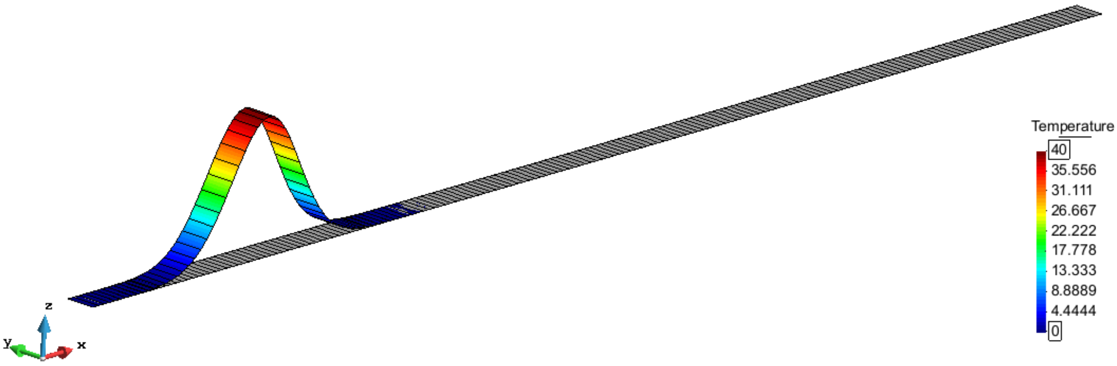

Figure 5.6: Initial distribution of temperatures for the second step of the HT verification example.

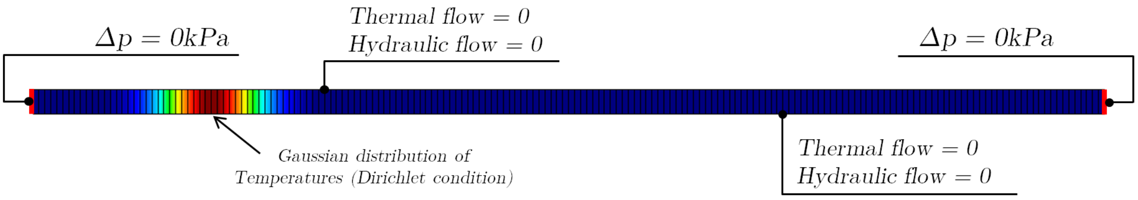

Figure 5.7: Boundary conditions for the second step of the HT verification example (Legend in Figure 5.6).

The thermal conductivity is assumed equal to zero and therefore the Péclet number tends to infinite (pure advection thermal problem). The analysis of the transient problem is carried out with time increments $\Delta t = 350$ s.The Courant number in all the elements of the mesh is less than 1 ($C = 0.84$), which is a necessary condition to obtain a non-oscillatory result using the method of characteristics.

As the time passes, the initial temperature distribution has to move from left to right with the correct velocity (0.006 m/s) while keeping the initial temperature distribution profile. The result of the analysis is shown in Figure 5.8 and Figure 5.9 for different times. These figures show that the method maintains the initial distribution of temperatures with small oscillations of ±0.10℃ at the top of the "bell".

The last verification consists in checking whether the velocities applied to the thermal distribution corresponds with the Darcy velocity of the fluid. For example, for $\Delta t = 31150$ s and knowing that the Darcy velocity of the fluid is $q_x^p = 0.006$ m/s, the top of the “bell” of the initial distribution has moved to the right $\Delta x = q_x^p \; \Delta t = 186.9$ m, which matches the displacement of the initial temperature distribution, as shown in Figure 5.8.

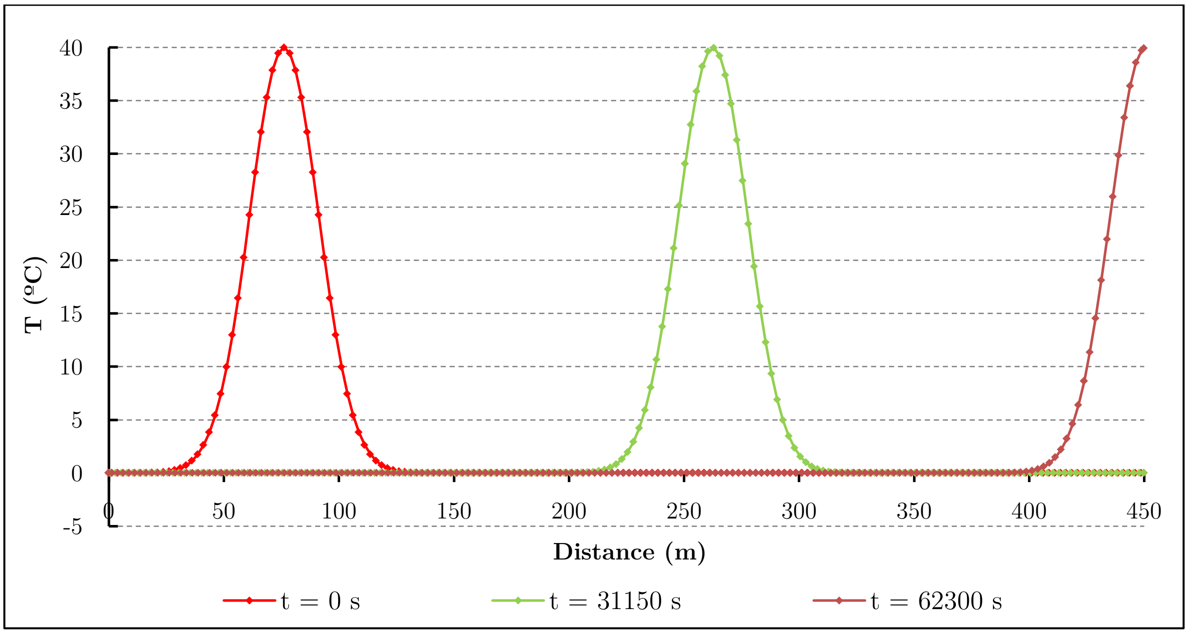

Figure 5.8: Distribution of temperatures using the α-ICG Method for different times using $\alpha_{ICG} = 1/4$.

(a) t = 0 s.

(b) t = 31150 s.

(c) t = 62300 s.

Figure 5.9: Distribution of temperatures using the α-ICG Method for different times using $\alpha_{ICG} = 1/4$ (Legend in Figure 5.6).

Additionally, during the transient analysis the pressures and Darcy velocity remain constant as expected with the hypothesis of the problem (constant viscosity of the fluid and no volume change of the fluid due to its thermal expansion).

Verification example 3: Hydro-mechanical coupling in continuum medium.

In order to verify the hydro-mechanical coupling of the model, the analysis of a one-dimensional consolidation problem of a saturated porous medium has been carried out. This example is based in a verification example of the HM model that appears in Segura (2007).

The geometry consists of a domain of 1×1m, discretized with 100 quadrilateral continuum elements. The geometry, the initial and boundary conditions and the material parameters are shown in Figure 5.10. The problem has an initial geostatic fluid pressure distribution, with an applied load of 15 kPa. Consolidation starts after this load is applied. For the analysis, gravity is omitted and linear elasticity is assumed under plane strain conditions.

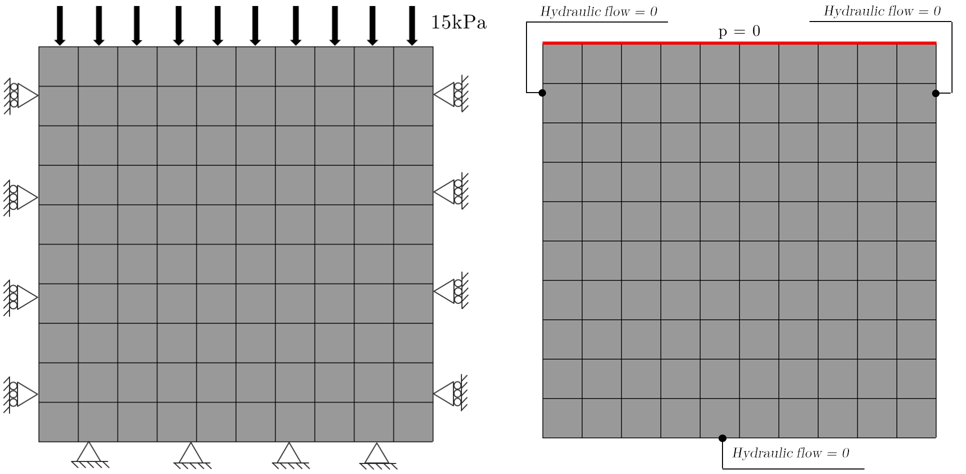

Linear elasticity

Plain strain

$E' = 1200$ kPa

$\nu' = 0.25$

$K^s = 1 \cdot 10^{10}$ kPa

$K^f = 3 \cdot 10^{12}$ kPa

$\gamma^f = 10$ kN/m^3

$\mu = 1 \cdot 10^{-11}$ kPa $\cdot$ d

$k^p = 1.5 \cdot 10^{-13}$ m^2

$\alpha_{Biot} = 1.0$

Figure 5.10: Mesh, initial and boundary conditions and material parameters for the HM verification problem.

Figure 5.11 shows the evolution of the fluid pressures with time on a deformed mesh. The figure shows the dissipation of the excess fluid pressure with time, and its proportionality to the settlement, as expected from a HM-coupling analysis.

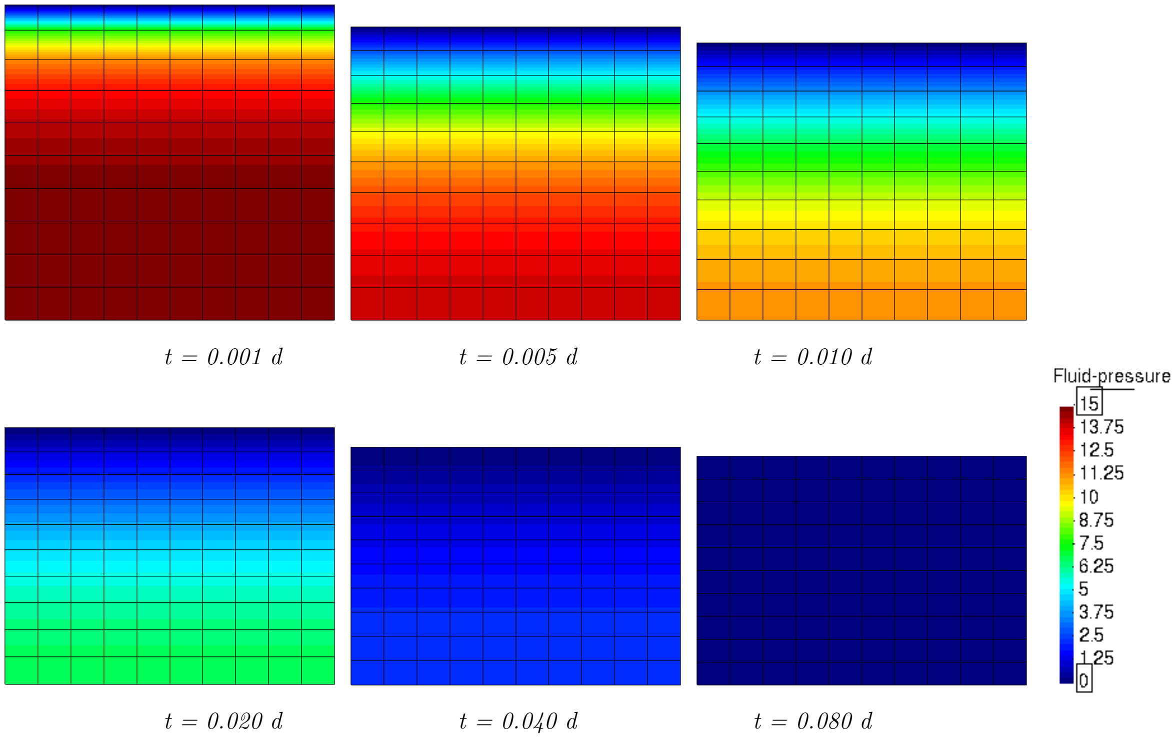

Figure 5.11: Fluid pressure evolution on the deformed mesh (factor ×30).

The final settlement can be obtained analytically as:

$$s_t = \frac{1}{E_m} Q_{load} \tag{5.9}$$

where E_m is the oedometric modulus that may be obtained as:

$$E_m = E' \left[\frac{1-\nu'}{1-\nu'-2\nu'^2} \right] = 1500 \text{ kPa} \left[\frac{1-0.25}{1-0.25-2\cdot 0.25^2} \right] = 1440 \text{ kPa} \tag{5.10}$$

Then the final settlement is:

$$s_t = \frac{1}{1440 \text{ kPa}} 15 \text{ kPa} \cdot \text{m} = 1.04 \text{ cm} \tag{5.11}$$

that matches the final settlement obtained with the numerical analysis.

Figure 5.12 and Figure 5.13 shows the fluid pressure evolution with depth and the settlement evolution computed with the FEM code. These solutions can also be calculated analytically combining the fluid mass balance equation and Darcy's law, obtaining the following expressions (Segura, 2007):

$$p = \sum_{m=0}^{m=\infty} \frac{2p_{ini}}{M} \sin(M\mathrm{Y}) \cdot e^{-M^2 T} \tag{5.12}$$

$$U_Y(\%) = 1 - \sum_{m=0}^{m=\infty} \frac{2}{M} \sin(MY) \cdot e^{-M^2 T} \tag{5.13}$$

where $M = \frac{\pi}{2}(2m+1)$ with $m = 0,1,2,...$ and C_v is the consolidation coefficient defined as:

$$C_v = \frac{k^p}{\mu} E_m = 21.6\ \mathrm{m}^2/\mathrm{d} \tag{5.14}$$

and the dimensionless variables:

$$Y = \frac{y}{H} \tag{5.15}$$

$$T = \frac{C_v t}{H^2} \tag{5.16}$$

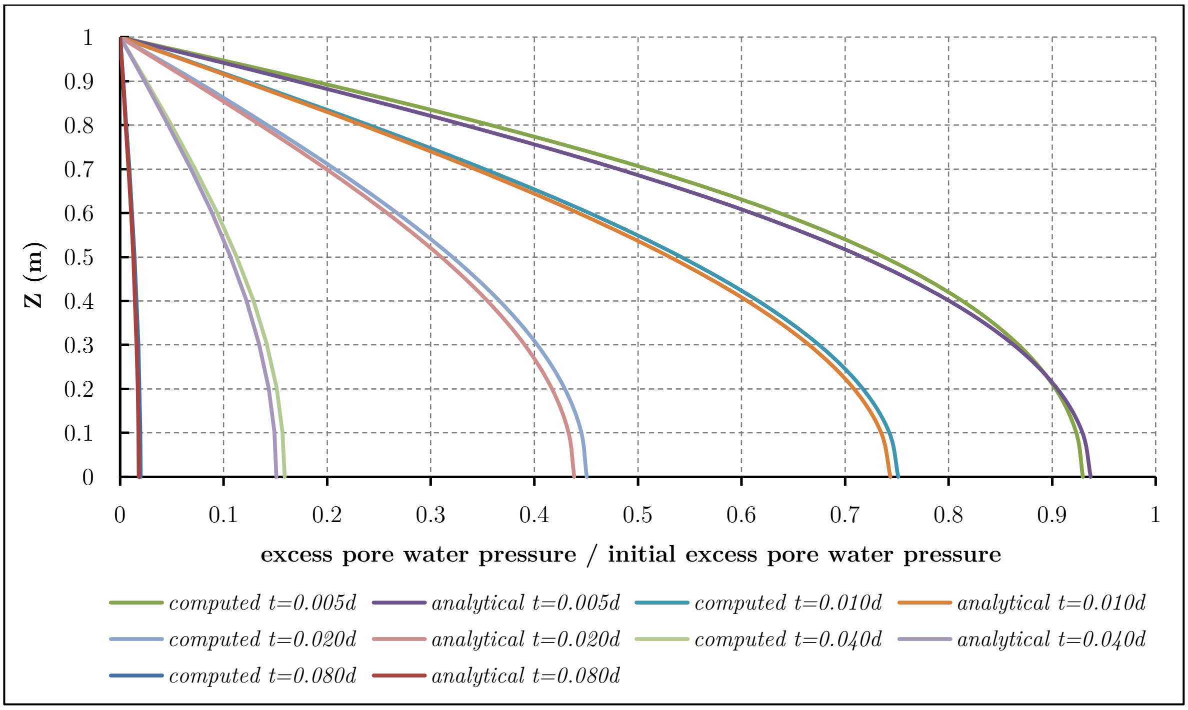

Figure 5.12: Fluid pressure distributions in depth for different instants of time.

Figure 5.12 and Figure 5.13 show that the analytical and the numerical solutions are practically identical.

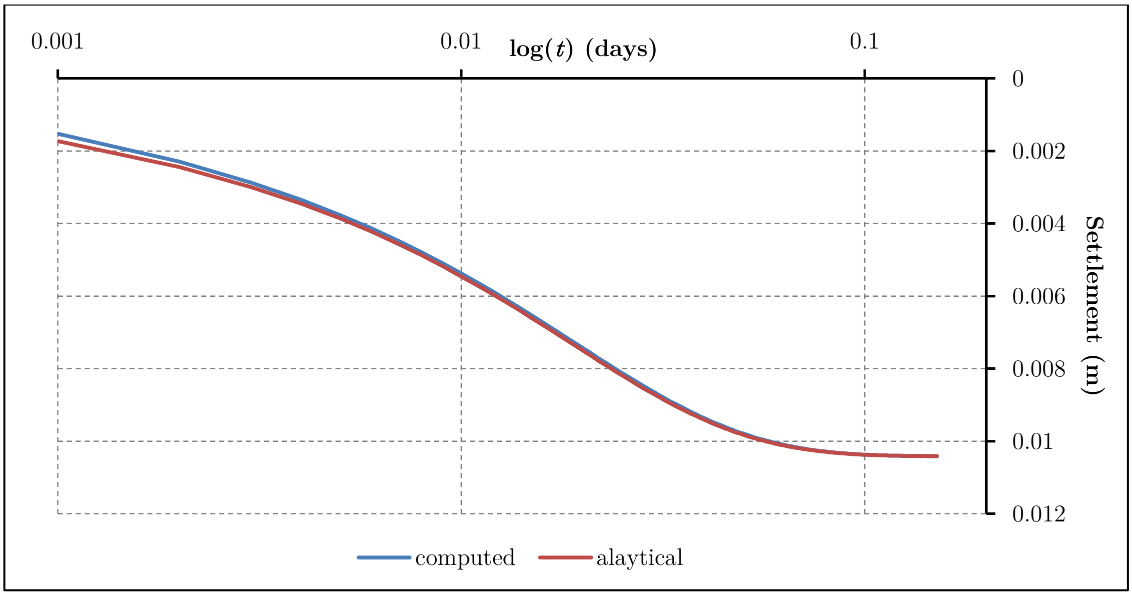

Figure 5.13: Settlement evolution with time.

Verification example 4: Thermo-hydro-mechanical coupling in continuum medium.

The objective of this example is to verify the thermo-hydro-mechanical coupling of the model, specifically the hydraulic and mechanical behaviour when a temperature increment is applied in the porous medium and the solid and the fluid tend to change their volume due to thermal expansions.

For simplicity, the geometry consists of a domain of 1×1m discretized with a single quadrilateral continuum element. This verification example proposes different small verification cases in terms of the value of the coefficients of thermal expansion of the solid (α_s^T) and the fluid (α_f^T):

- $\alpha_s^T \neq 0$ and $\alpha_f^T = 0$ ($\alpha_{Biot} = 0.1$ and $n = 0.10$)
- $\alpha_s^T = 0$ and $\alpha_f^T \neq 0$ ($\alpha_{Biot} = 0.1$ and $n = 0.10$)
- $\alpha_s^T = \alpha_f^T \neq 0$ ($\alpha_{Biot} = 0.1$ and $n = 0.10$)
- $\alpha_f^T = 10\alpha_s^T \neq 0$ ($\alpha_{Biot} = 0.1$ and $n = 0.10$)
- $\alpha_s^T = 0$ and $\alpha_f^T \neq 0$ ($\alpha_{Biot} = n = 0.20$)

Each case is computed with two different boundary conditions (drained and undrained analysis), that are shown in Figure 5.14.

For the numerical analysis linear elasticity is assumed under conditions of plane strain with material parameters $E' = 10000$ kPa and, for simplicity, $\nu' = 0$. Additionally, the effect of the gravity is omitted for both mechanical and hydraulic problems. The temperature increment applied is the same in all cases and equal to 40℃.

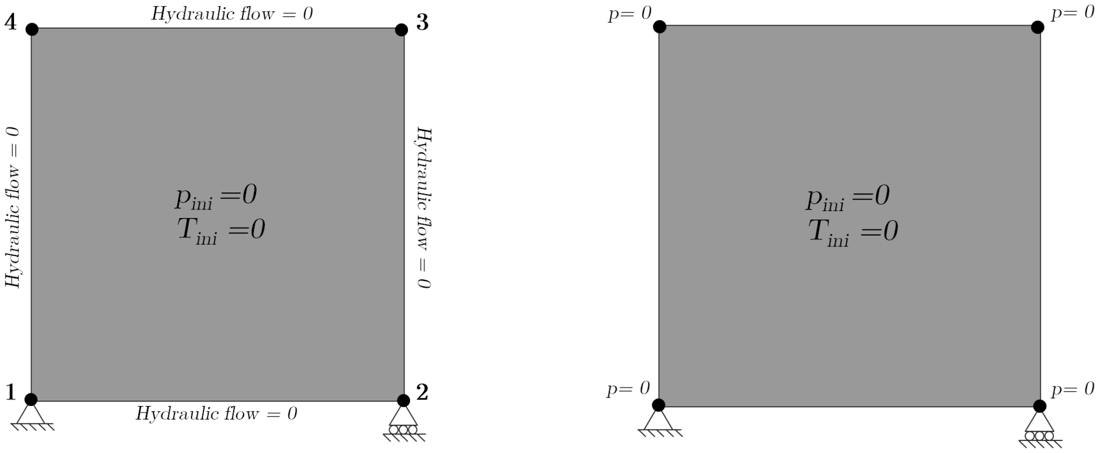

(a) Boundary conditions for the undrained analysis. *(b) Boundary conditions for the drained analysis.*

Figure 5.14: Mesh and boundary conditions for the THM verification example.

For the undrained analysis it is assumed that the flow is restricted at the boundaries (hydraulic flow equal to zero) and therefore the fluid cannot enter or leave the domain. For the drained analysis, the fluid flow is allowed at the boundaries (pressure equal to zero imposed at the four nodes of the element) and therefore the fluid can enter or leave the domain.

a) Undrained analysis with $\alpha_s^T \neq 0$, $\alpha_f^T = 0$, $\alpha_{Biot} = 1.0$ and $n = 0.10$

For this case $\alpha_s^T = 0.001$℃$^{-1}$ and $\alpha_f^T = 0$℃$^{-1}$. Table 5.1 shows the numerical results at the four nodes of the element. Additionally, the computed in-plane effective stresses at the Gauss points ($\sigma'_{x,y}$) are equal to the fluid pressures but with the opposite sign.

Table 5.1: Numerical results for the undrained analysis with $\alpha_s^T \neq 0$ and $\alpha_f^T = 0$℃$^{-1}$. Compressive pressures and outgoing hydraulic flow are positive. $\alpha_{Biot} = 1.0$ and $n = 0.10$.

Node	DISPL-X (m)	DISPL-Y (m)	PRESSURE (kPa)	H-FLOW (m^3)
1	0.00000E+00	0.00000E+00	1.40000E+02	0.00000E+00
2	5.40000E-02	0.00000E+00	1.40000E+02	0.00000E+00
3	5.40000E-02	5.40000E-02	1.40000E+02	0.00000E+00
4	0.00000E+00	5.40000E-02	1.40000E+02	0.00000E+00

The same values can be obtained analytically. Since the fluid thermal expansion is null ($\alpha_f^T = 0$), the fluid is incompressible and it cannot enter or leave the domain, the pore volume change (Eq 4.40) has to be zero, i.e:

$$n\ \alpha_{v,s}^T \Delta T + \alpha_{Biot}(\Delta\varepsilon_v - \alpha_{v,s}^T \Delta T) = 0 \tag{5.17}$$

$$\Delta\varepsilon_v = -\frac{(\alpha_{Biot} - n)\alpha_{v,s}^T \Delta T}{\alpha_{Biot}} = 0.108 \tag{5.18}$$

And the final displacements, considering $u_z = 0$, are:

$$u_{x,y} = u_0 + \frac{\Delta\varepsilon_v}{2} L = 0 + \frac{0.108}{2} \times 1\text{m} = \underline{0.054\text{ m}} \tag{5.19}$$

that matches the numerical result. Additionally, the stresses in the continuum (and excess fluid pressure) may be obtained as the difference between the free thermal mechanical expansion and the real expansion:

$$\Delta p = \Delta\sigma' = (0.054 - 0.04)E' = 140\text{ kPa} \tag{5.20}$$

that matches the value obtained in the numerical analysis.

b) Drained analysis with $\alpha_s^T \neq 0$, $\alpha_f^T = 0$, $\alpha_{Biot} = 1.0$ and $n = 0.10$

In this case $\alpha_s^T = 0.001℃^{-1}$ and $\alpha_f^T = 0℃^{-1}$. Table 5.2 shows the numerical results at the four nodes of the element. Additionally, the computed in-plane effective stresses at Gauss points $\sigma'_{x,y}$ are equal to zero.

Table 5.2: Numerical results for the drained analysis with $\alpha_s^T \neq 0$ and $\alpha_f^T = 0℃^{-1}$. Compressive pressures and outgoing hydraulic flows are positive. $\alpha_{Biot} = 1.0$ and $n = 0.10$.

Node	DISPL-X (m)	DISPL-Y (m)	PRESSURE (kPa)	H-FLOW (m^3)
1	0.00000E+00	0.00000E+00	0.00000E+00	7.00000E-03
2	4.00000E-02	0.00000E+00	0.00000E+00	7.00000E-03
3	4.00000E-02	4.00000E-02	0.00000E+00	7.00000E-03
4	0.00000E+00	4.00000E-02	0.00000E+00	7.00000E-03

The same values can be obtained analytically. Since the problem is drained and fluid can enter or leave the domain, a free thermal expansion will occur and the strain increment may be calculated as:

$$\Delta\varepsilon_{mech} = \alpha_s^T \Delta T = 0.04 \tag{5.21}$$

And the final displacements:

$$u_{x,y} = u_0 + \Delta\varepsilon_{mech} L = 0 + 0.04 \times 1\text{m} = \underline{0.04\text{ m}} \tag{5.22}$$

that match those obtained numerically. Additionally, since the fluid can enter or leave the domain, the excess fluid pressure will be null. To obtain the outgoing fluid volume, the volumetric strain increment of the pores may be calculated as:

$$\Delta\varepsilon_{v,pores} = (n - \alpha_{Biot})\ \alpha^T_{v,s}\Delta T + \alpha_{Biot}\Delta\varepsilon_{v,mech} = -0.028 \tag{5.23}$$

And the available volume for the fluid is obtained as:

$$V_{drainage} = \Delta V_{fluid} - \Delta V_{pores} = -\Delta\varepsilon_{v,pores}L^3 = \underline{0.028\ \text{m}^3} \tag{5.24}$$

that equals the sum of the outgoing flow at the four nodes of the domain obtained in the numerical analysis.

c) Undrained analysis with $\boldsymbol{\alpha^T_s = 0}$, $\boldsymbol{\alpha^T_f \neq 0}$, $\boldsymbol{\alpha_{Biot} = 1.0}$ and $\boldsymbol{n = 0.10}$

In this case $\alpha^T_s = 0℃^{-1}$ and $\alpha^T_f = 0.001℃^{-1}$. Table 5.3 shows the numerical results at the four nodes of the element. Additionally, the computed in-plane effective stresses at the Gauss points ($\sigma'_{x,y}$) are equal to the fluid pressures but with the opposite sign.

Table 5.3: Numerical results for the undrained analysis with $\alpha^T_s = 0℃^{-1}$ and $\alpha^T_f \neq 0$. Compressive pressures and outgoing hydraulic flows are positive. $\alpha_{Biot} = 1.0$ and $n = 0.10$.

Node	DISPL-X (m)	DISPL-Y (m)	PRESSURE (kPa)	H-FLOW (m³)
1	0.00000E+00	0.00000E+00	6.00000E+01	0.00000E-00
2	6.00000E-03	0.00000E+00	6.00000E+01	0.00000E-00
3	6.00000E-03	6.00000E-03	6.00000E+01	0.00000E-00
4	0.00000E+00	6.00000E-03	6.00000E+01	0.00000E-00

It is possible to obtain the same values analytically. In this case, since the thermal expansion of the solid is null ($\alpha^T_s = 0$), and the fluid cannot enter or leave the domain (undrained analysis), the thermal expansion of the fluid will lead to a strain increment of the domain:

$$\Delta\varepsilon_{v,fluid} = n\ \alpha^T_{v,f}\Delta T = 0.012 \tag{5.25}$$

And the final displacements, considering $u_z = 0$, are:

$$u_{x,y} = u_0 + \frac{\Delta\varepsilon_{v,fluid}}{2}L = 0 + \frac{0.012}{2} \times 1\text{m} = \underline{0.006\ \text{m}} \tag{5.26}$$

In addition, the excess fluid pressure due to the inability of the fluid to leave the domain may be calculated as:

$$\Delta p = E'\ \Delta\varepsilon_{fluid} = \underline{60\ \text{kPa}} \tag{5.27}$$

that matches the value obtained in the numerical analysis.

d) Drained analysis with $\boldsymbol{\alpha_s^T = 0}$, $\boldsymbol{\alpha_f^T \neq 0}$, $\boldsymbol{\alpha_{Biot} = 1.0}$ and $\boldsymbol{n = 0.10}$

In this case $\alpha_s^T = 0℃^{-1}$ and $\alpha_f^T = 0.001℃^{-1}$. Table 5.4 shows the numerical results at the four nodes of the element. Additionally, the computed in-plane effective stresses at the Gauss points ($\sigma'_{x,y}$) are equal to zero.

Table 5.4: Numerical results for the drained analysis with $\alpha_s^T = 0℃^{-1}$ and $\alpha_f^T \neq 0$. Compressive pressures and outgoing hydraulic flows are positive. $\alpha_{Biot} = 1.0$ and $n = 0.10$.

Node	DISPL-X (m)	DISPL-Y (m)	PRESSURE (kPa)	H-FLOW (m^3)
1	0.00000E+00	0.00000E+00	0.00000E+00	3.00000E-03
2	0.00000E+00	0.00000E+00	0.00000E+00	3.00000E-03
3	0.00000E+00	0.00000E+00	0.00000E+00	3.00000E-03
4	0.00000E+00	0.00000E+00	0.00000E+00	3.00000E-03

It is possible to obtain the same values analytically. In this case, since the thermal expansion of the solid is null ($\alpha_s^T = 0℃^{-1}$), and the fluid can enter/leave the domain, the strains, fluid pressures and stresses increments are null. However, due to the thermal expansion of the fluid, there is a flow leaving the domain, with a volume calculated as:

$$V_{drainage} = \Delta\varepsilon_{v,fluid} L^3 = (n\ 3\alpha_f^T \Delta T) L^3 = \underline{0.012\ \text{m}^3} \tag{5.28}$$

that equals the sum of the outgoing flow at the four nodes of the domain obtained in the numerical analysis.

e) Undrained analysis with $\boldsymbol{\alpha_s^T = \alpha_f^T \neq 0}$, $\boldsymbol{\alpha_{Biot} = 1.0}$ and $\boldsymbol{n = 0.10}$

In this case $\alpha_s^T = \alpha_f^T = 0.001℃^{-1}$. Table 5.5 shows the numerical results at the four nodes of the element. Additionally, the computed in-plane effective stresses ($\sigma'_{x,y}$) at the Gauss points are equal to the fluid pressures but with the opposite sign.

Table 5.5: Numerical results for the undrained analysis with $\alpha_s^T = \alpha_f^T = 0.001℃^{-1}$. Compressive pressures and outgoing hydraulic flow are positive. $\alpha_{Biot} = 1.0$ and $n = 0.10$.

Node	DISPL-X (m)	DISPL-Y (m)	PRESSURE (kPa)	H-FLOW (m^3)
1	0.00000E+00	0.00000E+00	2.00000E+02	0.00000E+00
2	6.00000E-02	0.00000E+00	2.00000E+02	0.00000E+00
3	6.00000E-02	6.00000E-02	2.00000E+02	0.00000E+00
4	0.00000E+00	6.00000E-02	2.00000E+02	0.00000E+00

The same values can be obtained analytically. Since the fluid cannot enter or leave the domain (undrained analysis), the thermal expansion of the solid and the fluid will lead to a strain increment of the domain:

$$\Delta\varepsilon_v = n\alpha_{v,f}^T\Delta T + (1-n)\alpha_{v,s}^T\Delta T = 0.12 \tag{5.29}$$

And considering $u_z = 0$, the final displacements are:

$$u_{x,y} = u_0 + \frac{\Delta\varepsilon_v}{2}L = 0 + \frac{0.12}{2} \times 1\text{m} = \underline{0.06\text{ m}} \tag{5.30}$$

Additionally, the stresses in the continuum (and excess fluid pressure) may be obtained as the difference between the free thermal mechanical expansion and the real thermal expansion:

$$\Delta p = \Delta\sigma'_x = \Delta\sigma'_y = (0.06 - 0.04)E' = 200\text{ kPa} \tag{5.31}$$

that matches the value obtained in the numerical analysis.

f) Drained analysis with $\boldsymbol{\alpha_s^T = \alpha_f^T \neq 0}$, $\boldsymbol{\alpha_{Biot} = 1.0}$ and $\boldsymbol{n = 0.10}$

In this case $\alpha_s^T = \alpha_f^T = 0.001℃^{-1}$. Table 5.6 shows the numerical results at the four nodes of the element. Additionally, the computed in-plane effective stresses at the Gauss points ($\sigma'_{x,y}$) are equal to zero.

Table 5.6: Numerical results for the drained analysis with $\alpha_s^T = \alpha_f^T = 0.001℃^{-1}$. Compressive pressures and outgoing hydraulic flow are positive. $\alpha_{Biot} = 1.0$ and $n = 0.10$.

Node	DISPL-X (m)	DISPL-Y (m)	PRESSURE (kPa)	H-FLOW (m³)
1	0.00000E+00	0.00000E+00	0.00000E+00	1.00000E-02
2	4.00000E-02	0.00000E+00	0.00000E+00	1.00000E-02
3	4.00000E-02	4.00000E-02	0.00000E+00	1.00000E-02
4	0.00000E+00	4.00000E-02	0.00000E+00	1.00000E-02

The same values can be obtained analytically. Since the problem is drained and fluid can enter/leave the domain, a free thermal expansion will occur and the mechanical strain increment may be calculated as:

$$\Delta\varepsilon_{mech} = \alpha_s^T\Delta T = 0.04 \tag{5.32}$$

And the final displacements are:

$$u_{x,y} = u_0 + \Delta\varepsilon_{mech}L = 0.04 \times 1\text{m} = \underline{0.04\text{ m}} \tag{5.33}$$

which match those obtained numerically. Additionally, since the fluid can enter/leave the domain, the excess fluid pressure will be null.

To obtain the outgoing fluid volume, the volumetric stain increment of the pores may be obtained as:

$$\Delta\varepsilon_v = (n - \alpha_{Biot})\ \alpha_{v,s}^T\Delta T + \alpha_{Biot}\Delta\varepsilon_{v,mech} = -0.028 \tag{5.34}$$

And the available volume for the fluid is:

$$\Delta V_{pores} = \Delta\varepsilon_v L^3 = -0.028 \text{ m}^3 \tag{5.35}$$

In addition, the fluid increment volume is calculated as:

$$\Delta V_{fluid} = \Delta\varepsilon_{v,fluid} L^3 = (n\ \alpha_{v,s}^T \Delta T) L^3 = 0.012 \text{ m}^3 \tag{5.36}$$

The difference between the fluid volume increment and the available volume increment for the fluid results in the total incoming/outgoing fluid:

$$V_{drainage} = \Delta V_{fluid} - \Delta V_{pores} = \underline{0.04 \text{ m}^3} \tag{5.37}$$

that matches the result obtained in the numerical analysis.

g) Undrained analysis with $\boldsymbol{\alpha_f^T = 10\alpha_s^T \neq 0}$, $\boldsymbol{\alpha_{Biot} = 1.0}$ and $\boldsymbol{n = 0.10}$

In this case $\alpha_s^T = 0.001℃^{-1}$ and $\alpha_f^T = 10\alpha_s^T$. Table 5.7 shows the numerical results at the four nodes of the element. Additionally, the computed in-plane effective stresses at the Gauss points $(\sigma'_{x,y})$ are equal to the pressures but with the opposite sign.

Table 5.7: Numerical results for the undrained analysis with $\alpha_f^T = 10\alpha_s^T \neq 0$. Compressive pressures and outgoing hydraulic flow are positive. $\alpha_{Biot} = 1.0$ and $n = 0.10$.

Node	DISPL-X (m)	DISPL-Y (m)	PRESSURE (kPa)	H-FLOW (m^3)
1	0.00000E+00	0.00000E+00	7.40000E+02	0.00000E+00
2	1.14000E-01	0.00000E+00	7.40000E+02	0.00000E+00
3	1.14000E-01	1.14000E-01	7.40000E+02	0.00000E+00
4	0.00000E+00	1.14000E-01	7.40000E+02	0.00000E+00

The same values can be obtained analytically. Since the fluid thermal expansion is null $(\alpha_f^T = 0)$ and the fluid cannot enter or leave the domain, the pore volume change (Eq 4.40) has to be zero, i.e:

$$n\ \alpha_{v,s}^T \Delta T + \alpha_{Biot}(\Delta\varepsilon_v - \alpha_{v,s}^T \Delta T) + n\ \alpha_{v,f}^T \Delta T = 0 \tag{5.38}$$

$$\Delta\varepsilon_v = -\frac{(\alpha_{Biot} - n)\alpha_{v,s}^T \Delta T + n\ \alpha_{v,f}^T \Delta T}{\alpha_{Biot}} = 0.228 \tag{5.39}$$

And considering $u_z = 0$, the final displacements are:

$$u_{x,y} = u_0 + \frac{\Delta\varepsilon_v}{2} L = 0 + \frac{0.228}{2} \times 1\text{m} = \underline{0.114 \text{ m}} \tag{5.40}$$

that match those obtained numerically. Additionally, the in-plane effective stresses in the continuum (and excess fluid pressure) may be obtained as the difference between the free thermal mechanical expansion and the real thermal expansion:

$$\Delta p = \Delta\sigma'_{x,y} = (0.114 - 0.04)E' = 740 \text{ kPa} \tag{5.41}$$

that matches the value obtained in the numerical analysis.

h) Drained analysis with $\boldsymbol{\alpha_f^T = 10\alpha_s^T \neq 0}$, $\boldsymbol{\alpha_{Biot} = 1.0}$ and $\boldsymbol{n = 0.10}$

In this case $\alpha_s^T = 0.001$°C^{-1} and $\alpha_f^T = 10\alpha_s^T$, which is a realistic relation for geomaterials. Table 5.8 shows the numerical results at the four nodes of the element. Additionally, the computed in-plane effective stresses at the Gauss points ($\sigma'_{x,y}$) are equal to zero.

Table 5.8: Numerical results for the drained analysis with $\alpha_f^T = 10\alpha_s^T \neq 0$. Compressive pressures and outgoing hydraulic flow are positive. $\alpha_{Biot} = 1.0$ and $n = 0.10$.

Node	DISPL-X (m)	DISPL-Y (m)	PRESSURE (kPa)	H-FLOW (m³)
1	0.00000E+00	0.00000E+00	0.00000E+00	3.70000E-02
2	4.00000E-02	0.00000E+00	0.00000E+00	3.70000E-02
3	4.00000E-02	4.00000E-02	0.00000E+00	3.70000E-02
4	0.00000E+00	4.00000E-02	0.00000E+00	3.70000E-02

The same values can be obtained analytically. Since the problem is drained and fluid can enter/leave the domain, a free thermal expansion will occur and the mechanical strain increment and the final displacements are the same obtained by Eqs. (5.32) and (5.33), that match those obtained numerically. Additionally, since the fluid can leave the domain, the excess fluid pressure will be null.

The pore volume increment is the same as calculated in Eqs. (5.34) and (5.35). In addition, the fluid volume increment is:

$$\Delta V_{fluid} = \Delta\varepsilon_{v,fluid} L^3 = (n\ \alpha_{v,f}^T \Delta T) L^3 = 0.12 \text{ m}^3 \tag{5.42}$$

The difference between the fluid volume expansion and the pore volume expansion results in the total entering/outgoing fluid:

$$V_{drainage} = \Delta V_{fluid} - \Delta V_{pores} = \underline{0.148 \text{ m}^3} \tag{5.43}$$

that matches the result obtained in the numerical analysis.

i) Undrained analysis with $\boldsymbol{\alpha_f^T \neq 0}$, $\boldsymbol{\alpha_s^T = 0}$ and $\boldsymbol{\alpha_{Biot} = n = 0.20}$

In this case $\alpha_s^T = 0℃^{-1}$ and $\alpha_f^T = 0.001℃^{-1}$. Table 5.9 shows the numerical results at the four nodes of the element. Additionally, the computed in-plane effective stresses at the Gauss points are $\sigma'_{x,y} = 600$ kPa.

Table 5.9: Numerical results for the undrained analysis with $\alpha_s^T = 0℃^{-1}$ and $\alpha_f^T = 0.001℃^{-1}$. Compressive pressures and outgoing hydraulic flow are positive. $\alpha_{Biot} = n = 0.20$.

Node	DISPL-X (m)	DISPL-Y (m)	PRESSURE (kPa)	H-FLOW (m³)
1	0.00000E+00	0.00000E+00	3.00000E+03	0.00000E+00
2	6.000000E-02	0.00000E+00	3.00000E+03	0.00000E+00
3	6.000000E-02	6.000000E-01	3.00000E+03	0.00000E+00
4	0.00000E+00	6.000000E-01	3.00000E+03	0.00000E+00

The same values can be obtained analytically. Since the coefficient of thermal expansion for the solids is equal to zero $(\alpha_s^T = 0℃^{-1})$, the total strain increment comes from the fluid thermal expansion and may be calculated as:

$$\Delta\varepsilon_{v,fluid} = \alpha_{v,f}^T \Delta T = 0.06 \tag{5.44}$$

And the final displacements:

$$u_{x,y} = u_0 + \Delta\varepsilon_{v,fluid} L = 0 + 0.06 \times 1\text{m} = \underline{0.06\ \text{m}} \tag{5.45}$$

that match those obtained numerically. Additionally, the in-plane effective stress increment may be calculated as:

$$\Delta\sigma'_{x,y} = \Delta\varepsilon_{v,fluid} E' = 600\ \text{kPa} \tag{5.46}$$

that also match the effective stress increment obtained from the numerical analysis. Finally, the pressure increment may be obtained as:

$$\sigma'_{x,y} = \sigma_{x,y} + \alpha_{Biot}\, p \ \rightarrow\ \Delta p = \frac{\Delta\sigma'_{x,y}}{\alpha_{Biot}} = \frac{600\ \text{kPa}}{0.20} = \underline{3000\ \text{kPa}} \tag{5.47}$$

j) Drained analysis with $\boldsymbol{\alpha_f^T \neq 0}$, $\boldsymbol{\alpha_s^T = 0}$ and $\boldsymbol{\alpha_{Biot} = n = 0.20}$

In this case $\alpha_s^T = 0℃^{-1}$ and $\alpha_f^T = 0.001℃^{-1}$, which is a realistic relation for geomaterials. Table 5.10 shows the numerical results at the four nodes of the element. Additionally, the computed in-plane effective stresses at the Gauss points $(\sigma'_{x,y})$ are equal to zero.

Table 5.10: Numerical results for the drained analysis with $\alpha_s^T = 0°\mathrm{C}^{-1}$ and $\alpha_f^T = 0.001°\mathrm{C}^{-1}$. Compressive pressures and outgoing hydraulic flow are positive. $\alpha_{Biot} = n = 0.20$.

Node	DISPL-X (m)	DISPL-Y (m)	PRESSURE (kPa)	H-FLOW (m³)
1	0.00000E+00	0.00000E+00	0.00000E+00	6.00000E-03
2	0.00000E+00	0.00000E+00	0.00000E+00	6.00000E-03
3	0.00000E+00	0.00000E+00	0.00000E+00	6.00000E-03
4	0.00000E+00	0.00000E+00	0.00000E+00	6.00000E-03

The same values can be obtained analytically. Since the problem is drained and fluid can enter/leave the domain, a free thermal expansion will occur and the mechanical strain increment may be calculated as:

$$\Delta\varepsilon_{mech} = \alpha_s^T \Delta T = 0.00 \tag{5.48}$$

And the final displacements will be null, matching the numerical result. Additionally, since the fluid can enter/leave the domain, the excess fluid pressure will be null.

To obtain the incoming fluid volume, considering that $\alpha_s^T = 0$ and that the pore volume remains constant ($\Delta V_{pores} = 0$), the volumetric strain increment of the fluid is calculated as:

$$\Delta\varepsilon_{v,fluid} = 3\alpha_f^T \Delta T = 0.12 \tag{5.49}$$

and the volume expansion increment of the fluid:

$$\Delta V_{fluid} = n\ \Delta\varepsilon_{v,fluid} L^3 = 0.024\ \mathrm{m}^3 \tag{5.50}$$

The difference between the fluid volume expansion and the pore volume expansion results in the total incoming/outcoming fluid volume from the domain:

$$V_{drainage} = \Delta V_{fluid} - \Delta V_{pores} = \underline{0.024\ \mathrm{m}^3} \tag{5.51}$$

that is the fluid leaving the domain matching the sum of the outgoing flow at the four nodes of the domain obtained in the numerical analysis.

Verification example 5: Thermo-hydro-mechanical coupling in continuum medium.

This verification example has been carried out in order to verify the transient thermo-hydro-mechanical coupling of the model in a porous continuum medium. The geometry consists of a domain of 1×1m, discretized with 100 quadrilateral continuum elements.

The analysis is divided in two steps. The first step consists in the application of a temperature increment of 40°C to the whole domain while the flow is prescribed at the boundaries (undrained analysis). In the second step, flow is allowed at the boundaries (drained analysis) and a transient analysis is performed until reaching steady-state conditions.

The geometry, the initial and boundary conditions for both steps and the material parameters used in the numerical analysis are presented in Figure 5.15. In addition, the effect of the gravity is omitted and linear elasticity is assumed under plane strain conditions.

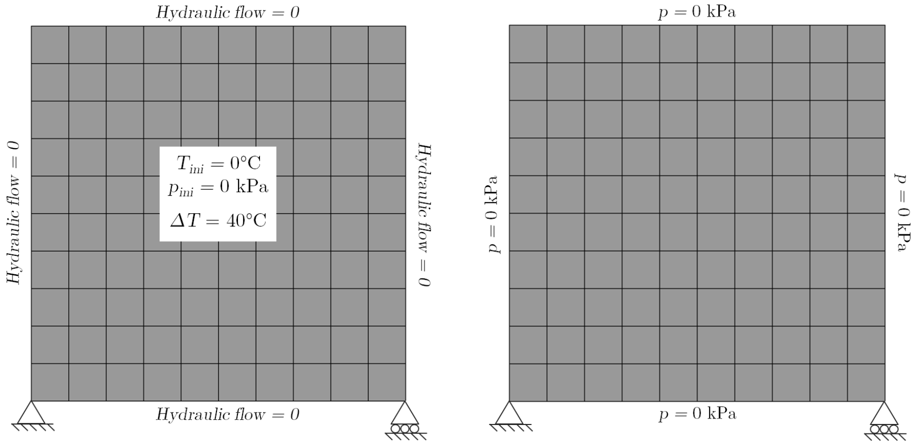

(a) step 1

(b) step 2

$E' = 10$ MPa

$\nu' = 0.0$

$K^f = K^s = 3 \cdot 10^{12}$kPa

$\gamma^f = 10$ kN/m^3

$\mu = 1 \cdot 10^{-11}$ kPa · d

$k^p = 1.5 \cdot 10^{-13}$ m^2

$\alpha_{Biot} = 1.0$

$\alpha_s^T = 0.0°C^{-1}$

$\alpha_f^T = 0.001°C^{-1}$

$c = 1 \cdot 10^{-3}$ J/(kg · °C)

$\rho = 1$ Tn/m^3

$k^T = 1.5$ J/(m · °C · s)

Figure 5.15: Mesh, initial and boundary conditions and material parameters for the THM verification problem.

In a first step a temperature increment of 40°C is applied to the whole domain considering undrained conditions (Figure 5.15.a). The numerical results of this step are:

$$\Delta u_{x,max} = 0.006 \text{ m} \qquad \Delta u_{y,max} = 0.006 \text{ m} \qquad \Delta p = 60 \text{ kPa} \qquad V_{drainage} = 0 \text{ m}^3$$

It is also possible to obtain these values analytically. In this case, since the thermal expansion of the solid is null ($\alpha_s^T = 0°C^{-1}$), and the fluid cannot leave the domain (undrained analysis), the thermal expansion of the fluid will lead to a strain increment of the domain:

$$\Delta\varepsilon_v = n \; \alpha_{v,f}^T \Delta T = 0.012 \tag{5.52}$$

and considering $u_z = 0$, the final displacements are:

$$u_{(x,y),max} = u_0 + \frac{\Delta\varepsilon_v}{2} L = 0 + \frac{0.012}{2} \times 1\text{m} = \underline{0.006 \text{ m}} \tag{5.53}$$

that match those obtained in the numerical analysis. In addition, the excess fluid pressure due to the inability of the fluid to leave the domain may be calculated as:

$$\Delta p = E' \; \Delta\varepsilon_v = \underline{60 \text{ kPa}} \tag{5.54}$$

that matches the value obtained in the numerical analysis.

In the second step the flow is allowed at the boundaries (Figure 5.15.b) and the transient analysis is performed until reaching steady-state conditions (drained analysis). The thermal strain increment and the excess fluid pressure generated during the first step will decrease until reaching the initial configuration of pressures and displacements, as shown in Figure

5.16. This process will lead to an outgoing flow from the domain as in a consolidation analysis.

The total fluid volume that leaves the domain at the end of the second step (steady-state) is proportional to the increment of thermal expansion of the fluid during the first step, and may be calculated analytically as:

$$\Delta V_{drainage} = \Delta\varepsilon_v L^3 = n\ \alpha^T_{v,f} \Delta T L^3 = \underline{0.012\ \mathrm{m}^3} \tag{5.55}$$

that matches the volume obtained from the numerical analysis.

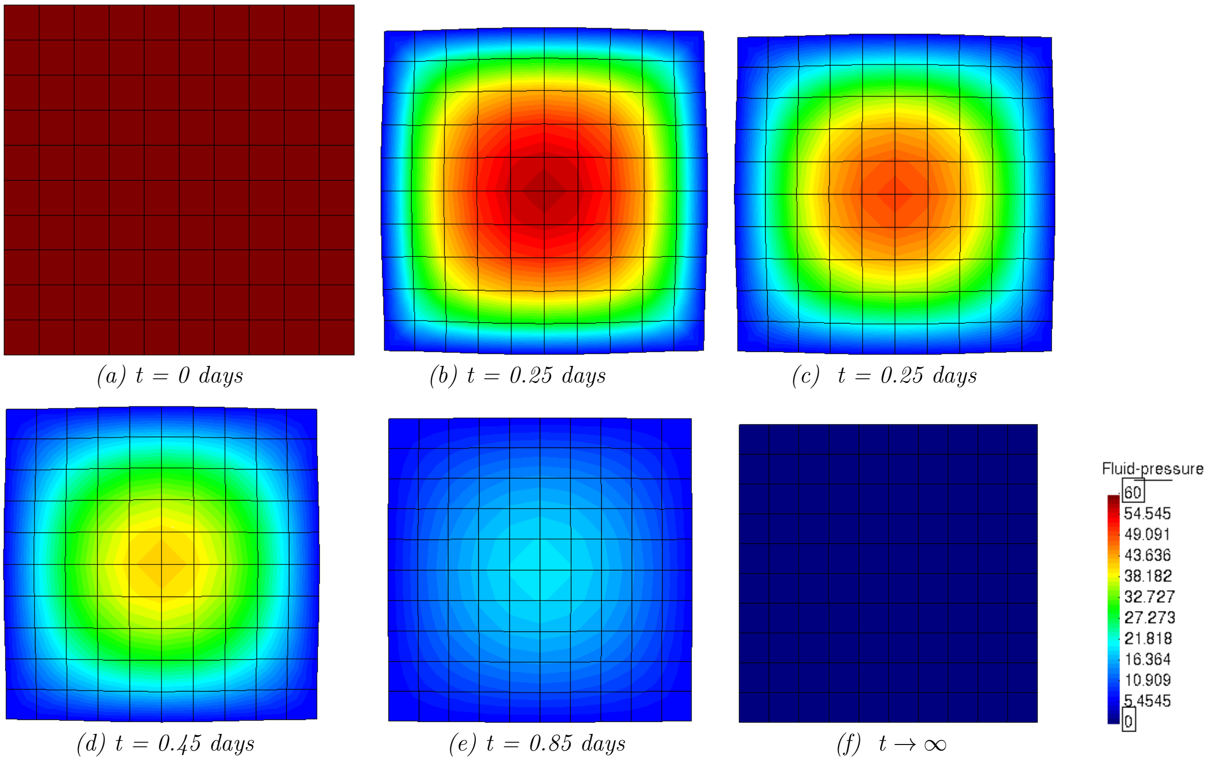

(a) t = 0 days (b) t = 0.25 days (c) t = 0.25 days

(d) t = 0.45 days (e) t = 0.85 days (f) $t \to \infty$

Figure 5.16: Fluid pressure evolution in deformed mesh during the second step (factor x50).

Verification example 6: 3-D thermo-hydro-mechanical coupling in continuum medium.

The objective of this example is to verify the thermo-hydro-mechanical coupling of the model in 3-D, specifically the hydraulic and mechanical behaviour when a temperature increment is applied in the porous medium and the solid and fluid tend to change their volume due to thermal expansions.

For simplicity, the geometry consists of a domain of 1×1×1m discretized with a single cubic continuum element. This verification example includes four cases in terms of the fluid restrictions (drained and undrained analysis) and the mechanical restrictions (free expansion and with restricted expansion in the vertical direction).

- Undrained analysis under free thermal expansion conditions (Figure 5.17.a)
- Drained analysis under free thermal expansion conditions (Figure 5.17.b)
- Undrained analysis with restricted thermal vertical expansion (Figure 5.17.c)
- Drained analysis with restricted thermal vertical expansion (Figure 5.17.d)

For the numerical analysis linear elasticity is assumed under conditions of plane strain with material parameters $E' = 10000$ kPa, $\nu' = 0.0$, $\alpha_s^T = \alpha_f^T = 0.001℃^{-1}$, $\alpha_{Biot} = 1.0$ and $n = 0.1$. Additionally, the effect of the gravity is omitted for both mechanical and hydraulic problems. The temperature increment applied is the same in all cases and equal to 40℃.

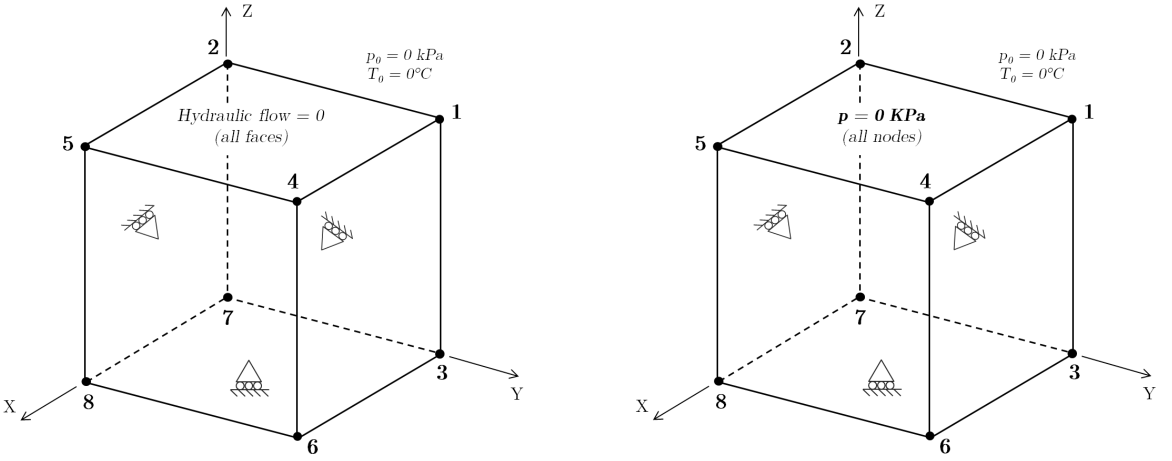

(a) Boundary conditions for the undrained analysis and free thermal expansion

(b) Boundary conditions for the drained analysis and free thermal expansion

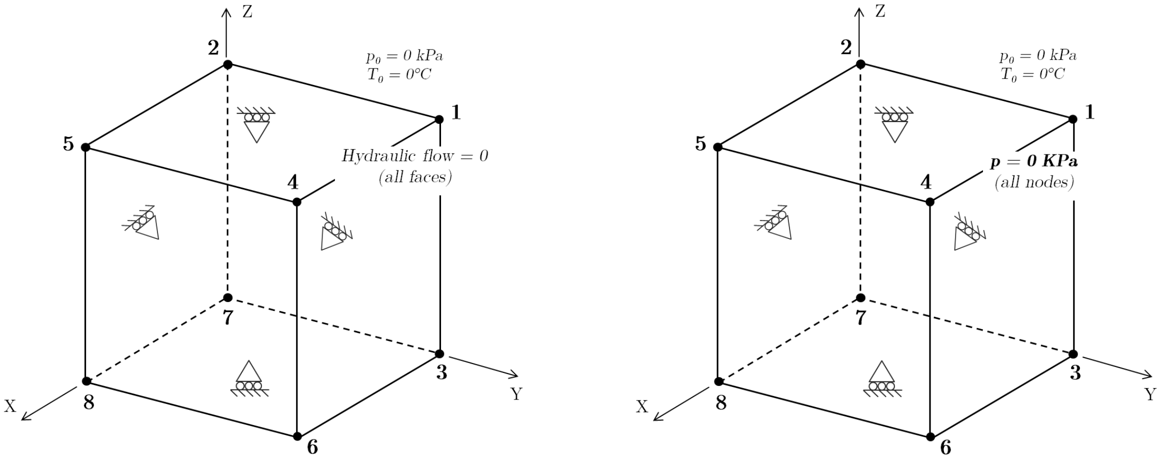

(c) Boundary conditions for the undrained analysis with restricted thermal expansion in Z.

(d) Boundary conditions for the drained analysis with restricted thermal expansion in Z.

Figure 5.17: Mesh and boundary conditions for the 3-D THM verification example.

For the undrained analysis it is assumed that the flow is restricted at the boundaries (hydraulic flow equal to zero) and therefore the fluid cannot enter or leave the domain. For the drained analysis, the fluid flow is allowed at the boundaries (fluid pressure equal to zero imposed at the four nodes of the element) and therefore the fluid can enter or leave the domain.

a) Undrained analysis and free thermal expansion

Table 5.11 shows the numerical results at the eight nodes of the element with the boundary conditions shown in Figure 5.17.a. Additionally, the computed effective stresses at Gauss points are equal to zero.

Table 5.11: Numerical results for the 3-D undrained analysis with free thermal expansion and $\alpha_s^T = \alpha_f^T = 0.001$℃$^{-1}$. *Compressive pressures and outgoing hydraulic flow are positive.* $\alpha_{Biot} = 1.0$ *and* $n = 0.10$.

Node	DISPL-X (m)	DISPL-Y (m)	DISPL-Z (m)	PRESSURE (kPa)	H-FLOW (m^3)
1	0.00000E+00	4.00000E-02	4.00000E-02	0.00000E+00	0.00000E+00
2	0.00000E+00	0.00000E+00	4.00000E-02	0.00000E+00	0.00000E+00
3	0.00000E+00	4.00000E-02	0.00000E+00	0.00000E+00	0.00000E+00
4	4.00000E-02	4.00000E-02	4.00000E-02	0.00000E+00	0.00000E+00
5	4.00000E-02	0.00000E+00	4.00000E-02	0.00000E+00	0.00000E+00
6	4.00000E-02	4.00000E-02	0.00000E+00	0.00000E+00	0.00000E+00
7	0.00000E+00	0.00000E+00	0.00000E+00	0.00000E+00	0.00000E+00
8	4.00000E-02	0.00000E+00	0.00000E+00	0.00000E+00	0.00000E+00

The same values can be obtained analytically. Since the fluid cannot enter or leave the domain (undrained analysis), the thermal expansion of the fluid will lead to a strain increment of the domain:

$$\Delta\varepsilon_v = \alpha_{v,f}^T \Delta T = 0.12 \tag{5.56}$$

And the final displacements are:

$$u_{x,y,z} = u_0 + \frac{\Delta\varepsilon_v}{3} L = 0 + \frac{0.12}{3} \times 1\text{m} = \underline{0.04\ \text{m}} \tag{5.57}$$

Additionally, stresses in the continuum (and excess fluid pressure) may be obtained as the difference between the free thermal mechanical expansion and the real expansion:

$$\Delta p = \Delta\sigma' = (0.04 - 0.04)E' = 0\ \text{kPa} \tag{5.58}$$

that matches the value obtained in the numerical analysis.

b) Drained analysis and free thermal expansion

Table 5.12 shows the numerical results at the eight nodes of the element with the boundary conditions shown in Figure 5.17.b. Additionally, the computed effective stresses at Gauss points are equal to zero.

Table 5.12: Numerical results for the 3-D drained analysis with free thermal expansion and $\alpha_s^T = \alpha_f^T = 0.001℃^{-1}$. Compressive pressures and outgoing hydraulic flow are positive. $\alpha_{Biot} = 1.0$ and $n = 0.10$.

Node	DISPL-X (m)	DISPL-Y (m)	DISPL-Z (m)	PRESSURE (kPa)	H-FLOW (m³)
1	0.00000E+00	4.00000E-02	4.00000E-02	0.00000E+00	0.00000E+00
2	0.00000E+00	0.00000E+00	4.00000E-02	0.00000E+00	0.00000E+00
3	0.00000E+00	4.00000E-02	0.00000E+00	0.00000E+00	0.00000E+00
4	4.00000E-02	4.00000E-02	4.00000E-02	0.00000E+00	0.00000E+00
5	4.00000E-02	0.00000E+00	4.00000E-02	0.00000E+00	0.00000E+00
6	4.00000E-02	4.00000E-02	0.00000E+00	0.00000E+00	0.00000E+00
7	0.00000E+00	0.00000E+00	0.00000E+00	0.00000E+00	0.00000E+00
8	4.00000E-02	0.00000E+00	0.00000E+00	0.00000E+00	0.00000E+00

The same values can be obtained analytically. Since the problem is drained and fluid can enter/leave the domain, a free thermal expansion will occur and the mechanical strain increment may be calculated as:

$$\Delta\varepsilon_{mech} = \alpha_s^T \Delta T = 0.04 \tag{5.59}$$

Then the final displacements are:

$$u_{x,y} = u_0 + \Delta\varepsilon_{mech} L = 0.04 \times 1\text{m} = \underline{0.04\text{ m}} \tag{5.60}$$

which match those obtained numerically. Additionally, since the fluid can enter/leave the domain, the excess fluid pressure will be null. To obtain the incoming/outgoing fluid volume, the volumetric stain increment of the pores may be obtained as:

$$\Delta\varepsilon_{v,pores} = (n - \alpha_{Biot})\ \alpha_{v,s}^T \Delta T + \alpha_{Biot} \Delta\varepsilon_{v,mech} = 0.012 \tag{5.61}$$

And the available volume for the fluid is obtained as:

$$\Delta V_{pores} = \Delta\varepsilon_{v,pores} L^3 = 0.012\text{ m}^3 \tag{5.62}$$

In addition, the volume increment of the fluid is calculated as:

$$\Delta V_{fluid} = \Delta\varepsilon_{v,fluid} L^3 = (n\ \alpha_{v,s}^T \Delta T) L^3 = 0.012\text{ m}^3 \tag{5.63}$$

The difference between the volume expansion increment of the fluid and the available volume increment for the fluid results in the total incoming/outgoing fluid:

$$V_{drainage} = \Delta V_{fluid} - \Delta V_{pores} = \underline{0.0\ \mathrm{m}^3} \tag{5.64}$$

that matches the result obtained in the numerical analysis.

c) Undrained analysis with restricted in the vertical direction

Table 5.13 shows the numerical results at the eight nodes of the element with the boundary conditions shown in Figure 5.17.c. Additionally, the computed effective stresses at Gauss points are $\sigma'_x = \sigma'_y = 200$ kPa and $\sigma'_z = -400$ kPa.

Table 5.13: Numerical results for the 3-D undrained analysis with restricted expansion in Z and $\alpha_s^T = \alpha_f^T = 0.001°\mathrm{C}^{-1}$. Compressive pressures and outgoing hydraulic flow are positive. $\alpha_{Biot} = 1.0$ and $n = 0.10$.

Node	DISPL-X (m)	DISPL-Y (m)	DISPL-Z (m)	PRESSURE (kPa)	H-FLOW (m³)
1	0.00000E+00	6.00000E-02	0.00000E+00	2.00000E+02	0.00000E+00
2	0.00000E+00	0.00000E+00	0.00000E+00	2.00000E+02	0.00000E+00
3	0.00000E+00	6.00000E-02	0.00000E+00	2.00000E+02	0.00000E+00
4	6.00000E-02	6.00000E-02	0.00000E+00	2.00000E+02	0.00000E+00
5	6.00000E-02	0.00000E+00	0.00000E+00	2.00000E+02	0.00000E+00
6	6.00000E-02	6.00000E-02	0.00000E+00	2.00000E+02	0.00000E+00
7	0.00000E+00	0.00000E+00	0.00000E+00	2.00000E+02	0.00000E+00
8	6.00000E-02	0.00000E+00	0.00000E+00	2.00000E+02	0.00000E+00

The same values can be obtained analytically. Since the fluid cannot enter or leave the domain (undrained analysis), the thermal expansion of the fluid will lead to a strain increment of the domain:

$$\Delta\varepsilon_v = \alpha_{v,f}^T \Delta T = 0.12 \tag{5.65}$$

And considering that $u_z = 0$, the final displacements are:

$$u_{x,y} = u_0 + \frac{\Delta\varepsilon_v}{2} L = 0 + \frac{0.12}{2} \times 1\mathrm{m} = \underline{0.06\ \mathrm{m}} \tag{5.66}$$

Additionally, the in-plane continuum effective stresses $\sigma'_{z,y}$ (and excess fluid pressure) may be obtained as the difference between the free thermal mechanical expansion and the real expansion:

$$\Delta p = \Delta\sigma'_{x,y} = (0.06 - 0.04)E' = 200\ \mathrm{kPa} \tag{5.67}$$

that matches the value obtained in the numerical analysis. The out-of-plane effective σ'_z may be computed in the same way:

$$\Delta\sigma'_z = (0.00 - 0.04)E' = -400\ \mathrm{kPa} \tag{5.68}$$

that also matches the value obtained in the numerical analysis.

It is important to note that this example is equivalent to the 2-D analysis presented in Verification example 4 e) (Table 5.5), computed under plane strain conditions, and leads to the same results.

d) Drained analysis with restricted in the vertical direction

Table 5.14 shows the numerical results at the eight nodes of the element with the boundary conditions shown in Figure 5.17.d. Additionally, the computed effective stresses at Gauss points are $\sigma'_x = \sigma'_y = 0$ kPa and $\sigma'_z = -400$ kPa.

Table 5.14: Numerical results for the 3-D drained analysis with restricted expansion in Z and $\alpha_s^T = \alpha_f^T = 0.001$°C^{-1}. Compressive pressures and outgoing hydraulic flow are positive. $\alpha_{Biot} = 1.0$ and $n = 0.10$.

Node	DISPL-X (m)	DISPL-Y (m)	DISPL-Z (m)	PRESSURE (kPa)	H-FLOW (m³)
1	0.00000E+00	4.00000E-02	0.00000E+00	0.00000E+00	5.00000E-03
2	0.00000E+00	0.00000E+00	0.00000E+00	0.00000E+00	5.00000E-03
3	0.00000E+00	4.00000E-02	0.00000E+00	0.00000E+00	5.00000E-03
4	4.00000E-02	4.00000E-02	0.00000E+00	0.00000E+00	5.00000E-03
5	4.00000E-02	0.00000E+00	0.00000E+00	0.00000E+00	5.00000E-03
6	4.00000E-02	4.00000E-02	0.00000E+00	0.00000E+00	5.00000E-03
7	0.00000E+00	0.00000E+00	0.00000E+00	0.00000E+00	5.00000E-03
8	4.00000E-02	0.00000E+00	0.00000E+00	0.00000E+00	5.00000E-03

The same values can be obtained analytically. Since the problem is drained and fluid can enter or leave the domain, a free thermal expansion will occur and the mechanical strain increment may be calculated as:

$$\Delta\varepsilon_{mech} = \alpha_s^T \Delta T = 0.04 \tag{5.69}$$

Then the final displacements are:

$$u_{x,y} = u_0 + \Delta\varepsilon_{mech} L = 0.04 \times 1\text{m} = \underline{0.04\text{ m}} \tag{5.70}$$

which match those obtained numerically. Additionally, since the fluid can enter/leave the domain, the excess fluid pressure will be null. To obtain the entering/outgoing fluid volume, the volumetric strain increment of the pores may be obtained as:

$$\Delta\varepsilon_{v,pores} = (n - \alpha_{Biot})\, \alpha_{v,s}^T \Delta T + \alpha_{Biot} \Delta\varepsilon_{v,mech} = -0.028 \tag{5.71}$$

And the available volume for the fluid is obtained as:

$$\Delta V_{pores} = \Delta\varepsilon_{v,pores} L^3 = -0.028\text{ m}^3 \tag{5.72}$$

In addition, the volume increment of the fluid is calculated as:

$$\Delta V_{fluid} = \Delta\varepsilon_{v,fluid} L^3 = (n\ \alpha_{v,f}^T \Delta T) L^3 = 0.012 \text{ m}^3 \tag{5.73}$$

The difference between the volume expansion increment of the fluid and the available volume increment for the fluid results in the total entering/outgoing fluid:

$$V_{drainage} = \Delta V_{fluid} - \Delta V_{pores} = \underline{0.04 \text{ m}^3} \tag{5.74}$$

Additionally, the out-of-plane effective stresses σ'_z may be calculated as the difference between the free thermal mechanical expansion and the real expansion:

$$\Delta\sigma'_z = (0.00 - 0.04)E' = -400 \text{ kPa} \tag{5.75}$$

that matches the value obtained in the numerical analysis.

It is important to note that this example is equivalent to the 2-D analysis presented in Verification example 4 f) (Table 5.6), computed under plane strain conditions, and leads to the same results.

5.1.2. THM model verification examples in interfaces

This section presents three verification examples of the THM fully-coupled model with large advection developed in Chapter 4 for the zero-thickness interface elements. Summarizing, the main verifications are focused on:

1) the advective heat transport with the hydraulic flow using the α-Implicit Characteristic Galerkin Method (hydro-thermal coupling) and,
2) the influence of thermal fluid expansion, specifically in the pressure and stress-strain variations and the generated flow (thermo-hydro-mechanical coupling).

Verification example 7: Hydro-Thermal coupling in interfaces without fluid thermal expansion and constant fluid viscosity

The objective of this example is to verify the hydro-thermal coupling of the model in zero-thickness interface elements, specifically the stability of the advection phenomenon that occurs due to the existence of the fluid flow and its correct velocity transport. For simplicity, the following assumptions are made: pure advection, constant fluid viscosity, no volume change of the fluid due to thermal effects ($\alpha_f^T = 0℃^{-1}$) and gravity omitted for the hydraulic problem.

The geometry consists of a domain of 450m, discretized with 180 zero-thickness interface elements, as shown in Figure 5.18 with the material parameters of the numerical analysis. Constant hydraulic conductivity is assumed.

$K^f = \ 3 \cdot 10^{12}$ kPa
$\gamma^f = 10$ kN/m^3
$\mu = 1 \cdot 10^{-11}$kPa $\cdot$ s
$\alpha_f^T = 0$°C^{-1}

$c = 700$ J/(kg $\cdot$ °C)
$\rho = 1000$ kg/m^3
$k_{\mathrm{L}}^T = 0$ J/(m $\cdot$ °C $\cdot$ s)
$k_{\mathrm{L}}^p = 9 \cdot 10^{-12}$ m^2

$k_{\mathrm{T}}^T = 0$ J/(m^2 $\cdot$ °C $\cdot$ s)
$k_{\mathrm{T}}^p = 1 \cdot 10^{-5}$ s^{-1}
$\alpha_{ICG} = 0.25$
$r_N = 0.1$ m

Figure 5.18: Mesh and material properties of the HT verification example.

In a first step the temperature of the domain is equal to zero and the steady-state hydraulic problem is solved considering the boundary conditions shown in Figure 5.19. The results of this step are shown in Figure 5.20 (lineal distribution of fluid pressures), with Darcy velocity equal to 0.006 m/s (from the left to the right). This value can also be obtained analytically as:

$$q_L^p = -r_N \frac{k_{\mathrm{L}}^p}{\mu^f}\left(\frac{\Delta p}{L}\right) = -0.1 \text{ m} \frac{9 \cdot 10^{-12} \text{ m}^2}{1 \cdot 10^{-11} \text{ kPa} \cdot \text{s}}\left(\frac{20 - 50 \text{ kPa}}{450 \text{ m}}\right) = 0.006 \text{ m/s} \tag{5.76}$$

that matches the value obtained in the numerical analysis.

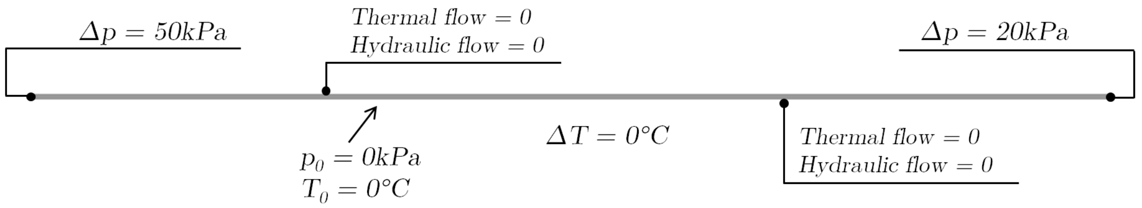

Figure 5.19: Boundary conditions for the first step of the HT verification example.

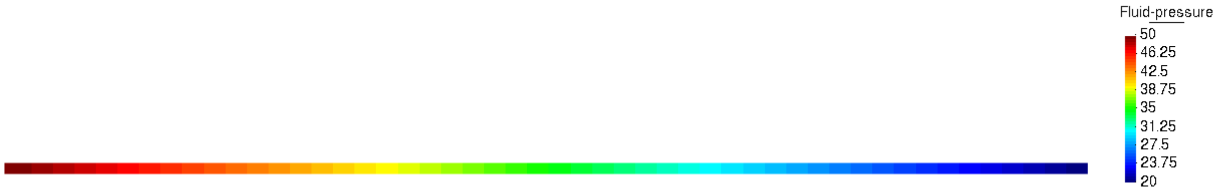

Figure 5.20: Fluid pressure distribution for the first step of the HT verification example.

In a second step, a Gaussian distribution of temperatures (with a maximum value of 40°C) is applied as a Dirichlet condition while the fluid flow remains constant (Figure 5.21).

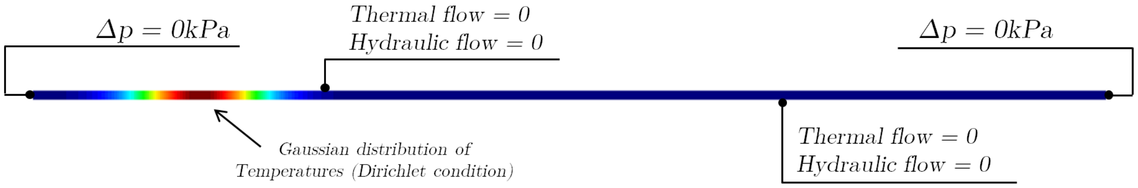

Figure 5.21: Boundary conditions for the second step of the HT verification example (Legend in Figure 5.23).

The thermal conductivity is assumed equal to zero and therefore the Péclet number tends to infinite (pure advection thermal problem). The transient problem is carried out with time increments $\Delta t = 350$ s. The Courant number in all the elements of the mesh is less than 1 ($C = 0.84$), which is a necessary condition to obtain a non-oscillatory result using the method of characteristics.

As the time passes, the initial temperature distribution has to move from left to right with the correct velocity (0.006 m/s) and keeping the initial temperature distribution profile. The result of the analysis is shown in Figure 5.22 and Figure 5.23 for different times. These figures show that the method maintains the initial distribution of temperatures with small oscillations of ±0.10℃ at the top of the “bell”.

(a) t = 0 s.

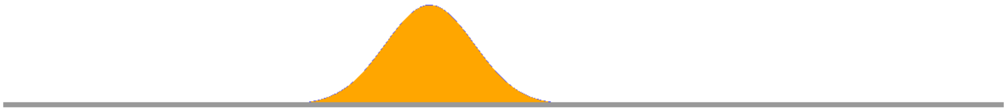

(b) t = 20650 s.

(c) t = 41300 s.

(d) t = 63700 s.

Figure 5.22: Distribution of temperatures using the α-ICG Method for different times using $\alpha_{ICG} = 1/4$.

The last verification consists in checking whether the velocity applied to the thermal distribution matches the Darcy velocity of the fluid. For example, for $\Delta t = 41300$ s and knowing that the Darcy velocity of the fluid is $q_{\mathrm{L}}^{p} = 0.006$ m/s, the top of the “bell” of the initial distribution has moved to the right $\Delta L = q^p_{\mathrm{L}}\ \Delta t = 247.80$ m, which matches the displacement of the initial temperature distribution, as shown in Figure 5.22.

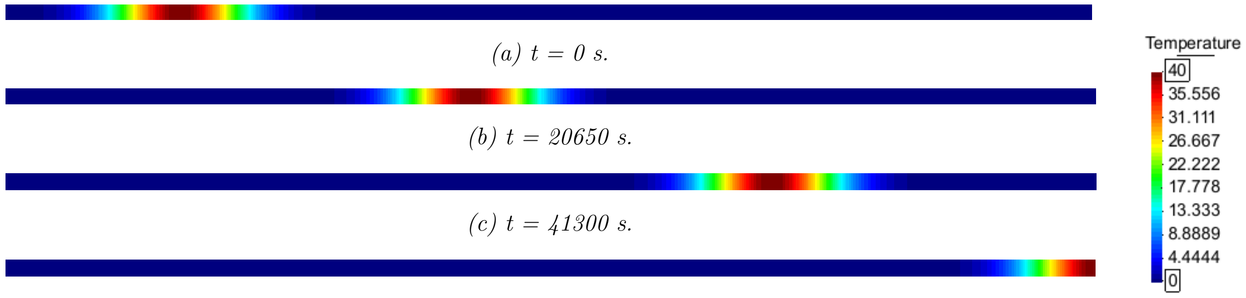

(a) t = 0 s.

(b) t = 20650 s.

(c) t = 41300 s.

(d) t = 63700 s.

Figure 5.23: Distribution of temperatures using the α-ICG Method for different times using $\alpha_{ICG} = 1/4$.

Additionally, during the transient analysis the pressure and Darcy velocity remain constant as expected with the hypothesis of the problem (constant viscosity of the fluid and no volume change of the fluid due to its thermal expansion).

Verification example 8: Hydro-mechanical coupling in interface elements

In order to verify the hydro-mechanical coupling of the model, a one-dimensional consolidation problem of a discontinuity has been carried out. This example is based on a verification example of the HM model that appears in (Segura, 2007).

The geometry consists of a domain of 1m, discretized with 10 zero-thickness interfaces. The geometry, the initial and boundary conditions and the material parameters are shown in Figure 5.24. The initial fluid pressure is null and the interface is loaded with 15 kPa. Consolidation begins immediately after application of the load. Linear elasticity and constant longitudinal hydraulic conductivity are assumed.

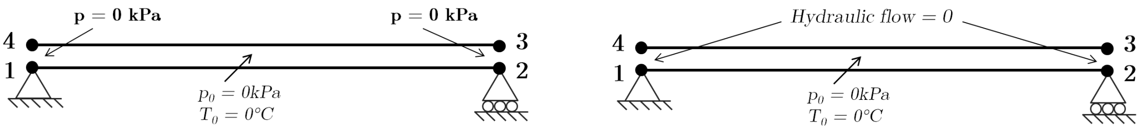

Linear elasticity

$K_n = 20000$ kPa/m

$K^f = 3 \cdot 10^{12}$ kPa

$\gamma^f = 10$ kN/m^3

$\mu = 1 \cdot 10^{-11}$ kPa · d

$k^p_{\mathrm{L}} = 1.08 \cdot 10^{-12}$ m^2

$r_N = 0.01$ m

$\alpha_{Biot} = 1.0$

$M_{Biot} = 1 \cdot 10^{10}$

Figure 5.24: Mesh, initial and boundary conditions and material parameters for the HM verification problem.

The fluid pressure evolution with time can be calculated analytically combining the fluid mass balance equation and Darcy's law, obtaining the following expression, analogous to the one obtained for the continuum media (Segura, 2007):

$$p = \sum_{m=0}^{m=\infty} \frac{2p_{ini}}{M} \sin(M\mathrm{X}) \cdot e^{-M^2 T} \tag{5.77}$$

where $M = \frac{\pi}{2}(2m+1)$ with $m = 0,1,2,\ldots$ and C_v is the consolidation coefficient defined as:

$$C_v = K_n r_N \frac{k_{\mathrm{L}}^p}{\mu} \tag{5.78}$$

and the dimensionless variables X and T are::

$$X = \frac{x}{L} \tag{5.79}$$

$$T = \frac{C_v t}{L^2} \tag{5.80}$$

In order to obtain the same fluid pressure distribution than in the continuum medium consolidation example, the same value of the consolidation coefficient must be used for both cases. Assuming a constant interface aperture of $r_N = 0.01$ m, the longitudinal permeability for the interface must be:

$$\frac{k^p}{\mu} E_m = K_n r_N \frac{k_{\mathrm{L}}^p}{\mu} \quad \Rightarrow \quad k_{\mathrm{L}}^p = 1.08 \cdot 10^{-12} \ \mathrm{m}^2 \tag{5.81}$$

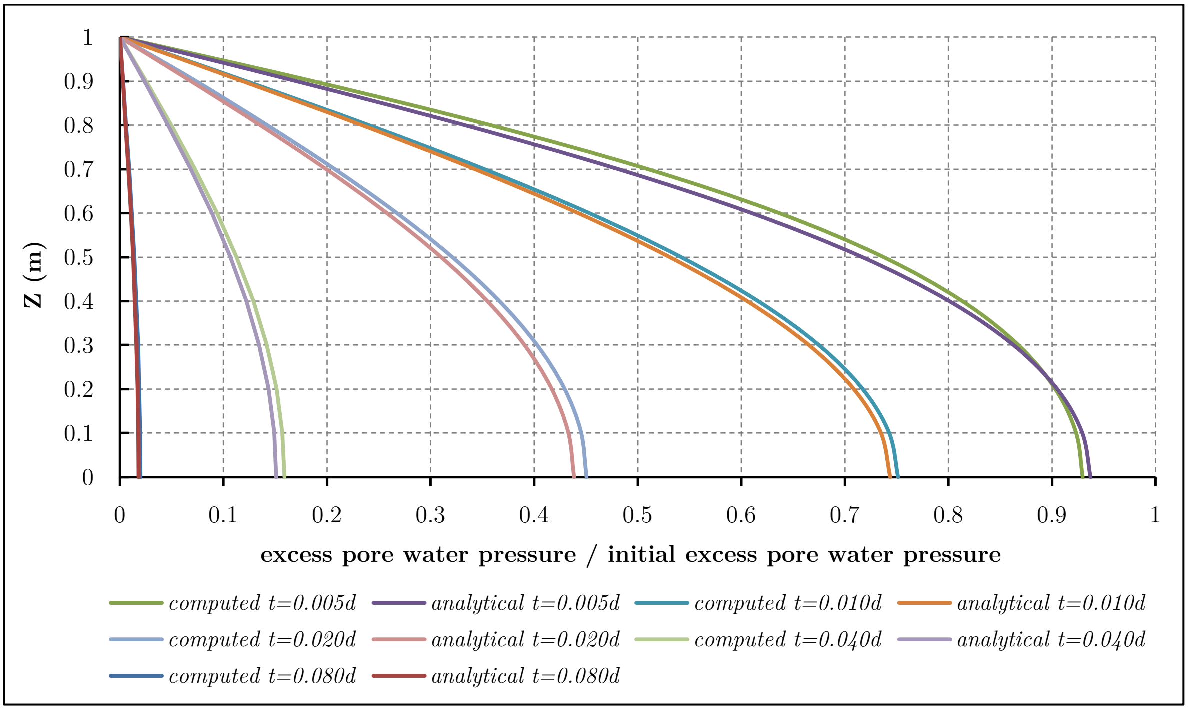

Figure 5.25: Fluid pressure distributions with depth at different times.

Figure 5.25 shows the fluid pressure distribution for different times, in which the analytical and the numerical solutions are practically identical and equal to those obtained for the consolidation example in continuum medium (Figure 5.12).

Verification example 9: Thermo-hydro-mechanical coupling in zero-thickness interface elements

The objective of this example is to verify the thermo-hydro-mechanical coupling of the model, specifically the hydraulic and mechanical behaviour when a temperature increment is applied to an interface and the fluid tends to change its volume due to thermal expansions.

For simplicity, the geometry consists of a domain of 1m discretized with a single zero-thickness interface element. This verification example includes two cases in terms of the boundary conditions (drained and undrained analysis), that are shown in Figure 5.26.

For the numerical analysis, linear elasticity is assumed under conditions of plane strain with material parameter $K_n = 200000$ kPa/m. Additionally, the effect of the gravity is omitted. The temperature increment applied is the same for both cases and equal to 40℃.

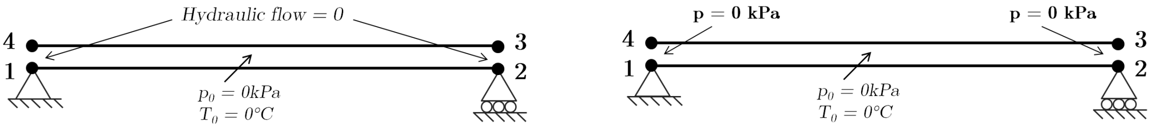

(a) Boundary conditions for the undrained analysis. *(b) Boundary conditions for the drained analysis.*

Figure 5.26: Mesh and boundary conditions for the THM verification example.

a) Drained analysis

In this case $\alpha_f^T = 0.001℃^{-1}$ and $r_N = 0.01$ m. Table 5.15 shows the numerical results at the four nodes of the element. Additionally, the computed effective stresses at the Gauss points are equal to zero.

Table 5.15: Numerical results for the drained analysis with $\alpha_f^T = 0.001℃^{-1}$ and $r_N = 0.01$ m. Compressive pressures and outgoing hydraulic flow are positive.

Node	DISPL-X (m)	DISPL-Y (m)	PRESSURE (kPa)	H-FLOW (m^3)
1	0.00000E+00	0.00000E+00	0.00000E+00	3.00000E-04
2	0.00000E+00	0.00000E+00	0.00000E+00	3.00000E-04
3	0.00000E+00	0.00000E+00	0.00000E+00	3.00000E-04
4	0.00000E+00	0.00000E+00	0.00000E+00	3.00000E-04

The same values can be obtained analytically. The fluid thermal expansion may be obtained as:

$$\Delta\varepsilon_{v,fluid} = \alpha_{v,f}^{T}\Delta T = 3\alpha_{f}^{T}\Delta T = 0.12 \tag{5.82}$$

and the fluid volume increment as:

$$\Delta V_{fluid} = \Delta\varepsilon_{v,fluid}(L \times \mathrm{r_N} \times 1\mathrm{m}) = \underline{0.0012\ \mathrm{m}^3} \tag{5.83}$$

which is the fluid leaving the domain and matches the sum of the outgoing flow at the four nodes of the domain obtained in the numerical analysis. Additionally, since the fluid leaves the domain without restrictions, the pressures and stresses will be null.

b) Undrained analysis

In this case $\alpha_f^T = 0.001℃^{-1}$ and $r_N = 0.01$ m. Table 5.16 shows the numerical results at the four nodes of the element. Additionally, the computed effective stresses at the Gauss points are equal to the fluid pressures but with the opposite sign.

Table 5.16: Numerical results for the undrained analysis with $\alpha_f^T = 0.001℃^{-1}$ and $r_N = 0.01$ m. Compressive pressures and outgoing hydraulic flow are positive.

Node	DISPL-X (m)	DISPL-Y (m)	PRESSURE (kPa)	H-FLOW (m^3)
1	0.00000E+00	0.00000E+00	2.40000E+02	0.00000E+00
2	0.00000E+00	0.00000E+00	2.40000E+02	0.00000E+00
3	0.00000E+00	1.20000E-03	2.40000E+02	0.00000E+00
4	0.00000E+00	1.20000E-03	2.40000E+02	0.00000E+00

The same values can be obtained analytically. Since the fluid cannot leave the domain (undrained analysis), the opening of the interface is proportional to the fluid thermal expansion:

$$u_y = \Delta r_N = r_N\ \Delta\varepsilon_{v,fluid} = \underline{0.0012\ \mathrm{m}} \tag{5.84}$$

And the excess fluid pressure may be obtained as:

$$\Delta p = K_n \Delta r_N = \underline{240\ \mathrm{kPa}} \tag{5.85}$$

matching the values obtained in the numerical analysis.

5.2. Practical Application: Hydraulic Fracture

This section describes the application of the THM advective model with zero-thickness interface elements to hydraulic fracture modelling. A brief introduction to hydraulic fracture is presented, followed by the numerical modelling of a hydraulic fracture problem in 2-D, taking special attention on the effect of the temperatures, and comparing the obtained results with those obtained with the HM model. Additionally, a performance parallelization analysis of the FEM code is presented.

5.2.1. Introduction to Hydraulic Fracture

Hydraulic fracturing is a common technique used in Petroleum Engineering, which aims to induce the fracturing of the rock mass by pumping a highly pressurized fluid at a certain rate into the geological formation (Figure 5.27).

The initiation and propagation of induced fractures in a reservoir from a wellbore increase its hydraulic conductivity and therefore may improve the oil recovery. Thus, this method is used to improve the hydrocarbons production, especially in low permeability reservoirs. Additionally, when the pumping stops and the fluid pressure decreases, the fractures would tend to close. To avoid the fracture closing two solutions may be applied: to fill the created paths with solid elements (proppant) or the acid attack in the fracture surface to avoid a perfect closing.

The temperature of a reservoir located at high depth could be very high (60-70℃ or more), while the injected fluid temperature is lower (5-20℃). Thus, when the fluid is injected to the reservoir, the heat transport along the discontinuities (advection) may produce thermal expansion of the porous medium and of the fluid filling the discontinuities and may also modify the fluid properties (density and viscosity).

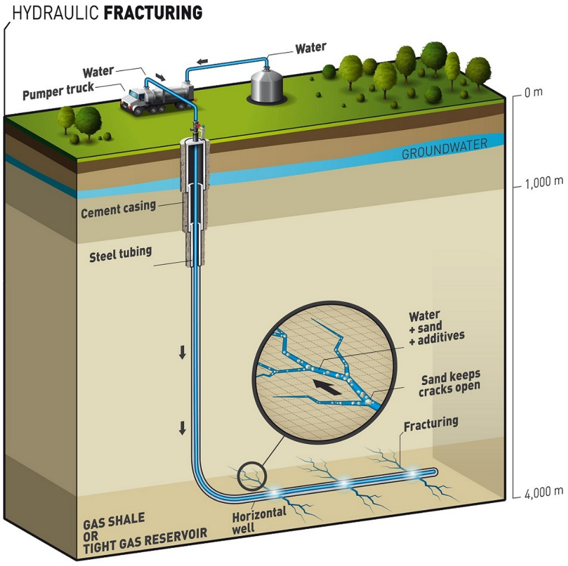

Figure 5.27: Scheme of a hydraulic fracture procedure in an oil or gas reservoir.

One of the most important aspects of this technique is the fluid injection efficiency, which is the ratio between the fluid remaining in the fractures at the end of the fracture process and the fluid injected at the beginning. It gives knowledge of the amount of injected fluid that is lost across the discontinuity to the matrix (leak-off), which reduces the efficiency of the process. This is usually corrected creating a thin layer, known as filter cake, on the fracture faces with the aid of some additives in the fluid during the injection process.

Hydraulic fracture techniques are also used in other engineering activities, such as in the creation of impermeable barriers for contaminant containment, in the injection of slurry wastes or in the measurement of in-situ stresses in rock masses, and it may also appear naturally (i.e. dike intrusion into a geologic formation or magma driven fractures).

Despite the fact that hydraulic fracture is a technique that has been extensively used since the 1960's, its modelling is still under development. It is a complex non-linear mathematical problem that involves the mechanical interaction of the propagating fracture with the fluid dynamics of the injected fluid and with the thermal effects due to the temperature difference between the reservoir and the injected fluid and the heat transport of the fluid along the discontinuities. The strong coupling between several mechanisms makes necessary to involve different disciplines in order to study the hydraulic fracture problem, such as fluid mechanics, fracture mechanics and thermal mechanics.

At the beginning of hydraulic fracturing any model was used to study the fracture processes. However, due to the increasing complexity of the exploited reservoirs, some analytical formulation and numerical tools began to be developed. The first analytical models were the so-called planar2D models such as the Perkins Kern Nordgren, or PKN model (Perkins & Kern, 1961) and its latter modification to include the effects of fluid leak-off (Nordgren, 1972); or the Geertsma De-Klerk Khristianovich, or GDK model (Geertsma & De Klerk, 1969). Later, the pseudo3D models appeared as an extension of the previous ones. At the same time, the planar3D models appeared, which have been used in the industry up to the present. More information about these models can be found in Yew (1997) and (Adachi, et al. (2007). Nowadays, the new methods are based in a real 3D analysis carried out with the FEM or DEM, where the meshes are three-dimensional and the equations are solved in three dimensions in a fully-coupled scheme. The mechanical behavior is usually modeled with the FEM (Li et al. 2012, Secchi & Schrefler 2012), sometimes combined with the FDM for the fluid. These models have the advantage of being the most realistic, but are still under development and involve a large number of parameters and an important computational cost.

An extension about the state of the art of hydraulic fracture can be found in Garolera (2017).

5.2.2. Single fracture modelling in 2-D

The aim of this example is to develop the numerical modelling of hydraulic fracturing using zero-thickness interface elements considering thermal effects. This example follows the works of Segura (2007), Segura & Carol (2008b) and Garolera (2017), where the fully-coupled hydro-mechanical formulation with interfaces was used to simulate the same practical example for a single fracture in 2D. Although the analysis carried out by Segura assumed a linear elastic behaviour of the interfaces with very low modulus, the analysis performed by Garolera (2017) has considered the elasto-plastic constitutive law for interfaces described in section 4.2, and has shown a good agreement with the analytical models (GDK and PKN) and with the numerical solution given by Boone & Ingraffea (1990) in 2D.

While these previous works have only considered the HM coupling in the numerical analysis, in this thesis the analysis is carried using the THM model with advection developed in Chapter 4, but considering constant fluid viscosity. While the reservoir is usually located at great depth and it is subjected to high temperatures, the injected fluid is at ambient temperature. Thus, the objective of this analysis is to understand the thermal mechanisms that occur in hydraulic fracture problems and its effect on the mechanical and hydraulic fields, in order to achieve more realistic results of hydraulic fracture analysis. The results of the analysis are compared to previous analytical and numerical results obtained from a simpler HM-only coupling.

Thus, the fundamental objective of this example is to explore the capabilities of zero-thickness interface elements equipped with realistic non-linear constitutive law and using the THM model with advection for the hydraulic fracturing modelling.

The original geometry of the problem is taken from Boone & Ingraffea (1990) and consists of a semicircular domain of radius 80 meters representing a transversal cross-section of the borehole (Figure 5.28), where the fracture path is inserted along the abscissa axis and which is discretized with a FEM mesh made of 2262 linear triangular elements and 160 zero-thickness interface elements (Figure 5.29a).

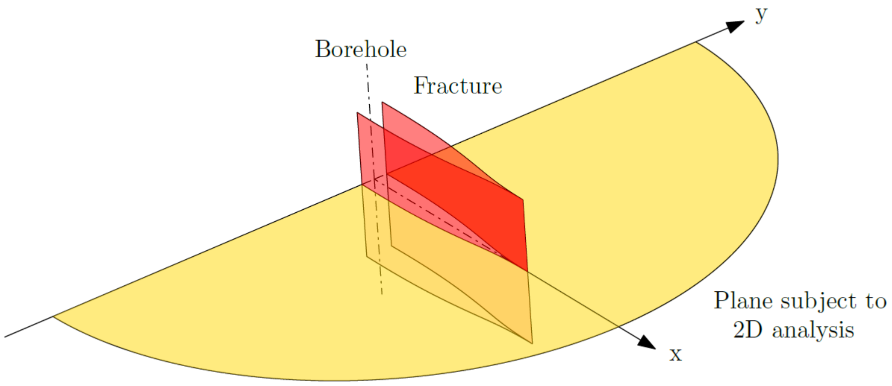

Figure 5.28: Scheme of the hydraulic fracture test (Garolera, 2017).

In this case, although the HM analysis parameters and the length of the zero-thickness interface elements (0.50 m) are the same as those used in Garolera (2017) and Segura (2007), the maximum time-step is given by the Courant condition -Eq. (2.117)-, which is related to the thermal advective problem and results in a maximum time-step of $\Delta t_{max} = 0.25$s. Additionally, the minimum time-step for the transient thermal analysis – which affects the continuum medium transversal to the interfaces – is given by Thomas & Zhou (1997):

$$\Delta t \geq \rho c \frac{h_T^2}{6k^T} \tag{5.86}$$

where h_T^2 is the transversal dimension of the continuum elements transversal to the interfaces and k^T is the thermal conductivity for continuum medium. In this case, since the time-step is given by the Courant condition ($\Delta t_{max} = 0.25s$), the time-step condition for the transient analysis in the continuum medium becomes a maximum size condition of the elements transversal to the interfaces equal to:

$$h_T \leq \sqrt{\frac{6k^T \Delta t}{\rho c}} = 0.020\text{m} \tag{5.87}$$

Thus, for this example, a rectangular domain meshed with hexagonal elements (Figure 5.29.b) has been used, where the transversal length of the elements close to the interface is equal to $h_T = 0.020$m, growing gradually away from the interface. This mesh if formed by 3748 continuum elements and 160 interface elements with a total of 3975 nodes and 15900 degrees of freedom. It is important to note that with the old mesh (Figure 5.29.a), significant temperature oscillations appear in the continuum medium parallel to the fracture. This fact results in incorrect strains and stresses when the temperatures are coupled with the mechanical field in the thermo-mechanical analysis, which may be orders of magnitude bigger than the correct strains and stresses and may lead to meaningless solutions.

The analysis is divided in two steps. The initial and boundary conditions for each one (Figure 5.30) are described as follows:

1. **Initialization (previous to the injection):** a distributed load of 1.0 MPa is applied on the outer boundary in order to simulate the *in situ* initial stress. Initial pore pressures are assumed to be zero in the entire domain and the initial temperatures are assumed to be equal to 60℃ in the entire domain.
2. **Injection:** a fluid is injected at the fracture mouth with a constant rate of Q = 0.0001 m^3/s for the impervious case and Q = 0.0005 m^3/s for the pervious case. The horizontal and vertical movement are restricted on the outer boundary and the initial pressure is assumed to be zero in the entire domain. For the thermal problem a convective-type boundary condition has been adopted to impose the thermal flow at the fracture mouth, considering a fluid temperature of 10℃. The analysis is carried out under transient conditions with increasing time steps with a total duration of 25 s.

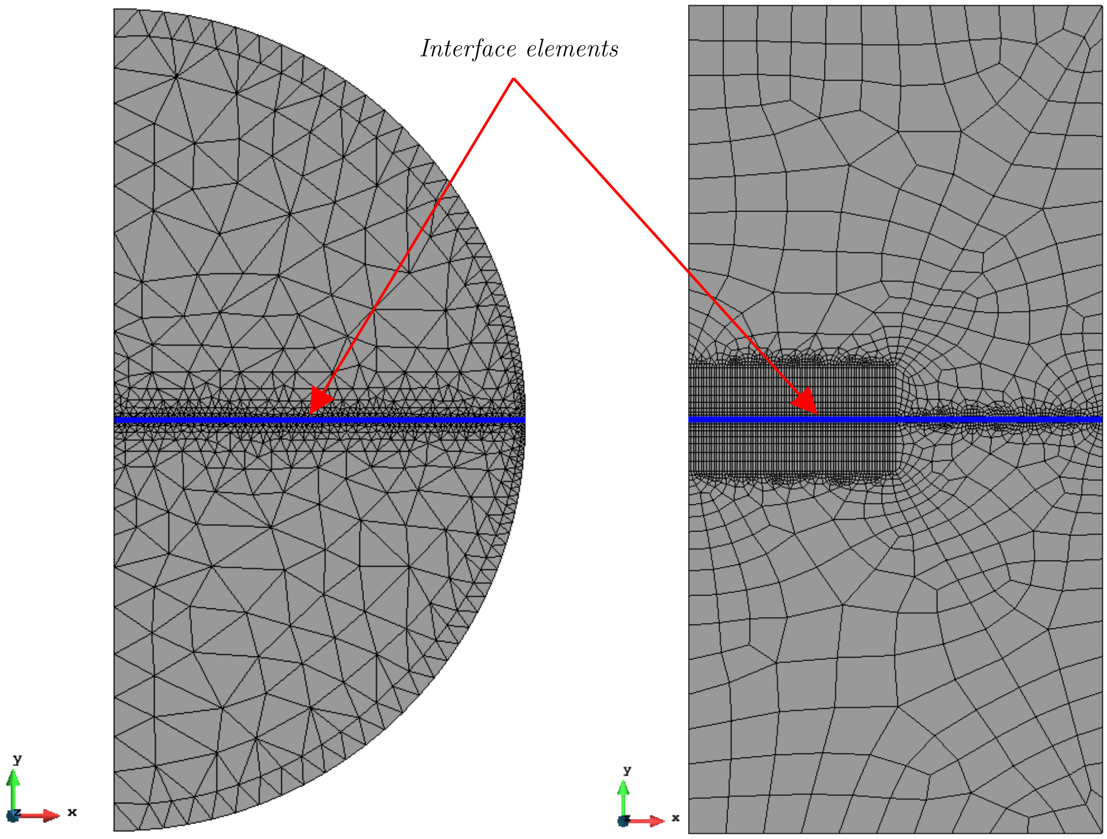

(a) (b)

Figure 5.29: FEM mesh for the single fracture analysis (a) original mesh (b) mesh used in this thesis.

Linear elasticity is assumed for the continuum porous medium, with parameters extracted from Boone & Ingraffea (1990), which are the same used by Segura (2007), Segura & Carol (2008b) and Garolera (2017). The energy-based constitutive law described in section 4.4 is used for the interfaces, with high values of normal shear stiffness in order to avoid elastic deformations, so that the deformations can be assumed inelastic. Additionally, in order to compare with analytical methods, fictitious strength parameters (with low values) are used. Specifically, cohesion (c_0) and tensile strength (χ_0) have very small values and, to avoid numerical instabilities due to the low confinement, a low friction angle ($\tan\phi$) is selected. The values of fracture energies G_f^I and G_f^{IIa} are not relevant due to the use of residual strength parameters. The analysis is carried out under plain strain conditions and the parameters used for the analysis are shown in Table 5.18.

For the hydraulic problem an initial hydraulic longitudinal permeability equal to zero is assumed, and during the analysis its value is controlled by the cubic law, which is function of the opening of the interface. The injected fluid is assumed to be water and the Biot modulus (M_J) has a very high value to avoid compressibility effects. The value of the hydraulic transversal conductivity of the interfaces (K_{T}^{p}) is irrelevant because the symmetry of the problem prevents the hydraulic flow to cross the interface transversally. The hydraulic parameters used for the analysis are shown in Table 5.19.

Table 5.17: Material properties of continuum porous medium.

Parameter	***Value***		***Units***
$\boldsymbol{E}$ (Young modulus)	14400		MPa
$\boldsymbol{\nu}$ (Poisson ratio)	0.2		
$\boldsymbol{n_0}$ (initial porosity)	0.19		
$\boldsymbol{Ks}$ (skeleton compressibility)	36000		MPa
$\boldsymbol{Kf}$ (fluid compressibility)	10^{10}		MPa
$\boldsymbol{\rho^f}$ (fluid density)	10^{-3}		kT/m^3
$\boldsymbol{\mu}$ (water viscosity at 20ºC)	10^{-9}		MPa · s
$\boldsymbol{k^T}$ (thermal conductivity)	1.50		J/(m · ℃ · s)
$\boldsymbol{\alpha_s^T}$(linear solid thermal exp.)	$1.2 \cdot 10^{-5}$		℃$^{-1}$
$\boldsymbol{c}$ (heat capacity)	840		J/(kg · ℃)
$\boldsymbol{\alpha_f^T}$ (linear water thermal exp.)	$6.9 \cdot 10^{-5}$		℃$^{-1}$
$\boldsymbol{\alpha_{Biot}}$(Biot coefficient)	0.0		
	Impervious	*Pervious*	
$\boldsymbol{k^p}$ (hydraulic permeability)	10^{-22}	10^{-14}	m^2

Table 5.18: Mechanical properties for interfaces.

Parameter	***Value***	***Units***
$\boldsymbol{Kn}$	10^6	MPa/m
$\boldsymbol{Kt}$	10^6	MPa/m
$\boldsymbol{\tan\phi}$ (friction angle)	0.20	
$\boldsymbol{\chi_0}$ (tensile strength)	0.002	MPa
$\boldsymbol{c_0}$ (cohesion)	0.01	MPa

Table 5.19: Hydraulic properties for interfaces.

Parameter	***Value***	***Units***
$\boldsymbol{k_L^p}$ (initial longitudinal conductivity)	0.0	m^2
$\boldsymbol{K_T^p}$ (transversal conductivity)	1.0	s^{-1}
$\boldsymbol{M_J}$ (Biot Modulus)	10^{10}	
$\boldsymbol{\alpha_{Biot}}$ (Biot coefficient)	1.0	
$\boldsymbol{\rho^f}$ (fluid density)	10^{-3}	kT/m^3
$\boldsymbol{\mu}$ (water viscosity at 20ºC)	10^{-9}	MPa · s
$\boldsymbol{r_N}$ (initial aperture)	0.00	m

Table 5.20: Thermal properties for interfaces.

Parameter	***Value***	***Units***
$\boldsymbol{k_L^T}$ (water longitudinal thermal conductivity)	0.591	J/(m · ℃ · s)
$\boldsymbol{K_T^T}$ (transversal thermal conductivity)	0.1	J/(m^2 · ℃ · s)
$\boldsymbol{c^f}$ (water heat capacity)	4180	J/(kg · ℃)
$\boldsymbol{\alpha_f^T}$ (linear water thermal exp)	$6.9 \cdot 10^{-5}$	℃$^{-1}$

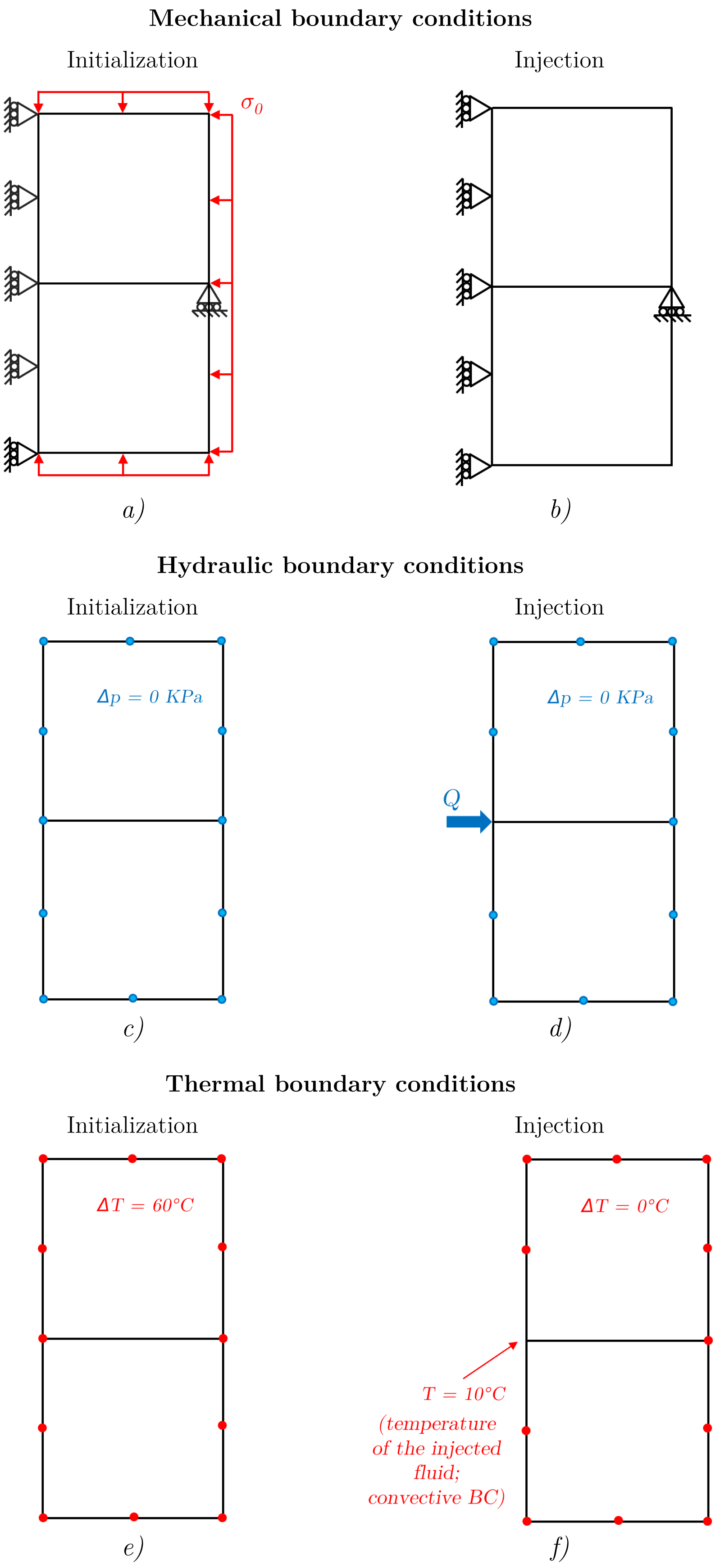

Mechanical boundary conditions

Initialization — a)

Injection — b)

Hydraulic boundary conditions

Initialization — c)

Injection — d)

Thermal boundary conditions

Initialization — e)

Injection — f)

Figure 5.30: Boundary conditions for the initialization and injection steps.

For the thermal analysis it is assumed that the fluid (water) fills the interfaces, and subsequently the water longitudinal thermal conductivity, water heat capacity and water density are assumed for interfaces. The value of the thermal transversal conductivity of the interfaces (K_{T}^{T}), as for the hydraulic problem, is irrelevant because the symmetry of the problem prevents the thermal flow to cross the interface transversally. The thermal parameters used for the analysis are shown in Table 5.20. Additionally, for the thermal advective analysis using the current THM model and the Implicit Characteristic Galerkin Method, $\alpha_{ICG} = 0.0$.

The analysis is carried out considering two hypotheses for the hydraulic analysis. In the first one the fracture is assumed to be embedded in an impervious medium and leak-off cannot occur, while in the second one the fracture is in a pervious continuum medium and leak-off is permitted. The parameters for both analyses are the same except for the hydraulic conductivity, shown in Table 5.18, and the hydraulic flow rate which is Q = 0.0001 m^3/s for the impervious case and Q = 0.0005 m^3/s for the pervious one.

Results: propagation without leak-off (impervious case)

In this case it is assumed that the permeability of the continuum medium is low enough (Table 5.17) to consider that the injected fluid cannot leak to the rock mass.

Figure 5.31 and Figure 5.32 show the temperature distribution in a deformed mesh at the end of the analysis, and Figure 5.33 shows the temperature profile evolution along the mid-plane fracture at different times. The first conclusion obtained from these figures is that the THM model with advection is capable to reproduce the transport of temperatures along the fracture without oscillations when the advection dominates the problem. The advection occurs at the interface elements (not in the continuum medium) and Péclet numbers tends to infinite (1.33E+10), so it can be considered to be a pure advection problem. Additionally, the Courant condition is satisfied in all interface elements, with a maximum value of 0.85. Finally, it is also observed that the injected cold fluid fractures the rock mass and heat interchange occurs between them, where the thermal flow is spent in cooling the injected fluid and the rock mass and the rock mass heats the injected fluid. Figure 5.34 shows the temperature mouth crack evolution during the analysis.

Figure 5.35 shows the numerical solutions for the crack mouth opening displacement (CMOD) evolution during the injection, both for the HM and THM analysis. The figure shows that, when the temperature is considered in the analysis, the CMOD is larger (11% at the end of the injection) than in the HM analysis. The main mechanisms that produce this extra opening are:

1. Contraction of the rock mass due to the temperature difference between the injected fluid (10℃) and the rock mass (60℃).
2. Expansion of the fluid that fills the fracture. The fluid is injected at 10℃ and it is heated by the rock mass (60℃).

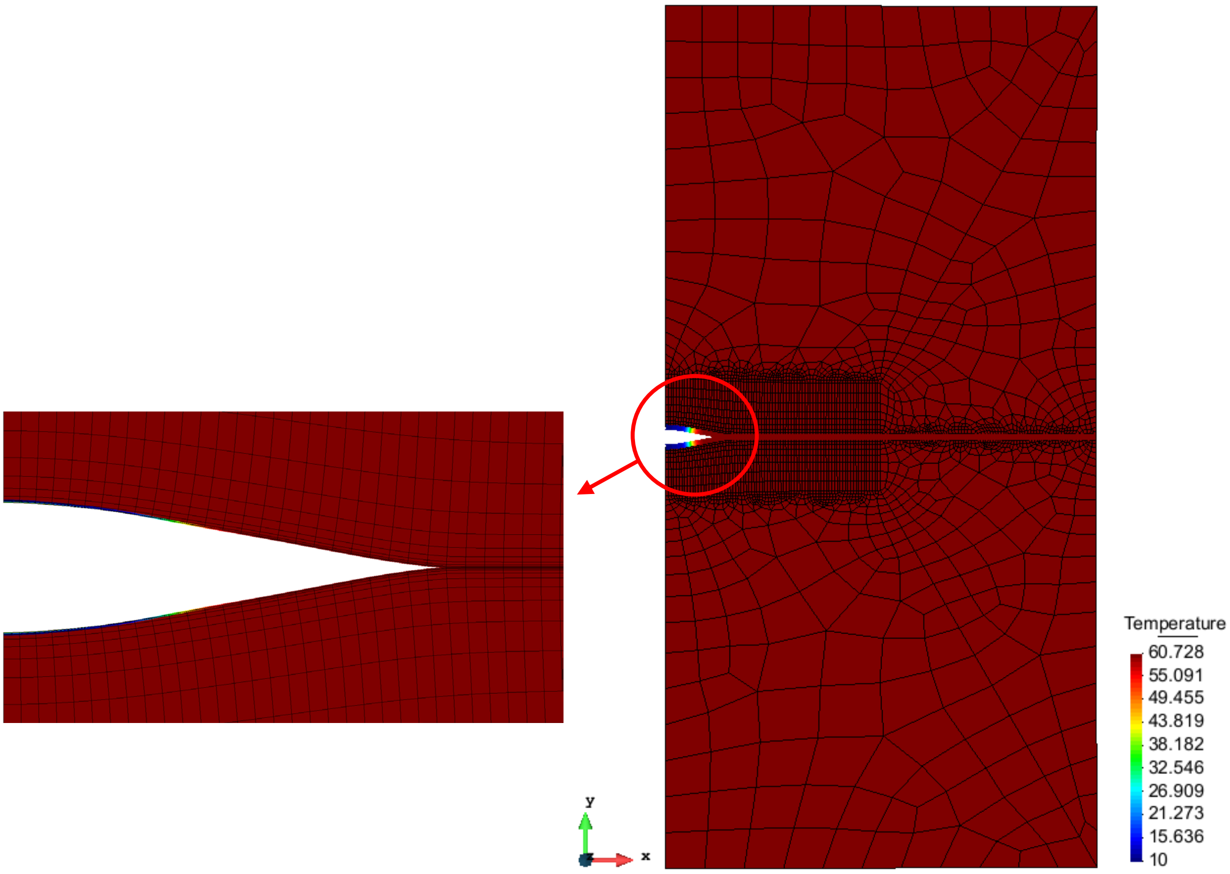

Figure 5.31: Temperature distribution in a deformed mesh (factor ×10000) at the end of the analysis without leak-off.

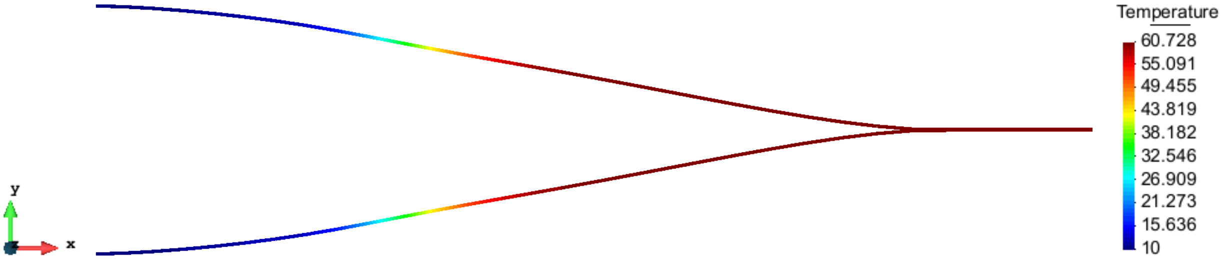

Figure 5.32: Temperature distribution at the interfaces in a deformed mesh (factor ×10000) at the end of the analysis without leak-off.

The analysis shows that the pressures that develop during the fluid injection are similar for both HM and THM analysis, as shown in Figure 5.37 (crack mouth pressure evolution) and in Figure 5.38 (pressure profile evolution along the mid-plane fracture at the end of the analysis). In both analyses, the "fluid lag" phenomenon described by Garolera, et al. (2014), which consists in the existence of negative pressures near the crack due to the delay between opening the crack and filling the fluid, does not appear. A possible explanation may be the use of a more refined mesh in this thesis. Additionally, the crack length slightly decreases (around 4% shorter -0.5m-) when the temperature is considered in the analysis, as shown in Figure 5.36.

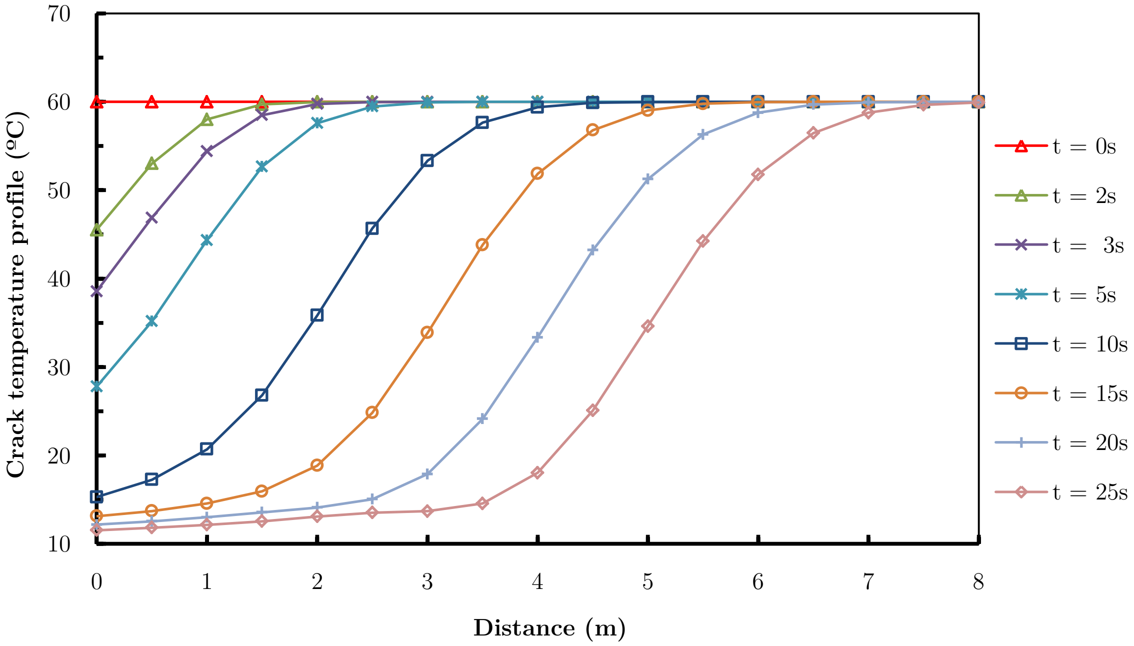

Figure 5.33: Temperature profile evolution along the mid-plane fracture in the case without leak-off.

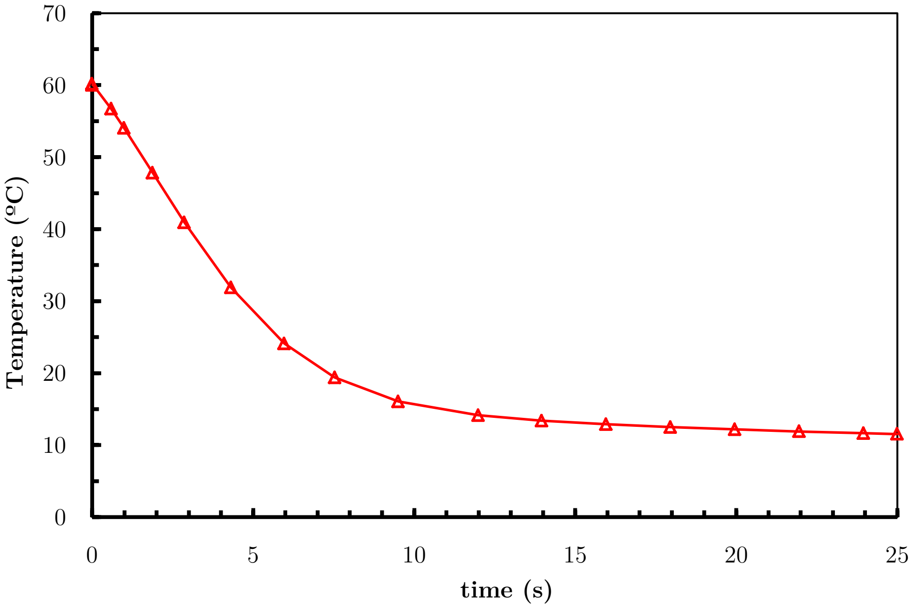

Figure 5.34: Crack mouth temperature evolution in the case without leak-off.

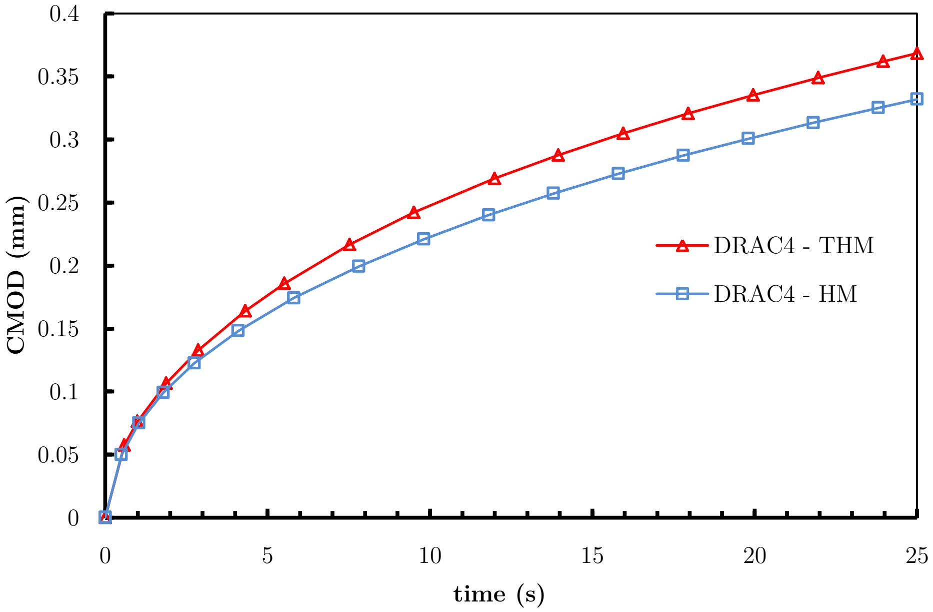

Figure 5.35: Crack mouth opening displacement evolution in the case without leak-off. Comparison between the HM analysis and the THM analysis with advection.

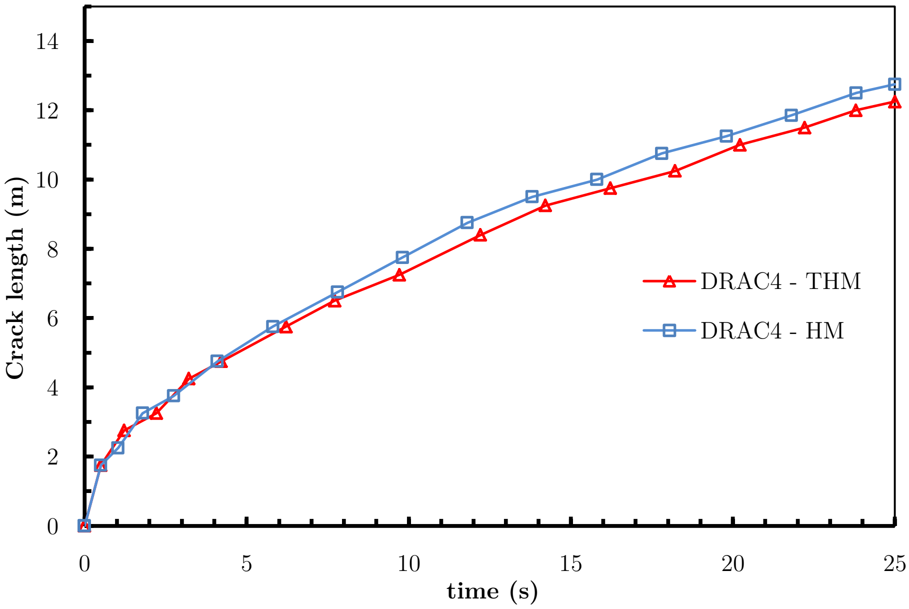

Figure 5.36: Crack length evolution in the case without leak-off. Comparison between the HM analysis and the THM analysis with advection.

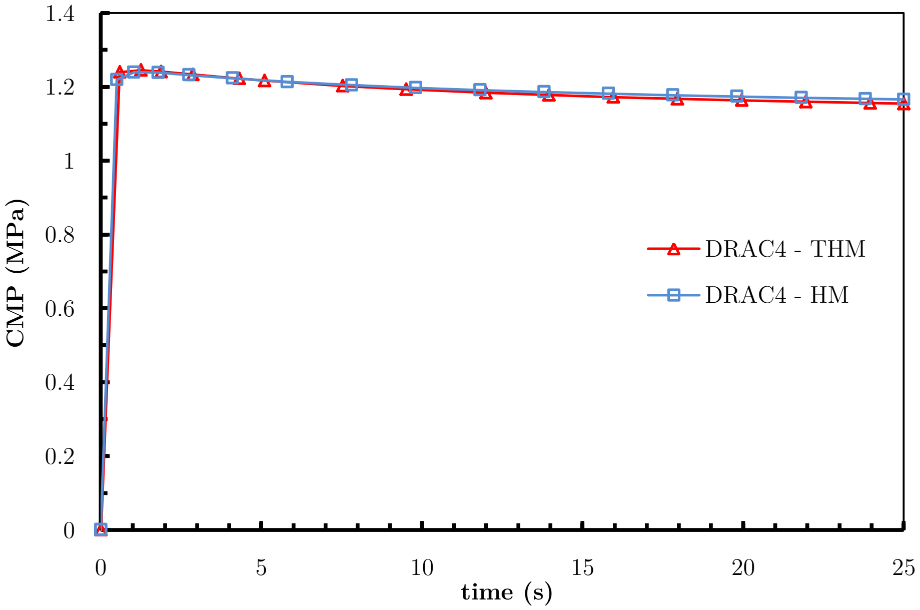

Figure 5.37: Crack mouth pressure evolution in the case without leak-off. Comparison between the HM analysis and the THM analysis with advection.

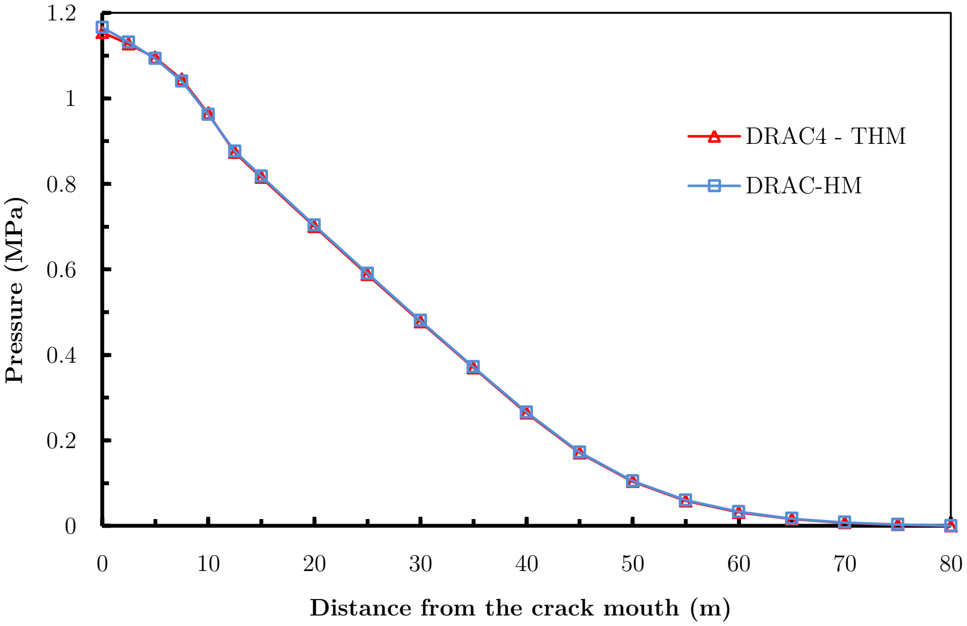

Figure 5.38: Pressure profile evolution along the mid-plane fracture in the case without leak-off at the end of the analysis (t = 25 s). Comparison between the HM analysis and the THM analysis with advection.

In conclusion, the main difference between the HM and THM analyses for the impervious case is that, when temperature is considered, there is an extra-opening of the fracture (approximately 11% at the mouth crack) and that the crack length slightly decreases during the fluid injection.

Finally, Figure 5.39 and Figure 5.40 show the temperature distribution in a deformed mesh and along the mid-plane fracture, respectively, at the end of the analysis when the standard Galerkin weighting is used for the thermal advective FEM analysis. The figures show that the temperature field oscillates strongly along the fracture and its crack opening is clearly wrong.

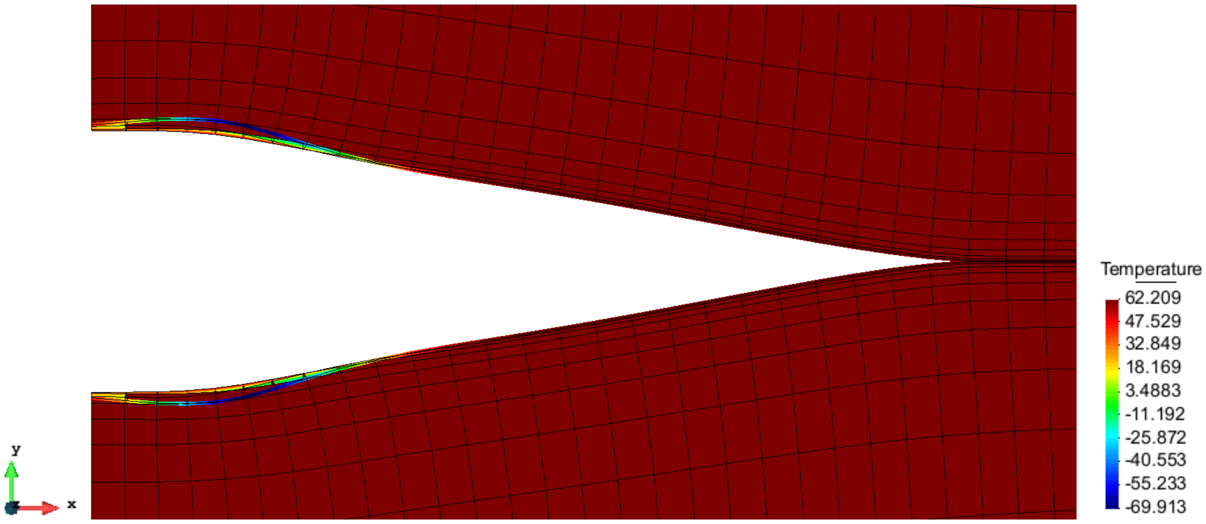

Figure 5.39: Temperature distribution in a deformed mesh (factor ×10000) at the end of the analysis without leak-off using the standard Galerkin weighting for the thermal advective FEM analysis.

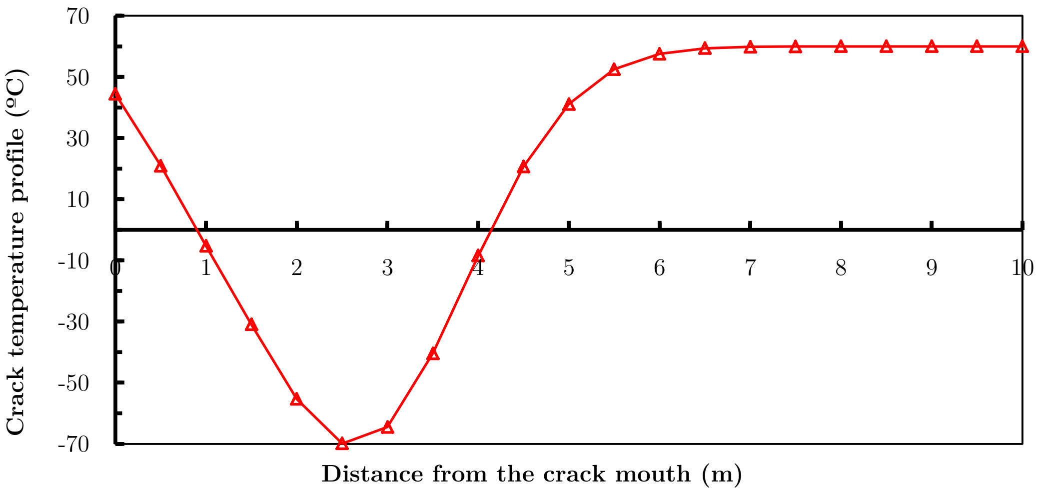

Figure 5.40: Temperature profile distribution along the mid-plane fracture without leak-off using the standard Galerkin weighting for the thermal advective FEM analysis (t = 25 s).

Results: propagation with leak-off (pervious case)

In this case it is assumed that the permeability of the continuum medium is high enough (Table 5.17) to consider that the injected fluid can leak to the rock mass.

As for the impervious case, Figure 5.41 and Figure 5.42 show the temperature distribution in a deformed mesh at the end of the analysis, and Figure 5.43 shows the temperature profile evolution along the mid-plane fracture at different times. The first conclusion obtained from these figures is that the THM model with advection is capable of reproducing the transport of temperatures along the fracture, but in contrast to the impervious case, in which temperature profile was smooth, in this case it exhibits a "wave" oscillation moving with the temperature front and the crack tip. This oscillation was not observed in the case without leak-off. Whether it is caused by numerical effects or is a physical phenomenon remains to be clarified more precisely. However, the fact that its wave length includes several elements and also that it moves smoothly and consistently with the temperature and crack fronts may be indications of a physical origin.

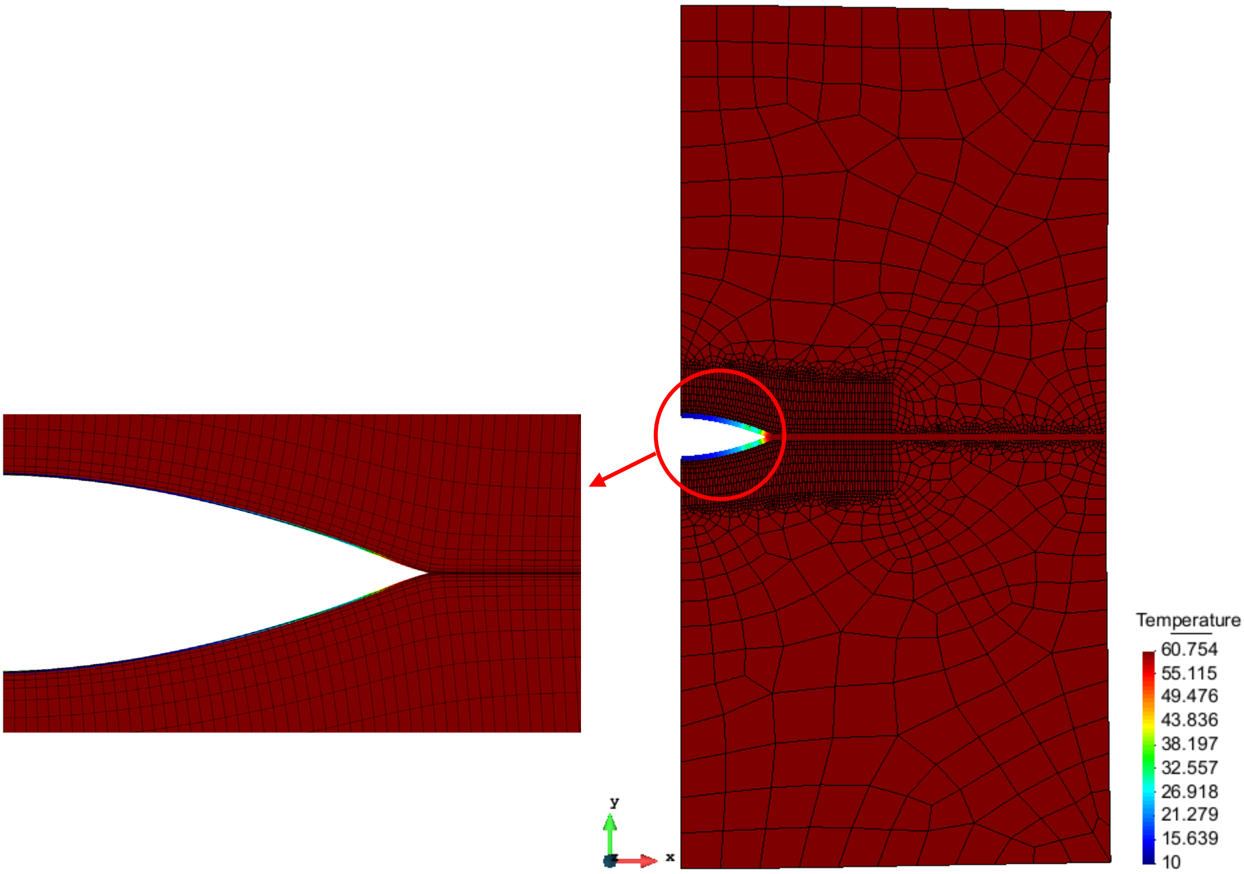

Figure 5.41: Temperature distribution in a deformed mesh (factor ×10000) at the end of the analysis with leak-off.

Also, the advection occurs at the interface elements with high Péclet numbers (1.33E+10) and the Courant condition is satisfied at all interface elements, with a maximum value of 0.85. Finally, it is also observed that the injected cold fluid fractures the rock mass and heat interchange occurs between them, where the thermal flow is spent in cooling the injected fluid and the rock mass and the rock mass heats the injected fluid. Figure 5.44 shows the temperature mouth crack evolution during the analysis.

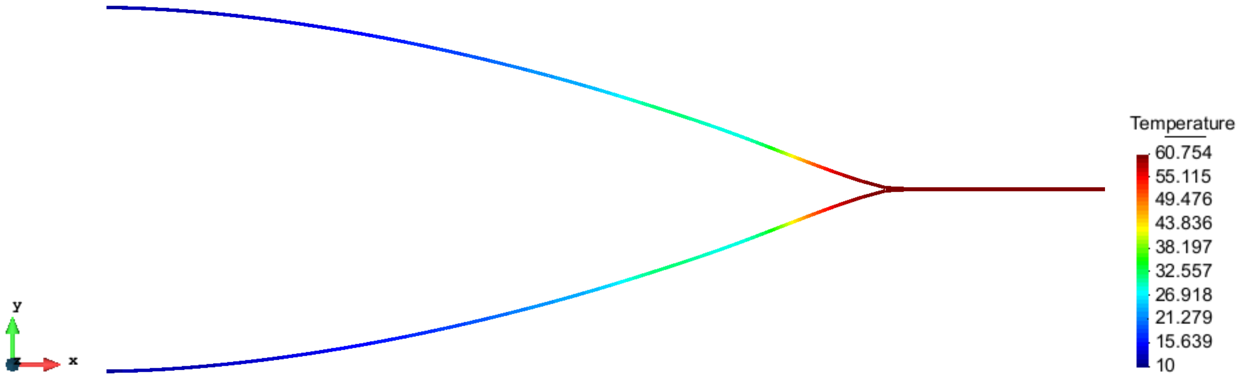

Figure 5.42: Temperature distribution at the interfaces in a deformed mesh (factor ×10000) at the end of the analysis with leak-off.

Figure 5.45 shows the numerical solutions for the crack mouth opening displacement (CMOD) evolution during the injection, both for the HM and THM analysis. The figure shows that, when the temperature is considered in the analysis, the CMOD is larger (10.6% at the end of the injection) than in the HM analysis.

As for the impervious case, the analysis shows that the pressures that develop during the fluid injection are similar for both HM and THM cases, as shown in Figure 5.47 (crack mouth pressure evolution) and in Figure 5.48 (pressure profile evolution along the mid-plane fracture at the end of the analysis). Similar to the impervious case, the “fluid lag” phenomenon described by Garolera, et al. (2014), does not appear. However, unlike what happens in the impervious case, the crack length is similar when the temperature is considered in the analysis, as shown in Figure 5.46.

The conclusion is that the main difference between the HM and THM analyses for the pervious case is that, when temperature is considered, there is an extra-opening of the fracture (approximately 10% at the mouth crack) and that the crack length is similar during the fluid injection. Additionally, unlike what happens in the impervious case, a temperature oscillation appears close to the crack tip.

Finally, Figure 5.49 and Figure 5.50 show the temperature distribution in a deformed mesh and along the mid-plane of fracture, respectively, at the end of the analysis when the standard Galerkin weighting is used for the thermal advective FEM analysis. The figures show that the temperature field oscillate strongly along the fracture and its opening is clearly wrong.

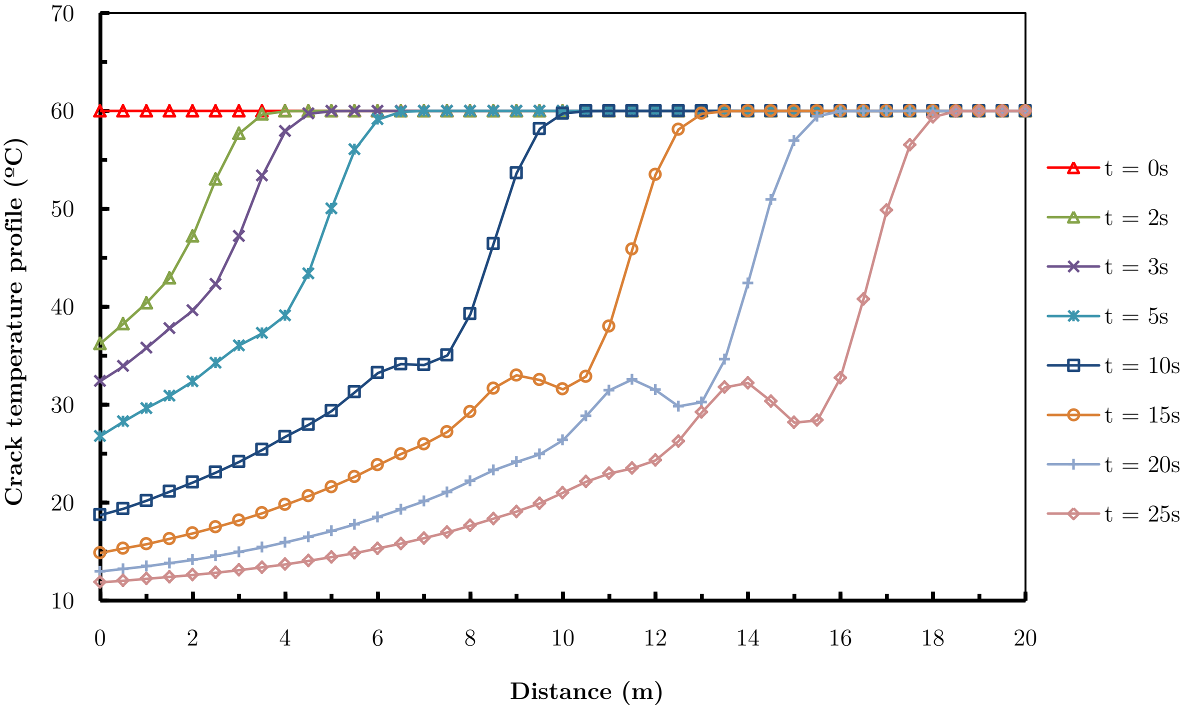

Figure 5.43: Temperature profile evolution along the mid-plane fracture in the case with leak-off.

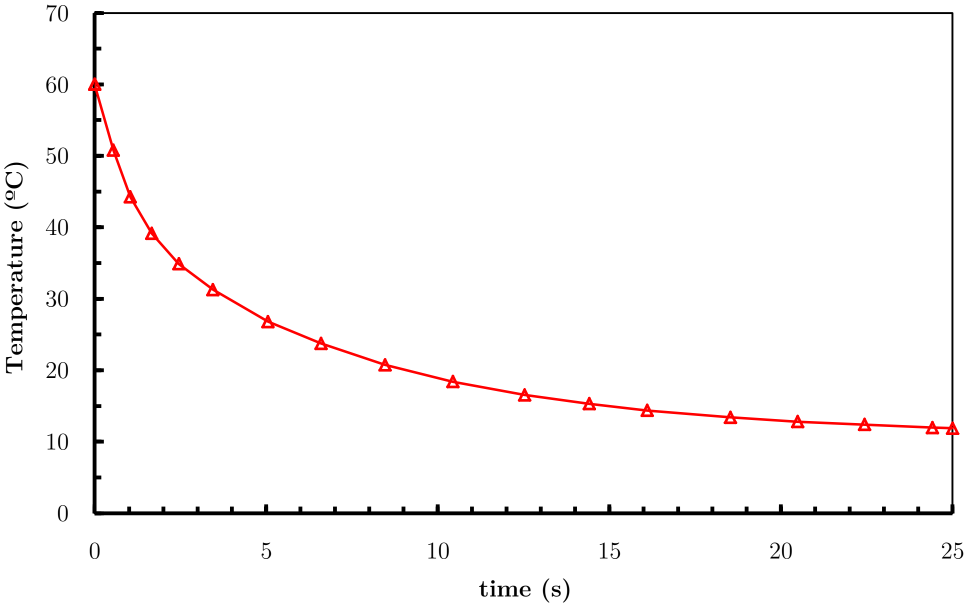

Figure 5.44: Crack mouth temperature evolution in the case with leak-off.

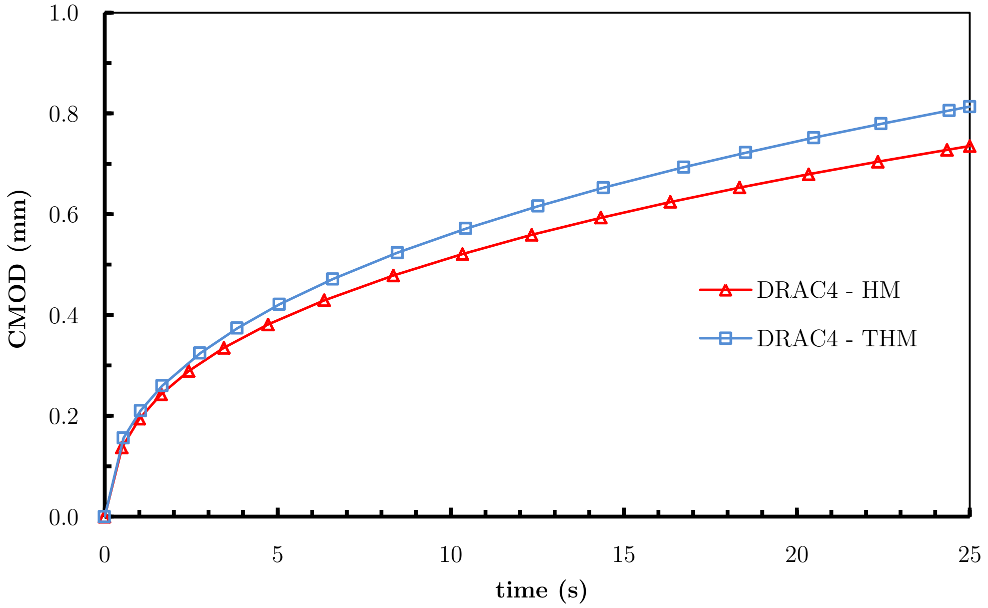

Figure 5.45: Crack mouth opening displacement evolution in the case with leak-off. Comparison between the HM analysis and the THM analysis with advection.

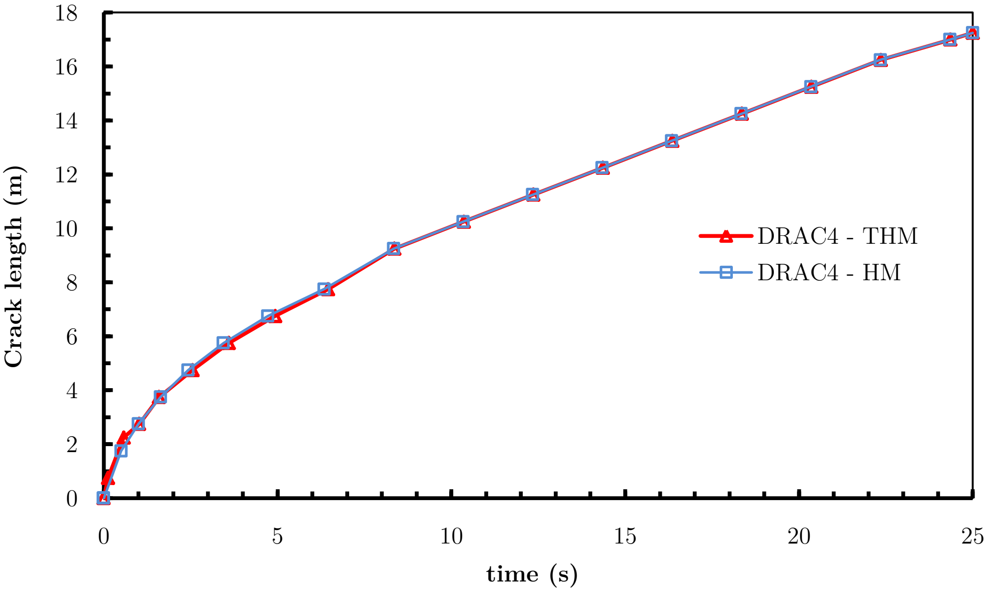

Figure 5.46: Crack length evolution in the case with leak-off. Comparison between the HM analysis and the THM analysis with advection.

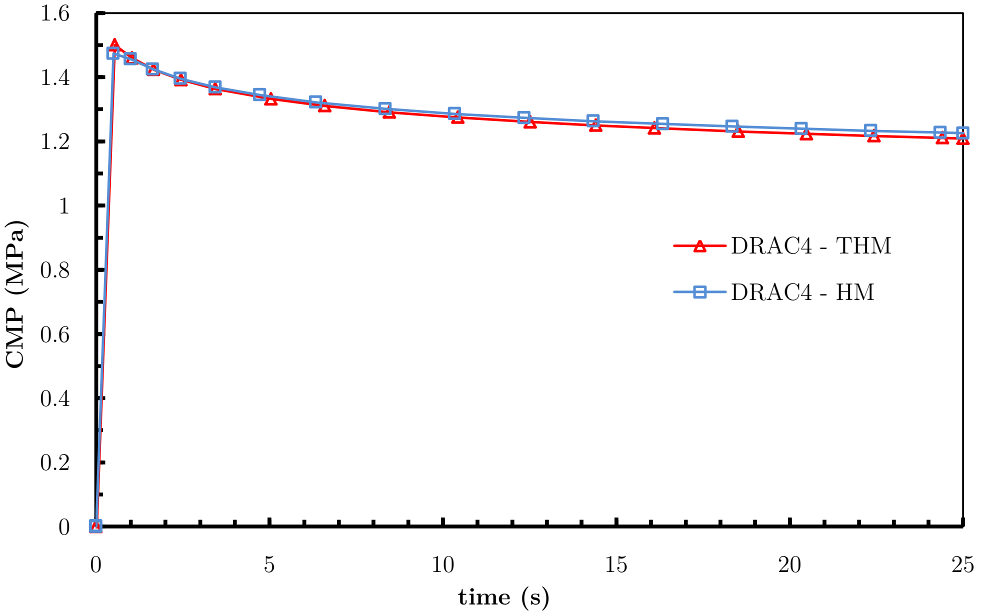

Figure 5.47: Crack mouth pressure evolution in the case with leak-off. Comparison between the HM analysis and the THM analysis with advection.

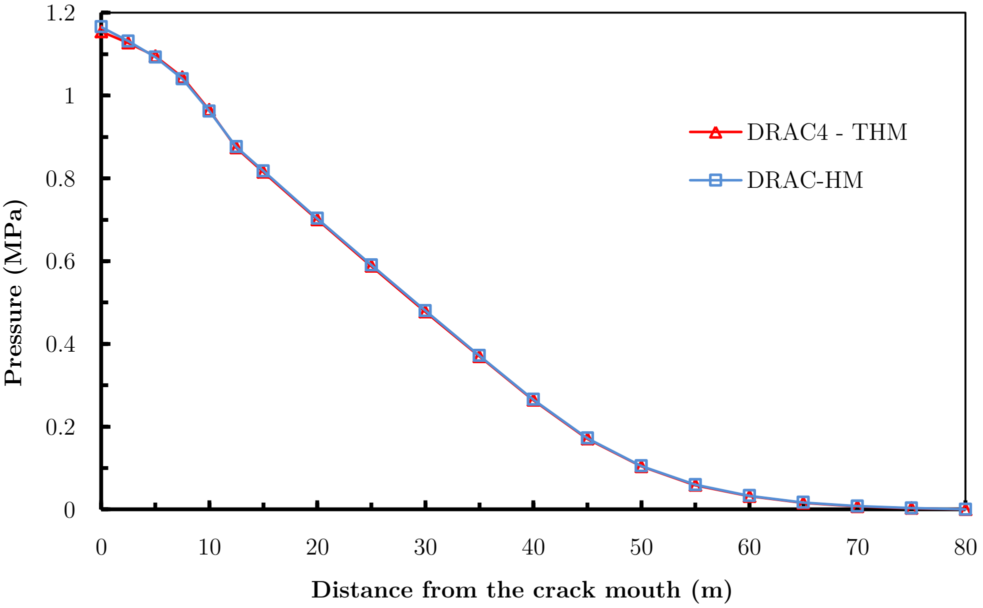

Figure 5.48: Pressure profile evolution along the mid-plane fracture in the case without leak-off at the end of the analysis (t = 25 s). Comparison between the HM analysis and the THM analysis with advection.

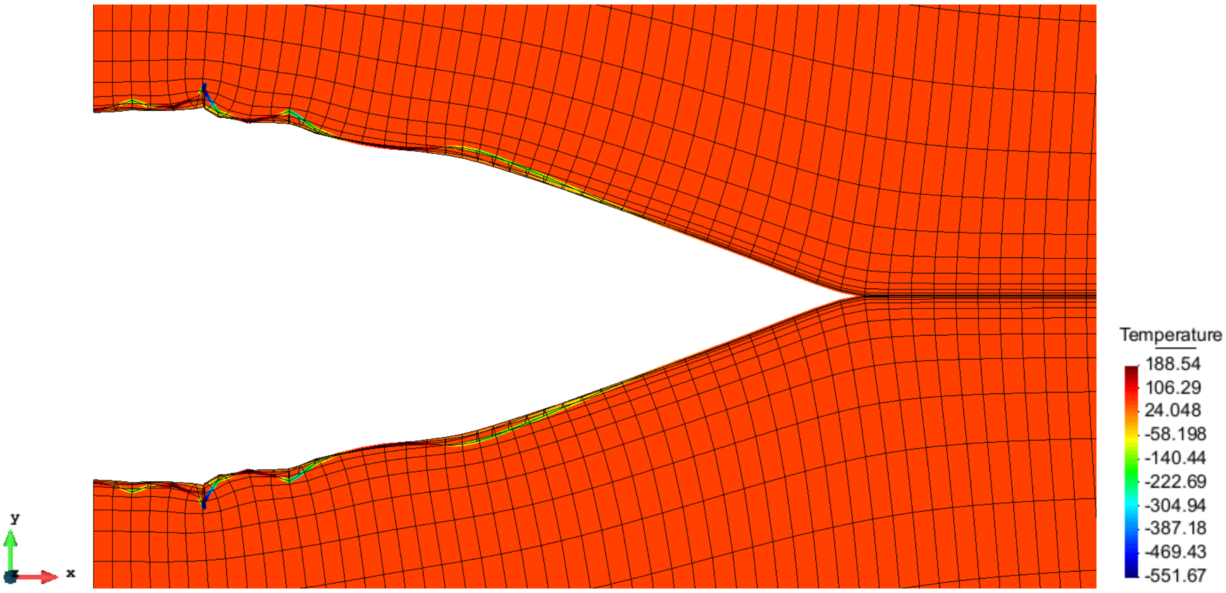

Figure 5.49: Temperature distribution in a deformed mesh (factor ×10000) at the end of the analysis with leak-off using the standard Galerkin weighting for the thermal advective FEM analysis.

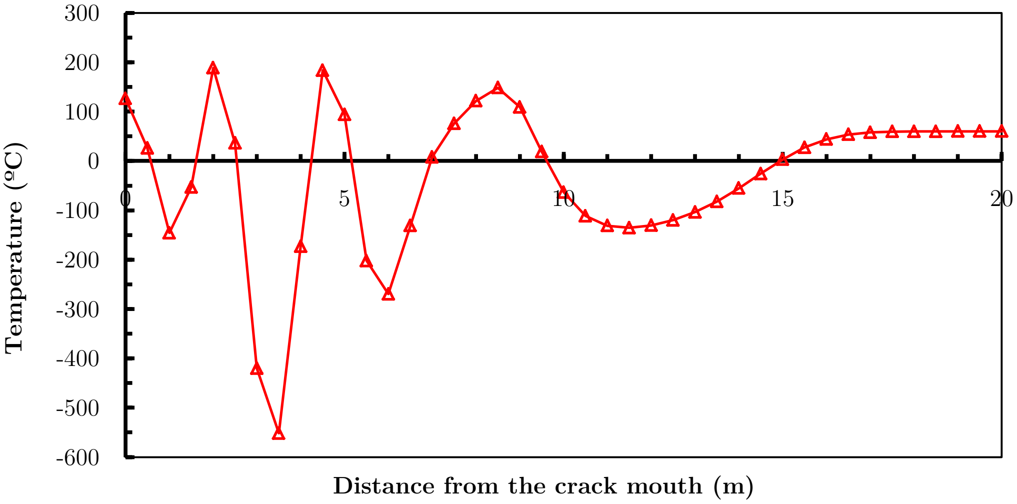

Figure 5.50: Temperature profile distribution along the mid-plane fracture with leak-off using the standard Galerkin weighting for the thermal advective FEM analysis (t = 25 s).

Parallelization performance analysis

As explained in Section 1.3, one of the main efforts in this thesis has been the numerical implementation of the THM model in the FEM code DRAC and its parallelization. For the parallelization the changes have focused on the modification of the code structure, the optimal partitioning of the FEM mesh using the library *METIS* (METIS_WebPage, 2013), the implementation of the parallel library *PETSc* (PETSc_Software, 2018) –which provides several parallel solvers–, the implementation of the parallel reading and writing (*input/output*) operations using the library *HDF5* (The_HDF_Group, 2018), the adaptation of the *HDF5 outputs* to the format visualization of *Paraview* (Paraview_WebPage, 2018), the minimization of RAM use and the optimal distribution of tasks between processors. In a first phase, in collaboration with other members of the group (Garolera, 2017), the parallelization of the HM code has been done. Then, the parallelization has been extended to the THM code.

The numerical analysis performed in the previous sections for single-fracture HF problems have been carried out with the parallel code using 24 processors. For this purpose, the high performance computer cluster TITANI (Civil Engineering School, UPC) has been used. This cluster is composed by 5 computer nodes Dell PowerEdge R630 and each node is composed by 2 processors of 12 cores Intel Xeon E5-2650L (1.8GHz), cache 30MB and 256GB of RAM.

Additionally, in order to verify the degree of parallelization achieved with the numerical parallelization of the FEM code DRAC, a scalability test has been performed for the HF pervious case. The simulations have been performed using the GMRES iterative solver and the ASM preconditioner provided by PETSc.

Figure 5.51 shows the evolution of the total time calculation as a function of the number of processors used. The figure shows that calculation times are high for the size of the mesh used. This may be due to the THM coupling (displacements, pressures and temperatures with different order of magnitude values), the element composition of the mesh (continuum and zero-thickness interfaces) and the shape of some continuum elements (some elongated elements), that lead to a bad conditioning of the global matrix.

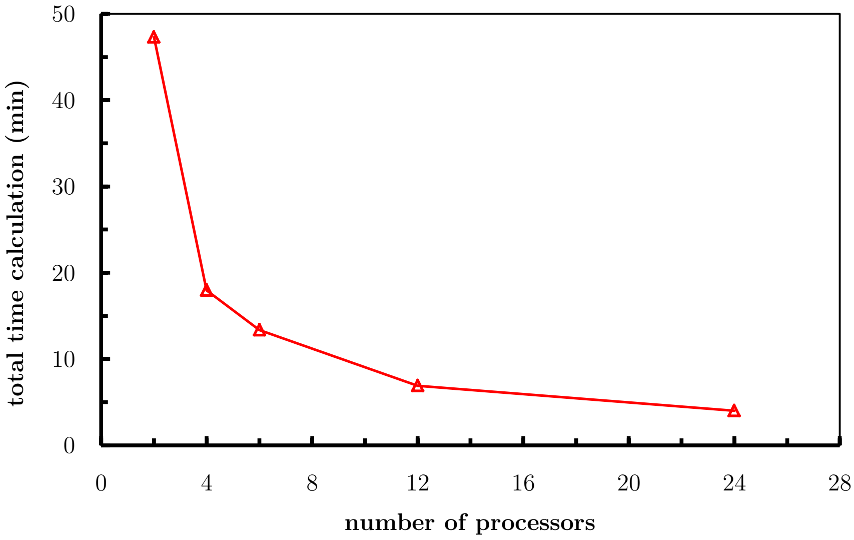

Figure 5.51: Required total time for the calculation with respect to the number of processors for the pervious HF case.

Figure 5.52 shows the speed-up curve of the calculations, where the horizontal axis shows the number of processors used, and the vertical axis the time of calculation normalized with respect to the time spent in the same calculation using two processors (taken as reference for the speed-up test). This figure shows a good degree of scalability of the parallelization.

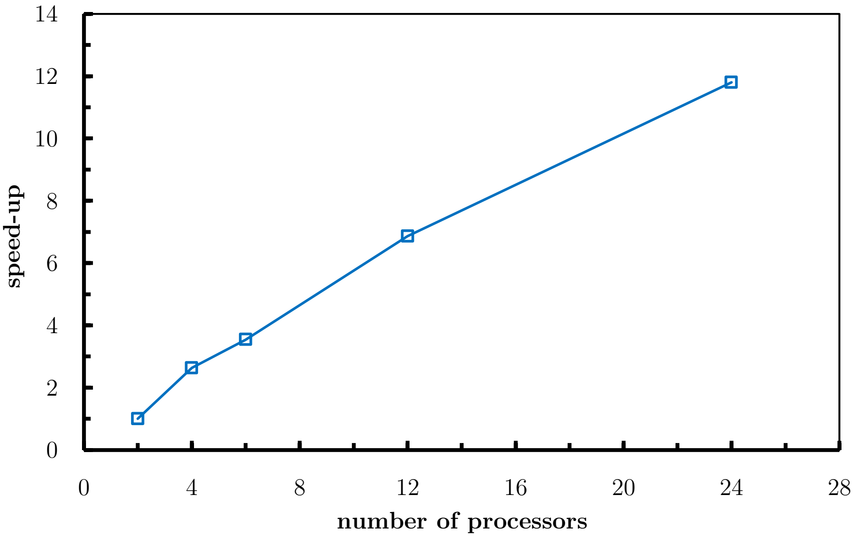

Figure 5.52: Speed-up for the calculation for the pervious HF case.

Finally, Figure 5.53 shows the subdomains resulting from the mesh partitioning done with METIS, using 4 and 24 processors.

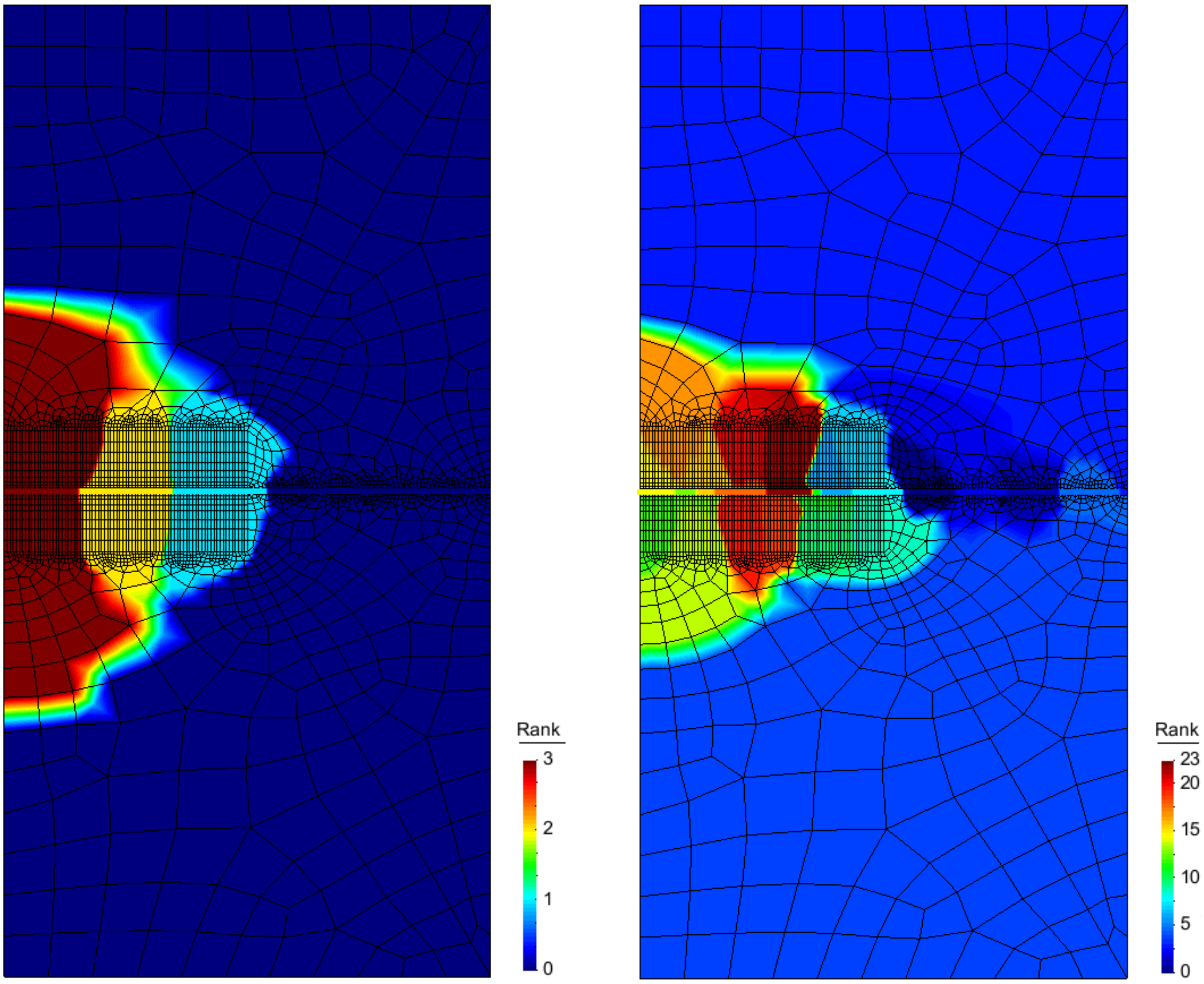

Figure 5.53: Resulting subdomains of the mesh partitioning done with METIS for 4 and 24 processors.

Chapter 6

Summary, conclusions and future research

The general objective of this thesis is the study, formulation, numerical implementation and verification (with simple application examples) of a coupled numerical model able to reproduce the thermo-hydro-mechanical advective behaviour that occur in discontinuities or fractures in which heat is transported by the fluid at high speed. The numerical approach is carried out in the geomechanical context of a fractured porous medium, using the FEM with zero-thickness interface elements to represent the discontinuities or fractures, and assuming saturated conditions, a single incompressible fluid (with constant density) and small strains. It is also assumed that all the non-linear behaviour occurs at the interface elements by means of an elasto-plastic constitutive law based on fracture mechanics, while poro-elasticity is used for the porous continuum medium.

Due to the high hydraulic velocities developed in discontinuities, the main thermal transport may occur through them and the advection may be the dominant heat transfer mode. The solution of the heat problem with large advection becomes unstable when solving the problem with the classic Galerkin weighting in FEM. Thus, one of the main objectives of this thesis, previous to the THM coupled formulation, is the study and numerical formulation of the heat equation with a methodology able to reproduce numerically the large advective heat transport problem.

Finally, the THM model with large advection is applied to an important case of interest that can be found in Petroleum Engineering: hydraulic fracture (HF) processes where the temperature of the injected fluid may lead to the generation of important temperature gradients that modifies the fluid properties (such as viscosity or density) and the stress field by means of induced thermal deformations. These modifications may affect the fracture process, with opening or closing of the fractures and, for instance, the production of the reservoir. In these cases, the hydraulic fracture area is situated at great depth, where the temperatures are high, while the injected fluid is located on the surface at ambient temperature. Thus, the injection of the fluid may produce important temperature gradients that could lead to significant variations of the mechanical behaviour of these fractures and the oil and gas production of the reservoir.

In the following sections the summary and conclusions of the main topics of this thesis are presented, about the numerical solution of large advection problem using the FEM, the formulation, numerical implementation and verification of the THM coupling model with large advection in continuum medium and zero-thickness interface elements and the application example to hydraulic fracture with temperatures. The last section deals with some possible future developments.

6.1. Summary and conclusions: numerical solution of large advection problems using the FEM

One of the main objectives of this thesis is the study and numerical formulation of a methodology to solve large advection problems using the FEM, in particular heat transport with a fluid. The standard Galerkin method leads to unstable solutions when the advection dominates the problem ($Pe > 1$) and a different method is necessary to reach a stable solution. Thus, chapters 2 and 3 present a review of different methodologies to solve the large advection problem for steady- and transient-states.

For the steady-state, the selected method is known as SUPG, a well-known method that leads to stable solutions when $Pe > 1$. However, since this method cannot be used to solve the transient problem, several methodologies are described in order to solve it, paying especial attention to the Characteristic-based methods. These methods carry the study of the transport phenomena in a Lagrangian manner, following the particle (or heat) with the fluid movement, by setting a moving coordinate system that depends on the fluid velocity and its position in time.

In this context, this thesis starts with the study of the existing explicit Characteristic Galerkin Method developing, as a first step, its implicit form. Additionally, this thesis proposes a new variation of this method adding an α parameter that allows to determine different temporal derivative positions of the advective volume, leading to the α-Implicit Characteristic Galerkin Method. With this new method, the large advective transient solution becomes stable if the Courant condition is fulfilled.

Chapters 2 and 3 are dedicated to the development of the formulation of this method and its numerical implementation, both for continuum medium and zero-thickness interface elements. The method has been tested with different values of α, concluding that the best value to reach stable solutions is $\alpha = 0.25$ and becomes unstable when $\alpha \geq 0.50$ or $\alpha < 0$.

6.2. Summary and conclusions: THM coupling with large advection

One of the most important tasks of this thesis, and which has entailed the main effort, has been the formulation and numerical implementation in the FEM code DRAC of the thermo-hydro-mechanical coupling with large advection, for continuum medium and zero-thickness interface elements.

First, the THM coupling has been implemented following a staggered scheme, solving the HM coupling with the existing code DRAC and the thermal problem with a new code, T-DRAC where the thermal advective problem has been implemented. Later, the formulation and numerical implementation has been extended to a fully-coupled scheme on DRAC, solving the problem with a Newton-Raphson iterative strategy. The staggered scheme has been developed in the early stages of the thesis and has been used to verify the correct performance of the fully-coupled implementation by comparing results of simple academic examples. Then, the fully-coupled scheme has been used to solve the verification and practical application examples.

The interactions considered in this thesis between the thermal, hydraulic and thermal fields, for a saturated and fractured porous medium, may be summarized as:

- **Thermal expansion:** the first phenomenon is the thermal expansion of the solid material phase due to the temperature increment and its coefficient of thermal expansion, which only affects to continuum porous medium and not the interfaces. This thermal expansion produces the variation of the total volume (thermal strains) and, consequently, of the total pore volume, modifying the available space for the fluid in the porous medium. Additionally, the temperature variation affects the fluid that fills the pores or discontinuities, leading to volume changes of the fluid that are proportional to its coefficient of thermal expansion. These changes of the pores and fluid volume modify the pressure distribution in the hydraulic problem, and subsequently the effective stresses in the mechanical problem.
- **Advection:** fluid velocities (Darcy velocities) from the hydraulic problem generate heat transport and modify the thermal field. This affects mainly the interface elements, which conform preferential paths where fluid may flow at high speed.
- **Longitudinal and transversal heat transmissivity in interfaces:** the opening of the discontinuities may change the quantity of fluid that fills them (considering saturated medium), leading to a variation on the in-plane heat transmissivity, since the heat storage capacity depends on the quantity of fluid filling the discontinuities. Moreover, the transversal heat transmissivity may be also modified with the opening of the interfaces in the transversal direction that the heat flow has to cross.
- **Fluid density and dynamic viscosity variations:** as shown in Figure 4.1., density and dynamic viscosity of water varies with temperature. The variation of the dynamic viscosity of the fluid leads to a variation of the hydraulic conductivity and the fluid velocity field, which produces heat transport with the fluid and a variation of the

distribution of temperatures obtained from the thermal analysis. However, the variation of water density in the temperature range from 10 to 60℃, which is the range of temperature variation in the applications of interest in this thesis, is around 1.5%. For this reason, the variation of density of the fluid is omitted in the THM formulation of this thesis. Although the density is assumed constant, its thermal expansion is considered as explained in the previous section "thermal expansion".

- **Effective stresses:** fluid pressures from the hydraulic problem modify the effective stresses of the mechanical problem by means of the effective stress principle (assuming saturated conditions).
- **Longitudinal hydraulic transmissivity in interfaces:** from a hydraulic point of view, the interface opening modifies its hydraulic storage capacity and longitudinal conductivity, which depends on the aperture.

6.3. Summary and conclusions: application to hydraulic fracture and parallel performance

Finally, this thesis presents an application example to hydraulic fracture, considering a single fracture problem in 2-D. The fundamental objective of this example is to understand the thermal mechanisms that occur in hydraulic fracture problems and how they affect the mechanical and hydraulic fields. The results have been compared with those obtained using a HM model developed by Segura (2007) and Garolera (2017), which does not consider thermal effects.

The results of the analysis, where a cold fluid (10℃) is injected into a warm rock mass (60℃) show that the THM model is able to reproduce the large advection thermal problem without oscillations in the impervious HF example. However, a single "wave" oscillation moving with the temperature front and the crack tip appears in the pervious one. Whether it is caused by numerical effects or is a physical phenomenon remains to be clarified more precisely. For both pervious and impervious analysis, the crack mouth opening is larger when the thermal field is considered (around 10%), mainly due to heat interchange between the rock mass and the fluid, which produces the contraction of the rock mass and the expansion of the injected fluid. Additionally, the crack length tends to be slightly smaller for the impervious HF case and similar for the pervious one.

Without this model, the heat transfer would only occur by conduction with a heat advance of a few centimetres from the mouth of the crack, and consequently the hydraulic fracture analysis with temperature would not have been possible. Additionally, it has been shown that the solution of the problem using the standard Galerkin weighting leads to unstable numerical solutions, while the Implicit Characteristic Galerkin Method stabilizes the solution.

Additionally, in order to improve the efficiency of the calculations, the parallelization of code DRAC has been performed in collaboration with other members of the research group

(Garolera, 2017); first for the HM code and later extended for the THM with advection code. The changes have focused on the modification of the code structure, the optimal partitioning of the FEM mesh using the library *METIS*, the implementation of the parallel library *PETSc* –which provides several parallel solvers–, the implementation of the parallel reading and writing (*input/output*) operations using the library *HDF5*, the adaptation of the *HDF5 outputs* to the format visualization of *Paraview*, the minimization of RAM use and the optimal distribution of tasks between processors. As shown in section 5.2.2 the results obtained from the parallel performance analysis have shown a good degree of scalability of the parallel code.

6.4. Future research

The research work developed and the results obtained in this doctoral thesis have allowed to envisage some possible enhancements that would extend the applicability of the developed THM model with large advection and would make more efficient the numerical calculations. Some of the possible future developments are listed below:

- Perform the analysis of multi-stage hydraulic fracture problems and its extension to 3D.
- Multiphase fluid flow: thermal effects can induce phase transitions of the injected fluids from liquid to gas. Additionally, the reservoirs composition are a mixture of oil, water and gas. Thus, it will be optimal to simulate the hydraulic fracture problems with the real composition of the fluids and its phase transitions in the numerical models. These enhancements are conditioned to the formulation of the problem for variable density and compressible fluids.
- Consider a second node temperature variable in order to distinguish between the temperature of the solid and the temperature of the fluid, and the coupling between them in a convective manner.
- Consider a new advective field of proppant concentration and its coupling with the actual THM coupled model, in order to consider the transport of proppant with the fluid in hydraulic fracture problems.
- Apply the current THM model with large advection to CO_2 injection problems.
- The current parallelization of the FEM code DRAC does not consider that the non-linear behaviour may be concentrated in a few subdomains (or processors), and the speed of the entire calculation may be penalized by the speed of these subdomains. The so-called load-balancing algorithms may avoid this trouble performing the mesh partitioning by distributing the elements considering the computation effort of each subdomain, and not only considering the number of elements of each subdomain and the minimization of border elements between them, as it is done now.
- To develop a fracture energy-based constitutive law for zero-thickness interface elements with partial closure effect. Current constitutive models consider either full closure when unloading or no closure at all. An elasto-plastic model with damage could model partial

closure in order to reproduce more realistic effects for hydraulic fracture problems using proppant.

- In the current code the interface elements are pre-inserted and fractures can only propagate along them. By pre-inserting a sufficient number of interfaces, the fracture can develop with relative freedom, but with an expensive computational effort. To improve this methodology and avoid having to pre-insert a high number of interfaces in the mesh, allowing the fracture to develop in the whole domain, two options may be considered: the use of zero-thickness interface elements with node relocation or use a hybrid zero-thickness/XFEM formulation.

References

Adachi, J., Siebrits, E., Peirce, A. & Desroches, J., 2007. Computer simulation of hydraulic fractures. *International Journal of Rock Mechanics and Mining Sciences,* Volume 4(5), p. 739–757.

Adey, R. & Brebbia, C., 1974. Finite element solution of effluent dispersion. In: *Numerical Methods in Fluid Mechanics.* Southampton (UK): Pentech Press, pp. 325-54.

Amadei, B., Sture, S., Saeb, S. & Atkinson, R., 1989. *An evaluation of masonry joint shear strength in existing buildings. Report to NSF, Dept. of Civil, Environmental and Architectural Engineering,* Boulder: University of Colorado.

Bercovier, M., Pironneau, O., Harbani, Y. & Leveine, E., 1982. Characteristics and finite element methods applied to equation of fluids. In: *The Mathematics of Finite Elements and Applications.* Academic Press, London: ed. J.R. Whiteman, pp. 471-8, vol V.

Bercovier, M., Pironneau, O. & Sastri, V., 1983. Finite elements and characteristics for some parabolic-hyperbolic problems. *Applied Mathematics Modelling,* Volume 7, pp. 89-96.

Biaocchi, C., Brezzi, F. & Franca, L., 1993. Virtual bubbles and Galerkin-least-squares type methods. *Computer Methods in Applied Mechanics and Engineering,* Volume 105, pp. 125-141.

Biot, M., 1941. A general theory of three dimensional consolidation. *Journal of Applied Physics,* Volume 12, pp. 155-164.

Boone, T. J. & Ingraffea, A. R., 1990. A numerical procedure for simulation of hydraulically-driven fracture propagation in poroelastic media.. *International Journal for Numerical and Analytical Methods in Geomechanics,* Volume 14(1), pp. 27-47.

Brezzi, F., Bristeau, M.O., Franca, L.P, Mallet, M., Rogé, G., 1992. A relationship between stabilized finite element methods and the Galerkin method with bubble functions. *Computer Methods in Applied Mechanics and Engineering,* Volume 96, pp. 117-129.

Brooks, A. & Hughes, T., 1982. Streamline upwind/Petrov-Galerkin formulations for convection dominated flows with particular emphasis on the incompressible Navier-Stokes equations. *Computer Methods in Applied Mechanics and Engineering,* Volume 32, pp. 199-259.

Caballero, A., 2005. 3D meso-mechanical numerical analysis of concrete fracture using interface elements. *PhD Thesis*: Universitat Politècnica de Catalunya. Barcelona.

Caballero, A., Willam, K. & Carol, I., 2008. Consistent tangent formulation for 3d interface modeling of cracking/fracture in quasi-brittle materials. *Computer Methods in Applied Mechanics and Engineering,* Volume 197(33–40), p. 2804 – 2822.

Cardle, J., 1995. A modification of the Petrov-Galerkin method for the transient convection diffusion equation. *International Journal for Numerical Methods in Engineering,* Volume 38, pp. 171-81.

Carey, G. & Jiang, B., 1988. Least square finite elements for first order hyperbolic systems. *International Journal for Numerical Methods in Engineering,* Volume 26, pp. 81-93.

Carol, I., Lopez, C. M. & Roa, O., 2001. Micromechanical analysis of quasi-brittle materials using fracture-based interface elements. *International Journal for Numerical Methods in Engineering,* Volume 52, p. 193–215.

Carol, I. & Prat, P., 1990. A statically constrained microplane model for the smeared analysis of concrete cracking. In: *Computer-Aided Analysis and Design of Concrete Structures, Vol II.* Ed: Pineridge Press, p. 919–930.

Carol, I. & Prat, P., 1995. A multicrack model based on the theory of multisurface plasticity and two fracture energies. In: *Computational Plasticity, COMPLAS IV, Vol. II.* Ed: Pineridge Press, p. 1583–1594.

Carol, I., Prat, P. & Lopez, C., 1997. Normal/shear cracking model: application to discrete crack analysis. *Journal of engineering mechanics,* Volume 123(8), pp. 765-773.

Christie, I., Griffiths, A. & Zienkiewicz, O., 1976. Finite element methods for second orde differential equations with significant first derivatives. *International Journal for Numerical Methods in Engineering,* Volume 10, pp. 1389-96.

Cockburn, B., Karniadakis, B. & Shu, C., 2000. Discontinuous Galerkin Methods. Theory, Computation and Applications. *Notes in Computational Sciene and Engineering, Springer.*

Codina, R., 1992. Stability analysis of forward Euler scheme for convection diffusion equation using the SUPG formulation in space. *Int. J. Num. Meth. Eng.,* Volume 36, pp. 1445-64.

Codina, R., 1998. Comparison of some finite elements methods for solving the diffusion-convection-reaction equation. *Computer Methods in Applied Mechanics and Engineering,* Volume 156, pp. 185-210.

Codina, R., Oñate, E. & Cervera, M., 1992. The intrinsic time for the streamline upwind Petrov-Galerkin formulation using quadratic elements. *Computer Methods in Applied Mechanics and Engineering,* Volume 94, pp. 239-62.

Costarelli, S., Stortia, M., Paza, R., Dalcina, L., Idelsohn, S., 2013. GPGPU implementation of the BFECC algorithm for pure advection equations. *Cluster Computing,* Volume 17(2), pp. 243-254.

de Sampaio, P., Lyra, P., Morgan, K. & Weatherill, N., 1993. Petrov-Galerkin solutions of the incompressible Navier-Stokes equations in primitive variables with adaptive remeshing. *Computer Methods in Applied Mechanics and Engineering,* Volume 106, pp. 143-78.

Desai, C., Zamman, M., Lightner, J. & Siriwardane, H., 1984. Thin-layer element for interfaces and joints. *International Journal of Numerical and Analytical Methods in Geomechanics,* Volume 4(8), pp. 19-43.

Donea, J., 1984. A Taylor-Galerkin method for convective transport problems. *International Journal for Numerical Methods in Engineering,* Volume 20, pp. 101-19.

Douglas, J. & Russell, T., 1982. Numerical methods for convection dominated diffusion problems based on combining the method of characteristics with finite element or finite difference procedures. *SIAM Journal on Mathematical Analysis,* Volume 19, pp. 871-85.

Ewing, R. & Russell, T., 1981. Multistep Galerkin methods along characteristics for convection-diffusion problems. In: *Advances in Computation Methods for PDE's.* Rutgers University, Brunswick, N.J.: ed. R. Vichnevetsky and R.S. Stepleman, pp. 28-36. Volume IV, IMACS.

Franca, L. & Farhat, C., 1994. Bubble functions prompt unusual stabilized finite element methods. *Computer Methods in Applied Mechanics and Engineering,* Volume 123, pp. 299-308.

Garolera, D., 2017. Zero-thickness interface elements in petroleum geomechanics: sand production and hydraulic fracture. *PhD Thesis:* Universitat Politècnica de Catalunya, Barcelona.

Garolera, D. et al., 2014. Hydro-mechanical coupling in zero-thickness interface elements, formulation and applications in geomechanics. *Rock Engineering and Rock Mechanics: Structures in and on Rock Masses – Ed: Alejano, Perucho, Olalla & Jiménez. Taylor & Francis Group, London, 978-1-138-00149-7,* pp. 1379-1384.

Garolera, D., Lopez, C., Carol, I. & Papanastasiou, P., 2005. Micromechanical analysis of the rock sanding problem. *Journal of the Mechanical Behavior of Materials,* Volume 16, p. 45–53.

Geertsma, J. & De Klerk, F., 1969. A Rapid Method of Predicting Width and Extent of Hydraulically Induced Fractures. *J. Pet. Tech,* Volume 246, p. 1571–1581.

Ghaboussi, J., Wilson, E. & Isenberg, J., 1973. Finite element for rock joints and interfaces. *ASCE Journal of the Soil Mechanics and Foundations Division,* Volume 99(SM10), p. 833–848.

Goodman, R., Taylor, R. & Brekke, T., 1968. A model for the mechanics of jointed rock. *ASCE Journal of the Soil Mechanics and Foundations Division,* Volume 94(SM3), p. 637–659.

Guymon, G., Scott, V. & Herrmann, L., 1970. A general numerical solution of the two dimensional diffusion-convection equation by the finite element method.. *Water Resources Res.,* Volume 6, pp. 1611-17.

Heinrich, J. & Zienkiewicz, O., 1977. Quadratic finite element schemes for two dimensional convective-transport problem. *Int. J. Num. Meth. Eng,* Volume 11, pp. 1831-44.

Hirsch, C., 1989. *Numerical Computation of Internal and External Flows, Vol. 1.* Ed:John Wiley.

Huber, M.L.; Perkins, R.A.; Laesecke, A.; Friend, D.G.; Sengers, J.V.; Assael, M.J.; Metaxa, I.N.; Vogel, E.; Mares, R.; Miyagawa, K., 2009. New International Formulation for the Viscosity of H2O. *Journal of Physical Chemistry,* 38(2), pp. 101-125.

Hughes, T., 1995. Multiscale phenomena: Green's function, the Dirichlet-to-Neumann formulation, subgrid scale models, bubbles and the origin of stabilized formulations. *Computer Methods in Applied Mechanics and Engineering,* Volume 127, pp. 387-401.

Hughes, T. & Atkinson, J., 1980. A variational basis of "upwind" finite elements. In: *Variational Methods in the Mechanics of Solids.* Pergamon Press, Oxford: Ed. S. Nemat-Nasser, pp. 387-91.

Hughes, T. & Brooks, A., 1979. A multidimensional upwind scheme with no crosswind diffusion. *In ASME Monograph AMD-34 (Hughes, T.J.R., Ed.). NYC.,* Volume 34.

Hughes, T., Franca, L. & Hulbert, G., 1989. A new finite element formulation for cumputational fluid dynamics. VIII. the Galerkin/least squares methods for advective-diffusive systems. *Computer Methods in Applied Mechanics and Engineering,* Volume 73, pp. 173-189.

Hughes, T., Franca, L. & Mallet, M., 1987. A new finite element formulation for computational fluid dynamics: I. Symmetric forms of the compressible Euler and Navier-Stokes equations and the second law of thermodynamics.. *Computer Methods in Applied Mechanics and Engineering,* Volume 63, pp. 97-112.

Hughes, T. & Mallet, M., 1986. A new finite element formulation for computational fluid dynamics: III. The generalized streamline operator for multidimensional advective-diffusive systems. *Computer Methods in Applied Mechanics and Engineering,* Volume 58, pp. 305-328.

Hughes, T. & Tezduyar, T., 1984. Finite element methods for first-order hyperbolic systems with particular emphasis on the compressible Euler equations. *Computer Methods in Applied Mechanics and Engineering,* Volume 45, pp. 217-284.

IAPWS, 2008. Release on the IAPWS Formulation for the Viscosity of Ordinary Water Substance. *International Association for the Properties of Water and Steam.* Berlin.

Idelsohn, S., Heinrich, J. & Oñate, E., 1996. Petrov-Galerkin methods for the transient advective-diffusive equation with sharp gradients. *International Journal for Numerical Methods in Engineering,* Volumen 39, pp. 1455-73.

Idelsohn, S. & Oñate, E., 1994. Finite element and finite volumes. Two good friends. *International Journal for Numerical Methods in Engineering,* Volume 37, pp. 3323-41.

Idiart, A., López, C. & Carol, I., 2011. Chemo-mechanical analysis of concrete cracking and degradation due to external sulfate attack: A meso-scale model. *Cement & Concrete Composites,* Volume 33 , pp. 411-423.

Jiang, B. & Carey, G., 1988. A stable least-square finite element method for non-linear hyperbolic problems. *International Journal for Numerical Methods in Engineering,* Volume 8, pp. 933-42.

Johnson, C., 1986. Stramline diffusion elements for problems in fluid mechanics. In: *Finite Elements in Fluids.* Wiley, Chichester (UK): R.H. Gallagher et. al., pp. 251-61, Vol. 6.

Johnson, C., Navertu, U. & Pitkaranta, J., 1984. Finite element methods for linear hyperbolic problems. *Computer Methods in Applied Mechanics and Engineering,* Volume 45, pp. 285-312.

Lewis, R. & Schrefler, B., 1998. *The Finite Element Method in the Static and Dynamic Deformation and Consolidation of Porous Media.* 2nd ed. Chichester: John Wiley & Sons.

Li, L. et al., 2012. Numerical Simulation of 3D Hydraulic Fracturing Based on an Improved Flow-Stress-Damage Model and a Parallel FEM Technique. *Rock Mechanics and Rock Engineering,* Volume 45(5), pp. 801-818.

Lin, P. & Morton, K., 1997. Characteristic Galerkin schemes for scalar conservation laws in two and three space dimensions. *SIAM Journal on Numerical Analysis,* Volume 34, pp. 779-96.

Löhner, R., Morgan, K. & Zienkiewicz, O., 1985. An adaptive finite element procedure for compressible high speed flows. *Computer Methods in Applied Mechanics and Engineering,* Volume 51, pp. 441-65.

López, C. M., 1999. Análisis microestructural de la fractura del hormigón utilizando elementos finitos tipo junta. Aplicación a diferentes hormigones. *PhD thesis*: Universitat Politècnica de Catalunya, Barcelona.

Maji, P. & Biswas, G., 1999. Analysis of flow in the spiral casing using a streamline upwind Petrov-Galerkin method. *International Journal for Numerical Methods in Engineering,* Volume 45, pp. 147-74.

METIS_WebPage, 2013. *METIS and ParMETIS WebPage.* [Online] Available at: http://glaros.dtc.umn.edu/gkhome/views/metis [Accessed 28 06 2018].

Morton, K., 1985. Generalized Galerkin methods for hyperbolic problems. *Computer Methods in Applied Mechanics and Engineering,* Volume 52, pp. 847-71.

Nadukandi, P., Oñate, E. & García, J., 2010. A high resolution Petrov-Galerkin method for the 1D convection-diffusion-reaction problem. *Computer Methods in Applied Mechanics and Engineering,* pp. 525-546.

Nadukandi, P., Oñate, E. & García, J., 2012. A high resolution Petrov-Galerkin method for the convection-diffusion-reaction problem. Part II - A multidimensional extension. *Computer Methods in Applied Mechanics and Engineering,* pp. 327-352.

Nguen, N. & Reynen, J., 1984. A space-time least square finite element scheme for advection-diffusion equations. *Computer Methods in Applied Mechanics and Engineering,* Volume 42, pp. 331-42.

Nordgren, R., 1972. *Propagation of a Vertical Hydraulic Fracture,* s.l.: Society of Petroleum Engineers.

Olofsson, T., 1985. A non-linear model for the mechanical behavior of continuous rock joints.. In: *International Symposium on Fundamentals of Rock Joints.* Bjorkliden, Sweden: Centek Publishers, pp. 395-404.

Oñate, E., 1998. Derivation of stabilized equations for numerical solution of advective-diffusive transport and fluid flow problems. *Computer Methods in Applied Mechanics and Engineering,* Volume 151, pp. 233-65.

Oñate, E. & Idelsohn, S., 1988. A mesh free finite point method for advective-diffusive transport problems. *Computational Mechanics,* Volume 21, pp. 283-292.

Oñate, E.; Idelsohn, S.; Zienkiewicz, O.C.; Taylor, R.L.; Sacco, C., 1996b. A stabilized finite point method for fluid mechanics. *Computer Methods in Applied Mechanics and Engineering,* Volume 139, pp. 315-247.

Oñate, E., Idelsohn, S. & Zienkiewicz, O. T. R., 1996. A finite point method in computational mechanics. Applications to convective transport and fluid flow. *International Journal for Numerical Methods in Engineering,* Volumen 39, pp. 3839-66.

Oron, A. & Berkowitz, B., 1998. Flow in rock fractures: The local cubic law assumption reexamined. *Water Resources Research,* 34(11), pp. 2811-2825.

Pande, G. N., Beer, G. G. & Williams, J. R., 1990. *Numerical methods in rock mechanics.* Ed:John Wiley & Sons.

Paraview_WebPage, 2018. *Paraview Official WebPage.* [Online] Available at: https://www.paraview.org/ [Accessed 28 06 2018].

Pérez, A., 2013. *Modelización mesomecánica 3D de la fisuración y fractura por efectos térmicos en geomateriales.* Master Thesis: Universitat Politècnica de Catalunya, Barcelona..

Pérez-Foguet, A., Rodríguez-Ferran, A. & Huerta, A., 2001. Consistent tangent matrices for substepping schemes. *Computer Methods in Applied Mechanics and Engineering,* Volume 190(35–36), p. 4627–4647.

Perkins, T. & Kern, L., 1961. Widths of Hydraulic Fractures*. Journal of Petroleum Technology.* Volume 13. Issue 09.

PETSc_Software, 2018. *PETSc Official WebPage.* [Online] Available at: https://www.mcs.anl.gov/petsc/ [Accessed 28 06 2018].

Pironneau, O., 1982. On the transport diffusion algorithm and its application to the Navier-Stokes equation. *Numerical Math.,* Volume 38, pp. 309-32.

Pironneau, O., Liou, J. & Tezduyar, T., 1992. Characteristic Galerkin and Galerkin least squares space-time formulations for the advection-diffusion equation with time dependent domain. *Computer Methods in Applied Mechanics and Engineering,* Volumen 100, pp. 117-41.

Prat, P.; Gens, A.; Carol, I.; Ledesma, A.; Gili, J., 1993. DRAC: A computer software for the analysis of rock mechanics problems. In: H. Liu, ed. *Application of Computer Methods in Rock Mechanics.* Publisher: Shaanxi Science and Technology Press, pp. 1361-68.

Riera, C., 2016. *Modelització mesomecànica 3D d'atac sulfàtic extern en formigó.* Master Thesis: Universitat Politècnica de Catalunya, Barcelona.

Roa, O. et al., 2002. On the use of generated geometries for the numerical analysis of trabecular bone specimens. *Computer Methods in Biomechanics and Biomedical Engineering. Proceedings of the Int. Conf. on Science & Technology.*

Secchi, S. & Schrefler, B., 2012. A method for 3-D hydraulic fracturing simulation. *International Journal of Fracture,* Volume 178(1-2), p. 245–258.

Segura, J., 2007. Coupled HM analysis using zero-thickness interface elements with double nodes. *PhD Thesis. Universitat Politècnica de Catalunya, Barcelona.*

Segura, J. & Carol, I., 2004. On zero-thickness interface elements for diffusion problems. *International Journal for Numerical and Analytical Methods in Geomechanics,* Volume 28(9), p. 947–962.

Segura, J. & Carol, I., 2008a. Coupled HM analysis using zero-thickness interface elements with double nodes. Part I: Theoretical model. *International Journal for Numerical and Analytical Methods in Geomechanics,* Volume 32(18), p. 2083–2101.

Segura, J. & Carol, I., 2008b. Coupled HM analysis using zero-thickness interface elements with double nodes. Part II: Verification and application. *International Journal for Numerical and Analytical Methods in Geomechanics,* Volume 32(18), p. 2103–2123.

Sharma, K. & Desai, C., 1992. Analysis and implementation of thin-layer element for interfaces and joints. *ASCE Journal of Engineering Mechanics,* Volume 118(12), pp. 2442-2462.

Smith, I. & Griffths, D., 2004. *Programming the finite element method.* Fourth ed. Ed: John Willey and Sons.

Terzaghi, K., 1925. *Erdbaumechanik auf Bodenphysikalischer Grundlage.* Leipzig: Franz Deuticke.

The_HDF_Group, 2018. *The HDF Group WebPage.* [Online] Available at: https://support.hdfgroup.org/HDF5/ [Accessed 28 06 2018].

Thomas, H. & Zhou, Z., 1997. Minimum time-step size for diffusion problem in FEM analysis. *International Journal for Numerical Methods in Engineering,* Volume 40, pp. 3865-3880.

Warpinski, N., Abou-Sayed, I., Moschovidis, Z. & Parker, C., 1994. Comparison Study of Hydraulic Fracturing Models-Test Case: GRI Staged Field Experiment No.3. *SPE Production & Facilities,* Volume 9(01), pp. 7-16.

Witherspoon, P., Wang, J., Iwai, K. & Gale, J., 1980. Validity of cubic law for fluid flow in a deformable rock fracture. *Water Resources Research,* 16(6), pp. 1016-1024.

Yew, C., 1997. *Mechanics of Hydraulic Fracturing.* Ed:Elseiver Science.

Yu, C. & Heinrich, J., 1986. Petrov-Galerkin methods for the time dependent convective transport equation. *International Journal for Numerical Methods in Engineering,* Volume 23, pp. 883-901.

Yu, C. & Heinrich, J., 1987. Petrov-Galerkin method for multidimensional, time dependent convective diffusion equation.. *International Journal for Numerical Methods in Engineering,* Volume 24, pp. 2201-15.

Zienkiewicz, O., Best, B., Dullage, C. & Stagg, K., 1970. *Analysis of nonlinear problems in rock mechanics with particular reference to jointed rock systems.* Belgrade, Second International Congress on Rock Mechanics.

Zienkiewicz, O. & Bettess, P., 1982. Soils and other saturated media under transient, dynamic conditions: general formulation and the validity of varius simplifying assumptions. In: Zienkiewicz & Pande, eds. *Soil Mechanics - Transient and Cyclic Loads.* Ed.:Wiley.

Zienkiewicz, O. & Codina, R., 1996. A general algoritm for compressible and incompressible flow. Part I: The split, characteristic scheme. *International Journal for Numerical Methods in Fluids,* Volumen 20, pp. 869-85.

Zienkiewicz, O., Gallagher, R. & Hood, P., 1976. Newtonian and non-Newtonian viscous incompressible flow. Temperature induced flows and finite element solutions. *The Mathematics of Finite Element Methods (ed J. Whiteman). Academic Press, London.,* Volume II.

Zienkiewicz, O., Heinrich, J. & Huyakorn, P. M. A., 1977. An upwind finite element scheme for two dimensional convective transport equations.. *Int. J. Num. Meth. Eng.,* Volume 10, pp. 131-144.

Zienkiewicz, O., Löhner, R. & Morgan, K., 1985. High speed inviscid compressive flow by the finite element method. In: *The Mathematics of Finite Elements and Applications.* Academic Press, London: ed. J.R. Whiteman, pp. Volume VI, pp. 1-25.

Zienkiewicz, O., Löhner, R., Morgan, K. & Nakazawa, S., 1984b. The solution of non-linear hyperbolic equation systems by the finite element method. *International Journal for Numerical Methods in Fluids,* Volume 4, pp. 1043-63.

Zienkiewicz, O., Löhner, R., Morgan, K. & Nakazawa, S., 1984. Finite element in fluid mechanics - a decade of progress. In: *Finite Elements in Fluids.* Wiley, Chichester (UK): ed R.H. Gallagher et al, pp. Volume 5, chapter 1, pp 1-26.

Zienkiewicz, O., Löhner, R., Morgan, K. & Peraire, J., 1986. High speed compressible flow and other advection dominated problems of fluid mechanics. En: *Finite Elements in Fluids.* Wiley, Chichester (UK): ed. R.H. Gallagher et al, pp. Volume 6, chap. 2, pp. 41-88.

Zienkiewicz, O. & Taylor, R., 2000a. *The Finite Element Method: Vol 1. The basis.* Fifth ed. Oxford: Butterworth Heinemann.

Zienkiewicz, O. & Taylor, R., 2000b. *The Finite Element Method: Vol 2. Solid Mechanics.* Fifth ed. Oxford: Butterworth Heinemann.

Zienkiewicz, O. & Taylor, R., 2000c. *The Finite Element Method: Vol 3. Fluid Dynamics.* Fifth ed. Oxford: Butterworth-Heinemann.

Appendix A

Acronyms

FEM - Finite Element Method

DFM - Difference Finite Method

THM - Thermo-Hydro-Mechanical

TH - Thermo-Hydraulic

HM - Hydro-Mechanic

TM - Thermo-Mechanic

PVW - Principle of Virtual Works

SUPG - Streamline Upwind Petrov-Galerkin

GLS - Galerkin Least Squares

FIC - Finite Increment Calculus

ICG - Implicit Characteristic Galerkin

HF - Hydraulic Fracture

CMOD - Crack Mouth Opening Displacement

CMP - Crack Mouth Pressure